



HAL
open science

Antibacterial Mechanisms of Pristine Zinc-Based Layered Double Hydroxides

Jazia Awassa

► **To cite this version:**

Jazia Awassa. Antibacterial Mechanisms of Pristine Zinc-Based Layered Double Hydroxides. Materials Science [cond-mat.mtrl-sci]. Université de Lorraine, 2022. English. NNT: 2022LORR0155 . tel-04073021

HAL Id: tel-04073021

<https://hal.univ-lorraine.fr/tel-04073021>

Submitted on 18 Apr 2023

HAL is a multi-disciplinary open access archive for the deposit and dissemination of scientific research documents, whether they are published or not. The documents may come from teaching and research institutions in France or abroad, or from public or private research centers.

L'archive ouverte pluridisciplinaire **HAL**, est destinée au dépôt et à la diffusion de documents scientifiques de niveau recherche, publiés ou non, émanant des établissements d'enseignement et de recherche français ou étrangers, des laboratoires publics ou privés.



**UNIVERSITÉ
DE LORRAINE**

**BIBLIOTHÈQUES
UNIVERSITAIRES**

AVERTISSEMENT

Ce document est le fruit d'un long travail approuvé par le jury de soutenance et mis à disposition de l'ensemble de la communauté universitaire élargie.

Il est soumis à la propriété intellectuelle de l'auteur. Ceci implique une obligation de citation et de référencement lors de l'utilisation de ce document.

D'autre part, toute contrefaçon, plagiat, reproduction illicite encourt une poursuite pénale.

Contact bibliothèque : ddoc-theses-contact@univ-lorraine.fr
(Cette adresse ne permet pas de contacter les auteurs)

LIENS

Code de la Propriété Intellectuelle. articles L 122. 4

Code de la Propriété Intellectuelle. articles L 335.2- L 335.10

http://www.cfcopies.com/V2/leg/leg_droi.php

<http://www.culture.gouv.fr/culture/infos-pratiques/droits/protection.htm>



Université de Lorraine

Ecole Doctorale C2MP (Chimie - Mécanique - Matériaux - Physique)

Laboratoire de Chimie Physique et Microbiologie pour les Matériaux et l'Environnement
(LCPME)

Thèse

Présentée et soutenue publiquement pour l'obtention du titre de

DOCTEUR DE L'UNIVERSITE DE LORRAINE

Mention : **Science des Matériaux**

Spécialité : **Chimie des matériaux**

Par **Jazia AWASSA**

Sous la direction de **Christian RUBY** et **Sofiane El-KIRAT-CHATEL**

Mécanismes Antibactériens des Hydroxydes Doubles Lamellaires à Base de Zinc

Le 5 Octobre 2022

Membres du jury :

Rapporteurs :	Mme Vanessa PREVOT	Directrice de recherche, CNRS, Université Clermont Auvergne, Président de jury
	M. Etienne DAGUE	Directeur de recherche, CNRS, Université de Toulouse
Directeur de thèse :	M. Christian RUBY	Professeur, Université de Lorraine
Co-directeur de thèse :	M. Sofiane El-KIRAT-CHATEL	Chargé de recherche, CNRS, Université de Lorraine
Membres invités :	Mme. Audrey BEAUSSART	Chargée de recherche, CNRS, Université de Lorraine
	M. Damien CORNU	Maître de conférences, Université de Lorraine

Dedication

This thesis is dedicated to

the soul of my dearest father... my very first love

the one who I love the most

the one who believed in me and brought the best out of me

the one who watched out after me through my endless working nights

the one who lost his life battle against the worst type of diseases

Today, I make your dream come true...

"Our dead are never dead to us, until we have forgotten them"

George Eliot

Acknowledgments

As with any research work that results in the production of a thesis, on the cover there should not be only the name of the researcher, but also the names of the all those unsung motivators, those who to varying degrees provided guidance, encouragement and assistance, and without whom I would not have succeeded. I am very grateful to all those people, who have given me so much of their support, time and energy throughout the three years of my PhD.

First of all, I would like to express my sincere gratitude to my thesis director **Christian Ruby**, for his continuous support, patience, availability and motivation. His immense experience and knowledge have taught me a lot during my PhD period, and I am forever grateful for that. Christian is the kindest person I have ever met, thank you for all sympathy and positive vibes you provided throughout this journey.

Moving to my thesis co-director, **Sofiane El-Kirat-Chatel**, no words can explain how thankful I am to you. You have never failed to provide me with the positive energy and enthusiasm to continue this work. Thank you for all what you have taught me, for always being available when needed. Most importantly, thank you for giving me an example of who I seek to be like in the future, and what I want to orient my future career toward.

It is also relevant to thank the old and the new directors of the LCPME, **Mr. Alain Walcarius** and **Mr. Christophe Gantzer**. I was more than honored to be welcomed by you in your laboratory, and I am grateful for the real sympathy you showed toward me.

My sincere gratitude also goes to **Mrs. Vanessa Prevot** and **Mr. Etienne Dague** for accepting to review my manuscript and for participating in the jury of my PhD defense.

The members of my thesis follow up committee **Mrs. Audrey Beaussart** and **Mr. Gregoire Herzog** are also acknowledged for their insightful suggestions and discussions concerning my PhD project.

I would also like to acknowledge the members of Chemistry and Spectrochemistry of Interfaces (CSI). Starting with our team leader, **Mr. Cédric Carteret**, thank you for being such a great leader and for teaching me the basics of LDH synthesis. **Damien Cornu**, thank you in participating in all my PhD meetings, for your fruitful discussions, for your guidance of this thesis through implementing new ideas and correcting my scientific papers. The closest to my heart within the team, **Samantha Soulé**, thank you for being such an incredible motivator, and for teaching me how to take the baby steps toward the world of LDH nanoparticles and films. I would not ever forget to acknowledge the “SpectroWoman” of our team, **Fabiène Quiles**, for teaching me how to analyze biological samples using spectroscopy techniques and for all her interest and availability for scientific consultancy. I would also like to thank my colleague and my friend, **Chloé Retourney**, for helping me in microbiology experiments, for providing me with her magical tricks to deal with bacteria, and for always being there to listen and share happy moments. Additionally, I would also like to express my kind gratitude for having such amazing officer partners: **Baptiste Arbez** and **Saeid Ekrami**. Thank you for making things much easier and for being such good friends and supporters. In general, I would like to thank all the actors of the team, who made me enjoy a great atmosphere: **Mustapha Abdelmoula**, **Erwan André**, **Gregory Francius**, **Aurélien Renard**, **Roumain Coustel**, **Manuel Dossot**, **Jérôme Grausem**. Although no longer a part of the team, I would like to also thank the old post-docs, **Rana Omar** and **David Siniscalco** for their kind presence and fruitful scientific discussion.

I am also grateful for **Claire Genois** for helping with all the ICP experiments and for her mindful advices. Of course, I am thankful as well for the smiley face I saw every morning while taking a first step into the lab, **Gerard Paquôt**, your sense of humor made this whole journey way more enjoyable.

My heartfelt gratitude goes to my small Lebanese family in Nancy, who were the source of love and happy moments during this journey. To you **Sara**, my influencer, to all the support and love we shared, to all our memories and laughters, to all the series and movies and to “Ammoush” who we gathered on his love :D. **Ahmad**, my brother, thank you for always being there, for looking after me and for always picking me up whenever I was late at work. **Khadoura** and **Hallak** “Drayre” thank you for never failing to make me laugh and never missing an opportunity to start up a fight between me and my fiancé. The hilarious **Mkanna**, the top chef **Jizzini**, the kindest heart **Jano**, the “malek halewet el jeben” **Farhat**, the brave straight to the point **Mira**, the funniest **Abboudi**, to my friend since college and the future doctor **Batoul** thank you for being there and making all this much easier.

During my adventure in Nancy, I was also grateful to meet the love of my life and my soul mate. **Youssof**, you are a once in a life time kind of person that I would never give up on. I am thankful for coming here to meet you. Thank you for your help, support, tenderness and most importantly, thank you for making me a better version of who I am.

To my friends outside France, my best friend and safe place **Nour**, **Asma** my inspiring motivator, **Amoula** my second mother whom I spent half of my life in her house, **Hamza** the comedian, **Suzana** my food partner since grade 7, **Fatima** the great dedicated doctor, **Kaku** my Barbie, **Nato** my “ahdam wehde b hayeteh”, **Ali** my good friend and brother, **Soukaina** and **Nour** the writers of women motivations, thank you for encouraging me to go to France and pursue my PhD from the first place.

To my sister from another mother and my human diary **Ranime**, to my other second mother and **Ghada**, although I’ve just met you in 2021, you became my second family. Thank you for all your support and love .

Last but not least, my greatest gratitude goes to the members of my family, my hidden heroes. Here comes the hardest part... Whenever I think of any of you, I run out of words. **Mom**, you’re a warrior, a perfect example of a superwoman who fought for the sake of her children. I’m forever in dept to you. My beloved sisters and brother: **Ayoush** the oldest and the wisest, the sacrificing **Joujou** my idol and nanny since day 1, **Mona** the purest soul, **Hiba** the most generous, **Mimo** my better half and my twin, **Hamoudi** my understanding one, **Jalal** my backbone and my second father, thank you for always taking care of me and showering me with love and motivation. My auntie **Jazia** whom I was called after, my brothers in law as well as all my nephews, thank you for providing with so much love and support. I love each and every one of you insanely.

Abbreviations

Aⁿ⁻: Intercalating anion

AFM: Atomic Force Microscopy

Ag: Silver

Al: Aluminum

ATR: Attenuated Total Reflectance

Au: Gold

Be: Beryllium

BET: Brunauer–Emmett–Teller

Bi: Bismuth

Br⁻: Bromide anions

Ca: Calcium

Cd: Cadmium

Cl⁻: Chloride anions

ClO₄⁻: Perchlorate anions

cm: Centimeter

Co: Cobalt

CO₂: Carbon dioxide

CO₃²⁻: Carbonate anions

Cr: Chromium

Cu: Copper

d: Interlamellar distance

DNA: Deoxyribonucleic acid

e⁻: Electron

ESR: Electron Spin Resonance

F⁻: Fluoride anions

Fe: Iron

Fe(CN)₆³⁻: Hexacyanoiron (III) ion

Fe(CN)₆⁴⁻: Hexacyanidoferrate (II) ion

FEG: Field emission gun

FS: Force spectroscopy

FT: Fourier-Transform

g: Gram

Abbreviations

Ga: Gallium

h: hour

h⁺: Hole

H⁺: Proton

H₂O: Water

H₂O₂: Hydrogen peroxide

ICP: Inductively Coupled Plasma

In: Indium

IR: InfraRed

L: Liter

L(003): Crystallite coherent domain in (003) direction

L(110): Crystallite coherent domain in (003) direction

La: Lanthanum

LB: Lysogeny broth

LDH: Layered double hydroxide

Li: Lithium

M(II): Divalent metal cation

M(III): Trivalent metal cation

Mg: Magnesium

MIC: Minimum inhibitory concentration

min: Minute

mg: Milligram

mL: Milliliter

mm: Millimeter

mmol: Millimole

Mn: Manganese

mol: Mole

MOPS: 3-(N-Morpholino)-Propane sulfonic Acid

N₂: Nitrogen

Ni: Nickel

nm: Nanometer

NO₃⁻: Nitrate anions

NPs: Nanoparticles

Abbreviations

O₂: Oxygen

OD: Optical density

OH⁻: Hydroxide anions

Pa: Pascal

Pb: Lead

Pd: Palladium

PXRD: Powder X-ray Diffraction

ROS: Reactive oxygen species

s: Second

Sb: Stibium

SEM: Scanning Electron Microscopy

Si: Silicon

SiO₂: Silica

Sn: Tin

SO₄²⁻: Sulfate anions

Sr: Strontium

t: Time

TBS: Tris-buffered saline

TEM: Transmission Electron Microscopy

Ti: Titanium

TSB: Tryptic soy broth

UVA: Ultraviolet light type A

V: Vanadium

v: volume

w: weight

XPS: X-ray Photoelectron Spectroscopy

XRD: X-ray diffraction

Y: Yttrium

Zn: Zinc

ZnO: Zinc oxide

Zr: Zirconium

λ: Wavelength

μ: Micro

Abbreviations

μg: Microgram

μL: microliter

General summary

General introduction.....	1
Chapter 1: Antibacterial mechanisms of layered double hydroxides: State of the art.....	8
Chapter 2: Materials and methods	65
Chapter 3: Antibacterial activity of pristine layered double hydroxides by divalent metal ions release.....	104
Chapter 4: Antibacterial activity of Zn(II)-based layered double hydroxide nanoparticles by direct surface interactions.....	142
Chapter 5: Enhancing the antibacterial activity of Zn(II)-based layered double hydroxide nanoparticles in the presence of UVA light	178
Chapter 6: The contribution of direct contact and divalent metal ions release to the antibacterial activity of Zn(II)-based layered double hydroxide nanoparticles.....	203
General conclusions and perspectives.....	217
Annex I.....	221
Annex II.....	225
Résumé étendu de la thèse en français	227

General Introduction

Layered double hydroxides (LDHs) are clay lamellar solids having a structure based on the stacking of brucite-like sheets comprising divalent and trivalent metal hydroxides. These sheets hold a net positive charge which is compensated by negatively charged intercalating anions and water molecules present in the interlaminar regions [1–3]. Due to their interesting properties, including flexible composition, high anion exchange capacity, and biocompatibility, LDHs have found themselves several technological applications such as, sorption of pollutants [4], catalysis [5], bio-sensors [6], drug storage delivery [7], photocatalytic water remediation [8], and more recently antimicrobial applications [9–12].

Bacterial contamination and subsequent pathogenic infections have been recognized for several years as a critical threat affecting the quality of human healthcare all over the world [13–15]. With the rapid spread of antimicrobial resistance phenomena caused by the excessive use of antibiotics, a growing interest was drawn toward the fabrication of new materials preventing biofouling or pathogenic bacteria proliferation [15–17]. Recent advances in the field of material science had opened up new gates for designing new antimicrobials based on synthetic inorganic materials [15,18,19]. In fact, inorganic antibacterial agents are considered advantageous over organic antibacterial ones due to their improved safety, recyclability and enhanced stability [20]. In this context, the use of inorganic LDH and LDH-composites materials as efficient antibacterial agents could provide one possible mean to fight bacterial infections.

In fact, several studies were conducted to determine the potential applications of LDH and LDH-composite materials in several antimicrobial applicational fields including water purification [21,22], food packaging [23,24], wound healing dressings [25], and textile industries [26]. Most of the work reporting the antibacterial properties of LDHs mainly deals with antibacterial molecules-intercalated LDHs. This is because LDHs possess high potential as carriers of biological molecules due to their ability to intercalate large anionic molecules [27–29]. However, the majority of intercalated biomolecules are based on commercial antibiotics, which hinders the use of antibacterial molecules-intercalated LDH hybrids against several resistant strains. Moreover, some surveys reported the loading antimicrobial nanoparticles (NPs), *e.g.*, Ag⁰, Au⁰, ZnO, within the LDH matrix to provide an efficient antibacterial effect [30–33]. Although these NPs-loaded LDH

composites exhibited significant antibacterial effects, the toxicity caused by their aggregation and high dose exposure behavior still remains a major challenge for their use in antibacterial applications [34–36]. The synthesis of both types of antibacterial LDH composites, *e.g.*, antibacterial molecules-intercalated and NPs-loaded LDHs, needs additional chemicals and multi-step synthesis protocols which increase the cost and time to obtain these LDH-based antibacterial agents.

On the other hand, some recent studies proved that unmodified pristine LDHs, more precisely Zn(II)-based LDHs, could also act as efficient antibiotic-free antimicrobial materials [11,12,37]. Indeed, pristine antibacterial LDHs are antibiotic-free, easily prepared and inexpensive. However, the remaining challenge here is that their followed antibacterial mechanism is still not well understood and experimentally non-validated.

Deciphering the followed antibacterial mode of action could provide several advantages on how to tune the different physico-chemical properties of LDHs to maximize their antibacterial effect. The suggested antibacterial mechanisms of pristine LDHs found in the literature are: **(1)** direct contact interactions between the surface of LDH and bacterial cell wall [10,11,38–40], **(2)** release of constituent divalent metal ions [10,11,37–40], **(3)** generation of biologically toxic reactive oxygen species (ROS) by LDHs in presence of light [37–40]. Despite the fact that these hypotheses were proposed to explain the antibacterial effects of pristine LDHs, no real experimental set ups were done neither to validate any of them nor to determine which mechanism dominates their antibacterial activity.

This thesis work aims at investigating the different suggested antibacterial mechanisms of pristine Zn(II)-based LDH by addressing several critical questions: “Do these proposed mechanisms truly exist?”, “How can we experimentally validate them?”, “Which physico-chemical parameters control the antibacterial action through a certain suggested mechanism?”, “What role does each mechanism plays in different antibacterial tests assays?”, and finally “Which mechanism dominates the antibacterial action?”

As a start up point, several general properties about LDHs are described in **Chapter 1**, followed by explaining the several suggested antibacterial mechanisms of the different types of antibacterial LDHs. We explain the different antibacterial mode of actions starting from physico-chemical

considerations, followed by various experimental observations of these mechanisms and finally providing some considerations on how to tune the properties of LDHs to maximize the antimicrobial effect through a given mechanism. At the end of this chapter, we highlight the advantages of pristine LDHs over LDH-composites and the importance of unraveling their antibacterial mode of action which is one of the main objectives of this thesis work.

In **Chapter 2**, we report the different experimental methods and techniques used to achieve the objectives of this work. The principles of each used technique and used experimental set ups are explained in details.

We start addressing our real research work in **Chapter 3**, where we present a global investigation carried out on different pristine LDH samples to determine which physico-chemical parameters, *e.g.*, crystallinity, nature of divalent metal, type of intercalated anion, M(II)/M(III) molar ratio, influence the release of divalent metal ions in broth aqueous media. The properties of Zn(II)-based LDHs are systematically analyzed due to their relatively well-established antimicrobial behavior. Finally, the relationship between divalent metal ions release (initially controlled by different physico-chemical properties) and the antibacterial activity of LDHs against *Staphylococcus aureus* and *Escherichia coli* is established (**Mechanism 2**).

In **Chapter 4**, we move to deciphering the antibacterial mechanism of Zn(II)-based LDHs by direct contact interactions (**Mechanism 1**). This is done through the comparison of the antibacterial activity of micron- and nano-sized pristine LDHs. Moreover, we take advantage of our original approach to functionalize Atomic Force Microscopy (AFM) tips with LDHs to decipher the specific interactions present between Zn(II)-based LDHs and living *S. aureus* cells by means of AFM-based force spectroscopy (FS) method.

Furthermore, the enhancement of Zn(II)-based LDHs antibacterial effect in the presence UVA through the possible generation of ROS (**Mechanism 3**) is addressed in **Chapter 5**. The contribution of ROS generation to the antibacterial effect of Zn(II)-based LDHs is further evidenced by several antibacterial activity tests performed in both dark and UVA conditions. AFM imaging and Fourier-transform infrared (FT-IR) spectroscopy are also used to compare the topography and biochemical composition of treated *S. aureus* cells in presence and absence of possible generated ROS.

After providing experimental evidences about these three suggested mechanisms, the role of each of metal ions release (**Mechanism 2**) and direct contact (**Mechanism 1**) contributing to the antibacterial activity of Zn(II)-based LDHs in dark is finally determined in **Chapter 6**. The mechanism of divalent metal ions release is suppressed using a scavenger of released Zn^{2+} ions, thus allowing us to compare **Mechanism 1** and **2**, and to evaluate their participation in different antibacterial activity tests assays. Such evaluation finally allows us to determine the dominating mechanism governing the antibacterial activity of pristine Zn(II)-based LDHs against *S. aureus* in different environments, *e.g.*, liquid broth media, liquid buffer media and agar solids.

We finally end up with providing general conclusions of this thesis work about each individual antibacterial mechanism. We also report some promising perspectives concerning the future use of pristine Zn(II)-based LDHs as efficient antibiotic-free antibacterial agents.

References

- [1] V. Rives, ed., Layered double hydroxides: present and future, Nova Science Publishers, Huntington, N.Y, 2001.
- [2] F.L. Theiss, G.A. Ayoko, R.L. Frost, Synthesis of layered double hydroxides containing Mg²⁺, Zn²⁺, Ca²⁺ and Al³⁺ layer cations by co-precipitation methods—A review, *Appl. Surf. Sci.* 383 (2016) 200–213.
- [3] M. Bini, F. Monteforte, Layered Double Hydroxides (LDHs): Versatile and Powerful Hosts for Different Applications, *J. Anal. Pharm. Res.* 7 (2018).
- [4] A.-L. Johnston, E. Lester, O. Williams, R.L. Gomes, Understanding Layered Double Hydroxide properties as sorbent materials for removing organic pollutants from environmental waters, *J. Environ. Chem. Eng.* 9 (2021) 105197.
- [5] Z. Yang, C. Zhang, G. Zeng, X. Tan, D. Huang, J. Zhou, Q. Fang, K. Yang, H. Wang, J. Wei, K. Nie, State-of-the-art progress in the rational design of layered double hydroxide based photocatalysts for photocatalytic and photoelectrochemical H₂/O₂ production, *Coord. Chem. Rev.* 446 (2021) 214103.
- [6] Inmauddin, ed., Layered double Hydroxide Based Biosensors, in: *Mater. Res. Found.*, 1st ed., Materials Research Forum LLC, 2019: pp. 131–156.
- [7] X. Bi, H. Zhang, L. Dou, Layered Double Hydroxide-Based Nanocarriers for Drug Delivery, *Pharmaceutics.* 6 (2014) 298–332.
- [8] L. Wang, Z. Zhu, F. Wang, Y. Qi, W. Zhang, C. Wang, State-of-the-art and prospects of Zn-containing layered double hydroxides (Zn-LDH)-based materials for photocatalytic water remediation, *Chemosphere.* 278 (2021) 130367.
- [9] A.M. León-Vallejo, F.D. Velázquez-Herrera, Á. Sampieri, G. Landeta-Cortés, G. Fetter, Study of layered double hydroxides as bactericidal materials against *Corynebacterium ammoniagenes*, a bacterium responsible for producing bad odors from human urine and skin infections, *Appl. Clay Sci.* 180 (2019) 105194.
- [10] G. Mishra, B. Dash, S. Pandey, D. Sethi, Ternary layered double hydroxides (LDH) based on Cu- substituted Zn Al for the design of efficient antibacterial ceramics, *Appl. Clay Sci.* 165 (2018) 214–222.
- [11] S.A.A. Moaty, A.A. Farghali, R. Khaled, Preparation, characterization and antimicrobial applications of Zn-Fe LDH against MRSA, *Mater. Sci. Eng. C.* 68 (2016) 184–193.
- [12] F. Peng, D. Wang, D. Zhang, H. Cao, X. Liu, The prospect of layered double hydroxide as bone implants: A study of mechanical properties, cytocompatibility and antibacterial activity, *Appl. Clay Sci.* 165 (2018) 179–187.
- [13] D. Pittet, S. Dharan, S. Touveneau, V. Sauvan, T.V. Perneger, Bacterial Contamination of the Hands of Hospital Staff During Routine Patient Care, *Arch. Intern. Med.* 159 (1999) 821.
- [14] L. Hall-Stoodley, J.W. Costerton, P. Stoodley, Bacterial biofilms: from the Natural environment to infectious diseases, *Nat. Rev. Microbiol.* 2 (2004) 95–108.
- [15] C. Forano, F. Bruna, C. Mousty, V. Prevot, Interactions between Biological Cells and Layered Double Hydroxides: Towards Functional Materials, *Chem. Rec.* 18 (2018) 1150–1166.
- [16] G. Mi, D. Shi, M. Wang, T.J. Webster, Reducing Bacterial Infections and Biofilm Formation Using Nanoparticles and Nanostructured Antibacterial Surfaces, *Adv. Healthc. Mater.* 7 (2018) 1800103.

- [17] Y. Wang, Y. Yang, Y. Shi, H. Song, C. Yu, Antibiotic-Free Antibacterial Strategies Enabled by Nanomaterials: Progress and Perspectives, *Adv. Mater.* 32 (2020) 1904106.
- [18] S. Malekhaiaf Häffner, M. Malmsten, Membrane interactions and antimicrobial effects of inorganic nanoparticles, *Adv. Colloid Interface Sci.* 248 (2017) 105–128.
- [19] C. Wang, P. Makvandi, E.N. Zare, F.R. Tay, L. Niu, Advances in Antimicrobial Organic and Inorganic Nanocompounds in Biomedicine, *Adv. Ther.* 3 (2020) 2000024.
- [20] R. Kumar, A. Umar, G. Kumar, H.S. Nalwa, Antimicrobial properties of ZnO nanomaterials: A review, *Ceram. Int.* 43 (2017) 3940–3961.
- [21] W. Kamal, W.M.A. El Rouby, A.O. El-Gendy, A.A. Farghali, Bimodal applications of LDH-chitosan nanocomposite: water treatment and antimicrobial activity, *IOP Conf. Ser. Mater. Sci. Eng.* 464 (2018) 012005.
- [22] S.A.A. Moaty, A.A. Farghali, R. Khaled, Preparation, characterization and antimicrobial applications of Zn-Fe LDH against MRSA, *Mater. Sci. Eng. C.* 68 (2016) 184–193.
- [23] H.-M. Cheng, X.-W. Gao, K. Zhang, X.-R. Wang, W. Zhou, S.-J. Li, X.-L. Cao, D.-P. Yan, A novel antimicrobial composite: ZnAl-hydroxalite with *p*-hydroxybenzoic acid intercalation and its possible application as a food packaging material, *New J. Chem.* 43 (2019) 19408–19414.
- [24] L. Tamaro, V. Vittoria, V. Bugatti, Dispersion of modified layered double hydroxides in Poly(ethylene terephthalate) by High Energy Ball Milling for food packaging applications, *Eur. Polym. J.* 52 (2014) 172–180.
- [25] W. Zhang, Y. Zhao, W. Wang, J. Peng, Y. Li, Y. Shangguan, G. Ouyang, M. Xu, S. Wang, J. Wei, H. Wei, W. Li, Z. Yang, Colloidal Surface Engineering: Growth of Layered Double Hydroxides with Intrinsic Oxidase-Mimicking Activities to Fight Against Bacterial Infection in Wound Healing, *Adv. Healthc. Mater.* 9 (2020) 2000092.
- [26] S. Mallakpour, Z. Radfar, C.M. Hussain, Current advances on polymer-layered double hydroxides/metal oxides nanocomposites and bionanocomposites: Fabrications and applications in the textile industry and nanofibers, *Appl. Clay Sci.* 206 (2021) 106054.
- [27] Y. Wang, D. Zhang, Synthesis, characterization, and controlled release antibacterial behavior of antibiotic intercalated Mg–Al layered double hydroxides, *Mater. Res. Bull.* 47 (2012) 3185–3194.
- [28] M.A. Djebbi, A. Elabed, Z. Bouaziz, M. Sadiki, S. Elabed, P. Namour, N. Jaffrezic-Renault, A.B.H. Amara, Delivery system for berberine chloride based on the nanocarrier ZnAl-layered double hydroxide: Physicochemical characterization, release behavior and evaluation of antibacterial potential, *Int. J. Pharm.* 515 (2016) 422–430.
- [29] Y. Salguero, L. Valenti, R. Rojas, M.C. García, Ciprofloxacin-intercalated layered double hydroxide-in-hybrid films as composite dressings for controlled antimicrobial topical delivery, *Mater. Sci. Eng. C.* 111 (2020) 110859.
- [30] L. Mao, J. Liu, S. Zheng, H. Wu, Y. Liu, Z. Li, Y. Bai, Mussel-inspired nano-silver loaded layered double hydroxides embedded into a biodegradable polymer matrix for enhanced mechanical and gas barrier properties, *RSC Adv.* 9 (2019) 5834–5843.
- [31] P.D. Marcato, N.V. Parizotto, D.S.T. Martinez, A.J. Paula, I.R. Ferreira, P.S. Melo, N. Durán, O.L. Alves, New Hybrid Material Based on Layered Double Hydroxides and Biogenic Silver Nanoparticles: Antimicrobial Activity and Cytotoxic Effect, *J. Braz. Chem. Soc.* 24 (2013) 266–272.

- [32] G. Mishra, B. Dash, S. Pandey, P.P. Mohanty, Antibacterial actions of silver nanoparticles incorporated Zn–Al layered double hydroxide and its spinel, *J. Environ. Chem. Eng.* 1 (2013) 1124–1130.
- [33] W.-D. Zhang, Y.-M. Zheng, Y.-S. Xu, Y.-X. Yu, Q.-S. Shi, L. Liu, H. Peng, Y. Ouyang, Preparation and Antibacterial Property of Waterborne Polyurethane/Zn–Al Layered Double Hydroxides/ZnO Nanocomposites, *J. Nanosci. Nanotechnol.* 13 (2013) 409–416.
- [34] P. Bélteky, A. Rónavári, N. Igaz, B. Szerencsés, I.Y. Tóth, I. Pfeiffer, M. Kiricsi, Z. Kónya, Silver nanoparticles: aggregation behavior in biorelevant conditions and its impact on biological activity, *Int. J. Nanomedicine*. Volume 14 (2019) 667–687.
- [35] G. Carja, Y. Kameshima, A. Nakajima, C. Dranca, K. Okada, Nanosized silver–anionic clay matrix as nanostructured ensembles with antimicrobial activity, *Int. J. Antimicrob. Agents*. 34 (2009) 534–539.
- [36] M. Sharma, P. Prasher, Metallic Nanoparticles at the Biointerface, in: C. Bhargava, A. Sachdeva (Eds.), *Nanotechnology*, 1st ed., CRC Press, 2020: pp. 261–276.
- [37] M. Lobo-Sánchez, G. Nájera-Meléndez, G. Luna, V. Segura-Pérez, J.A. Rivera, G. Fetter, ZnAl layered double hydroxides impregnated with eucalyptus oil as efficient hybrid materials against multi-resistant bacteria, *Appl. Clay Sci.* 153 (2018) 61–69.
- [38] H.A. Tabti, M. Adjdir, A. Ammam, B. Mdjahed, B. Guezzen, A. Ramdani, C.K. Bendeddouche, N. Bouchikhi, N. Chami, Facile synthesis of Cu-LDH with different Cu/Al molar ratios: application as antibacterial inhibitors, *Res. Chem. Intermed.* 46 (2020) 5377–5390.
- [39] M. Li, L. Li, S. Lin, Efficient antimicrobial properties of layered double hydroxide assembled with transition metals via a facile preparation method, *Chin. Chem. Lett.* 31 (2020) 1511–1515.
- [40] S. Dutta, T.K. Jana, S.K. Halder, R. Maiti, A. Dutta, A. Kumar, K. Chatterjee, Zn₂Al-CO₃ Layered Double Hydroxide: Adsorption, Cytotoxicity and Antibacterial Performances, *ChemistrySelect*. 5 (2020) 6162–6171.

Antibacterial mechanisms of layered double hydroxides: State of the art

Table of figures	10
Table of tables	13
1. Context	14
2. Layered double hydroxides: Generalities	14
2.1. Definition and history	14
2.2. Structural model and chemical variability	15
3. Antibacterial layered double hydroxide materials: Types and synthesis routes	21
3.1. Types of antibacterial LDHs	22
3.2. Synthesis routes of antibacterial LDHs	23
4. Antibacterial mechanisms of layered double hydroxide materials	26
4.1. Direct surface interactions	29
4.1.4. Experimental observations, limitations and maximization of the direct contact effect of LDHs	34
4.2. Dissolution through the release of antimicrobial molecules from antimicrobial molecules-intercalated LDHs	37
4.2.1. Controlled release of antibacterial molecules out of antibacterial molecules intercalated-LDHs	39
4.2.2. Influence of intercalating method on the release behavior	40

4.2.3.	Influence of the LDH host on the antibacterial activity of antibacterial molecules-intercalated LDH composites	41
4.2.4.	Principles for the design of an efficient antibacterial molecules-intercalated LDH	43
4.3.	Dissolution of metallic aqueous ions from pristine and nanoparticles-loaded LDHs	43
4.3.1.	Antimicrobial effect through the release of Zn^{2+}_{aq} and Cu^{2+}_{aq} from pristine LDHs	44
4.3.2.	Antimicrobial effect through the release of Ag^{+}_{aq} from Ag Nps-loaded LDHs	45
4.3.3.	Limitations of the proof of evidence of dissolution of ions out of LDH	46
4.4.	Generation of reactive oxygen species (ROS).....	46
4.4.1.	Generation of ROS by LDHs	46
4.4.2.	ROS generation by pristine LDHs	47
4.4.3.	ROS generation by supported nanoparticles on LDH.....	47
4.4.3.1.	Ag@AgCl-generated ROS	47
4.4.3.2.	ZnO-generated ROS.....	48
4.4.3.3.	Beyond ROS: Photothermal effect of Au-loaded LDH.....	48
4.4.3.4.	Limitations of the attribution of the ROS mechanism and general considerations for its effect	50
5.	Toward encouraging the use of pristine antibacterial LDHs.....	51
6.	Conclusion.....	52
	References	54

Table of figures

- Figure 1.** A schematic illustration of LDH structure. Divalent and trivalent metals (blue circles) are octahedrally linked to hydroxyl groups (red circles) constituting the laminar composition of the brucite-like metallic sheets. The interlaminar spacing comprise compensating negatively charged anions (green circles) and water molecules (orange circles).....16
- Figure 2.** A schematic illustration of different LDH polytypes with their associated stacking sequence. (a) LDH polytype 3R with stacking sequence of BC-CA-AB, (b) LDH polytype 2H with stacking sequence of BC-CA, (c) LDH polytype 1H with stacking sequence of BC-BC. The blue blocks refer to the lamellar metallic sheets with their specific orientation, whereas the orange circles represent the intercalating anions present in the interlaminar spacing.17
- Figure 3.** (a) pK_{sp} values for different $M(II)(OH)_2$ and $M(III)(OH)_3$ metal hydroxides. (b) Evolution of pK_{sp} values for different $M(II)M(III)$ LDHs. All pK_{sp} values are adapted from Ref. [53].19
- Figure 4.** Reliable limits for metallic sheets composition in the LDH structure in terms of trivalent molar ratio (x) and divalent to trivalent molar ratio (R).20
- Figure 5.** Different types and structures of antibacterial layered double hydroxides: Antibacterial molecules-intercalated LDHs, nanoparticles-loaded LDHs, pristine LDHs having a structure similar to that of typical LDHs.23
- Figure 6.** Schematic representation of the three different methods used to synthesize antibacterial LDHs: (1) Direct coprecipitation of mixed metallic salt solutions for pristine LDHs, this synthesis route is carried out in presence of antibacterial or nanoparticles source for antibacterial molecules-intercalated and NPs-loaded LDHs, (2) Anion-exchange reactions between previously prepared pristine LDHs and antibacterial molecules basic solution for antibacterial molecules-intercalated LDHs, (3) Rehydration of layered double oxides, previously obtained by calcination of pristine LDHs, in presence of antibacterial molecules or NPs source for antibacterial molecules-intercalated and NPs-loaded LDHs, respectively.24
- Figure 7.** A schematic illustration of the proposed antibacterial mechanisms of LDHs. (1) Direct surface contact interactions between pristine and nanoparticles-loaded LDHs with bacteria, (2) Dissolution of antibacterial molecules: release of antibacterial molecules by antibacterial molecules-intercalated LDHs and release of metal ions by pristine and nanoparticles-loaded LDHs,

and (3) Generation of reactive oxygen species (ROS) by pristine and nanoparticles-loaded LDHs. Scale is adjusted to clarify the illustration.....29

Figure 8. Mechanism of *B. subtilis* adhesion onto carbonate intercalated NiFe LDH. (A) Electrostatic interactions, (B) Anion exchange, (C) OH replacement and (D) H-bond and polar interactions. Reproduced from Ref. [122].....30

Figure 9. a) Confocal microscopy images of *S. aureus* and *E. coli* incubated with a mixture of propidium iodide (red color) and SYTO 9 (green color) and various samples. The images correspond to 25 h after incubation. Green fluorescence corresponds to live bacteria while red fluorescence corresponds to dead bacteria. b) The time dependent concentrations of live bacteria, evaluated by the ratio of G/R. c) TEM images of *E. coli* with or without treatment of different samples. Blue arrows correspond to bacterial adhesion. d) SEM images of *E. coli* with or without treatment of different samples. Red arrows correspond to direct connection with *E.coli* bacteria. Reproduced from Ref. [78].....32

Figure 10. a) HRTEM images of (1) Ag-LDHs(PVP), (2) Ag-LDHs@PDA and (3) Ag-LDHs@TA-Fe(III). b): EDS surface scans for (1) Ag-LDHs(PVP), (2) Ag-LDHs@PDA and (3) Ag-LDHs@TA-Fe(III). c): The MIC values of the different Ag-loaded LDHs against *E. coli*. Reproduced from Ref. [117].....36

Figure 11. Release profile of Kojic acid from ZnTi-KA-LDH and pure-KA in phosphate buffer saline solution at pH = 5. Reproduced from Ref. [145].....40

Figure 12. a) Release profiles of berberine chloride (BBC) from BBC-LDH hybrids obtained by anion exchange (BMAE) and coprecipitation (BMAC) synthesis routes. b) Inhibition zone diameters of free BBC and BBC-LDH hybrids. Reproduced from Ref. [141].41

Figure 13. a) SEM micrographs of the powders of o-hydroxybenzoate-LDH hybrids (ZnAl-o-BzOH). (1) non-milled ZnAl-o-BzOH and (2): ZnAl-o-BzOHm5 milled for 5 min. b) Evolution of *E. coli* growth in the presence of 4% (w/v) solutions of ZnAl-o-BzOH powders with different dimensions as a function of contact time (hours). c) Release of o-BzOH molecules from non-milled ZnAl-o-BzOH and ZnAl-o-BzOHm5 milled for 5 minutes, expressed as released fraction normalized to the expected final concentration (wt/wt.%) versus the contact time (hours). Reproduced from Ref. [103].....42

Figure 14. a) Antibacterial activity evaluation of GNR@LDH-PEG against: (1) *E. coli*, (2): *S. aureus*. b) SEM images of treated bacteria with GNR@LDH without 808 nm laser: (1) *E. coli*, (2)

S. aureus. c) SEM images of bacteria treated with GNR@LDH under 3 min irradiation with 808 nm laser: (1) *E. coli*, (b) *S. aureus*; *P < 0.01, 0.001 < **P < 0.005, ***P < 0.001, compared with control group, red arrows correspond to distorted cell membranes. Reproduced from Ref. [88]. 49

Table of tables

Table 1. Different LDH type minerals and their phenotype.	16
Table 2. Major cationic couples incorporated in LDHs cationic laminar sheets [38]. Blue boxes correspond to possible combination.	18
Table 3. Antibacterial performance of pristine and NPs-loaded LDHs and the proposed associated antibacterial mechanisms. MIC values correspond to the minimum inhibitory concentration required to inhibit the growth of a certain bacteria, whereas inhibition zone diameters correspond to the obtained inhibitory diameter zone generated by LDHs when being tested in agar disk or agar well diffusion tests.	26
Table 4. Antibacterial performance of organic biomolecules-intercalated LDHs reported in the literature. MIC values correspond to the minimum inhibitory concentration required to inhibit the growth of a certain bacteria, whereas inhibition zone diameters correspond to the obtained inhibitory diameter zone generated by antimicrobial molecules-intercalated LDHs when being tested in agar disk or agar well diffusion tests.	37

1. Context

Infectious diseases caused by microbial contaminations are threatening human health all over the world [1]. Infections by pathogenic microorganisms are of serious concern to several fields such as food industries [2], textile industries [3], healthcare [4], and pharmaceutical products [5]. Traditional antibiotic drugs can usually treat bacterial infections. However, their extensive use had led to bacterial resistance and the spread of resistant strains [6,7]. Recent advances in the field of material science had opened up new gates for designing new antimicrobials as synthetic inorganic materials as metallic nanoparticles [8,9], silica-based materials [10,11], and metal oxides [12,13]. In this research theme, the use of pristine layered double hydroxides (LDH) as antibiotic-free antibacterial agents could play a very significant role. In order to determine which physico-chemical parameters must be optimized to obtain an efficient antimicrobial LDH, the governed antimicrobial mechanisms must be well established, controlled and understood.

This chapter mainly deals with explaining the proposed antibacterial mechanisms of different LDH-based materials. We first start with explaining some generalities about LDH materials including their discovery and structural composition. Then we move toward their use in antibacterial applications and explaining their antibacterial mode of action through providing information from our published review paper entitled as “Direct contact, dissolution and generation of reactive oxygen species: How to optimize the antibacterial effects of layered double hydroxides” which could also be found in **Annex I**. At the end, a main focus is dedicated toward the advantages of pristine antibacterial LDHs over LDH antimicrobial hybrids or heterocompounds, where we emphasize on the importance of unraveling their unclear antibacterial mechanisms.

2. Layered double hydroxides: Generalities

2.1. Definition and history

The term "layered double hydroxide" denoted as LDH has been widely used for anionic clay minerals referring to their structural features. Such structural features highlight the presence of alternate stacks of plane sheets of $M(OH)_6$ octahedron including two types of metal cations and interlamellar spaces occupied by hydrated anions.

LDHs, also known as hydrotalcite minerals, were first discovered by the Swedish mineralogist Hochstetter back in 1842. Hydrotalcites are present in nature in foliated plates and/or fibrous masses, and can be easily crushed into white powder similar to talc. The notation “hydrotalcite” was given due to the presence of water molecules (hydro-) and its resemblance of talc (-talcite) [14]. The first exact formula of the referred hydrotalcite, $[\text{Mg}_6\text{Al}_2(\text{OH})_{16}\text{CO}_3 \cdot 4\text{H}_2\text{O}]$, was discovered in 1915 by E. Manasse, professor of Minerology at the University of Florence, Italy [15]. The first laboratory synthesis of this mineral was conducted by Feitknecht in 1935, by adding a basic solution to a solution containing divalent M(II) and trivalent metal cations M(III) [16]. However, it was not until the 1960s that the structure of LDHs was described by Allmann and Taylor using X-Ray Diffraction [17,18].

2.2. Structural model and chemical variability

2.2.1. Structural aspects and polytypes

LDHs belong to the family of anionic clays and are lamellar solids having a structure based on the stacking of cationic sheets of metal hydroxides. These metal sheets have a structure similar to that of $[\text{Mg}(\text{OH})_2]$ but part of the M(II) divalent cations is substituted by M(III) trivalent cations leading to the formation of positively charged layers [19,20]. Therefore, both divalent and trivalent metal cations are octahedrally linked to hydroxyl (OH) groups and are stacked up on top of each other to yield a layered structure similar to that of brucite mineral $[\text{Mg}(\text{OH})_2]$ [19,20]. In order to ensure the electroneutrality of the material, the excess in net positive charge of the laminar sheets is compensated by weakly bound intercalated anions (A^{n-}) in the interlamellar space, usually surrounded by water molecules. A typical LDH structure is illustrated in **Figure 1**. *Figure 1*

The general formula of LDHs can be expressed as follows: $[\text{M}(\text{II})_{(1-x)} \text{M}(\text{III})_x (\text{OH})_2]^{x+} [\text{A}^{n-}]_{x/n} \cdot y\text{H}_2\text{O}]^{x-}$, where M(II) and M(III) denote respectively divalent and trivalent metal cations, A^{n-} is an intercalated anion compensating the positive charge of the lamellar sheets, and x is the molar fraction of trivalent cations $\text{M}(\text{III})/[\text{M}(\text{III}) + \text{M}(\text{II})]$. The value of x is usually between 0.22 and 0.33 [20,21], representing the charge density of the sheets, and therefore determines the relative proportion of anions that can be intercalated in the interlamellar region. Note that the formula can also be written in the following form: $[\text{M}(\text{II})_R \text{M}(\text{III}) (\text{OH})_{2(1+R)}]^{+} [(\text{A}^{n-})_{1/n} \cdot y\text{H}_2\text{O}]^{-}$, where R is the molar ratio of divalent to trivalent cations M(II)/M(III).

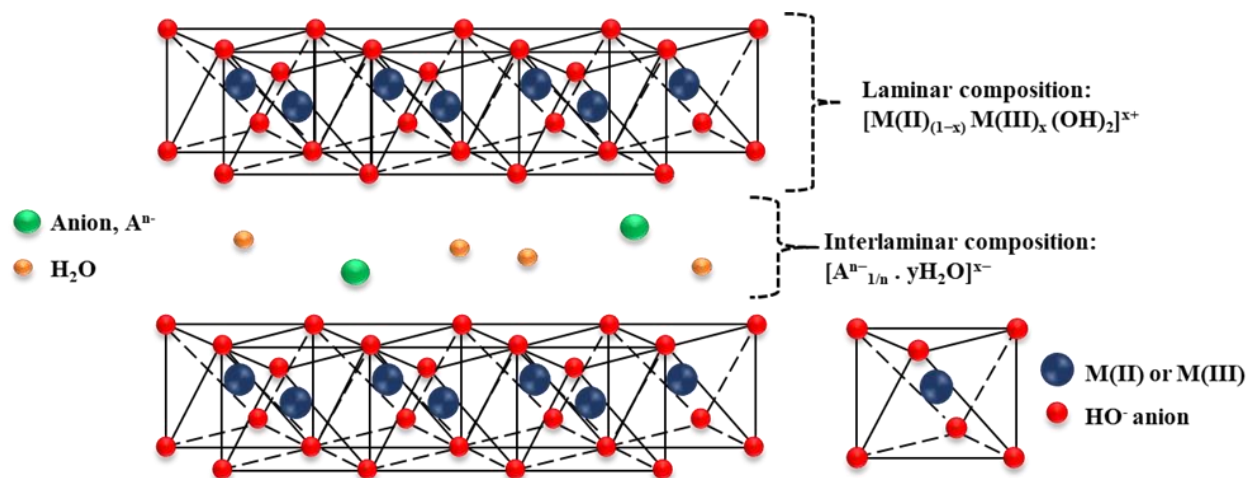


Figure 1. A schematic illustration of LDH structure. Divalent and trivalent metals (blue circles) are octahedrally linked to hydroxyl groups (red circles) constituting the laminar composition of the brucite-like metallic sheets. The interlaminar spacing comprise compensating negatively charged anions (green circles) and water molecules (orange circles).

According to the literature, LDHs crystallize in two types of crystal symmetry which differ by the stacking sequence of the sheets: rhombohedral R or hexagonal H symmetry (**Table 1, Figure 2**), described in a hexagonal lattice with parameters c and a [22,23]. These parameters correspond to the periodicity in the plane of the sheets and the periodicity of the stacking of the same sheets, respectively. The lattice parameter a is directly related to the intermetallic distance, whereas the lattice parameter c is related to the stacking of the sheets and therefore to the nature of the intercalated anion.

Table 1. Different LDH type minerals and their phenotype.

Mineral	Composition			Polytype	Reference
	M(II)	M(III)	A ⁿ⁻		
Hydrotalcite	Mg	Al	CO ₃ ²⁻	3R	[23,24]
Mannasseite	Mg	Al	CO ₃ ²⁻	2H	[24,24]
Meixnerite	Mg	Al	OH ⁻	3R	[25]
Pyroaurite	Mg	Fe	CO ₃ ²⁻	3R	[17]
Sjögrenite	Mg	Fe	CO ₃ ²⁻	2H	[26]
Coalingite	Mg	Fe	CO ₃ ²⁻	3R	[27]
Iowaite	Mg	Fe	Cl ⁻	3R	[28]
Stichtite	Mg	Cr	CO ₃ ²⁻	3R	[29]
Barbertonite	Mg	Cr	CO ₃ ²⁻	2H	[29]
Takovite	Ni	Al	CO ₃ ²⁻	3R	[30]

Reevesite	Ni	Fe	CO ₃ ²⁻	3R	[31]
Honessite	Ni	Fe	SO ₄ ²⁻	3R	[24]

Most synthetic LDHs produced in the laboratory crystallizes according to a 3R rhombohedral polytype belonging to the space group of $R\bar{3}m$ [17,22,23,32], with a stacking sequence of BC–CA–AB–BC; the unit cell is then made up of three sheets and the lattice parameter c is equal to three times the basal spacing " d " (**Figure 2a**). For example, the pyroaurite mineral of chemical formula $[Mg_6Fe_2(OH)_{16}]CO_3 \cdot 4H_2O$ is a 3R polytype, characterized by the lattice parameters $a = 3.109 \text{ \AA}$ and $c = 23.410 \text{ \AA}$.

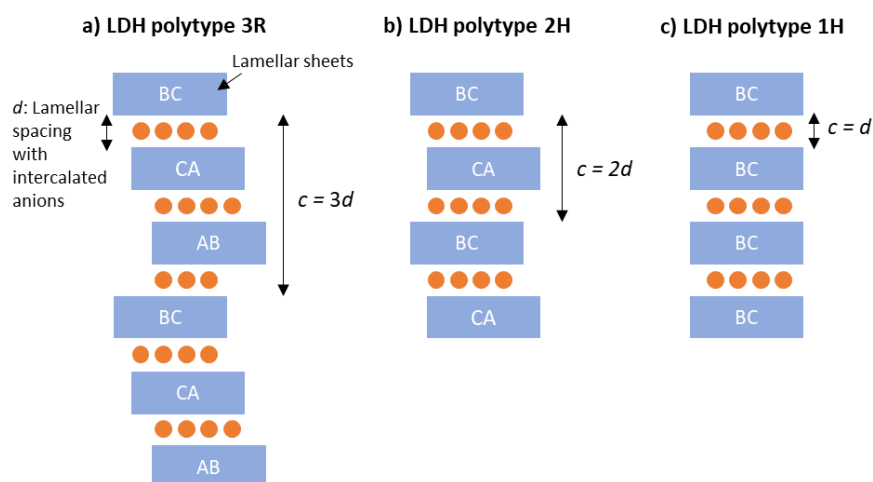


Figure 2. A schematic illustration of different LDH polytypes with their associated stacking sequence. (a) LDH polytype 3R with stacking sequence of BC-CA-AB, (b) LDH polytype 2H with stacking sequence of BC-CA, (c) LDH polytype 1H with stacking sequence of BC-BC. The blue blocks refer to the lamellar metallic sheets with their specific orientation, whereas the orange circles represent the intercalating anions present in the interlamellar spacing.

A two-layer polytype of hexagonal symmetry denoted as 2H belonging to the space group $P63mm$ [17,22,23,32], with a stacking sequence of BC–CB–BC can also be observed (**Figure 2b**). The lattice parameter c in this case is equal to twice the basal spacing. An example of this polytype, is the mineral Sjögrenite of chemical formula $[Mg_6Fe_2(OH)_{14}]CO_3 \cdot 5H_2O$ which crystallizes in hexagonal symmetry with lattice parameters $a = 3.1 \text{ \AA}$ and $c = 15.5 \text{ \AA}$.

The 1H polytype has also been observed for LDHs whose sheets are for materials whose sheets are made of Mg^{2+} and Al^{3+} cations and their interlayer space is composed of sulfate anions SO_4^{2-} [24]. The lattice parameter c for this LDH polytype is therefore equal to the basal spacing and the

stacking sequence is referred as BC-BC (**Figure 2c**). **Table 1** provides some examples of LDH type minerals, their chemical composition, and their associated polytype.

2.2.2. Composition of the cationic sheets

One very interesting property of LDH materials is their customizable composition. The chemical composition of LDHs, and more particularly the composition of the cationic sheets, can be freely modulated. Therefore, the nature of divalent and trivalent metal cations as well as the M(II)/M(III) molar ratio can be tuned according to the targeted applications. For example, Al(III)-based LDHs are preferred over Fe(III) for anti-corrosion applications. Mg(II)-based LDHs with minimal M(II)/M(III) molar ratio are well desired for biocompatible bone implants and osteogenic applications [33,34]. On the other hand, Zn(II) and Cu(II)-based LDHs and a higher ratio of M(II)/M(III) are much more efficient for antibacterial applications [34–37].

Table 2. Major cationic couples incorporated in LDHs cationic laminar sheets [38]. Blue boxes correspond to possible combination.

		M ²⁺											M ⁺	
		Mg	Fe	Co	Ni	Cu	Zn	Ca	Sr	Be	Cd	Pb	Mn	Li
M ³⁺	Al	Blue	Blue	Blue	Blue	Blue	Blue	Blue	Blue	Blue		Blue	Blue	Blue
	Cr	Blue		Blue	Blue	Blue	Blue	Blue		Blue	Blue			
	Fe	Blue	Blue	Blue	Blue	Blue	Blue	Blue	Blue		Blue			
	Co	Blue	Blue	Blue	Blue		Blue							
	Ni				Blue									
	Bi	Blue	Blue		Blue		Blue							
	Sb	Blue			Blue					Blue				
	Ga	Blue	Blue	Blue	Blue	Blue	Blue	Blue						
	In	Blue			Blue		Blue							
	V	Blue					Blue							
	Y	Blue			Blue				Blue					
	La	Blue			Blue		Blue	Blue						
M ⁴⁺	Ti	Blue		Blue	Blue	Blue								
	Sn					Blue	Blue							

Table 2 lists the many cations that have already been incorporated in the sheets. An important aspect which has to be respected is the cation radius (r). Sometimes, a large cationic radius can be incompatible with the brucite-like sheet. As a result, the octahedral site is destroyed and a new coordination is formed with some water molecules in the interlaminar spacing [19]. The ionic radii are in the range 60-80 pm for divalent cations and 62-69 pm for trivalent ones (with the main exception, Al: $r = 50$ pm) [39]. However, the incorporation of some bulky divalent and trivalent metal cations such as Cd^{2+} [40], Ca^{2+} [41], Pd^{2+} [42,43], Mn^{2+} [44], Y^{3+} [45], Cr^{3+} [41] and La^{3+} [42,43] were achieved without modifying the LDH octahedral structure. In addition, syntheses with tetravalent cations were carried out [46-47]. LDHs were also synthesized with monovalent Li^+ cations and Al^{3+} trivalent cations [48]. It should also be noted that the synthesis can be performed with a mixture of several divalent or trivalent cations to form a ternary [49,50] and even a quaternary [51,52] LDH material.

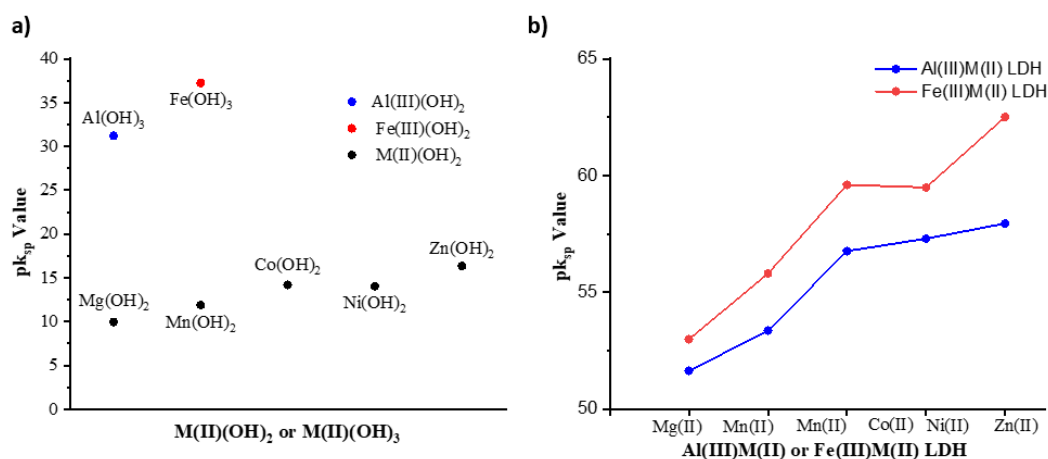


Figure 3. (a) pK_{sp} values for different $\text{M}(\text{II})(\text{OH})_2$ and $\text{M}(\text{III})(\text{OH})_3$ metal hydroxides. (b) Evolution of pK_{sp} values for different $\text{M}(\text{II})\text{M}(\text{III})$ LDHs. All pK_{sp} values are adapted from Ref. [53].

The choice of trivalent and divalent metal cations also plays a role in the stability of the LDH. The relative stability and solubility of LDHs are related to those of their corresponding metal hydroxides [53]. Generally, the stability of the LDH, relative to its component cations, increases with the stability of both the trivalent and divalent metal hydroxides. $\text{Al}(\text{OH})_3$ metal hydroxides exhibit a lower pK_{sp} value than $\text{Fe}(\text{OH})_3$ (**Figure 3a**), and are thus considered more soluble and less stable. Analogously, $\text{M}(\text{II})\text{Al}(\text{III})$ LDHs have been proved to be more stable than $\text{M}(\text{II})\text{Fe}(\text{III})$ LDHs (**Figure 3b**). The order of stability of LDHs bearing different divalent metals $\text{M}(\text{II})$ follows

the same trend as that of their corresponding $M(II)OH_2$: $Mg(II) < Mn(II) < Co(II) \approx Ni(II) < Zn(II)$, for a given $M(III)$.

Another major structural parameter of LDHs is the mole fraction of trivalent cations, denoted by x , which represents the charge density of the cationic sheets. Some authors describe systematically LDHs by the divalent versus trivalent ratio $R=M(II)/M(III)$, generally with an integer value where $R = 1/x - 1$. In LDH systems, the x or R value is reliable to a certain range in order not to induce structural changes (**Figure 4**).

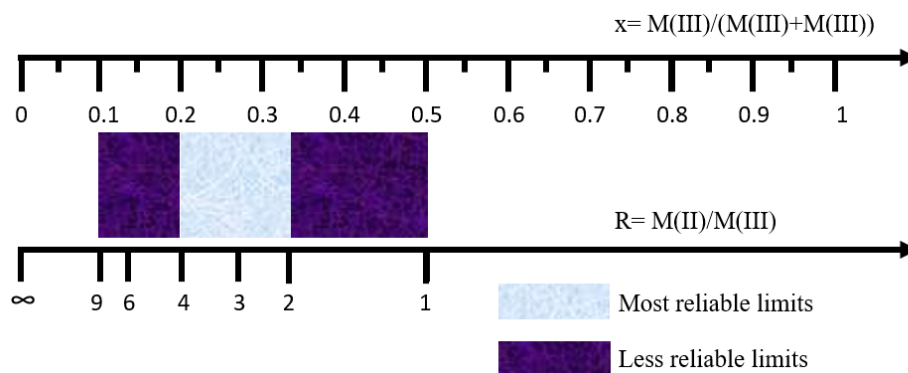


Figure 4. Reliable limits for metallic sheets composition in the LDH structure in terms of trivalent molar ratio (x) and divalent to trivalent molar ratio (R).

In general, x value should fall in the range of 0.2 and 0.33 (*i.e.*, $2 \leq R \leq 4$) [39]. A value of x greater than 0.33 is generally less reliable due to electrostatic repulsion between neighboring trivalent metals in the layers which could be associated with the creation of $M(III)-O-M(III)$ unfavorable bonds. Whereas a value of lower than 0.20 could correspond to a very close distance with the intercalated anions, and would therefore lead to a collapse of the laminar structure or the synthesis of simple hydroxides. However, there are some exceptions, as in the case of $Fe(II)/Fe(III)$ green rusts where the charge density can evolve up to $x = 1$ ($R = 0.5$) [54,55], or even for $Ni(II)$ -based LDHs where the charge density can also be reduced to $x = 1$ ($R = 9$) [56].

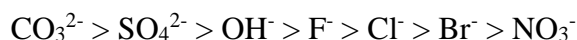
2.2.3. Composition of the interlaminar spacing

For the majority of natural and laboratory synthesized LDHs, carbonate is the intercalated anionic species due to the very strong affinity of the brucite-like sheets for this type of anion, and by the presence of carbon dioxide (CO_2) in the atmosphere [57]. However, it is possible to intercalate a large number of anions instead of carbonate in the interlaminar region. This is itself a very interesting

property of LDH materials which encouraged several researchers to work on the intercalation chemistry of LDHs in order to intercalate several anionic species, thus targeting a wide range of applications.

In fact, there is almost no limit on the nature of the species that can be intercalated, except provided of course that the species is stable and negatively charged in the operating conditions. Thus, simple inorganic anions such as carbonate (CO_3^{2-}), nitrate (NO_3^-), perchlorate (ClO_4^-) or halides (F^- , Cl^- , Br^- , I^-) can be intercalated in the interlaminar region [57,58]. Coordination complexes like ferricyanides ($\text{Fe}(\text{CN})_6^{3-}$) and ferrocyanides ($\text{Fe}(\text{CN})_6^{4-}$) [59,60], organic anions such as antimicrobial molecules and antibiotics [61,62], lysozymes [63,64], amino acids [65,66] and DNA [67,68] can also act as charge-compensating intercalated anions. The distance of the interlaminar domain can therefore extend from 3 Å to more than 40 Å in the case of organic biomolecules. This distance is notably influenced by the charge of the anion, its symmetry, its orientation, as well as the water molecules present around this anion.

Since the main focus of this manuscript is to discuss LDHs used for antibacterial applications, the preferred intercalation and synthesis methods of antibacterial LDHs will be discussed further in the following part. However, we can already affirm that they are greatly influenced by the affinity of the sheets for these various anions. This affinity depends on several parameters, including the charge and the size of the intercalated anions: thus, small species highly charged molecules will be significantly more favorable than large, lightly charged ones. In fact, a classification according to the affinity of the sheets for different inorganic anions was established [57]:



3. Antibacterial layered double hydroxide materials: Types and synthesis routes

Despite the success achieved by the use of antibiotics to fight pathogenic bacteria, bacterial contaminations and subsequent infections still present a significant threat on the global healthcare [69]. Moreover, the excessive use of traditional antibacterial drugs, *e.g.*, antibiotics, has led to the emergence of antibiotic-resistant bacteria [6,7]. Recent advances in the field of material science had opened up new channels for designing new antimicrobials based on synthetic inorganic

materials [70–72]. In fact, inorganic antibacterial materials are considered advantageous over organic antibacterial materials due to their higher stability, recyclability and improved safety [73]. Among the various inorganic materials, layered double hydroxides (LDHs) were extensively studied due to their interesting properties as anion exchangeability, compositional flexibility, and biocompatibility, thus making them good candidates for several antimicrobial application fields such as water purification [74,75], food packaging [76,77], wound healing dressings [78], and textile industries [79].

3.1. Types of antibacterial LDHs

By examining the literature, three types of antibacterial LDHs could be identified (**Figure 5**): antimicrobial molecules-intercalated LDH hybrids, nanoparticles-loaded LDH composites and pristine LDHs having a structure similar to that of typical LDHs explained previously (**Section 2.2**).

Several surveys showed that LDHs possess high potential as carriers of functional antibacterial molecules due to their interesting property of intercalating large anionic biomolecules in the interlaminar spacing [80–82]. This would lead to the formation of antibacterial molecules-intercalated LDH hybrids which are capable of inducing an efficient antibacterial effect. LDHs can also be loaded with nanoparticles (NPs) such as gold, silver, copper and zinc oxide NPs which are known to treat several diseases caused by bacterial infections [83–88]. The assembly of metallic NPs-in inorganic matrices as of LDHs can provide an inexpensive and biocompatible means to help limit the problem of aggregation and high exposure dose of free NPs [89]. These two types of LDHs are referred as LDH composites where some modifications have been performed to obtain such antibacterial agent.

Some previous work reporting the antibacterial activity of LDH-composites, *e.g.*, antibacterial molecules and NPs-loaded LDHs, developed several control experiments to prove that the pristine LDH matrices do not contribute to the antibacterial activity imposed by the LDH-composites [90–93]. However, recent studies showed that even pristine LDHs, more precisely Zn(II) and Cu(II)-based pristine LDHs, could induce an efficient antibacterial without any further modification [36,94–96].

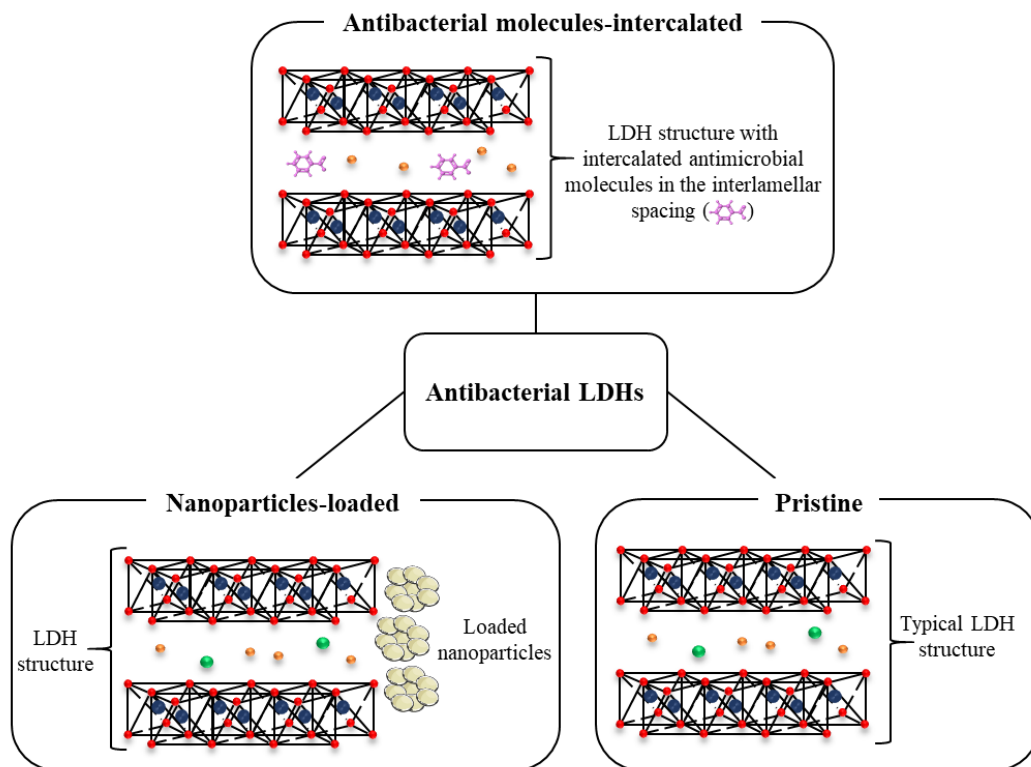


Figure 5. Different types and structures of antibacterial layered double hydroxides: Antibacterial molecules-intercalated LDHs, nanoparticles-loaded LDHs, pristine LDHs having a structure similar to that of typical LDHs.

3.2. Synthesis routes of antibacterial LDHs

As with any other LDH material, the different types of antibacterial LDHs are prepared by three major methods illustrated in **Figure 6**.

3.2.1. Coprecipitation

Synthesis of LDHs using direct coprecipitation route is mainly the most employed method including a variety of divalent and trivalent metal cations as well as different intercalated anions. This method mainly relies on the slow addition of a solution of the desired anion to be intercalated into another solution having the divalent and trivalent metal cations in a specific ratio and finally increasing the pH by simultaneous addition of a base usually sodium hydroxide (**Figure 6 (1)**) or urea hydrolysis that subsequently leads to the precipitation of the LDH [19,97–99].

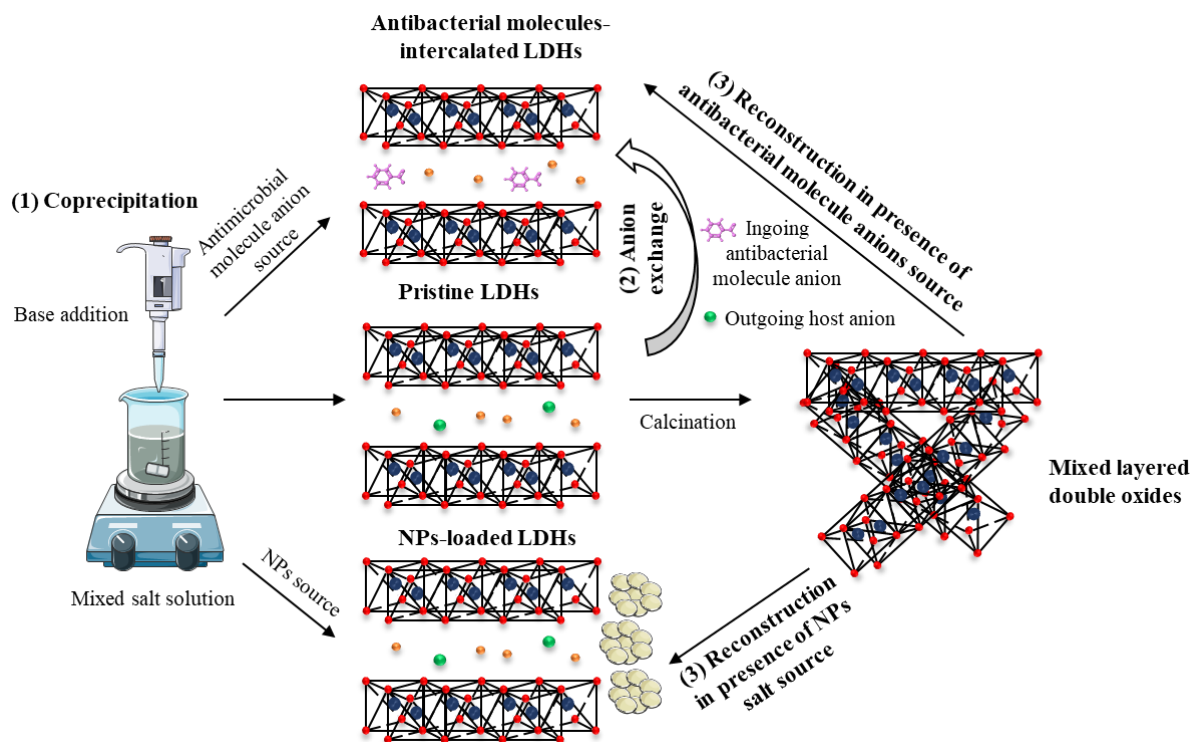


Figure 6. Schematic representation of the three different methods used to synthesize antibacterial LDHs: (1) Direct coprecipitation of mixed metallic salt solutions for pristine LDHs, this synthesis route is carried out in presence of antibacterial or nanoparticles source for antibacterial molecules-intercalated and NPs-loaded LDHs, (2) Anion-exchange reactions between previously prepared pristine LDHs and antibacterial molecules basic solution for antibacterial molecules-intercalated LDHs, (3) Rehydration of layered double oxides, previously obtained by calcination of pristine LDHs, in presence of antibacterial molecules or NPs source for antibacterial molecules-intercalated and NPs-loaded LDHs, respectively.

All pristine unmodified antimicrobial LDHs were prepared using coprecipitation method [34–36,100], since they do not exhibit any further structural or compositional change compared to typical LDHs used for other applications. Coprecipitation is often also used for synthesis of antimicrobial NPs-loaded LDHs in presence of an additional preparatory step either during the *in-situ* growth of the LDH matrix or through a post-synthetic step aiming to load the desired NPs into the LDH matrix [91,101]. In fact, several investigations on the synthesis of antibacterial molecules-intercalated LDHs using coprecipitation synthesis route were reported [102-104].

3.2.2. Anion-exchange

Due to their remarkable property in terms of anion exchange capacity, antibacterial molecules-intercalated LDHs can be synthesized by an indirect anion exchange route, which was commonly used for intercalation of larger anions as biological ones for example [58]. In this method LDHs with host anions as NO_3^- , CO_3^{2-} , and Cl^- are primarily prepared by coprecipitation, then the exchange with other desired intercalated anions can take place (**Figure 6 (2)**) [105,106]. In fact, anion-exchange synthesis is the most frequently used method to synthesize antibacterial molecules-intercalated LDHs [81,82,93,107,108].

It is important here to mention the importance of several factors during the anionic exchange where an appropriate solvent should be chosen to favor the exchange process, the pH must be maintained above 4 so that the hydroxyl layer will not break and the process is much more favored at higher temperatures [98,109].

3.2.3. Reconstruction: Calcination/Rehydration

One property of LDH clay materials is their ability to regain their original structure back after calcination followed by rehydration, this property is termed as “memory effect” [110]. In fact, calcining LDHs at mild temperatures (400-500°C) would transfer them to their respective metal oxides by eliminating interlayer water molecules, hydroxyl groups and previously intercalated anions. Furthermore, when these obtained mixed metal oxides are immersed in another solution containing other anions to be intercalated, *e.g.*, antibacterial molecules in case of antibacterial molecules-intercalated LDHs and NPs sources in case of NPs-loaded LDHs, the LDH structure can be regenerated back by rehydration (**Figure 6 (3)**) [111].

Indeed, several antibacterial molecules were successfully intercalated into the LDH interlamellar spacing using this synthesis method [62,112]. Antimicrobial NPs-loaded LDHs could also be prepared by reconstruction method, by which the NP source associated with the intercalating anion, *i.e.*, NPs salt source, is added to the LDH suspension after calcining the mother LDH [89].

4. Antibacterial mechanisms of layered double hydroxide materials

Each type of antibacterial LDH, *e.g.*, antibacterial molecules-intercalated LDHs, NPs-loaded LDHs and pristine LDHs, may induce a different antibacterial mode of action. **Figure 7** illustrates the three different suggested mechanisms explaining the antimicrobial activity of these different types of antibacterial LDHs: **(1)** direct surface interactions between pristine and NPs-loaded LDHs with the bacteria thus leading to their growth inhibition or death [36,78,89,92,95], **(2)** dissolution by through the controlled release of antibacterial molecules present in the LDH interlaminar region of antibacterial molecules-intercalated LDH composites [93,104], or through the release of constituent metal ions, *e.g.*, Zn^{2+} , Cu^{2+} , Ag^+ from NPs-loaded and pristine LDHs [95,101,113], and **(3)** generation of reactive oxygen species (ROS) by pristine and NPs-loaded LDHs to yield an efficient antibacterial effect [36,68,88,95,96,114]. **Table 3** reports the antibacterial performance of pristine and NPs-loaded LDHs together with the suggested antibacterial mechanisms provided in previous literature. The antibacterial performance of these LDHs associated to their antibacterial tests assays and mechanisms of action will be described in details further in the manuscript (**Sections 4.1 and 4.3**).

Table 3. Antibacterial performance of pristine and NPs-loaded LDHs and the proposed associated antibacterial mechanisms. MIC values correspond to the minimum inhibitory concentration required to inhibit the growth of a certain bacteria, whereas inhibition zone diameters correspond to the obtained inhibitory diameter zone generated by LDHs when being tested in agar disk or agar well diffusion tests.

LDH sample	Type	Tested Bacteria	Antibacterial performance	Proposed mechanism	Reference
Ag-ZnAl	NPs-loaded LDHs	Gram-positive: <i>Staphylococcus aureus</i> Gram-negative: <i>Escherichia coli</i>	Ag-LDH composite showed a greater antibacterial activity than unsupported nanosized silver with inhibition zone diameters and MIC values ranging between 7 and 14.7 mm and 0.3 and 0.7 $\mu\text{g/mL}$, respectively over several days	Surface interactions	[89]

Ag-ZnAl	NPs-loaded LDHs	Gram-positive: <i>S. aureus</i> Gram-negative: <i>E. coli</i>	Ag-LDHs showed efficient antibacterial activity with inhibition zone diameters ranging from 8 to 18 mm. Aged samples showed an enhanced antibacterial activity in comparison to samples obtained directly by coprecipitation due to their smaller size enabling more contact with the tested bacteria	Surface interactions	[92]
Ag-MgAl	NPs-loaded LDHs	Gram-positive: <i>S. aureus</i> Gram-negative: <i>E. coli</i>	Ag-LDH showed similar antimicrobial activity to that of free Ag NPs with MIC values of 6.6 and 12 µg/mL against <i>S. aureus</i> and <i>E. coli</i> , respectively	Surface interactions	[91]
ZnO-Water polyurethane (WPU)-ZnAl	NPs-loaded LDHs	Gram-positive: <i>S. aureus</i> Gram-negative: <i>E. coli</i>	ZnO-WPU-LDH completely inhibited (100% inhibition) the growth of tested bacteria which was validated by plate colony count method	Ions release, generation of ROS	[114]
ZnFe	Pristine LDHs	Gram-positive: <i>S. aureus</i> , <i>Staphylococcus epidermidis</i> , <i>Streptococcus pyogenes</i> Gram-negative: <i>E. coli</i> , <i>Proteus vulgaris</i> , <i>Klebsiella pneumoniae</i> , <i>Pseudomonas aeruginosa</i>	ZnFe LDHs showed an efficient antimicrobial activity very similar to that of conventional antibiotics with inhibition zone diameters of 16.8-22.9 mm depending on the type of tested bacteria and selectivity of LDHs toward different bacterial strains	Surface interactions, metal ions release	[94]
ZnAl	Pristine LDHs	Gram-positive: <i>S. aureus</i> , <i>S. epidermidis</i> Gram-negative: <i>P. aeruginosa</i>	ZnAl LDH samples exhibited an efficient antibacterial activity with MIC values ranging from 4000 to 10000 µg/mL depending on the Zn ^{II} :Al ^{III} molar ratio initially present in the LDH structure	Ions release, generation of ROS	[37]
Ternary CuZnAl	Pristine LDHs	Gram-positive: <i>S. aureus</i> Gram-negative: <i>E. coli</i>	Ternary LDH samples showed increasing antibacterial activities with inhibition zone diameters of 8-15 mm depending on the size of LDH particles	Surface interactions, ions release	[115]
AgCl-ZnAl	NPs-loaded LDHs	Gram-negative: <i>E. coli</i>	AgCl-LDHs showed efficient antibacterial activity with MIC values ranging from 3.83 and 9.45 µg/mL depending on the size of the powders	Surface interactions, generations of ROS	[116]

Ag-MgAl	NPs-loaded LDHs	Gram-negative: <i>E. coli</i>	Ag-LDHs showed an efficient antibacterial activity with MIC values between 63 and 500 µg/mL depending on the size and amount of loaded Ag NPs.	Ions release, surface interactions	[117]
Au-MgAl	NPs-loaded LDHs	Gram-positive: <i>S. aureus</i> Gram-negative: <i>E. coli</i>	Au-LDH inhibited the growth of tested bacteria by 25-100% only when being irradiated with Near Infrared (NIR) laser. Greater bacterial inhibition percentages were achieved with longer irradiation times and greater LDH loadings	Surface interactions, generations of ROS	[88]
ZnAl	Pristine LDHs	Gram-positive: <i>S. aureus</i> , <i>Streptococcus lactis</i> , <i>Bacillus cereus</i> Gram-negative: <i>E. coli</i> , <i>P. aeruginosa</i> , <i>Salmonella typhimurium</i>	ZnAl LDHs showed an efficient antibacterial activity with inhibition zone diameters of 9-21 mm and MIC values of 150-300 µg/mL depending on the type of tested	Ions release, surface interactions, generation of ROS	[95]
CuAl, NiAl, CoAl, MnAl, MgAl,	Pristine LDHs	Gram-positive: <i>S. aureus</i> Gram-negative: <i>E. coli</i>	LDH samples showed an efficient antibacterial activity with MIC values between 800 and 1500 µg/mL depending on the type of tested LDH sample	Ions release, surface interactions, generation of ROS	[96]
Ternary CuMgAl:CO ₃	Pristine LDHs	Gram-positive: <i>S. aureus</i> , <i>Bacillus subtilis</i> , <i>Enterococcus faecalis</i> Gram-negative: <i>E. coli</i> , <i>P. aeruginosa</i>	Ternary LDH samples showed increasing antibacterial activity with increasing Cu ^{II} :Al ^{III} molar ratio and MIC values up to 31000 µg/mL	Surface interactions, ions release	[36]

In the following four sub-sections, several suggested antibacterial mechanisms of the different types of antibacterial LDHs are discussed. Of course, it is not possible to isolate only one antibacterial mechanism, because some antimicrobial effects of LDHs result from the combination of direct contact, ion or antimicrobial molecules release and ROS generation. However, some specificities can be correlated to the different suggested mechanisms. For instance, the long-distance effect through molecules or ion release, or the effect of light for the ROS generation. Therefore, each section starts with different physico-chemical considerations, followed by various experimental observations of these mechanisms and is concluded with some considerations on how to tune the properties of LDHs to maximize the antimicrobial effect through the suggested mechanism.

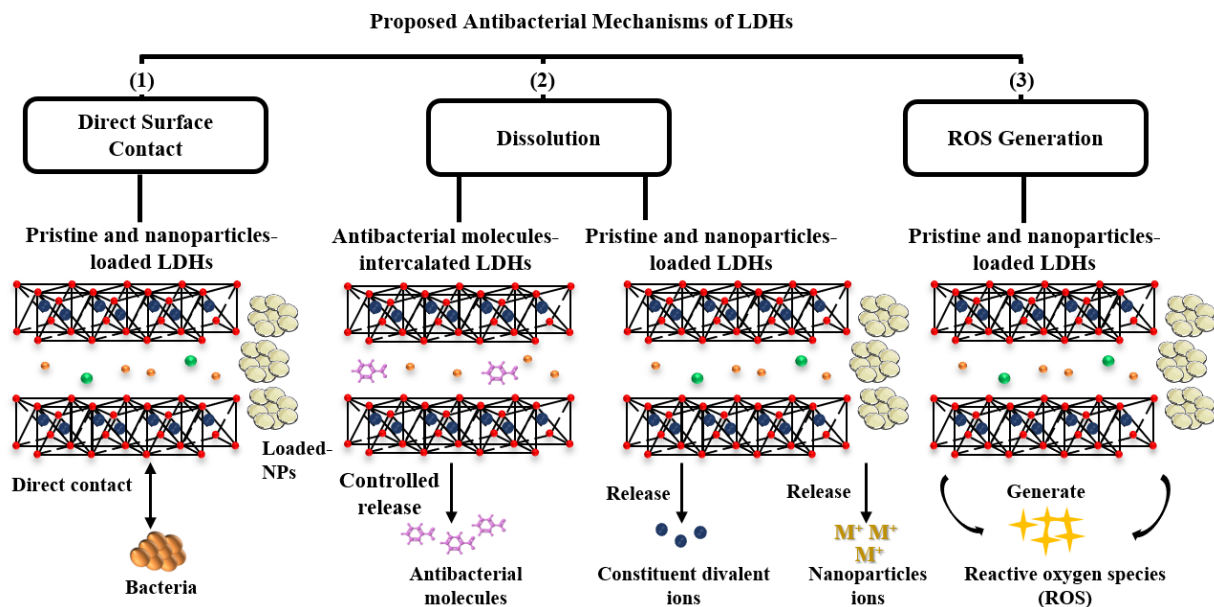


Figure 7. A schematic illustration of the proposed antibacterial mechanisms of LDHs. (1) Direct surface contact interactions between pristine and nanoparticles-loaded LDHs with bacteria, (2) Dissolution of antibacterial molecules: release of antibacterial molecules by antibacterial molecules-intercalated LDHs and release of metal ions by pristine and nanoparticles-loaded LDHs, and (3) Generation of reactive oxygen species (ROS) by pristine and nanoparticles-loaded LDHs. Scale is adjusted to clarify the illustration.

4.1. Direct surface interactions

Antibacterial activity by direct surface interactions requires a strong binding between the LDH and the targeted microorganism. This is achieved by electrostatic interactions ([Section 4.1.1](#)) and can be amplified by the topological structure of the LDH ([Section 4.1.2](#)). This direct contact implies a short-range effect of the LDH, excluding some antibacterial test assays to evaluate the antimicrobial effect ([Section 4.1.3](#)). Experimental observation of the antibacterial effect and the limitation of these observations to the direct contact mechanism will be given in [Section 4.1.4](#). The latter section is concluded with the determination of three parameters (charge, roughness and size) that can be tuned to maximize the antimicrobial effect.

4.1.1. Electrostatic interactions between bacteria and LDHs

From a physicochemical point of view, microorganisms as bacteria can be considered as living colloidal particles. This is due to their compositional polypeptides having ionizable weakly acidic and basic groups, *e.g.*, carboxyl and amino groups [118,119]. Therefore, materials possessing positively charged surfaces are believed to be ideal nuclei for microbial adhesion [120]. LDHs

have a positively charged surface with zeta potential values up to 30-50 mV [121], relatively large surface areas of 10-200 m²/g [122], and a high anion exchange capacity of f 200–400 mEq/100 g [123], thus meeting all the criteria for an ideal bacterial adhesion or adsorption [70]. For example, Jin *et al.* reported the removal of Gram-negative bacteria *Escherichia coli* by chloride-intercalated pristine MgAl and ZnAl LDHs for water purification applications [124]. LDH slurry systems showed a bacterial adsorption efficiency $\geq 99\%$. Similarly, the flow-through column showed an adsorption efficiency as high as 87 to 99%. Such findings suggested that LDHs could potentially be used as a sorbent material to purify untreated water from bacteria.

Liu *et al.* developed a carbonate intercalated NiFe LDH which was able to adsorb 45-55 mg/g of *Bacillus subtilis* under different experimental conditions [122]. The authors proposed different possible mechanisms of bacteria adsorption onto LDH particle surface including four types of interactions which are sketched in **Figure 8**. The first suggested interaction involved electrostatic interactions between the negatively charged bacterial membrane (due to the presence of PO₄⁻ groups) and the positively charged LDH surface (**Region A, Figure 8**). Bacterial adsorption could also be enhanced by anion exchange reactions, where PO₄⁻ groups present at the surface of the bacterium could gradually replace individual CO₃²⁻ on the LDH surface (**Region B, Figure 8**). Bacterial adsorption could be further achieved by the substitution of the OH groups on the LDH surface with the PO₄⁻ groups (**Region C, Figure 8**). The last suggested adhesion mechanism was that PO₄⁻ groups present on the bacterial surface and the OH groups on the LDH surface would interact with each other via hydrogen bonds and/or polar attractions (**Region D, Figure 8**).

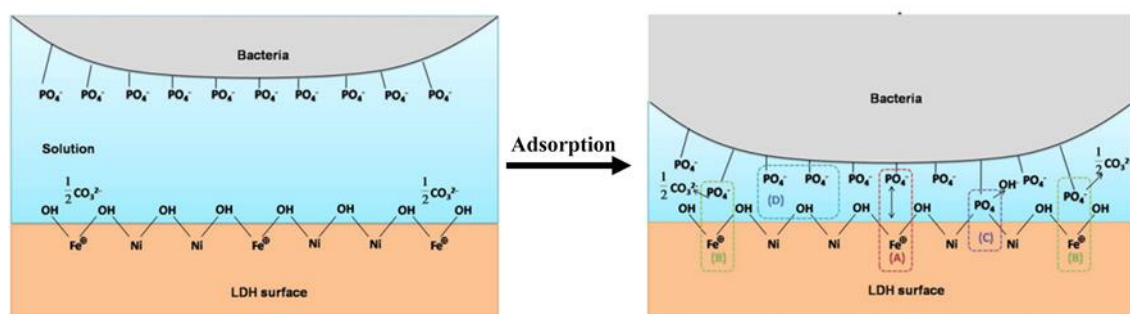


Figure 8. Mechanism of *B. subtilis* adhesion onto carbonate intercalated NiFe LDH. (A) Electrostatic interactions, (B) Anion exchange, (C) OH replacement and (D) H-bond and polar interactions. Reproduced from Ref. [122].

These mentioned investigations admitted the presence of surface interactions between LDHs and bacteria mediated by adhesion or adsorption phenomena. However, they did not actually correlate

such interactions to the antibacterial activity of LDHs where no antibacterial activity tests were carried out. In other words, adsorption or adhesion cannot solely explain antibacterial activity.

4.1.2. Topological adhesion of LDH on bacteria

One other possible reason explaining LDH-bacteria adhesion is the relative roughness of the LDH surface thus promoting the adhesion phenomena which may be a key factor contributing to their antibacterial activity [78,125]. It had been well known that the motility of bacteria is essential for bacterial normal functions [126], and that rough antimicrobial colloidal surfaces might adhere to bacteria and disturb its normal motility functions [11,127]. Zhang *et al.* successfully synthesized antibacterial composite of silica nanorods and unsmooth hollow Mn/Ni LDHs [78]. The antibacterial activities of SiO₂, Mn/Ni LDHs and SiO₂ nanorods @Mn/Ni LDHs were investigated against Gram-negative *E. coli* and Gram-positive *Staphylococcus aureus* bacteria, by standard cell viability Live/Dead Bac Light assay (**Figure 9a**). The ratio of green (alive bacteria) to red (dead bacteria) fluorescence (G/R) was also measured to compare the antibacterial efficiency of the different tested samples. As shown in **Figure 9b**, the ratio of G/R fluorescence in both Gram-positive and Gram-negative bacteria decreased significantly over time for hollow Mn/Ni LDHs as well as SiO₂@Mn/Ni LDHs samples, thus indicating their efficient antibacterial activity. The antibacterial activity of Mn/Ni LDHs and SiO₂@Mn/Ni LDHs was related to their bacterial adhesion properties to rough surfaces. As shown in **Figure 9c** and **d**, both hollow Mn/Ni LDHs and SiO₂ nanorods@Mn/Ni LDHs exhibited relatively good adhesion (blue arrows) and strong connection (red arrows) with *E.coli*. Therefore, the antibacterial activity of hollow Mn/Ni(OH)_x LDH structures was attributed to their ability to “seize” the bacteria thus disturbing its motility and leading to its death. Such findings come in line with those of Wang *et al.* who reported the enhancement of antibacterial function by loading lysozyme at the surface of ternary MgZnAl LDHs due to the rough surface of the host flower-like LDH providing better contact with bacteria and thus an amplified antibacterial effect [125]. LDH adhesion to bacteria could further affect the bacterial biological activities, such as blocking the channels for nutrients uptake and waste exclusion, which would subsequently lead to bacterial death or inhibition [34,93,128]. Moreover, LDH may also adsorb many essential nutrients for bacterial growth in medium, *e.g.*, proteins, celluloses, starch and proteins [93,128]. This would thus reduce the bioavailability of these necessary nutrients and inhibit the bacterial growth.

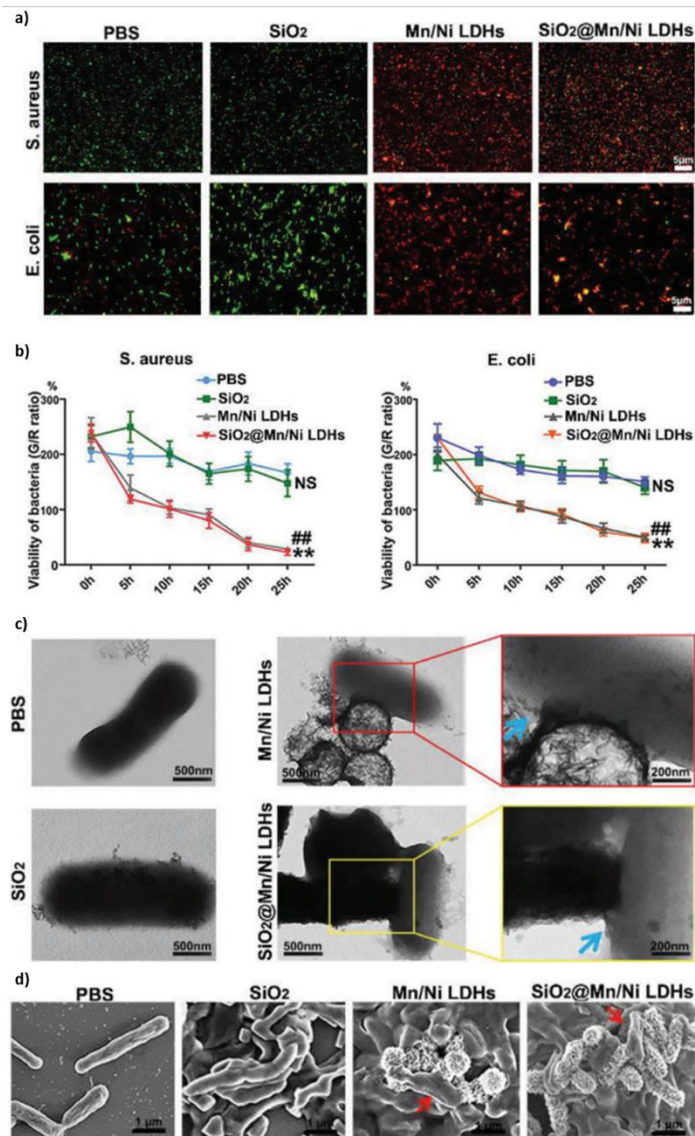


Figure 9. a) Confocal microscopy images of *S. aureus* and *E. coli* incubated with a mixture of propidium iodide (red color) and SYTO 9 (green color) and various samples. The images correspond to 25 h after incubation. Green fluorescence corresponds to live bacteria while red fluorescence corresponds to dead bacteria. b) The time dependent concentrations of live bacteria, evaluated by the ratio of G/R. c) TEM images of *E. coli* with or without treatment of different samples. Blue arrows correspond to bacterial adhesion. d) SEM images of *E. coli* with or without treatment of different samples. Red arrows correspond to direct connection with *E. coli* bacteria. Reproduced from Ref. [78].

Although these investigations suggested that the rough surface of LDHs aid in the adhesion phenomena leading to the achieved antibacterial effect [78,125], real measurements of LDH surface roughness are lacking. One good method to ensure the effectiveness of LDHs roughness in the antibacterial activity is to compare the antibacterial activity of different LDH samples having different surface roughness which could be evaluated easily by atomic force microscopy (AFM) for example [129,130].

4.1.3. Antibacterial test assays used to evaluate the direct contact antibacterial performance of LDHs

Different antibacterial test assays allowed the evaluation antibacterial performance of LDHs associated with direct contact. One very important point to consider while correlating the antibacterial performance of LDHs to their followed antibacterial mechanism is the used antibacterial test assay. Generally, evaluating the antibacterial performance of pristine and NPs-loaded LDHs could be achieved by agar disk or agar well diffusion methods [89,92,94,95], plate colony count method [114,131], or else by evaluating the minimum inhibitory concentration (MIC) of LDHs by broth macro or microdilution assays [37,89,95,95] (**Table 3**).

The principles of these antibacterial activity tests will be explained more in details in **Chapter 2** where we explain the experimental part of our research work. However, we can ensure from now that not all assays are suitable to suggest or validate the direct contact antibacterial mechanism. For instance, some studies suggested direct surface interaction as a mechanism explaining the antibacterial activities of NPs-loaded ZnAl LDHs [89,92]. However, reported inhibitions diameters were in the range of 7 to 18 mm in agar-agar gels, which seems in contradiction with a mechanism only driven by contact with the bacteria. Indeed, the mass transfer of particles through convection can be neglected in a gel, therefore the distance run by a particle in those experiments can be estimated with the Fick equation using the Stokes-Einstein equation for the diffusion coefficients [132]. At room temperature, in an agar-agar gel (typical viscosity: $\eta = 0.01$ Pa.s or 10 cPl) and with standard LDH particle aggregate (5 μm), the diffusion constant is in the order of magnitude of 4-16 m^2/s . During a standard duration of an experiment of disk diffusion or agar well diffusion (24 to 48h), the typical distance of the particle from the original position is 20 to 40 μm . Direct contact cannot be the explanation for the inhibition of the bacterial growth several millimeters away from the place in which LDHs were deposited. As a consequence, inhibition zone diameters measurements are not suitable to evaluate the antibacterial effect of LDHs by direct surface interactions. Therefore, other antibacterial tests assays as MIC determination and plate colony count methods should be employed to refer to direct contact mechanism of antibacterial LDHs.

4.1.4. Experimental observations, limitations and maximization of the direct contact effect of LDHs

Haffner *et al.* investigated the influence of particle size (from 42 to 208 nm) on pristine LDH interactions with bacteria-mimicking membranes (DOPE/DPG) [71]. LDH binding to bacteria-mimicking membranes and their destabilization increased significantly with decreasing particle size. Due to strong interactions with anionic lipopolysaccharide and peptidoglycan layers, direct membrane disruption was observed for both Gram-negative *E. coli* and Gram-positive *S. aureus* bacteria. Such membrane disruption was primarily evidenced by the leakage of the tested membrane liposomes which was enhanced with decreasing LDH particle sizes. The net negative charge of bacteria was also reduced due to the presence of electrostatic surface interactions which were thought to induce the observed membrane disruption.

In fact, the influence of LDH particle sizes on their antibacterial properties could also be determined by comparing the MIC values of LDHs having different particle sizes against the same microorganism. For instance, Dutta *et al.* reported a MIC value of 200 µg/mL for ~250 nm-sized Zn-based pristine LDH nanoparticles [95], which is remarkably lower than that of bulk Zn-based pristine LDHs (micron-sized agglomerated LDHs) prepared by Lobo-Sanchez *et al.* (MIC value of 10,000 µg/mL) [37]. Moreover, smaller-sized Zn(II)-based LDH nanoparticles (~50 nm) investigated by Moaty *et al.* presented even a lower MIC value of 15.6 µg/mL against the same bacterial strain [94]. In this context, LDH nanoparticles present a larger surface area and more active sites compared to bulk LDHs. Additionally, the great difference in MIC values between bulk LDHs and LDH nanoparticles could also be related to the ability of nanoparticles to provide a stable mobile suspension in solution, whereas bulk LDHs tend to sediment, thus limiting the accessible surface and contact with the tested *S. aureus* bacteria.

Moa *et al.* designed three different Ag-LDHs composites using three different synthesis methods [117]: Ag-LDHs@PDA and Ag-LDHs@TA-Fe(III) composites were prepared using a pre-synthesized polydopamine (PDA)/ tannic acid (TA)-Fe(III) layer as a nanoscale guide and PDA/TA itself as a reducing reagent to form uniform silver nanoparticles (AgNPs) on the surface of modified LDHs, Ag-LDHs(PVP) composites were prepared by the direct reduction of the precursor $[\text{Ag}(\text{NH}_3)_2]^+$ with polyvinyl pyrrolidone (PVP). **Figure 10a** shows the transmission electron microscopy (TEM) images of the loaded AgNPs in each composite, the size of loaded

Ag-NPs was 25, 65 and 15 nm for Ag-LDHs@TA-Fe(III), Ag-LDHs(PVP) and Ag-LDHs@PDA, respectively. Moreover, the amount of AgNPs loading was determined using energy dispersive spectroscopy (EDS) surface analysis (**Figure 10b**). Consequently, the antimicrobial performance of the Ag-LDHs composites was influenced by both the size and amount of loaded Ag NPs. Ag-LDHs(PVP) composite, having the highest Ag loading of 3.37% and medium-sized AgNPs, presented the lowest MIC value (**Figure 10c**), thus being the best tested antimicrobial composite. On the other hand, even with the lowest Ag loading, Ag-LDHs@TA-Fe(III) showed better antibacterial performance than that of Ag-LDHs@PDA, due to its very small particle sizes of loaded AgNPs.

A similar finding was reported by Nocchetti *et al.* [116], where AgCl-LDH composites with Ag loading of 4.9% and small AgCl NPs (64 nm) showed greater antibacterial performance compared to that of another AgCl-LDH composite with Ag loading of 12.1% but with a larger size (94.8 nm). Therefore, the antibacterial performance was rather dependent on the dimensions of loaded NPs, which corresponded to greater surface area and thereby promoted better contact with the bacteria probably leading to enhanced mobility of NPs adhering to bacteria. In fact, NPs as AgNPs can anchor to the bacterial cell wall and consequently impose membrane damages [133,134]. After adhesion to the bacterial wall, NPs can also penetrate the membrane to interact with cellular structures and biomolecules such as proteins, lipids, and DNA. Interaction between metallic NPs and cellular structures or biomolecules may subsequently lead to bacterial dysfunction and finally growth inhibition or death [133–136]

The previously mentioned investigations succeeded to correlate direct surface interactions between bacteria and LDHs to their antibacterial activity (**Mechanism 1, Figure 7**). However, the used experimental approaches were only achieved through the evaluation of the effect of LDH particle sizes [71,117] or else through qualitative adhesion observations using SEM or TEM imaging [78,125] without any quantification of the driving forces of interactions. In fact, other methods can be used to investigate and quantify LDHs-bacterial membrane. In this context, the use of recent AFM-based force spectroscopy modes would be helpful, *e.g.*, single-molecule and single-cell force spectroscopies (SPFS and SCFS, respectively [137,138]). The use of such force spectroscopy approaches would allow not only a qualitative but also a quantitative evaluation of the presented forces of interactions at the single-particle or single-cell levels.

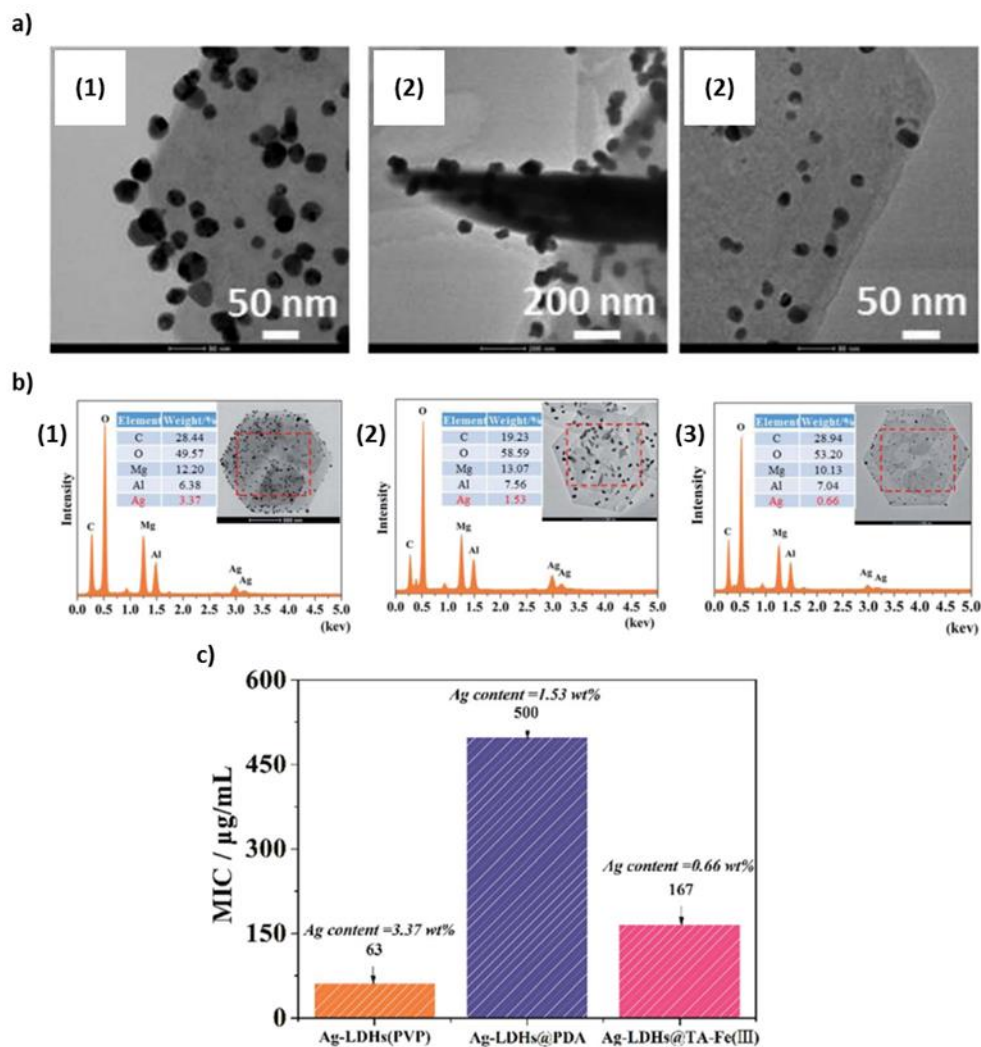


Figure 10. a) HRTEM images of (1) Ag-LDHs(PVP), (2) Ag-LDHs@PDA and (3) Ag-LDHs@TA-Fe(III). b): EDS surface scans for (1) Ag-LDHs(PVP), (2) Ag-LDHs@PDA and (3) Ag-LDHs@TA-Fe(III). c): The MIC values of the different Ag-loaded LDHs against *E. coli*. Reproduced from Ref. [117].

Even though there is still much missing information concerning the role of direct surface interactions in the antibacterial effect of pristine and NPs-loaded LDHs, one could still derive some factors which could help maximize such an effect:

- an increase in the positive charge of the LDH or the loaded NPs increases the chance of electrostatic interactions with the negatively charged bacterial membranes
- a rough surface of the LDH promoting adhesion to bacteria
- smaller LDH particles or loaded NPs providing enhanced mobility and maximum surface area for the interaction

4.2. Dissolution through the release of antimicrobial molecules from antimicrobial molecules-intercalated LDHs

LDH exposure to aqueous solutions in which dissolution can certainly take place may play an important role in their several potential applications including antibacterial ones (**Mechanism 2, Figure 7**). In particular, special investigations were conducted to study the dissolution of antibacterial molecules-intercalated LDHs to provide a controlled release of bioactive compounds.

Table 4. Antibacterial performance of organic biomolecules-intercalated LDHs reported in the literature. MIC values correspond to the minimum inhibitory concentration required to inhibit the growth of a certain bacteria, whereas inhibition zone diameters correspond to the obtained inhibitory diameter zone generated by antimicrobial molecules-intercalated LDHs when being tested in agar disk or agar well diffusion tests.

LDH host	Antimicrobial compound	Tested Bacteria	Antibacterial performance	Reference
MgAl	Phenoxyethyl-penicillin	Gram-positive: <i>S. aureus</i>	Penicillin-LDH showed efficient antibacterial activity with inhibition zone diameter ranging from 8 to 25 mm depending on the pH of the media	[62]
ZnAl	Cephazolin	Gram-positive: <i>S. aureus</i>	Cephazolin-LDH possessed an inhibition zone of 225 m ² in water and 240 m ² in presence of 0.8% NaCl	[93]
ZnAl	O-hydroxybenzoate (o-BzOH)	Gram-negative: <i>E. coli</i>	O-BzOH-LDH was able to reduce the growth of bacteria which was evidenced by plate count method. The antimicrobial properties of O-BzOH-LDH were enhanced with decreasing powder dimensions.	[103]
MgAl	Lysozyme (LYZ)	Gram-positive: <i>S. aureus</i>	LYZ-LDHs possessed great antibacterial activity (ranging from 40 to 97.5%) depending on the LYZ/LDH ratio and the pH of the bacteria-containing water	[139]
MgAl	Camphorsulfonic acid, Ciprofloxacin	Gram-positive: <i>S. aureus</i> , <i>S. epidermidis</i> , <i>S. pyogenes</i> Gram-negative: <i>E. coli</i> , <i>Proteus vulgaris</i> , <i>P. aeruginosa</i> , <i>Enterobacter cloacae</i>	Camphorsulfonic acid-LDH composite was active against Gram-negative bacteria with MIC between 1.4 and 10 mg/mL, Ciprofloxacin-LDH was active against both Gram-positive and Gram-negative with higher MIC of 1.3 mg/mL	[107]
MgAl	Turmeric curcuminoid	Gram-positive: <i>S. aureus</i> Gram-negative: <i>E. coli</i> , <i>P. aeruginosa</i>	Curcuminoid-LDH showed inhibition zone diameters against all tested strains ranging from 8 to 19 mm depending on the pH of the medium	[140]

MgAl	Berberine chloride (BBC)	Gram-positive: <i>S. aureus</i> , <i>B. subtilus</i> Gram-negative: <i>P. aeruginosa</i>	BBC-LDH hybrids showed inhibition zone diameters ranging from 2 to 9 mm depending on the type of tested bacteria and applied synthesis method. BBC-LDH hybrid prepared by coprecipitation showed a greater inhibitory effect than that synthesized by anion-exchange.	[141]
MgFeAl	Pipemidic Acid ions	Gram-negative: <i>E. coli</i> , <i>S. typhimurium</i>	Pipemidic acid-LDH showed efficient antimicrobial activity with MIC values of 3.5 and 4.5 mg/mL against <i>E. coli</i> and <i>S. typhimurium</i> , respectively	[142]
ZnAl	Benzoate anions (BZ)	Gram-positive: <i>S. aureus</i>	All hybrid BZ-LDH showed excellent antibacterial activities ensured by plate count method. BZ-LDH prepared by reconstruction route possessed the highest antibacterial activity among the other hybrids prepared by coprecipitation and anion-exchange routes	[143]
ZnAl	Chitosan polymer	Gram-positive: <i>S. aureus</i> , <i>B. subtilus</i> , <i>Lactobacillus sakei</i> , <i>E. faecalis</i> Gram-negative: <i>E. coli</i> , <i>P. aeruginosa</i> , <i>P. vulgaris</i>	Chitosan-LDH had superior activity to that of free chitosan and is active toward <i>L. sakei</i> (MIC=0.125 mg/mL), <i>S. aureus</i> (MIC=0.4 mg/mL), <i>E. coli</i> (MIC=0.2 mg/mL)	[74]
MgAl	3-(4-hydroxyphenyl)propionic acid (HPP) L-ascorbic acid (ASA) L-tyrosine (TYR) L-tryptophan (TRP)	Gram-positive: <i>S. aureus</i> Gram-negative: <i>E. coli</i>	All hybrids except HPP-LDH achieved 100% growth inhibition for both bacteria ensured by plate count method.	[144]
ZnTi	Kojic acid	Gram-positive: <i>S. aureus</i> Gram-negative: <i>E. coli</i> , <i>P. aeruginosa</i>	Kojic acid-LDH was efficient against <i>E. coli</i> and <i>P. aeruginosa</i> with inhibition zone diameters of 10.77 and 6.95 mm, respectively	[145]
CuAl-CMC polymer	Amoxicillin	Gram-positive: <i>S. aureus</i> Gram-negative: <i>E. coli</i>	Amoxicillin-LDH-CMC hybrids showed increasing inhibition zone diameters ranging from 8 to 25 mm depending on the LDH:CMC mass ratio	[146]
MgAl-LDPE polymer ZnAl-LDPE polymer	Salicylate anions (SA) Rosmarinate anions (RA)	Gram-positive: <i>S. aureus</i> Gram-negative: <i>E. coli</i>	SA-LDH-LDPE and RA-LDH-LDPE hybrids inhibited the growth of both tested bacteria evidenced by plate count method. The highest inhibition was observed for SA-ZnAl-LDPE	[147]

CaAl	Ciprofloxacin	Gram-positive: <i>S. aureus</i> Gram-negative: <i>E. coli</i> , <i>K. pneumoniae</i>	Ciprofloxacin-CaAl hybrids showed an inhibition zone diameter ranging between 43 and 60 mm and MIC values between 0.04 and 0.06 mg/L depending on the type of tested bacteria	[148]
------	---------------	-----------------------------------------------------------------------------------------	-------------------------------------------------------------------------------------------------------------------------------------------------------------------------------	-------

Most of the work highlighting the efficiency of LDHs to act as antibacterial materials is actually related to their ability to intercalate antibacterial organic biomolecules such as antibiotics [62,93,128], lysozymes [125,139] and antibacterial polymeric organic molecules [74]. This is probably due to LDHs remarkable property of intercalating a wide variety of anions within their interlamellar regions. Recently, antibacterial molecules-intercalated LDHs had been also incorporated with several polymeric matrices to design efficient antibacterial fillers for various applications as well [146,147]. **Table 4** reports some of the previous work done on the efficiency of antibacterial compounds-intercalated LDH composites.

4.2.1. Controlled release of antibacterial molecules out of antibacterial molecules intercalated-LDHs

Nearly all of the studies dealing with the antibacterial activity of antibacterial organic molecules-intercalated LDHs are mainly concerned with the controlled release of the active biomolecule out of the LDH matrix [80,104,142,145,146,149–151], which is the main contributor to the followed antibacterial mechanism.

One example of controlled release behavior of antibacterial molecule-intercalated LDHs is the controlled delivery of Kojic acid (KA) out of ZnTi LDH [145]. In phosphate-buffered saline (PBS, pH = 5), pure KA is released in one step and not gradually. However, the ZnTi-KA composite released KA anions in a slow gradual manner, where even after 12 h KA anions were still released. The prolonged release behavior of KA suggests the maintenance of a long-term antibacterial effect of the LDH hybrid. The long-term antibacterial activity of antimicrobial molecules intercalated-LDHs can be explained by two main reasons: (1) the protection of the LDH matrix for intercalated molecules by isolating them from a hostile environment, (2) the slow release of intercalated molecules from the LDH interlayer [104,106,128]. Moreover, the intercalation of KA into LDH also improved its stability at higher temperatures. Such enhancement of thermal stability of

antibacterial molecules when being intercalated in LDH matrices was also reported in other studies as well [107,152,153].

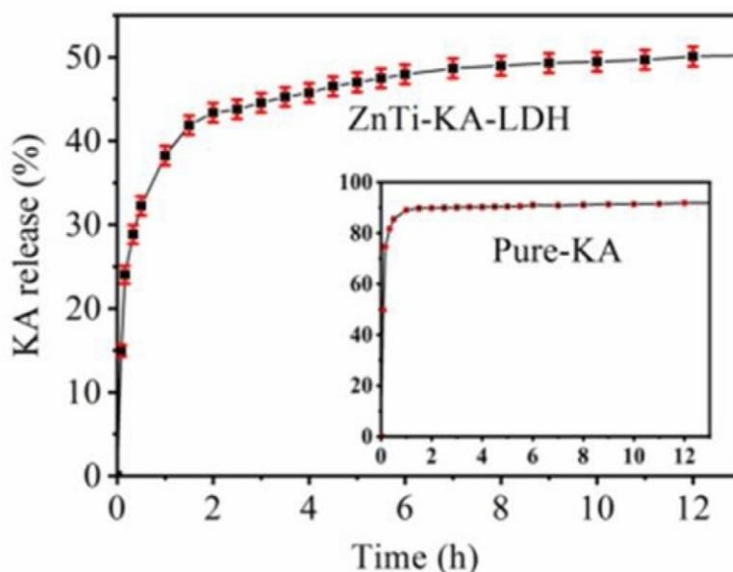


Figure 11. Release profile of Kojic acid from ZnTi-KA-LDH and pure-KA in phosphate buffer saline solution at pH = 5. Reproduced from Ref. [145].

4.2.2. Influence of intercalating method on the release behavior

One important factor influencing the antimicrobial activity of antibacterial molecules-LDH hybrids is the applied synthesis method. As with any other LDH material, antibacterial molecules intercalated-LDHs are prepared using coprecipitation, anion exchange and calcination/rehydration synthesis routes previously explained in [Section 3.2](#) and illustrated in [Figure 6](#).

Djebbi *et al.* compared the antibacterial behavior of the same LDH composite synthesized using two different methods, conventional anion exchange (AE) and direct coprecipitation (AC) routes [141]. The amount of intercalated antibacterial molecule berberine chloride (BBC) in the inorganic matrix, estimated by UV-Vis spectroscopy analysis, was found to be 24% and 93% in BMAE and BMAC, respectively. Moreover, the release profiles of BBC from AE and AC biohybrid LDHs were separately measured in PBS at pH = 7.4 ([Figure 12a](#)), and the released percentage of BBC from AC was greater than that from AE.

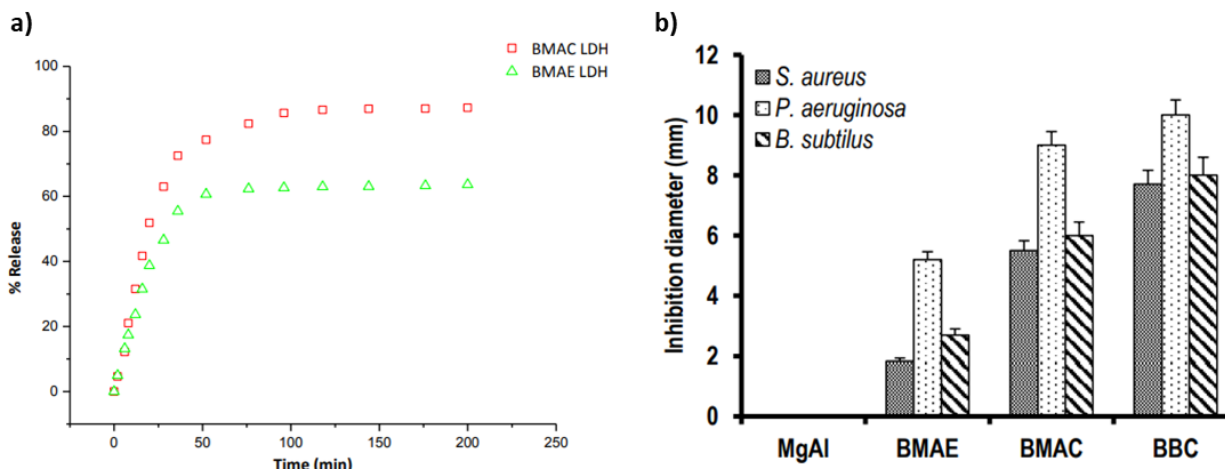


Figure 12. a) Release profiles of berberine chloride (BBC) from BBC-LDH hybrids obtained by anion exchange (BMAE) and coprecipitation (BMAC) synthesis routes. b) Inhibition zone diameters of free BBC and BBC-LDH hybrids. Reproduced from Ref. [141].

Consequently, the antimicrobial activity of AC was more efficient than that of AE (**Figure 12b**) due to an improvement in chemical stability, the greater amount of intercalated and released BBC. On contrary, Mishra *et al.* pointed out the lower antimicrobial efficiency and lower release behavior of Benzoate-LDH hybrids synthesized by coprecipitation in comparison to those synthesized by anion-exchange and reconstruction methods [143]. The authors attributed the difference in the antimicrobial performance of the hybrids synthesized using different methods to the different orientations of benzoate anions within the interlamellar space of the LDH in each case. Such different orientation resulted in a different loading and release behavior of antibacterial molecules as previously suggested by Wang *et al.* [82]. Such contradiction suggests that choosing a particular synthesis method to synthesize antibacterial molecules-intercalated LDHs is an important factor to be taken into consideration. Therefore, an optimization of the most efficient synthesis method should be performed according to the type, structure, and orientations of the antibacterial molecules intercalated in the LDH interlayer.

4.2.3. Influence of the LDH host on the antibacterial activity of antibacterial molecules-intercalated LDH composites

Bugatti *et al.* reported the influence of powder dimensions evaluated by granulometry analysis on the antimicrobial properties of antibacterial molecules-intercalated LDHs [103]. Antibacterial composites (ZnAl-o-BzOH) based on ZnAl LDH and o-hydroxybenzoate (o-BzOH), also known as salicylate, were synthesized by a direct coprecipitation method. The initial powder dimensions

were reduced by the high energy ball milling (HEBM) technique for 1 to 5 min influencing the size as well as the morphology of the powders. Large, agglomerated particles were found for the non-milled samples (**Figure 13a (1)**), while platelets with uniform and thinner sizes were present in the milled samples for 5 min (**Figure 13a (2)**). As a result, the amount of released o-BzOH molecules and the antimicrobial activity against *E. coli* was found much more effective for the samples with lower powder dimensions (**Figure 13b and c**). Therefore, particles with lower dimensions provided an enhanced release of o-BzOH anions and an enhanced antibacterial activity. A similar finding was suggested by Kuznetsova *et al.* who reported a remarkable impact of the hydrodynamic radius of the LDH composite powders on the release behavior of 2-mercaptobenzothiazole anions out of ZnAl LDH host and therefore an enhanced antibacterial activity [154].

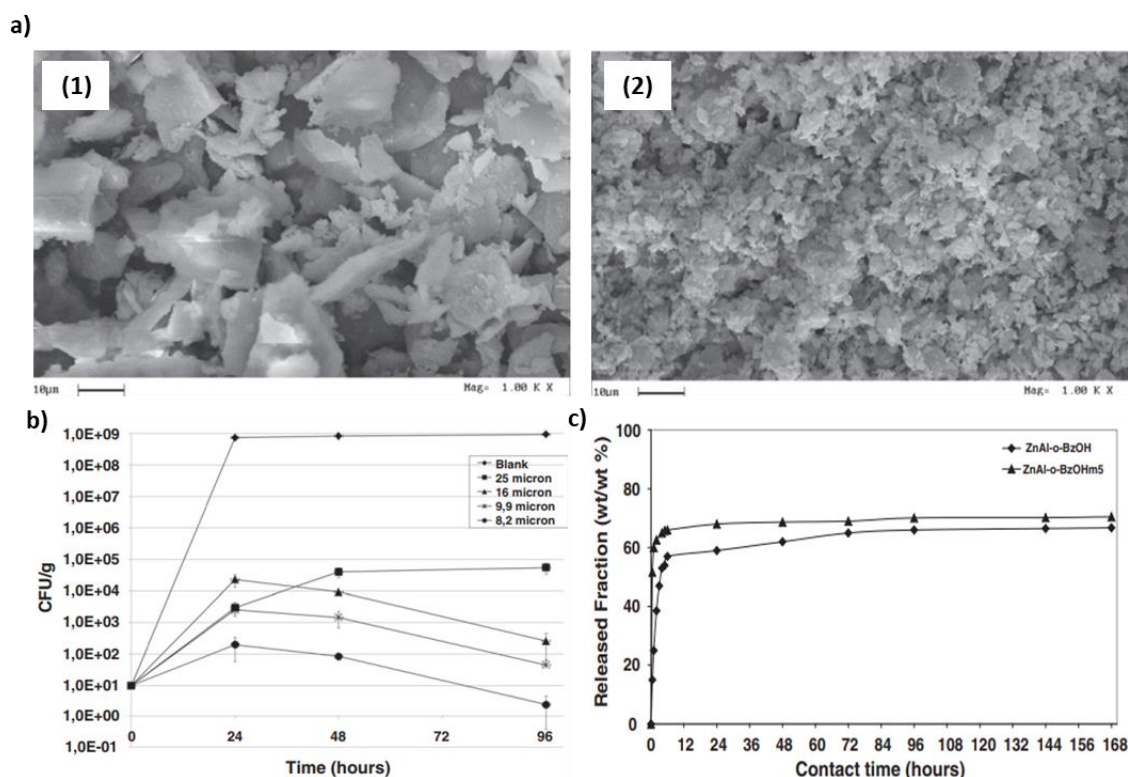


Figure 13. a) SEM micrographs of the powders of o-hydroxybenzoate-LDH hybrids (ZnAl-o-BzOH). (1) non-milled ZnAl-o-BzOH and (2): ZnAl-o-BzOHm5 milled for 5 min. b) Evolution of *E. coli* growth in the presence of 4% (w/v) solutions of ZnAl-o-BzOH powders with different dimensions as a function of contact time (hours). c) Release of o-BzOH molecules from non-milled ZnAl-o-BzOH and ZnAl-o-BzOHm5 milled for 5 minutes, expressed as released fraction normalized to the expected final concentration (wt/wt.%) versus the contact time (hours). Reproduced from Ref. [103].

Moreover, Coiai *et al.* had recently reported the contribution of the host LDH to the antimicrobial activity of antibacterial molecules-modified LDHs [147], where salicylic acid SA-ZnAl LDH hybrids provided higher antibacterial activity against Gram-negative *E. coli* and Gram-positive *S. aureus* bacteria in comparison to SA-MgAl LDH hybrids. The authors attributed the enhanced antibacterial activity of SA-ZnAl to the presence of zinc ions in the structure which may have contributed to the antibacterial performance of the hybrid alongside the antibacterial action of SA. The specific effect of Zn^{2+} ions as an antimicrobial agent will be detailed in **Section 4.3.1**. Such synergistic antibacterial effect of Zn^{2+} ions released out ZnAl LDHs and organic molecules intercalated in the LDH matrix was also reported by Li *et al.* [128].

4.2.4. Principles for the design of an efficient antibacterial molecules-intercalated LDH

When designing antibacterial molecules-intercalated LDH composites of controlled release behavior, several factors must be taken into consideration to provide an enhanced antibacterial behavior including:

- the efficiency of the antibacterial guest molecule itself
- the synthesis method of the composite and the orientation of antibacterial molecule within the interlamellar spacing of the LDH matrix allowing maximum loading
- the size and dimensions of the resulted composite controlling the release behavior of the hosted antibacterial biomolecule
- the type of LDH host matrix aiding in the antibacterial performance

4.3. Dissolution of metallic aqueous ions from pristine and nanoparticles-loaded LDHs

As suggested previously, the release of metallic ions is one other possible mechanism explaining the antibacterial activity of pristine and NPs-loaded LDHs (**Table 3**). Metal aqueous ions as Zn^{2+}_{aq} , Cu^{2+}_{aq} and Ag^{+}_{aq} can damage bacterial membrane functions by: (i) blocking the transport of nutrients and substances in and out of the membrane, (ii) reducing protein and enzymatic

expressions, (iii) or else by binding to bacterial intracellular DNA leading to its denaturation [34,155–158].

4.3.1. Antimicrobial effect through the release of $\text{Zn}^{2+}_{\text{aq}}$ and $\text{Cu}^{2+}_{\text{aq}}$ from pristine LDHs

Moaty *et al.* reported an efficient antibacterial activity against several Gram-positive and Gram-negative bacterial strains for ZnFe pristine LDH which was slightly weaker than that imposed by standard antibiotics [94]. The authors suggested that released zinc ions had a great effect on both bacteria because of the binding to their membranes which prolonged the lag phase of the growth cycle. Dutta *et al.* also reported a significant impact of Zn(II)Al(III) LDH on several Gram-positive and Gram-negative bacteria. The antibacterial efficiency varied in accordance with the applied dosage of LDH, where it was greatly enhanced for growing concentrations. Additionally, the antibacterial activity was also dependent on the type of tested bacteria. Among the tested microorganisms, Gram-negative bacteria were comparatively more sensitive toward the LDH sample than Gram-positive ones. The authors reported that released Zn^{2+} could strongly contribute to the observed antibacterial effect. Finally, the difference in the antibacterial activity between Gram-negative and Gram-positive bacteria was clarified by the different structures and the chemical composition of the cell surfaces of these two types of bacteria. Gram-positive bacteria possess an extra outer membrane that covers the peptidoglycan layer that is not present in Gram-negative bacteria [159].

Vallejo *et al.* reported the influence of the nature and amount of constituent divalent metal on the antibacterial activity of pristine LDHs [35]. LDH samples containing copper or magnesium as divalent metals were found to be less active against *Corynebacterium ammoniagenes*, whereas those containing zinc showed superior bactericidal activity ranging from 98.1% to 99.9% depending on the applied dosage. The reason behind the enhanced activity of Zn(II)-based LDHs was linked to the superior efficiency of the released zinc ions to induce an antibacterial effect than other released ions as Cu^{2+} and Mg^{2+} . The impact of the nature of constituent divalent metal was also reported by Li *et al.* who studied the antibacterial activity of different MAI-LDH (M: Mg^{2+} , Cu^{2+} , Ni^{2+} , Co^{2+} , and Mn^{2+}) against Gram-negative *E. coli*, and *S. aureus* Gram-positive bacteria. When the concentration of MAI-LDHs increased up to 1500 $\mu\text{g}/\text{mL}$, CuAl-LDH and MnAl-LDH showed the best bacterial inhibition compared to the other LDH samples. On the other hand, NiAl-

LDH and CoAl-LDH exhibited a limited antibacterial activity, whereas MgAl-LDH had no antibacterial ability. Similarly, Peng *et al.* compared the antimicrobial activity of MgAl and MgFe LDHs to those of ZnAl and ZnFe LDHs, where the two latter presented superior antibacterial properties [34].

Tabti *et al.* also synthesized a range of Cu-LDHs having different molar ratios of Cu:Al (Cu_{0.05}–Al_{0.15}, Cu_{0.10}–Al_{0.10}, Cu_{0.14}–Al_{0.06}, and Cu_{0.15}–Al_{0.05}) [36]. The antibacterial activity of the synthesized samples was estimated toward several bacterial strains, *e.g.*, *E. coli*, *P. aeruginosa*, *E. faecalis*, *S. aureus*, and *B. Subtilis*. Samples having a higher molar ratio of Cu(II)/Al(III) showed better antibacterial activity due to the presence of a greater amount of Cu²⁺ ions which were assumed to be ejected providing an enhanced impact.

4.3.2. Antimicrobial effect through the release of Ag⁺_{aq} from Ag Nps-loaded LDHs

Huang *et al.* reported the fabrication of hybrid of polypyrrole-silver coated layered double hydroxides (LDHs@PPy-Ag) for both enhanced gas carrier property and antibacterial activity [160]. The prepared LDH has able to completely inhibit the growth of bacteria. The antibacterial activity of the prepared LDH hybrid was attributed to the synergistic effect of polypyrrole and the loaded silver NPs. In particular, it was believed that the direct contact effect with loaded AgNPs alongside the Ag⁺ ions released from unstable AgNPs were responsible for the excellent observed antibacterial activity.

Yadollahi *et al.* prepared antibacterial nanocomposite hydrogels by the combination of carboxymethyl cellulose (CMC), LDH and silver nanoparticles (AgNPs) [161]. CMC-LDH hydrogels were prepared by intercalating CMC into different LDHs, *e.g.*, Mg(II)Al(III), Ni(II)Al(III), Cu(II)Al(III) and Zn(II)Al(III) LDHs. Ag/CMC-LDH nanocomposite hydrogels (Ag/CMC-Mg-LDH, Ag/CMC-Ni-LDH, Ag/CMC-Cu-LDH and Ag/CMC-Zn-LDH) were prepared through *in situ* formation of AgNPs within the CMC-LDHs. CMC-Mg-LDH and CMC-Ni-LDH showed no antibacterial activity against *E. coli* and *S. aureus*. On contrary, an antibacterial effect was observed for both CMC-Cu(II)-LDH and CMC-Zn(II)-LDH nanocomposites. Such an effect was attributed to the antibacterial features of Cu²⁺ and Zn²⁺ ions released from CMC-Cu-LDH and CMC-Zn-LDH nanocomposites, respectively. Ag/CMC-LDH

nanohybrids exhibited a superior antibacterial activity against both bacteria in comparison to their CMC-LDH counterparts. The authors attributed such enhanced antibacterial activity to the antibacterial effect of released Ag^+ ions from Ag/CMC-LDH nanohybrids. Metal ions were slowly released from metallic NPs as AgNPs, and then absorbed through the cell membrane. The released silver metallic ions were probably able to interact with functional groups of nucleic acids and proteins, *e.g.*, mercapto (-SH), amino (-NH), carboxyl (-COOH) groups [162]. This could further affect the normal physiological processes by damaging the enzymatic activity, changing the cell structure, and ultimately inhibiting the growth of microorganisms [136,162].

4.3.3. Limitations of the proof of evidence of dissolution of ions out of LDH

Although all the previously mentioned investigations suggest the contribution of released metallic ions to the antibacterial effect of pristine and NPs-loaded LDHs, the literature lacks real experimental setups validating such contribution, *e.g.*, quantitative evaluation of the concentration of released ions in solution and their antibacterial efficiency.

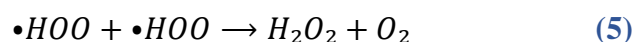
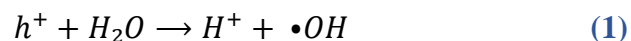
Some studies reported the influence of some physico-chemical parameters on the antibacterial activity of pristine LDHs, *i.e.*, nature of constituent divalent metal, the M(II)/M(III) molar ratio. However, these parameters were not related to dissolution capacity of LDHs which can in a way or another affect their antibacterial efficiency.

4.4. Generation of reactive oxygen species (ROS)

Reactive oxygen species (ROS) are produced by bacteria itself (endogenous) as a byproduct of aerobic respiration or generated in the host environment (exogenous) [163]. ROS were called “double-edged swords of life” in the mechanism of pathogen clearance [164]. First, successful pathogens can exploit endogenous ROS for their growth and adaptation. Second, exogenous ROS were thought to be the weapon providing an efficient antibacterial effect since they can directly damage bacterial membranes, DNA, lipids, and proteins by oxidative stress [163–165].

4.4.1. Generation of ROS by LDHs

When a suitable source of light irradiates LDHs, an electron (\bar{e}) and a hole (h^+) are created which could subsequently generate ROS by the following reactions [166]:



Where $\bullet OH$ are hydroxyl radicals, $\bullet O_2^-$ are superoxide radical anions, $\bullet HOO$ are hydrogen superoxide radicals, and H_2O_2 are hydrogen peroxide molecules, all belonging to the family of ROS. The generation of ROS by LDHs is another possible mechanism (**Mechanism 3, Figure 7**) explaining their antibacterial activity as suggested by several studies reported in **Table 3**.

4.4.2. ROS generation by pristine LDHs

Zhao *et al.* reported the synthesis of antibacterial ZnTi LDH nanosheets with lateral dimensions in the range of 40–80 nm [167]. Electron spin resonance (ESR) and X-ray photoelectron spectroscopy (XPS) measurements revealed that Ti^{3+} sites were generated within these nanosized LDH platelets. The antibacterial activity of ZnTi LDHs found upon visible-light illumination was explained by the generation of superoxide anion radicals ($\bullet O_2^-$) and hydroxyl radicals by trapping of electrons by Ti^{3+} ions and the reaction of generated holes with water or hydroxyl ions ($\bullet OH$), respectively. These generated ROS ($\bullet O_2^-$ and $\bullet OH$) were believed to be strong and nonselective oxidants, which could lead to the damage of bacteria by attacking cell membrane to cause cell lysis.

4.4.3. ROS generation by supported nanoparticles on LDH

4.4.3.1. Ag@AgCl-generated ROS

Nocchetti *et al.* successfully synthesized antibacterial LDH composites by loading AgCl NPs on ZnAl LDHs for Rhodamine B (RhB) dye photodegradation and antibacterial potential applications [116]. Kinetic experiments of the antibacterial activity of the prepared composites were performed in the dark and under irradiation ($\lambda > 350$ nm). No bacterial growth reduction was observed until 180 min upon treatment with LDH composites in dark conditions. On the other hand, the number of live bacteria treated with LDH composites was considerably reduced after 60 min of irradiation.

The superior antibacterial activity of the nanocomposites under irradiation for a very short time was explained by the formation of Ag clusters on AgCl and the production of reactive oxygen species (ROS), such as $\bullet O_2^-$, which was previously observed in the photodegradation process of RhB in presence of ROS quenchers.

4.4.3.2. ZnO-generated ROS

Zhang *et al.* reported the fabrication of antibacterial nanocomposites based on loading zinc oxides NPs (ZnO) on ZnAl LDHs which were further incorporated in water polyurethane (WPU) polymeric matrix [114]. The antibacterial activities of the pure WPU, WPU/ZnAl-LDHs and WPU/ZnO-loaded ZnAl-LDHs composite films with different ZnAl-LDHs/ZnO contents were tested against *E. coli* and *S. aureus*. It was noted that the pure WPU did not show any antibacterial activity, while the WPU/ZnAl-LDHs showed a weak antibacterial property. However, the WPU/ZnO-loaded ZnAl-LDHs composites showed a strong antibacterial activity which reached 99% at a very low loading of 0.3 wt%. The authors explained the enhanced antibacterial property of WPU/ZnO-loaded ZnAl-LDHs composites as follows: ZnO is a semiconductor with a wide bandgap, which could be stimulated by photon energy higher than the bandgap of ZnO (3.37 eV), and could lead to the movement of an electron from the valence band (V_b) to the conduction band (C_b) of the particle. Thus, a hole (h^+) in the valence band and a free electron (e^-) in the conduction band would be generated, triggering reactions (1)-(5) described in section 4.4.1. This in turn would damage the bacterial cells. Similar suggested antibacterial mechanism concerning the generation of ROS by ZnO-loaded ZnAl LDHs was also reported by Li *et al.* [12]. This mechanism was also cited for layered double oxides containing those types of oxide species as well [36,131].

4.4.3.3. Beyond ROS: Photothermal effect of Au-loaded LDH

Ma *et al.* reported the construction of an antibacterial core-shell gold nanorods-loaded LDHs (GNR@LDH) nanostructures by loading gold nanorods (GNR) on a MgAl LDH matrix [88]. As shown in Figure 14a, the antibacterial activity of the synthesized GNR@LDH nanostructures showed significant antibacterial activity against *E. coli* and *S. aureus* bacteria, only when being irradiated by Near Infrared (NIR) laser ($\lambda=808$ nm). When the concentration exceeded 200 $\mu\text{g/mL}$, GNR@LDH-PEG exhibited a significant antibacterial effect in 3 min of irradiation and even a higher effect (99.25% and 88.44% for *E.coli* and *S. aureus*, respectively).

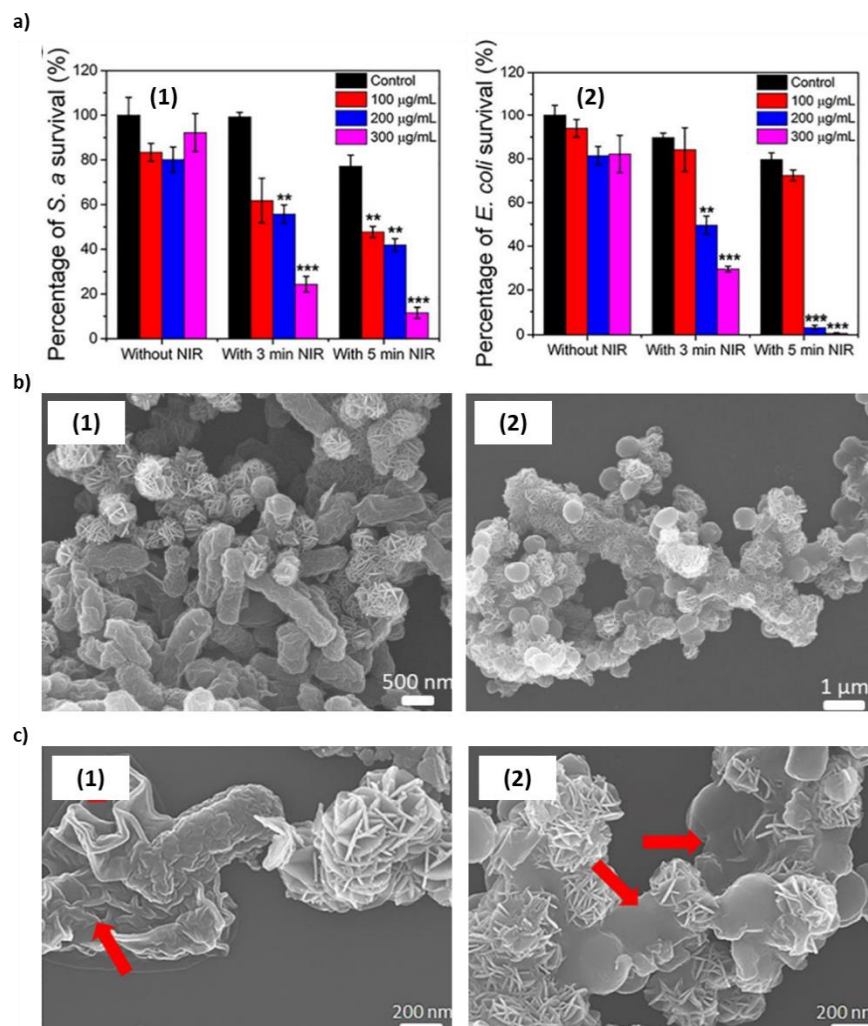


Figure 14. a) Antibacterial activity evaluation of GNR@LDH-PEG against: (1) *E. coli*, (2) *S. aureus*. b) SEM images of treated bacteria with GNR@LDH without 808 nm laser: (1) *E. coli*, (2) *S. aureus*. c) SEM images of bacteria treated with GNR@LDH under 3 min irradiation with 808 nm laser: (1) *E. coli*, (2) *S. aureus*; * $P < 0.01$, $0.001 < **P < 0.005$, $***P < 0.001$, compared with control group, red arrows correspond to distorted cell membranes. Reproduced from Ref. [88].

Moreover, the SEM images shown in **Figure 14b** and **c** revealed that both bacteria adhered to GNR@LDH nanostructures, probably due to their positively charged surface. However, before being irradiated by 808 nm laser, no obvious damages were detected on the bacterial membrane of the rod-shaped *E. coli* and spherical *S. aureus* (**Figure 14b**). On the contrary, under irradiation with a NIR laser for 3 min, some crumbles appeared on the surface and the cell membranes became incomplete, distorted, and even melted (**Figure 14c**, red arrows). Such observation suggested that bacterial adhesion to LDH nanostructures is not responsible for their antibacterial effect, but it rather served as a first step in promoting the antibacterial activity, as previously suggested by Gottenbos *et al.* [120]. In summary, GNR@LDH showed remarkable photothermal antibacterial

activity on both Gram-positive and Gram-negative bacteria. This consequently led to the damage and destruction of *E. coli* and *S. aureus* bacterial cell walls.

The authors mentioned the term “photothermal antibacterial properties”, however ROS generation was not reported. In fact, it is actually complicated to decide whether ROS were generated or not, since ROS measurements were not performed. In the case of the work from Ma *et al.* [88], a more likely explanation is that there is a photothermal effect. Additionally, it is somehow difficult to determine whether the observed damaged bacterial membranes were indeed due to the generation of ROS or the reported photothermal activity under irradiation. To validate such a hypothesis, the morphology of irradiated untreated bacteria should be examined as well.

4.4.3.4. Limitations of the attribution of the ROS mechanism and general considerations for its effect

The aforementioned studies suggested either the contribution of ROS [36,37,96,114,116,131], or the photothermal effect [88] to the antibacterial mechanism of pristine and NPs-loaded LDHs. A real measurement of ROS and the evaluation of their role is therefore necessary to distinguish the contribution of each to the antibacterial activity. ROS generation could be evaluated using different methods including fluorescence spectroscopy with fluorescent dye probes, ESR and chromatography methods [168].

Another helpful suggestion to ensure the contribution of the generation of ROS by LDHs to their antibacterial activity is to study the antibacterial effect of LDHs in function of generated ROS initially evaluated using both qualitative and quantitative approaches. For example, Dutta *et al.* confirmed that the antibacterial effect of ZnO NPs was related to bacterial membrane damage caused by generated ROS evaluated using fluorescent dye probes [169]. Additionally, a scavenger of ROS (histidine) was also used in different concentrations during antibacterial experiments in order to evaluate more precisely the role of the generated ROS in the adapted antibacterial mechanism. The antibacterial activity of ZnO NPs decreased significantly with increasing concentrations of added histidine thus ensuring the great contribution of generated ROS to the antibacterial performance of ZnO NPs.

In summary, ROS generation had been evidenced only for pristine LDHs (ZnTi LDH nanosheets). The possibilities for ROS generation are increased with nanoparticle loading, either with metal particles (Au), halogen-metal salts (AgCl) or oxides (ZnO).

ROS generation should be triggered by UV, visible or IR light. Of course, a reference measurement must be performed to ensure that the light source itself does not contribute to the observed antibacterial effect.

5. Toward encouraging the use of pristine antibacterial LDHs

Antibacterial molecules-intercalated LDH composites showed remarkable antibacterial properties against several tested bacterial strains. However, the majority of the intercalated biomolecules nature is based on commercial antibiotics. Therefore, the problem of antimicrobial resistance phenomena still presents a limitation toward their use against several resistant strains, where the World Health Organization (WHO) estimates 700,000 global deaths per year due to antimicrobial resistance phenomenon [170].

NPs-loaded LDH composites were also proven to act as efficient antibacterial agents, yet, the toxicity caused by their aggregation and direct exposure to a high dose of these NPs still remains a main challenge for their antimicrobial application uses. In addition, the synthesis of both types of antibacterial LDH composites, *e.g.*, antibacterial molecules-intercalated and NPs-loaded LDHs, requires additional chemicals and multi-step synthesis (sources of antibacterial molecules or NPs) which increases the cost and time to obtain these antimicrobial composite materials.

On the other hand, pristine antibacterial LDHs are antibiotic-free, easily and rapidly synthesized and inexpensive. These properties make pristine LDHs advantageous over other LDH composite systems. The remaining challenge here is that their mode of action is still not well understood. Despite the fact that some hypotheses were proposed to explain the antibacterial activity of pristine LDHs, the followed antibacterial mechanism is still far from being explained. Therefore, we highlight here the importance of deciphering the followed mechanism of antibacterial LDHs to fight against different bacteria. Once the mechanism is well understood, the physico-chemical properties of pristine LDHs could therefore be tuned to maximize their antimicrobial effect.

6. Conclusion

As reported in this chapter, LDH-based materials, *e.g.*, pristine LDHs, NPs loaded-LDHs and antibacterial molecules-intercalated LDHs, could be potentially used as efficient antibacterial agents against various Gram-positive and Gram-negative bacterial strains.

- (1) Direct surface interactions between negatively charged bacterial membranes and positively charged pristine or NPs-loaded LDHs constitute one possible mechanism explaining their antibacterial activity. Such interaction is maximized by substantial surface charges, rougher surfaces, smaller particle sizes and good dispersion of LDHs or loaded NPs to promote better interaction with bacterial membranes leading to their damage.
- (2) Dissolution of antibacterial molecules from antibacterial molecules-intercalated LDH composites is believed to be the main contributor to their antibacterial effect. The induced antibacterial effect by the controlled release of intercalated antibacterial molecules is dependent on the efficiency and amount of the intercalated antibacterial molecules, their orientation within the LDH matrix, the size of the composites controlling the dissolution behavior as well as the nature of the LDH host which could also aid in the antibacterial effect of these composites. Moreover, dissolution also occurs for pristine and NPs-loaded LDHs that partially release their constituent divalent metallic ions (especially Zn^{2+} and Cu^{2+}) and NPs metallic ions (Ag^+), respectively. The release behavior of these metallic ions is dependent on several factors and is increased for lower crystallinity of the particles, weakly interacting intercalated anions, larger divalent over trivalent ion ratio. The released metallic ions can further cause damages to the membrane functions by blocking the transport of nutrients and substances in and out the membrane, or by binding to bacterial intracellular DNA and proteins leading to their denaturation or deactivation.
- (3) Finally, upon being radiated by a suitable source of illumination, pristine (Ti-Zn LDH) as well as NPs-loaded ($Ag@AgCl$, ZnO and Au) LDHs can generate reactive oxygen species (ROS) such as $\bullet HO$, $\bullet O_2^-$ and H_2O_2 . These generated ROS are well known to be toxic to bacteria by which they can damage their bacterial membranes, DNA, lipids, and proteins by oxidative stress.

Antibacterial pristine LDHs are considered advantageous over other LDH composite systems, *e.g.*, antibacterial molecules-intercalated and NPs-loaded LDHs, due to their antibiotic-free nature, low cost, fast and ease of synthesis. However, the literature explaining the mechanism of action and physico-chemical properties of antibacterial pristine LDHs is still incomplete. In fact, once the followed antibacterial mechanism is determined, the physico-chemical properties of pristine antimicrobial LDHs could be tuned to maximize their effect. Hence, special investigations are highly encouraged to study in detail the antibacterial mechanisms of LDH-based materials, so that they could potentially be utilized as antibacterial agents in different fields of applications such as antibacterial coatings, food packaging products, wound healing and textiles products.

References

- [1] M.C. Fitzpatrick, C.T. Bauch, J.P. Townsend, A.P. Galvani, Modelling microbial infection to address global health challenges, *Nat. Microbiol.* 4 (2019) 1612–1619.
- [2] A. Chatterjee, J. Abraham, Microbial Contamination, Prevention, and Early Detection in Food Industry, in: *Microb. Contam. Food Degrad.*, Elsevier, 2018: pp. 21–47.
- [3] Md.S. Rahman, Md.I.H. Mondal, Md.S. Hasan, J. Alom, M.B. Ahmed, F. Ahmed, Microorganisms, infection and the role of medical textiles, in: *Antimicrob. Text. Nat. Resour.*, Elsevier, 2021: pp. 45–85.
- [4] A.M.G.A. Laheij, J.O. Kistler, G.N. Belibasakis, H. Välimaa, J.J. de Soet, European Oral Microbiology Workshop (EOMW) 2011, Healthcare-associated viral and bacterial infections in dentistry, *J. Oral Microbiol.* 4 (2012) 17659.
- [5] M.E. Eissa, Distribution of bacterial contamination in non-sterile pharmaceutical materials and assessment of its risk to the health of the final consumers quantitatively, *Beni-Suef Univ. J. Basic Appl. Sci.* 5 (2016) 217–230.
- [6] E. Christaki, M. Marcou, A. Tofarides, Antimicrobial Resistance in Bacteria: Mechanisms, Evolution, and Persistence, *J. Mol. Evol.* 88 (2020) 26–40.
- [7] C. Nathan, Resisting antimicrobial resistance, *Nat. Rev. Microbiol.* 18 (2020) 259–260.
- [8] A. Singh, P.K. Gautam, A. Verma, V. Singh, P.M. Shivapriya, S. Shivalkar, A.K. Sahoo, S.K. Samanta, Green synthesis of metallic nanoparticles as effective alternatives to treat antibiotics resistant bacterial infections: A review, *Biotechnol. Rep.* 25 (2020) e00427.
- [9] M. Sharma, P. Prasher, Metallic Nanoparticles at the Biointerface, in: C. Bhargava, A. Sachdeva (Eds.), *Nanotechnology*, 1st ed., CRC Press, 2020: pp. 261–276.
- [10] V. Selvarajan, S. Obuobi, P.L.R. Ee, Silica Nanoparticles—A Versatile Tool for the Treatment of Bacterial Infections, *Front. Chem.* 8 (2020) 602.
- [11] H. Song, Y. Ahmad Nor, M. Yu, Y. Yang, J. Zhang, H. Zhang, C. Xu, N. Mitter, C. Yu, Silica Nanopollens Enhance Adhesion for Long-Term Bacterial Inhibition, *J. Am. Chem. Soc.* 138 (2016) 6455–6462.
- [12] M. Li, Z.P. Xu, Y. Sultanbawa, W. Chen, J. Liu, G. Qian, Potent and durable antibacterial activity of ZnO-dotted nanohybrids hydrothermally derived from ZnAl-layered double hydroxides, *Colloids Surf. B Biointerfaces.* 181 (2019) 585–592.
- [13] L. Shkodenko, I. Kassirov, E. Koshel, Metal Oxide Nanoparticles Against Bacterial Biofilms: Perspectives and Limitations, *Microorganisms.* 8 (2020) 1545.
- [14] C. Hochstetter, Untersuchung über die Zusammensetzung einiger Mineralien, *J. Für Prakt. Chem.* 27 (1842) 375–378.
- [15] Manasse E., *Atti della Società toscana di scienze naturali. Processi verbali*, 1915.
- [16] W. Feitknecht, ber die -Form der Hydroxyde zweiwertiger Metalle, *Helv. Chim. Acta.* 21 (1938) 766–784.
- [17] R. Allmann, The crystal structure of pyroaurite, *Acta Crystallogr. B.* 24 (1968) 972–977.
- [18] H.F.W. Taylor, Segregation and cation-ordering in sjögrenite and pyroaurite, *Mineral. Mag.* 37 (1969) 338–342.
- [19] V. Rives, ed., *Layered double hydroxides: present and future*, Nova Science Publishers, Huntington, N.Y., 2001.
- [20] F. Cavani, F. Trifirò, A. Vaccari, Hydrotalcite-type anionic clays: Preparation, properties and applications., *Catal. Today.* 11 (1991) 173–301.

- [21] D.G. Evans, R.C.T. Slade, Structural Aspects of Layered Double Hydroxides, in: Springer-Verlag, Berlin/Heidelberg, 2005.
- [22] E.L. Crepaldi, J.B. Valim, Hidróxidos duplos lamelares: síntese, estrutura, propriedades e aplicações, *Quím. Nova.* 21 (1998) 300–311.
- [23] A.S. Bookin, Polytype Diversity of the Hydrotalcite-Like Minerals I. Possible Polytypes and their Diffraction Features, *Clays Clay Miner.* 41 (1993) 551–557.
- [24] A.S. Bookin, Polytype Diversity of the Hydrotalcite-Like Minerals II. Determination of the Polytypes of Experimentally Studied Varieties, *Clays Clay Miner.* 41 (1993) 558–564.
- [25] O.D. Pavel, R. Zăvoianu, R. Bîrjega, E. Angelescu, G. Costentin, M. Che, Exploring an alternative route for meixnerite synthesis. The impact of the gaseous environment on the reconstruction of the lamellar structure and the catalytic performances, *Appl. Clay Sci.* 104 (2015) 59–65.
- [26] A. Olowe, Re: Crystal Structures of Pyroaurite and Sjögrenite, in: P.K. Predecki, D.K. Bowen, J.V. Gilfrich, C.C. Goldsmith, T.C. Huang, R. Jenkins, I.C. Noyan, D.K. Smith (Eds.), *Adv. X-Ray Anal.*, Springer US, Boston, MA, 1995: pp. 749–755.
- [27] J. Pastor-Rodríguez, H.F.W. Taylor, Crystal structure of coalingite, *Mineral. Mag.* 38 (1971) 286–294.
- [28] R. Allmann, J.D.H. Donnay, About the structure of Iowaite¹, *Am. Mineral.* 54 (1969) 296–296.
- [29] S.J. Mills, P.S. Whitfield, S.A. Wilson, J.N. Woodhouse, G.M. Dipple, M. Raudsepp, C.A. Francis, The crystal structure of stichtite, re-examination of barbertonite, and the nature of polytypism in MgCr hydrotalcites, *Am. Mineral.* 96 (2011) 179–187.
- [30] D.L. Bish, G.W. Brindley, A reinvestigation of takovite, a nickel aluminum hydroxycarbonate of the pyroaurite group, *Am. Mineral.* 62 (1977) 458–464.
- [31] D.L. Bish, A. Livingstone, The crystal chemistry and paragenesis of honessite and hydrohonessite: the sulphate analogues of reevesite, *Mineral. Mag.* 44 (1981) 339–343.
- [32] K. El Malki, A. de Roy, J.P. Besse, Evolution related to hygrometry of two lamellar double hydroxide pillared structures [CuCrS₀₄] and [ZnAlS₀₄], *Nanostructured Mater.* 2 (1993) 169–173.
- [33] S. Cheng, L. Lan, M. Li, X. Chu, H. Zhong, M. Yao, F. Peng, Y. Zhang, Pure Mg–Al Layered Double Hydroxide Film on Magnesium Alloys for Orthopedic Applications, *ACS Omega.* 6 (2021) 24575–24584.
- [34] F. Peng, D. Wang, D. Zhang, H. Cao, X. Liu, The prospect of layered double hydroxide as bone implants: A study of mechanical properties, cytocompatibility and antibacterial activity, *Appl. Clay Sci.* 165 (2018) 179–187.
- [35] A.M. León-Vallejo, F.D. Velázquez-Herrera, Á. Sampieri, G. Landeta-Cortés, G. Fetter, Study of layered double hydroxides as bactericidal materials against *Corynebacterium ammoniagenes*, a bacterium responsible for producing bad odors from human urine and skin infections, *Appl. Clay Sci.* 180 (2019) 105194.
- [36] H.A. Tabti, M. Adjdir, A. Ammam, B. Mdjahed, B. Guezzen, A. Ramdani, C.K. Bendeddouche, N. Bouchikhi, N. Chami, Facile synthesis of Cu-LDH with different Cu/Al molar ratios: application as antibacterial inhibitors, *Res. Chem. Intermed.* 46 (2020) 5377–5390.
- [37] M. Lobo-Sánchez, G. Nájera-Meléndez, G. Luna, V. Segura-Pérez, J.A. Rivera, G. Fetter, ZnAl layered double hydroxides impregnated with eucalyptus oil as efficient hybrid materials against multi-resistant bacteria, *Appl. Clay Sci.* 153 (2018) 61–69.

- [38] J. Qu, Q. Zhang, X. Li, X. He, S. Song, Mechanochemical approaches to synthesize layered double hydroxides: a review, *Appl. Clay Sci.* 119 (2016) 185–192.
- [39] A. De Roy, Lamellar Double Hydroxides, *Mol. Cryst. Liq. Cryst. Sci. Technol. Sect. Mol. Cryst. Liq. Cryst.* 311 (1998) 173–193.
- [40] F.M. Vichi, O.L. Alves, Preparation of Cd/Al layered double hydroxides and their intercalation reactions with phosphonic acids, *J. Mater. Chem.* 7 (1997) 1631–1634.
- [41] C.O. Oriakhi, I.V. Farr, M.M. Lerner, Incorporation of poly(acrylic acid), poly(vinylsulfonate) and poly(styrenesulfonate) within layered double hydroxides, *J. Mater. Chem.* 6 (1996) 103.
- [42] J.N. Armor, T.A. Braymer, T.S. Farris, Y. Li, F.P. Petrocelli, E.L. Weist, S. Kannan, C.S. Swamy, Calcined hydrotalcites for the catalytic decomposition of N₂O in simulated process streams, *Appl. Catal. B Environ.* 7 (1996) 397–406.
- [43] J. Pérez-Ramírez, F. Kapteijn, J.A. Moulijn, High activity and stability of the Rh-free Co-based ex-hydrotalcite containing Pd in the catalytic decomposition of N₂O, *Catal. Lett.* 60 (1999) 133–138.
- [44] C. Barriga, J.M. Fernández, M.A. Ulibarri, F.M. Labajos, V. Rives, Synthesis and Characterization of New Hydrotalcite-like Compounds Containing Ni(II) and Mn(III) in the Hydroxide Layers and of Their Calcination Products, *J. Solid State Chem.* 124 (1996) 205–213.
- [45] J.M. Fernández, C. Barriga, M.A. Ulibarri, F.M. Labajos, V. Rives, New Hydrotalcite-like Compounds Containing Yttrium, *Chem. Mater.* 9 (1997) 312–318.
- [46] S. Velu, V. Ramaswamy, S. Sivasanker, New hydrotalcite-like anionic clays containing Zr⁴⁺ in the layers, *Chem. Commun.* (1997) 2107–2108.
- [47] S. Velu, K. Suzuki, M. Okazaki, T. Osaki, S. Tomura, F. Ohashi, Synthesis of New Sn-Incorporated Layered Double Hydroxides and Their Thermal Evolution to Mixed Oxides, *Chem. Mater.* 11 (1999) 2163–2172.
- [48] M. Nayak, T.R.N. Kutty, V. Jayaraman, G. Periaswamy, Preparation of the layered double hydroxide (LDH) LiAl₂(OH)₇·2H₂O, by gel to crystallite conversion and a hydrothermal method, and its conversion to lithium aluminates, *J. Mater. Chem.* 7 (1997) 2131–2137.
- [49] F. Kooli, K. Kosuge, T. Hibino, A. Tsunashima, Synthesis and properties of Mg-Zn-Al-SO₄ hydrotalcite-like compounds, *J. Mater. Sci.* 28 (1993) 2769–2773.
- [50] C.-M. Jiao, Z.-Z. Wang, X.-L. Chen, Y.- Hu, Synthesis of a magnesium/aluminum/iron layered double hydroxide and its flammability characteristics in halogen-free, flame-retardant ethylene/vinyl acetate copolymer composites, *J. Appl. Polym. Sci.* 107 (2008) 2626–2631.
- [51] A.J. Marchi, C.R. Apesteguía, Impregnation-induced memory effect of thermally activated layered double hydroxides, *Appl. Clay Sci.* 13 (1998) 35–48.
- [52] N.N. Das, R. Das, Synthesis, characterization and activation of quaternary layered double hydroxides for the one-pot synthesis of methyl isobutyl ketone, *React. Kinet. Mech. Catal.* (2010).
- [53] J.W. Boclair, P.S. Braterman, Layered Double Hydroxide Stability. 1. Relative Stabilities of Layered Double Hydroxides and Their Simple Counterparts, *Chem. Mater.* 11 (1999) 298–302.
- [54] J.-M.R. Génin, C. Ruby, C. Upadhyay, Structure and thermodynamics of ferrous, stoichiometric and ferric oxyhydroxycarbonate green rusts; redox flexibility and fougérite mineral, *Solid State Sci.* 8 (2006) 1330–1343.

- [55] C. Ruby, C. Upadhyay, A. Géhin, G. Ona-Nguema, J.-M.R. GÉnin, In Situ Redox Flexibility of Fe^{II-III} Oxyhydroxycarbonate Green Rust and Fougerite, *Environ. Sci. Technol.* 40 (2006) 4696–4702.
- [56] B. Grégoire, C. Ruby, C. Carteret, Hydrolysis of mixed Ni²⁺–Fe³⁺ and Mg²⁺–Fe³⁺ solutions and mechanism of formation of layered double hydroxides, *Dalton Trans.* 42 (2013) 15687.
- [57] S. Miyata, Anion-Exchange Properties of Hydrotalcite-Like Compounds, *Clays Clay Miner.* 31 (1983) 305–311.
- [58] U. Costantino, R. Vivani, M. Bastianini, F. Costantino, M. Nocchetti, Ion exchange and intercalation properties of layered double hydroxides towards halide anions, *Dalton Trans.* 43 (2014) 11587–11596.
- [59] J.W. Boclair, P.S. Braterman, B.D. Brister, Z. Wang, F. Yarberrry, Physical and Chemical Interactions between Mg:Al Layered Double Hydroxide and Hexacyanoferrate, *J. Solid State Chem.* 161 (2001) 249–258.
- [60] J. Zhang, Y. Xu, J. Liu, J. Zhou, Z.P. Xu, G. Qian, Fe(CN)₆³⁻/Fe(CN)₆⁴⁻ redox in the interlayer determined by the charge density of ZnCr-layered double hydroxides, *J. Solid State Chem.* 198 (2013) 506–510.
- [61] Y. Wang, D. Zhang, Synthesis, characterization, and controlled release antibacterial behavior of antibiotic intercalated Mg–Al layered double hydroxides, *Mater. Res. Bull.* 47 (2012) 3185–3194.
- [62] W.-Z. Li, J. Lu, J.-S. Chen, G.-D. Li, Y.-S. Jiang, L.-S. Li, B.-Q. Huang, Phenoxymethylpenicillin-intercalated hydrotalcite as a bacteria inhibitor, *J. Chem. Technol. Biotechnol.* 81 (2006) 89–93.
- [63] C. Mousty, V. Prévot, Hybrid and biohybrid layered double hydroxides for electrochemical analysis, *Anal. Bioanal. Chem.* 405 (2013) 3513–3523.
- [64] C. Forano, V. Prvot, Enzyme-Based Bioinorganic Materials, in: E. Ruiz-Hitzky, K. Ariga, Y.M. Lvov (Eds.), *Bio-Inorg. Hybrid Nanomater.*, Wiley-VCH Verlag GmbH & Co. KGaA, Weinheim, Germany, 2007: pp. 443–484.
- [65] J. Tronto, L.P. Cardoso, J. Barros Valim, J.M. Marchetti, M.V.B. Bentley, Studies of the Intercalation and " In Vitro " Liberation of Amino Acids in Magnesium Aluminium Layered Double Hydroxides, *Mol. Cryst. Liq. Cryst.* 390 (2003) 79–89.
- [66] S. Aisawa, H. Kudo, T. Hoshi, S. Takahashi, H. Hirahara, Y. Umetsu, E. Narita, Intercalation behavior of amino acids into Zn–Al-layered double hydroxide by calcination–rehydration reaction, *J. Solid State Chem.* 177 (2004) 3987–3994.
- [67] H. Nakayama, A. Hatakeyama, M. Tshako, Encapsulation of nucleotides and DNA into Mg–Al layered double hydroxide, *Int. J. Pharm.* 393 (2010) 105–112.
- [68] S. Yang, M. Liu, F. Deng, L. Mao, S. Yu, H. Huang, J. Chen, L. Liu, X. Zhang, Y. Wei, A novel fluorescent DNA sensor system based on polydopamine modified MgAl-layered double hydroxides, *Colloid Interface Sci. Commun.* 37 (2020) 100294.
- [69] S. Doron, S.L. Gorbach, Bacterial Infections: Overview, in: *Int. Encycl. Public Health*, Elsevier, 2008: pp. 273–282.
- [70] C. Forano, F. Bruna, C. Mousty, V. Prevot, Interactions between Biological Cells and Layered Double Hydroxides: Towards Functional Materials, *Chem. Rec.* 18 (2018) 1150–1166.
- [71] S. Malekhaia Häffner, M. Malmsten, Membrane interactions and antimicrobial effects of inorganic nanoparticles, *Adv. Colloid Interface Sci.* 248 (2017) 105–128.

- [72] C. Wang, P. Makvandi, E.N. Zare, F.R. Tay, L. Niu, Advances in Antimicrobial Organic and Inorganic Nanocompounds in Biomedicine, *Adv. Ther.* 3 (2020) 2000024.
- [73] R. Kumar, A. Umar, G. Kumar, H.S. Nalwa, Antimicrobial properties of ZnO nanomaterials: A review, *Ceram. Int.* 43 (2017) 3940–3961.
- [74] W. Kamal, W.M.A. El Rouby, A.O. El-Gendy, A.A. Farghali, Bimodal applications of LDH-chitosan nanocomposite: water treatment and antimicrobial activity, *IOP Conf. Ser. Mater. Sci. Eng.* 464 (2018) 012005.
- [75] S.A.A. Moaty, A.A. Farghali, R. Khaled, Preparation, characterization and antimicrobial applications of Zn-Fe LDH against MRSA, *Mater. Sci. Eng. C.* 68 (2016) 184–193.
- [76] H.-M. Cheng, X.-W. Gao, K. Zhang, X.-R. Wang, W. Zhou, S.-J. Li, X.-L. Cao, D.-P. Yan, A novel antimicrobial composite: ZnAl-hydroxalite with *p*-hydroxybenzoic acid intercalation and its possible application as a food packaging material, *New J. Chem.* 43 (2019) 19408–19414.
- [77] L. Tamarro, V. Vittoria, V. Bugatti, Dispersion of modified layered double hydroxides in Poly(ethylene terephthalate) by High Energy Ball Milling for food packaging applications, *Eur. Polym. J.* 52 (2014) 172–180.
- [78] W. Zhang, Y. Zhao, W. Wang, J. Peng, Y. Li, Y. Shanguan, G. Ouyang, M. Xu, S. Wang, J. Wei, H. Wei, W. Li, Z. Yang, Colloidal Surface Engineering: Growth of Layered Double Hydroxides with Intrinsic Oxidase-Mimicking Activities to Fight Against Bacterial Infection in Wound Healing, *Adv. Healthc. Mater.* 9 (2020) 2000092.
- [79] S. Mallakpour, Z. Radfar, C.M. Hussain, Current advances on polymer-layered double hydroxides/metal oxides nanocomposites and bionanocomposites: Fabrications and applications in the textile industry and nanofibers, *Appl. Clay Sci.* 206 (2021) 106054.
- [80] S.B. Khan, K. Alamry, N. Alyahyawi, A. Asiri, Controlled release of organic–inorganic nanohybrid: cefadroxil intercalated Zn–Al-layered double hydroxide, *Int. J. Nanomedicine. Volume 13* (2018) 3203–3222.
- [81] G. Mishra, B. Dash, D. Sethi, S. Pandey, B.K. Mishra, Orientation of Organic Anions in Zn-Al Layered Double Hydroxides with Enhanced Antibacterial Property, *Environ. Eng. Sci.* 34 (2017) 516–527.
- [82] Y. Wang, D. Zhang, Synthesis, characterization, and controlled release antibacterial behavior of antibiotic intercalated Mg–Al layered double hydroxides, *Mater. Res. Bull.* 47 (2012) 3185–3194.
- [83] B. Ballarin, A. Mignani, F. Mogavero, S. Gabbanini, M. Morigi, Hybrid material based on ZnAl hydroxalite and silver nanoparticles for deodorant formulation, *Appl. Clay Sci.* 114 (2015) 303–308.
- [84] U. Bogdanović, V. Lazić, V. Vodnik, M. Budimir, Z. Marković, S. Dimitrijević, Copper nanoparticles with high antimicrobial activity, *Mater. Lett.* 128 (2014) 75–78.
- [85] T.C. Dakal, A. Kumar, R.S. Majumdar, V. Yadav, Mechanistic Basis of Antimicrobial Actions of Silver Nanoparticles, *Front. Microbiol.* 7 (2016).
- [86] M.M. Mohamed, S.A. Fouad, H.A. Elshoky, G.M. Mohammed, T.A. Salaheldin, Antibacterial effect of gold nanoparticles against *Corynebacterium pseudotuberculosis*, *Int. J. Vet. Sci. Med.* 5 (2017) 23–29.
- [87] R. Pati, R.K. Mehta, S. Mohanty, A. Padhi, M. Sengupta, B. Vaseeharan, C. Goswami, A. Sonawane, Topical application of zinc oxide nanoparticles reduces bacterial skin infection in mice and exhibits antibacterial activity by inducing oxidative stress response and cell

- membrane disintegration in macrophages, *Nanomedicine Nanotechnol. Biol. Med.* 10 (2014) 1195–1208.
- [88] K. Ma, Y. Li, Z. Wang, Y. Chen, X. Zhang, C. Chen, H. Yu, J. Huang, Z. Yang, X. Wang, Z. Wang, Core–Shell Gold Nanorod@Layered Double Hydroxide Nanomaterial with Highly Efficient Photothermal Conversion and Its Application in Antibacterial and Tumor Therapy, *ACS Appl. Mater. Interfaces.* 11 (2019) 29630–29640.
- [89] G. Carja, Y. Kameshima, A. Nakajima, C. Dranca, K. Okada, Nanosized silver–anionic clay matrix as nanostructured ensembles with antimicrobial activity, *Int. J. Antimicrob. Agents.* 34 (2009) 534–539.
- [90] A.S. Cruz, J. Flores, R. Guerra, C. Felipe, E. Lima, Organic biocides hosted in layered double hydroxides: enhancing antimicrobial activity, *Open Chem.* 16 (2018) 163–169.
- [91] P.D. Marcato, N.V. Parizotto, D.S.T. Martinez, A.J. Paula, I.R. Ferreira, P.S. Melo, N. Durán, O.L. Alves, New Hybrid Material Based on Layered Double Hydroxides and Biogenic Silver Nanoparticles: Antimicrobial Activity and Cytotoxic Effect, *J. Braz. Chem. Soc.* 24 (2013) 266–272.
- [92] G. Mishra, B. Dash, S. Pandey, P.P. Mohanty, Antibacterial actions of silver nanoparticles incorporated Zn–Al layered double hydroxide and its spinel, *J. Environ. Chem. Eng.* 1 (2013) 1124–1130.
- [93] S.-J. Ryu, H. Jung, J.-M. Oh, J.-K. Lee, J.-H. Choy, Layered double hydroxide as novel antibacterial drug delivery system, *J. Phys. Chem. Solids.* 71 (2010) 685–688.
- [94] S.A.A. Moaty, A.A. Farghali, R. Khaled, Preparation, characterization and antimicrobial applications of Zn-Fe LDH against MRSA, *Mater. Sci. Eng. C.* 68 (2016) 184–193.
- [95] S. Dutta, T.K. Jana, S.K. Halder, R. Maiti, A. Dutta, A. Kumar, K. Chatterjee, Zn₂Al-CO₃ Layered Double Hydroxide: Adsorption, Cytotoxicity and Antibacterial Performances, *ChemistrySelect.* 5 (2020) 6162–6171.
- [96] M. Li, L. Li, S. Lin, Efficient antimicrobial properties of layered double hydroxide assembled with transition metals via a facile preparation method, *Chin. Chem. Lett.* 31 (2020) 1511–1515.
- [97] J. He, M. Wei, B. Li, Y. Kang, D.G. Evans, X. Duan, Preparation of Layered Double Hydroxides, in: X. Duan, D.G. Evans (Eds.), *Layer. Double Hydroxides*, Springer-Verlag, Berlin/Heidelberg, 2006: pp. 89–119.
- [98] G. Mishra, B. Dash, S. Pandey, Layered double hydroxides: A brief review from fundamentals to application as evolving biomaterials, *Appl. Clay Sci.* 153 (2018) 172–186.
- [99] P. Nalawade, B. Aware, V.J. Kadam, R.S. Hirlekar, Layered double hydroxides: A review, *J. Sci. Ind. Res.* 68 (2009) 267.
- [100] G. Rocha Oliveira, L.J. Dias do Amaral, M. Giovanela, J. da Silva Crespo, G. Fetter, J.A. Rivera, A. Sampieri, P. Bosch, Bactericidal Performance of Chlorophyllin-Copper Hydrotalcite Compounds, *Water. Air. Soil Pollut.* 226 (2015) 316.
- [101] M. Nocchetti, A. Donnadio, V. Ambrogi, P. Andreani, M. Bastianini, D. Pietrella, L. Latterini, Ag/AgCl nanoparticle decorated layered double hydroxides: synthesis, characterization and antimicrobial properties, *J. Mater. Chem. B.* 1 (2013) 2383.
- [102] J. Das, K.M. Parida, Heteropoly acid intercalated Zn/Al HTlc as efficient catalyst for esterification of acetic acid using n-butanol, *J. Mol. Catal. Chem.* 264 (2007) 248–254.
- [103] V. Bugatti, L. Esposito, L. Franzetti, L. Tammara, V. Vittoria, Influence of the powder dimensions on the antimicrobial properties of modified layered double hydroxide, *Appl. Clay Sci.* 75–76 (2013) 46–51.

- [104] M.A. Djebbi, A. Elabed, Z. Bouaziz, M. Sadiki, S. Elabed, P. Namour, N. Jaffrezic-Renault, A.B.H. Amara, Delivery system for berberine chloride based on the nanocarrier ZnAl-layered double hydroxide: Physicochemical characterization, release behavior and evaluation of anti-bacterial potential, *Int. J. Pharm.* 515 (2016) 422–430.
- [105] L.P.F. Benício, R.A. Silva, J.A. Lopes, D. Eulálio, R.M.M. dos Santos, L.A. de Aquino, L. Vergütz, R.F. Novais, L.M. da Costa, F.G. Pinto, J. Tronto, layered double hydroxides: nanomaterials for applications in agriculture, *Rev. Bras. Ciênc. Solo.* 39 (2015) 1–13.
- [106] V. Rives, M. del Arco, C. Martín, Intercalation of drugs in layered double hydroxides and their controlled release: A review, *Appl. Clay Sci.* 88–89 (2014) 239–269.
- [107] B. Kutlu, P. Schröttner, A. Leuteritz, R. Boldt, E. Jacobs, G. Heinrich, Preparation of melt-spun antimicrobially modified LDH/polyolefin nanocomposite fibers, *Mater. Sci. Eng. C* 41 (2014) 8–16.
- [108] U. Costantino, V. Bugatti, G. Gorrasi, F. Montanari, M. Nocchetti, L. Tammaro, V. Vittoria, New Polymeric Composites Based on Poly(ϵ -caprolactone) and Layered Double Hydroxides Containing Antimicrobial Species, *ACS Appl. Mater. Interfaces.* 1 (2009) 668–677.
- [109] N. Iyi, H. Yamada, T. Sasaki, Deintercalation of carbonate ions from carbonate-type layered double hydroxides (LDHs) using acid–alcohol mixed solutions, *Appl. Clay Sci.* 54 (2011) 132–137.
- [110] J. Rocha, M. del Arco, V. Rives, M.A. Ulibarri, Reconstruction of layered double hydroxides from calcined precursors: a powder XRD and ^{27}Al MAS NMR study, *J. Mater. Chem.* 9 (1999) 2499–2503.
- [111] K.L. Erickson, T.E. Bostrom, R.L. Frost, A study of structural memory effects in synthetic hydroxalces using environmental SEM, *Mater. Lett.* 59 (2005) 226–229.
- [112] J. Wang, Q. Liu, G. Zhang, Z. Li, P. Yang, X. Jing, M. Zhang, T. Liu, Z. Jiang, Synthesis, sustained release properties of magnetically functionalized organic–inorganic materials: Amoxicillin anions intercalated magnetic layered double hydroxides via calcined precursors at room temperature, *Solid State Sci.* 11 (2009) 1597–1601.
- [113] S. Kim, J. Fahel, P. Durand, E. André, C. Carteret, Ternary Layered Double Hydroxides (LDHs) Based on Co-, Cu-Substituted ZnAl for the Design of Efficient Photocatalysts: Ternary Layered Double Hydroxides (LDHs) Based on Co-, Cu-Substituted ZnAl for the Design of Efficient Photocatalysts, *Eur. J. Inorg. Chem.* 2017 (2017) 669–678.
- [114] W.-D. Zhang, Y.-M. Zheng, Y.-S. Xu, Y.-X. Yu, Q.-S. Shi, L. Liu, H. Peng, Y. Ouyang, Preparation and Antibacterial Property of Waterborne Polyurethane/Zn–Al Layered Double Hydroxides/ZnO Nanocomposites, *J. Nanosci. Nanotechnol.* 13 (2013) 409–416.
- [115] G. Mishra, B. Dash, S. Pandey, D. Sethi, Ternary layered double hydroxides (LDH) based on Cu- substituted Zn Al for the design of efficient antibacterial ceramics, *Appl. Clay Sci.* 165 (2018) 214–222.
- [116] M. Nocchetti, M. Pica, B. Ridolfi, A. Donnadio, E. Boccalon, G. Zampini, D. Pietrella, M. Casciola, AgCl-ZnAl Layered Double Hydroxides as Catalysts with Enhanced Photodegradation and Antibacterial Activities, *Inorganics.* 7 (2019) 120.
- [117] L. Mao, J. Liu, S. Zheng, H. Wu, Y. Liu, Z. Li, Y. Bai, Mussel-inspired nano-silver loaded layered double hydroxides embedded into a biodegradable polymer matrix for enhanced mechanical and gas barrier properties, *RSC Adv.* 9 (2019) 5834–5843.
- [118] V.P. Harden, J.O. Harris, The isoelectric point of bacterial cells, *J. Bacteriol.* 65 (1953) 198–202.

- [119] W.W. Wilson, M.M. Wade, S.C. Holman, F.R. Champlin, Status of methods for assessing bacterial cell surface charge properties based on zeta potential measurements, *J. Microbiol. Methods*. 43 (2001) 153–164.
- [120] B. Gottenbos, D.W. Grijpma, H.C. Van der Mei, J. Feijen, H.J. Busscher, Antimicrobial effects of positively charged surfaces on adhering Gram-positive and Gram-negative bacteria, *J. Antimicrob. Chemother.* 48 (2001) 7–13.
- [121] Z.P. Xu, G.S. Stevenson, C.-Q. Lu, G.Q. (Max) Lu, P.F. Bartlett, P.P. Gray, Stable Suspension of Layered Double Hydroxide Nanoparticles in Aqueous Solution, *J. Am. Chem. Soc.* 128 (2006) 36–37.
- [122] J. Liu, C. Duan, J. Zhou, X. Li, G. Qian, Z.P. Xu, Adsorption of bacteria onto layered double hydroxide particles to form biogranule-like aggregates, *Appl. Clay Sci.* 75–76 (2013) 39–45.
- [123] V. Prevot, Y. Tokudome, 3D hierarchical and porous layered double hydroxide structures: an overview of synthesis methods and applications, *J. Mater. Sci.* 52 (2017) 11229–11250.
- [124] S. Jin, P.H. Fallgren, J.M. Morris, Q. Chen, Removal of bacteria and viruses from waters using layered double hydroxide nanocomposites, *Sci. Technol. Adv. Mater.* 8 (2007) 67–70.
- [125] Z. Wang, H. Yu, K. Ma, Y. Chen, X. Zhang, T. Wang, S. Li, X. Zhu, X. Wang, Flower-like Surface of Three-Metal-Component Layered Double Hydroxide Composites for Improved Antibacterial Activity of Lysozyme, *Bioconjug. Chem.* 29 (2018) 2090–2099.
- [126] E. Tamar, M. Koler, A. Vaknin, The role of motility and chemotaxis in the bacterial colonization of protected surfaces, *Sci. Rep.* 6 (2016) 19616.
- [127] W. Yan, L. Yang, H. Wang, J. Zhang, W. Shen, Atomic-engineered gold@silvergold alloy nanoflowers for *in vivo* inhibition of bacteria, *Nanoscale*. 10 (2018) 15661–15668.
- [128] M. Li, Y. Sultanbawa, Z.P. Xu, W. Gu, W. Chen, J. Liu, G. Qian, High and long-term antibacterial activity against *Escherichia coli* via synergy between the antibiotic penicillin G and its carrier ZnAl layered double hydroxide, *Colloids Surf. B.* 174 (2019) 435–442.
- [129] Z. Yu, X. Li, Y. Peng, X. Min, D. Yin, L. Shao, MgAl-Layered-Double-Hydroxide/Sepiolite Composite Membrane for High-Performance Water Treatment Based on Layer-by-Layer Hierarchical Architectures, *Polymers*. 11 (2019) 525.
- [130] H.-J. Kim, S.H. Kim, H.-M. Kim, Y.S. Kim, J.-M. Oh, Surface roughness effect on the cellular uptake of layered double hydroxide nanoparticles, *Appl. Clay Sci.* 202 (2021) 105992.
- [131] Y. Qiao, Q. Li, H. Chi, M. Li, Y. Lv, S. Feng, R. Zhu, K. Li, Methyl blue adsorption properties and bacteriostatic activities of Mg-Al layer oxides via a facile preparation method, *Appl. Clay Sci.* 163 (2018) 119–128.
- [132] H.B. Drugeon, M.E. Juvin, J. Caillon, A.L. Courtieu, Assessment of formulas for calculating critical concentration by the agar diffusion method, *Antimicrob. Agents Chemother.* 31 (1987) 870–875.
- [133] B. Khalandi, N. Asadi, M. Milani, S. Davaran, A. Abadi, E. Abasi, A. Akbarzadeh, A Review on Potential Role of Silver Nanoparticles and Possible Mechanisms of their Actions on Bacteria, *Drug Res.* 67 (2016) 70–76.
- [134] Y. Qing, L. Cheng, R. Li, G. Liu, Y. Zhang, X. Tang, J. Wang, H. Liu, Y. Qin, Potential antibacterial mechanism of silver nanoparticles and the optimization of orthopedic implants by advanced modification technologies, *Int. J. Nanomedicine*. Volume 13 (2018) 3311–3327.

- [135] M. Godoy-Gallardo, U. Eckhard, L.M. Delgado, Y.J.D. de Roo Puente, M. Hoyos-Nogués, F.J. Gil, R.A. Perez, Antibacterial approaches in tissue engineering using metal ions and nanoparticles: From mechanisms to applications, *Bioact. Mater.* 6 (2021) 4470–4490.
- [136] E. Sánchez-López, D. Gomes, G. Esteruelas, L. Bonilla, A.L. Lopez-Machado, R. Galindo, A. Cano, M. Espina, M. Ettcheto, A. Camins, A.M. Silva, A. Durazzo, A. Santini, M.L. Garcia, E.B. Souto, Metal-Based Nanoparticles as Antimicrobial Agents: An Overview, *Nanomaterials*. 10 (2020) 292.
- [137] A. Beaussart, S. El-Kirat-Chatel, Microbial adhesion and ultrastructure from the single-molecule to the single-cell levels by Atomic Force Microscopy, *Cell Surf.* 5 (2019) 100031.
- [138] A. Beaussart, C. Feuillie, S. El-Kirat-Chatel, The microbial adhesive arsenal deciphered by atomic force microscopy, *Nanoscale*. 12 (2020) 23885–23896.
- [139] Q.-Z. Yang, Y.-Y. Chang, H.-Z. Zhao, Preparation and antibacterial activity of lysozyme and layered double hydroxide nanocomposites, *Water Res.* 47 (2013) 6712–6718.
- [140] A. Megalathan, S. Kumarage, A. Dilhari, M.M. Weerasekera, S. Samarasinghe, N. Kottegoda, Natural curcuminoids encapsulated in layered double hydroxides: a novel antimicrobial nanohybrid, *Chem. Cent. J.* 10 (2016) 35.
- [141] M.A. Djebbi, Z. Bouaziz, A. Elabed, M. Sadiki, S. Elabed, P. Namour, N. Jaffrezic-Renault, A.B.H. Amara, Preparation and optimization of a drug delivery system based on berberine chloride-immobilized MgAl hydrotalcite, *Int. J. Pharm.* 506 (2016) 438–448.
- [142] A. Santana-Cruz, J.L. Flores-Moreno, R. Guerra-González, M.D.J. Martínez-Ortiz, Antibacterial Activity of Pipemidic Acid ions-MgFeAl Layered Double Hydroxide Hybrid Against *E. coli* and *S. typhi*, *J. Mex. Chem. Soc.* 60 (2017).
- [143] G. Mishra, B. Dash, S. Pandey, D. Sethi, C.G. Kumar, Comparative Evaluation of Synthetic Routes and Antibacterial/Antifungal Properties of Zn–Al Layered Double Hydroxides Containing Benzoate Anion, *Environ. Eng. Sci.* 35 (2018) 247–260.
- [144] G. Totaro, L. Sisti, A. Celli, I. Aloisio, D. Di Gioia, A.A. Marek, V. Verney, F. Leroux, Dual chain extension effect and antibacterial properties of biomolecules interleaved within LDH dispersed into PBS by *in situ* polymerization, *Dalton Trans.* 47 (2018) 3155–3165.
- [145] X.-R. Wang, H.-M. Cheng, X.-W. Gao, W. Zhou, S.-J. Li, X.-L. Cao, D. Yan, Intercalation assembly of kojic acid into Zn-Ti layered double hydroxide with antibacterial and whitening performances, *Chin. Chem. Lett.* 30 (2019) 919–923.
- [146] S. Behzadi Nia, M. Pooresmaeil, H. Namazi, Carboxymethylcellulose/layered double hydroxides bio-nanocomposite hydrogel: A controlled amoxicillin nanocarrier for colonic bacterial infections treatment, *Int. J. Biol. Macromol.* 155 (2020) 1401–1409.
- [147] S. Coiai, F. Cicogna, S. Pinna, R. Spiniello, M. Onor, W. Oberhauser, M.-B. Coltelli, E. Passaglia, Antibacterial LDPE-based nanocomposites with salicylic and rosmarinic acid-modified layered double hydroxides, *Appl. Clay Sci.* 214 (2021) 106276.
- [148] M.L. Jadam, S.A. Syed Mohamad, H.M. Zaki, Z. Jubri, S.H. Sarijo, Antibacterial activity and physicochemical characterization of calcium-aluminium-ciprofloxacin-layered double hydroxide, *J. Drug Deliv. Sci. Technol.* 62 (2021) 102314.
- [149] A. Imran, S. López-Rayó, J. Magid, H.C.B. Hansen, Dissolution kinetics of pyroaurite-type layered double hydroxide doped with Zn: Perspectives for pH controlled micronutrient release, *Appl. Clay Sci.* 123 (2016) 56–63.
- [150] J.P. Raval, D.R. Naik, K.A. Amin, P.S. Patel, Controlled-release and antibacterial studies of doxycycline-loaded poly(ϵ -caprolactone) microspheres, *J. Saudi Chem. Soc.* 18 (2014) 566–573.

- [151] Y. Wang, D. Zhang, Q. Bao, J. Wu, Y. Wan, Controlled drug release characteristics and enhanced antibacterial effect of graphene oxide–drug intercalated layered double hydroxide hybrid films, *J. Mater. Chem.* 22 (2012) 23106.
- [152] Z. Geng, W. Zhen, Preparation, characterization, structure-property relationships, and thermal degradation kinetics of poly (lactic acid)/amidated potassium hydrogen phthalate intercalated layered double hydroxides nanocomposites, *Polym. Adv. Technol.* 30 (2019) 504–518.
- [153] C. Madhusa, K. Rajapaksha, I. Munaweera, M. de Silva, C. Perera, G. Wijesinghe, M. Weerasekera, D. Attygalle, C. Sandaruwan, N. Kottegoda, A Novel Green Approach to Synthesize Curcuminoid-Layered Double Hydroxide Nanohybrids: Adroit Biomaterials for Future Antimicrobial Applications, *ACS Omega.* 6 (2021) 9600–9608.
- [154] A. Kuznetsova, P.M. Domingues, T. Silva, A. Almeida, M.L. Zheludkevich, J. Tedim, M.G.S. Ferreira, A. Cunha, Antimicrobial activity of 2-mercaptobenzothiazole released from environmentally friendly nanostructured layered double hydroxides, *J. Appl. Microbiol.* 122 (2017) 1207–1218.
- [155] G. Borkow, J. Gabbay, Copper as a Biocidal Tool, *Curr. Med. Chem.* 12 (2005) 2163–2175.
- [156] S. Mittapally, R. Taranum, S. Parveen, Metal ions as antibacterial agents, *J. Drug Deliv. Ther.* 8 (2018) 411–419.
- [157] T. Ishida, Antibacterial mechanism of Ag⁺ ions for bacteriolyses of bacterial cell walls via peptidoglycan autolysins, and DNA damages, *MOJ Toxicol.* 4 (2018).
- [158] S. Midori-Ku, Comparative Bacteriolytic Mechanism for Ag⁺ and Zn²⁺ Ions against *Staphylococcus Aureus* and *Escherichia Coli*: A review, *Escherichia Coli.* (2019) 12.
- [159] P. Amornpitoksuk, S. Suwanboon, S. Sangkanu, A. Sukhoom, J. Wudtipan, K. Srijan, S. Kaewtaro, Synthesis, photocatalytic and antibacterial activities of ZnO particles modified by diblock copolymer, *Powder Technol.* 212 (2011) 432–438.
- [160] H. Huang, Multifunctional Polypyrrole-silver Coated Layered Double Hydroxides Embedded into a Biodegradable Polymer Matrix for Enhanced Antibacterial and Gas Barrier Properties, (2019) 11.
- [161] M. Yadollahi, H. Namazi, M. Aghazadeh, Antibacterial carboxymethyl cellulose/Ag nanocomposite hydrogels cross-linked with layered double hydroxides, *Int. J. Biol. Macromol.* 79 (2015) 269–277.
- [162] L. Wang, C. Hu, L. Shao, The antimicrobial activity of nanoparticles: present situation and prospects for the future, *Int. J. Nanomedicine.* Volume 12 (2017) 1227–1249.
- [163] H. Li, X. Zhou, Y. Huang, B. Liao, L. Cheng, B. Ren, Reactive Oxygen Species in Pathogen Clearance: The Killing Mechanisms, the Adaption Response, and the Side Effects, *Front. Microbiol.* 11 (2021) 622534.
- [164] R. Mittler, ROS Are Good, *Trends Plant Sci.* 22 (2017) 11–19.
- [165] B. Ezraty, A. Gennaris, F. Barras, J.-F. Collet, Oxidative stress, protein damage and repair in bacteria, *Nat. Rev. Microbiol.* 15 (2017) 385–396.
- [166] H. Abdolmohammad-Zadeh, M. Zamani-Kalajahi, In situ generation of H₂O₂ by a layered double hydroxide as a visible light nano-photocatalyst: Application to bisphenol A quantification, *Microchem. J.* 158 (2020) 105303.
- [167] Y. Zhao, C.J. Wang, W. Gao, B. Li, Q. Wang, L. Zheng, M. Wei, D.G. Evans, X. Duan, D. O’Hare, Synthesis and antimicrobial activity of ZnTi-layered double hydroxide nanosheets, *J. Mater. Chem. B.* 1 (2013) 5988.

- [168] Y. Zhang, M. Dai, Z. Yuan, Methods for the detection of reactive oxygen species, *Anal. Methods*. 10 (2018) 4625–4638.
- [169] R.K. Dutta, B.P. Nenavathu, M.K. Gangishetty, A.V.R. Reddy, Studies on antibacterial activity of ZnO nanoparticles by ROS induced lipid peroxidation, *Colloids Surf. B*. 94 (2012) 143–150.
- [170] WHO, New report calls for urgent action to avert antimicrobial resistance crisis, World Health Organization, 2019. <https://www.who.int/news/item/29-04-2019-new-report-calls-for-urgent-action-to-avert-antimicrobial-resistance-crisis>

Materials and methods

Table of figures	67
Table of tables	69
1. Context	70
2. Materials	70
3. Synthesis	71
3.1. Layered double hydroxides by low supersaturation slow coprecipitation	71
3.2. Layered double hydroxides by anion-exchange reactions	73
3.3. Layered double hydroxides nanoparticles by a fast coprecipitation method	74
3.4. Layered double hydroxide films by <i>in-situ</i> growth hydrothermal method on silicon wafers and AFM tips	75
4. Structural characterization	77
4.1. Inductively coupled plasma mass spectrometry	77
4.2. X-ray diffraction	79
4.3. Infra-red spectroscopy	81
4.4. Raman spectroscopy	84
4.5. X-ray photoelectron spectroscopy	86
4.6. Energy dispersive X-ray spectroscopy	88
5. Morphological characterization	89
5.1. Scanning electron Microscopy	89
5.2. Laser diffraction granulometry	91

Chapter 2: Materials and methods

5.3. Brunauer-Emmett-Teller Specific Area	92
6. Atomic force microscopy	94
6.1. Topographical characterization of LDHs and bacteria	94
6.2. Force spectroscopy.....	96
7. Antibacterial activity tests	97
7.1. Bacterial strains and culture conditions	97
7.2. Agar disc diffusion test	98
7.3. Broth micro- and macro-dilution tests	99
7.4. Colony forming unit count	100
References	103

Table of figures

Figure 1. A schematic illustration of the synthesis protocol of carbonate-intercalated M(II)Al(III) LDHs by low supersaturation slow coprecipitation. The red arrows represent the direction of the solutions addition.	72
Figure 2. A schematic illustration of the synthesis protocol of chloride, nitrate, and perchlorate-intercalated by anion-exchange reactions. The black arrow represents the direction of the solutions addition.	73
Figure 3. A schematic illustration of the synthesis protocol of nitrate-intercalated M(II)Al(III) LDH nanoparticles by a fast coprecipitation method.....	75
Figure 4. A schematic illustration of the synthesis protocol of nitrate-intercalated M(II)Al LDH films on silicon wafers (a) and AFM MLCT tips (b).....	76
Figure 5. A schematic illustration of ICP-MS setup.	78
Figure 6. A schematic illustration of X-ray diffraction setup.....	80
Figure 7. A schematic illustration of Michelson interferometer adopted for FT-IR system.	81
Figure 8. A schematic illustration of a multiple reflection ATR system.	82
Figure 9. A schematic illustration of Stokes and anti-Stokes Raman scattering.	85
Figure 10. A schematic illustration of Raman spectroscopy set up. The red arrows represent the direction of incident light beam from the laser, whereas the green ones represent the direction of the diffused light out of the sample.....	86
Figure 11. A schematic view of the photoemission process during an XPS experiment.....	87
Figure 12. A schematic illustration of XPS system.	88
Figure 13. A schematic illustration of an SEM instrument.	90
Figure 14. A schematic illustration of laser diffraction granulometry particle size analyzer.....	91
Figure 15. A schematic illustration of BET instrument.	93
Figure 16. A schematic illustration of atomic force microscopy set up and principle to perform surface topography imaging.	94
Figure 17. An example of force-distance curves obtained during approach/retract process of AFM-based force spectroscopy.	96
Figure 18. A schematic illustration of the experimental protocol used to determine inhibition zone diameters of LDH suspensions against <i>S. aureus</i> and <i>E. coli</i>	98

Figure 19. A schematic representation of 96-well micro-titer plate used to determine the minimum inhibitory concentration of LDHs against *S. aureus* and *E. coli* using broth microdilution method.

..... 100

Figure 20. A schematic representation of CFU count experiments. 101

Table of tables

Table 1. Different chemicals and products used to carry out this thesis work.	70
Table 2. Experimental conditions for the synthesis of carbonated LDHs by low supersaturation coprecipitation method.	72
Table 3. Experimental conditions for the synthesis of chloride-, nitrate-, perchlorate intercalated Zn(II)Al(III) LDHs with a molar Zn(II)/Al(III) molar ratio of 2.	73
Table 4. Experimental conditions for the synthesis of M(II)Al(III) LDH nanoparticles.	74
Table 5. Experimental conditions for the synthesis of nitrate-intercalated M(II)Al(III) LDH films.	76

1. Context

This chapter will discuss in details the experimental protocols used to carry out the objectives of this thesis work. We start from listing the chemicals and products (**Section 2**) used to carry out this thesis work. After that, the synthesis protocols applied to obtain different LDH powders (**Sections 3.1, 3.2 and 3.3**). Since one of our objectives is to functionalize atomic force microscopy (AFM) tips with LDH films to decipher their interactions with bacteria, the experimental conditions for the synthesis of these LDH films and tips functionalization will be described in **Section 3.4**. The structural and morphological characterization techniques used in this work will also be further described in details together with the operating parameters used to carry out this thesis work (**Sections 4 and 5**).

Atomic force microscopy (AFM) is a major technique used in this work not only to examine the surface topography of LDHs and bacteria, but also as a tool to measure adhesion force between them by means of force spectroscopy mode. For this reason, the principle of AFM for imaging and force measurements is described in separate section (**Section 6**). Finally, the antibacterial tests assays used to evaluate the antibacterial efficiency of the prepared LDH samples are detailed in **Section 7**.

2. Materials

The different chemicals and products used to carry out this thesis work are reported in **Table 1**.

Table 1. Different chemicals and products used to carry out this thesis work.

Chemicals/ Products	Symbol	Purity (%)	Mass percentage (%)	Concentration (mol/L)	Supplier
Aluminum nitrate nonahydrate	$\text{Al}(\text{NO}_3)_3 \cdot \text{H}_2\text{O}$	≥ 98	-	-	SIGMA-ALDRICH
Zinc nitrate hexahydrate	$\text{Zn}(\text{NO}_3)_2 \cdot 6\text{H}_2\text{O}$	≥ 99	-	-	SIGMA-ALDRICH
Copper (II) nitrate trihydrate	$\text{Cu}(\text{NO}_3)_2 \cdot 3\text{H}_2\text{O}$	≥ 99	-	-	SIGMA-ALDRICH
Nickel (II) nitrate hexahydrate	$\text{Ni}(\text{NO}_3)_2 \cdot 6\text{H}_2\text{O}$	≥ 99	-	-	SIGMA-ALDRICH
Cobalt (II) nitrate hexahydrate	$\text{Co}(\text{NO}_3)_2 \cdot 6\text{H}_2\text{O}$	98	-	-	SIGMA-ALDRICH
Magnesium nitrate hexahydrate	$\text{Mg}(\text{NO}_3)_2 \cdot 6\text{H}_2\text{O}$	≥ 99	-	-	SIGMA-ALDRICH
Sodium carbonate	Na_2CO_3	≥ 99.5	-	-	SIGMA-ALDRICH
Sodium hydroxide	NaOH	-	-	1	VWR Chemicals
Hydrochloric acid	HCl	-	37	-	SIGMA-ALDRICH
Nitric acid	HNO_3	-	65	-	SIGMA-ALDRICH
Perchloric acid	HClO_4	-	60	-	Raedel-de Haen
Ammonia solution	NH_4OH	-	35	-	Fisher Scientific

Ammonium nitrate	NH ₄ NO ₃	≥ 98	-	-	SIGMA-ALDRICH
Agar-agar	-	-	-	-	SIGMA-ALDRICH
Luria Bertani Broth	LB	-	-	-	SIGMA-ALDRICH
Tryptic Soy Broth	TSB	-	-	-	SIGMA-ALDRICH
Phosphate-Buffered Saline	PBS	-	-	-	SIGMA-ALDRICH
Ethylenediaminetetraacetic acid	EDTA	-	-	0.5	SIGMA-ALDRICH
Tris-buffered saline	TBS	-	-	-	SIGMA-ALDRICH
3-(N-morpholino)propane sulfonic acid	MOPS	≥ 99.5%	-	-	SIGMA-ALDRICH
L-Histidine	C ₆ H ₉ N ₃ O ₂	≥ 99	-	-	SIGMA-ALDRICH
2',7'-Dichlorodihydrofluorescein diacetate	H2DCFDA	-	-	-	SIGMA-ALDRICH
Antibiotic filter discs	-	-	-	-	Dominique Dutscher
Sterile cotton tipped swabs	-	-	-	-	COPAN
MLCT AFM tips	-	-	-	-	Bruker corporation
SNL AFM tips	-	-	-	-	Bruker corporation
Porous membranes (0.8 μm)	-	-	-	-	Millipore
UV _A lamp (4W, λ = 365 nm)	-	-	-	-	Labomoderne

3. Synthesis

3.1. Layered double hydroxides by low supersaturation slow coprecipitation

The concept of synthesizing LDHs by low supersaturation coprecipitation is similar to that of general coprecipitation synthetic route explained in **Chapter 1**. The cationic solution is added slowly in a reactor containing the anions to be intercalated in aqueous solution, with a slow addition of a basic solution thus allowing the pH to be controlled. The pH is fixed at a value between 8.5 and 11, which limits the formation of impurities (*e.g.*, simple metal oxy(hydroxides)), and generally allows obtaining compounds with few defects. Since the starting point of this work was to determine which type of pristine LDHs present the best antibacterial properties, the synthesis of pristine LDHs bearing different constituent divalent metals and M(II)/M(II) molar ratio was adopted from a previous thesis work carried out in our group by Arnaud Di Betto under the supervision of Prof. Cédric Carteret back in 2017 [1].

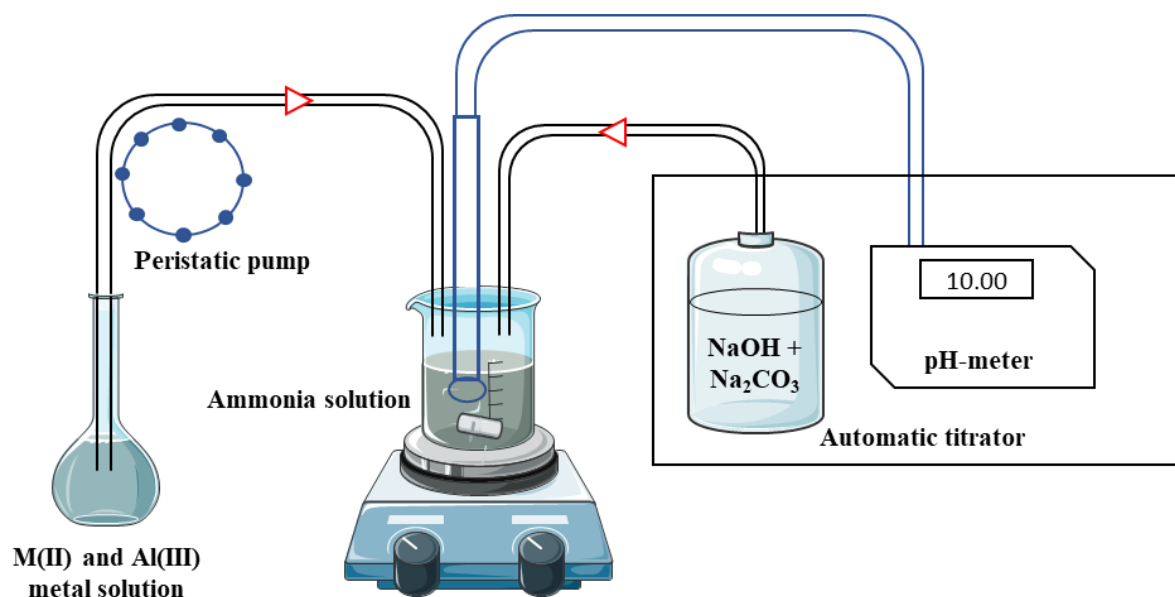


Figure 1. A schematic illustration of the synthesis protocol of carbonate-intercalated M(II)Al(III) LDHs by low supersaturation slow coprecipitation. The red arrows represent the direction of the solutions addition.

The synthesis of the carbonate-intercalated LDHs was achieved by low supersaturation coprecipitation. First a 0.05 mol/L ammonia solution was prepared then the pH of the solution was fixed to a value of 10 using a solution of 1% HNO₃. A solution of 0.4 mol/L M(II) and Al(III) nitrate salts (M(II) = Zn, Cu, Ni, Co, Mg) having a molar ratio M(II)/Al(III) of 2/1 or 3/1 was added slowly using a peristaltic pump operated at 0.3 mL/min into the ammonia solution. The pH was kept constant at 10 by an automatic titrator (736 GP Titrimo, Metrohm) using a solution of 1 mol/L NaOH and 0.25 mol/L Na₂CO₃. The experimental protocol is illustrated in **Figure 1**, and the detailed experimental conditions are given in **Table 2**. For most of the synthesis, a post-synthetic hydrothermal treatment in an autoclave at 80°C for 24 hours was performed to enhance the crystallinity of the powders. The obtained solids were then washed for 4 times in deionized water and collected by centrifugation at 10000 rpm, and finally dried in air at 80°C for 24 hours.

Table 2. Experimental conditions for the synthesis of carbonated LDHs by low supersaturation coprecipitation method.

M(II)/Al(III)	[M(II) + Al(III)] (mol/L)	V _{total} (L)	n(M(II))(mol)	n(Al(III)) (mol)	n _{total} (mol)
2	0.4	0.2	0.053	0.027	0.08
3	0.4	0.2	0.06	0.02	0.08

3.2. Layered double hydroxides by anion-exchange reactions

Following the synthesis of carbonate-intercalated LDHs, an anion exchange from carbonate to other anions was realized. The adopted method is that proposed by Iyi *et al.* [2], via dispersion of LDHs in an acid/alcohol medium. The anions to be intercalated are associated to the strong acids present in the solvent medium (HA) which are able to be easily intercalated in the interlamellar spacing under certain experimental conditions. The followed experimental protocol for the synthesis of chloride-, nitrate and perchlorate-intercalated Zn(II)Al(III) with Zn(II)/M(III) molar ratio of 2 by anion-exchange reactions is illustrated in **Figure 2**.

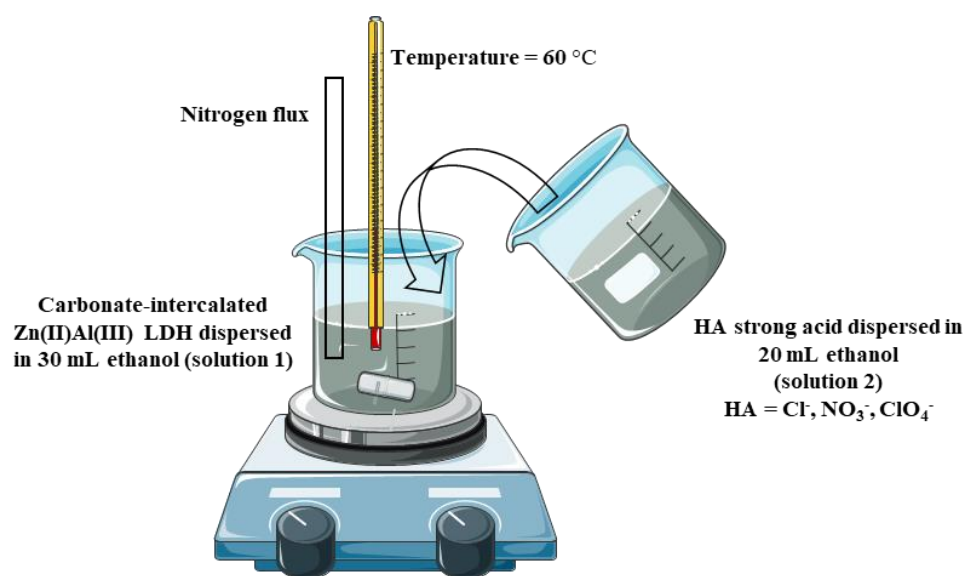


Figure 2. A schematic illustration of the synthesis protocol of chloride, nitrate, and perchlorate-intercalated by anion-exchange reactions. The black arrow represents the direction of the solutions addition.

A certain amount of carbonate-intercalated Zn(II)Al(III) LDHs with Zn(II)/M(III) molar ratio of 2 was dispersed in 30 mL ethanol (solution 1). In a second beaker, the required quantity of strong acid HA (HCl, HNO₃, HClO₄) dispersed in 20 mL ethanol (solution 2) was added to solution 1, in order to avoid brutal contact between the solid and the acid thus limiting the dissolution of LDHs. The whole exchange process was allowed to take place at 50°C for 1 hour under vigorous stirring and nitrogen (N₂) flow to promote a total exchange. The samples were then filtered on a Buchner funnel, washed with ethanol and finally dried in air at 80°C. The quantities and volumes needed to carry out the exchange reactions are reported in **Table 3**.

Table 3. Experimental conditions for the synthesis of chloride-, nitrate-, perchlorate intercalated Zn(II)Al(III) LDHs with a molar Zn(II)/Al(III) molar ratio of 2.

n (carbonate-intercalated LDH) (mmol)	n (HA) HA = Cl ⁻ , NO ₃ ⁻ , ClO ₄ ⁻ (mmol)	V _{total} (mL)	Temperature (°C)	Time (h)
1	1.986	50	50	1

3.3. Layered double hydroxides nanoparticles by a fast coprecipitation method

The conventional method for synthesizing LDH materials is coprecipitation at varied or constant pH, followed by a post-synthetic hydrothermal treatment at a certain temperature, resulting in aggregates with size of 1-10 μm [3]. Since we were concerned in studying the direct contact antibacterial mechanism of LDHs, synthesizing LDHs with smaller particle sizes which we refer to as “LDH nanoparticles” was of utmost importance. For this reason, we intended to synthesize LDH nanoparticles using the method adopted from Xu *et al.* which relies on a fast coprecipitation followed by controlled hydrothermal treatment. The fast coprecipitation procedure (**Figure 3**) induced by the rapid addition of metal salt mixture to the base solution would favor the continuous nucleation of the particles with respect to their growth. Therefore, the LDH particle size can be reduced to the 50-300 nm in such suspensions [3,4].

Table 4. Experimental conditions for the synthesis of M(II)Al(III) LDH nanoparticles.

M(II)/Al(III)	n(M(II)) (mmol)	n(Al(III)) (mmol)	V(M(II) + Al(III)) (mL)	[NaOH] (mol/L)	V(NaOH) (mol/L)	V _{total} (mL)
2	2	1	10	0.15	40	50

Nitrate-intercalated M(II)Al(III) LDH nanoparticles (M(II) = Mg, Zn) were synthesized by a fast coprecipitation method, where a solution containing a mixture of M(II) and Al(III) nitrate salts having a molar ratio M(II)/Al(III) of 2/1 was very quickly added (within 5 seconds) to 0.15 mol/L NaOH solution, under nitrogen atmosphere and vigorous stirring for almost 20 minutes. The LDH slurry was obtained by centrifugation at 10,000 rpm, washed twice and dispersed again in 50 mL decarbonated water. The resultant suspension was then transferred to a stainless-steel autoclave with a Teflon lining and heated at 80°C for 24 h. LDH nanoparticles were then obtained by

centrifugation and air drying at 80°C. The experimental conditions used to carry out the explained protocol are reported in **Table 4**.

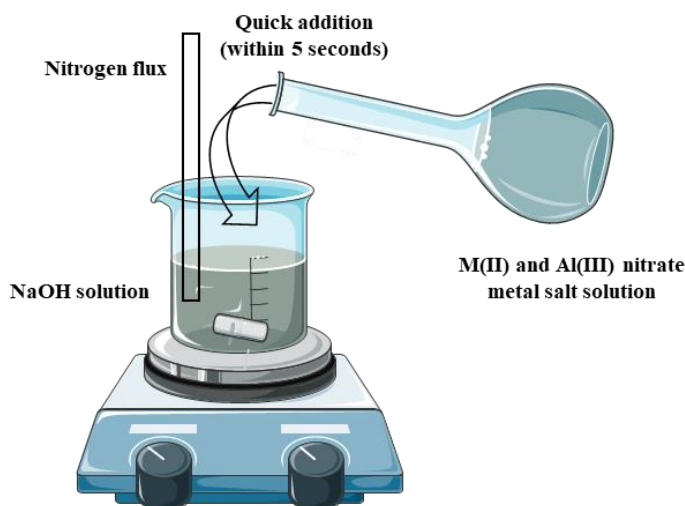
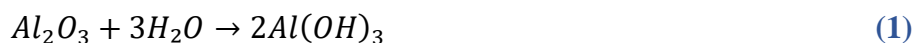


Figure 3. A schematic illustration of the synthesis protocol of nitrate-intercalated M(II)Al(III) LDH nanoparticles by a fast coprecipitation method.

3.4. Layered double hydroxide films by *in-situ* growth hydrothermal method on silicon wafers and AFM tips

The *in-situ* growth approach is considered a promising choice to develop LDH films directly on the substrate providing several advantages such as the ease of synthesis, controlled film thickness, distinct surface morphologies, strong adhesion between LDH and the substrate, and the feasibility to coat complex geometries (as AFM pyramidal tips) [5]. In *in-situ* growth approaches, a substrate is immersed in a suitable solution, and the LDH film crystallizes and grows *in-situ* on the surface of the substrate. In this work, we used aluminum-coated silicon wafers as a substrate for the LDH film growth. The coated aluminum is oxidized to form Al_2O_3 oxides which provides a source of Al^{3+} , whereas M^{2+} are provided from a certain metal salt source. The formed Al_2O_3 will further react with water molecules to give rise to $Al(OH)_3$ hydroxides (Equation (1)), whereas $M(OH)^+$ hydroxides are obtained as a result of the presence of M^{2+} in an alkaline solution (Equation (2)). Subsequently, an LDH phase is produced as a result of the reaction between the formed $Al(OH)_3$, $M(II)(OH)_2$ and intercalating A^{n-} provided from the M(II) salt solution (Equation (3)).



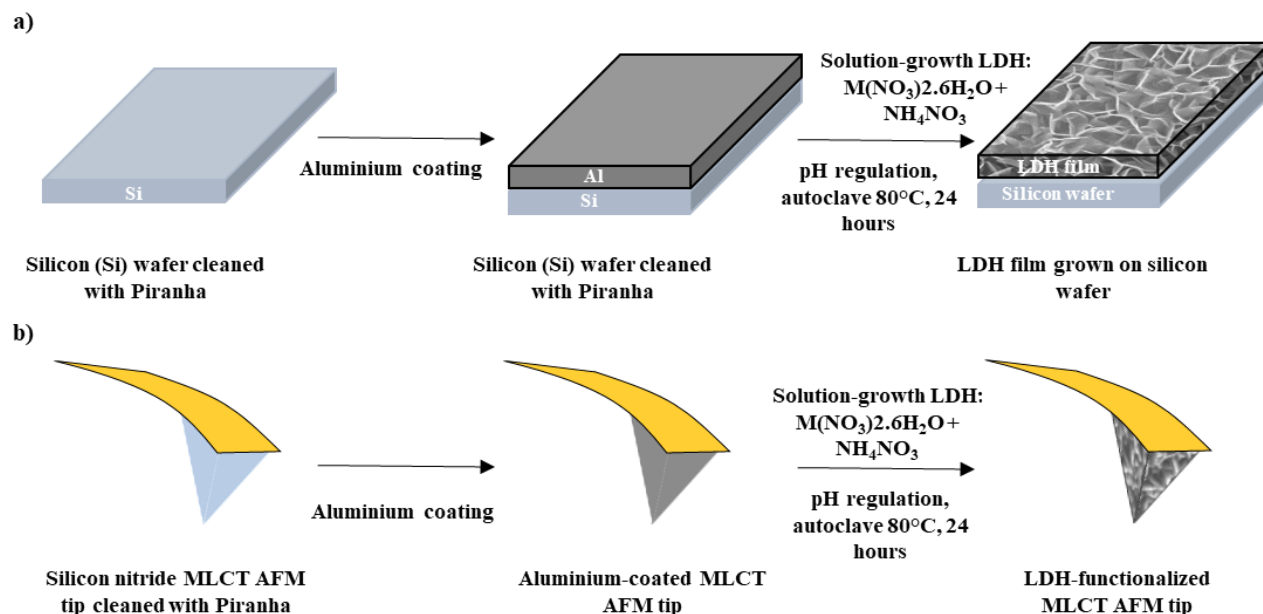
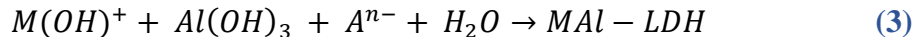


Figure 4. A schematic illustration of the synthesis protocol of nitrate-intercalated M(II)Al LDH films on silicon wafers (a) and AFM MLCT tips (b).

The synthesis of nitrate-intercalated LDH films M(II)Al(III) (M(II) = Zn, Mg) in this work was adopted from Zhang *et al.* [6] with some slight modifications (**Figure 4a**). Silicon wafers were first cleaned with piranha solution, washed thoroughly with water and ethanol, and then coated by plasma sputtering (Q150T S, Quorum) with a thin layer of aluminum (~10 nm). $M(NO_3)_2 \cdot 6H_2O$ (M=Zn, Mg) and NH_4NO_3 were dissolved in deionized water, and 1% ammonia solution was then slowly added until the desired pH was obtained. This solution was transferred to a stainless-steel autoclave with a Teflon lining where coated aluminum samples were immersed. The autoclave was heated for 24 h at $80^\circ C$. The obtained LDH films grown on silicon wafers were then washed with distilled water and ethanol then dried in air at room temperature. The experimental conditions used for the synthesis of M(II)Al(III) films are reported in **Table 5**.

Table 5. Experimental conditions for the synthesis of nitrate-intercalated M(II)Al(III) LDH films.

LDH film	n (M(II)) (mmol)	n(NH_4NO_3) (mmol)	Volume (mL)	pH
Zn(II)Al	2.5	30	50	6.5
Mg(II)Al	2.5	30	50	9.5

Silicon nitride (MLCT) AFM tips were further functionalized with LDH films the same way done on silicon wafers (**Figure 4b**), *i.e.*, cleaning with piranha, aluminum deposition followed by *in-situ* solution growth of M(II)Al(III) LDH films on the surface of the tips.

4. Structural characterization

4.1. Inductively coupled plasma mass spectrometry

Inductively coupled plasma mass spectrometry (ICP-MS) is an analytical technique used to determine low concentrations of elements in liquids, solids and gases. ICP-MS uses an Argon (Ar) plasma source to ionize elements in a sample. These ions are then sorted according to their mass number using a mass spectrometer. In general, the ICP-MS is a relatively easy instrument to use providing several advantages in detecting and quantifying elements due to its extremely low detection limits, large linear range and possibilities to detect isotope composition of an element.

In order to analyze solid samples, the solid should be first dissolved in a nitric acid to prevent adsorption of metals onto the polypropylene sample bottle or onto instrument tubing and glassware [7]. The solution to be characterized is then transported using a peristaltic pump to a nebulizer, where it is converted into a fine aerosol with argon gas (**Figure 5**). The fine droplets of the aerosol, which represent only 1–2% of the sample, are separated from larger droplets using a spray chamber, and then transported into a plasma torch. The plasma torch is operated at elevated temperatures (7000-10000 degrees Kelvin) in order to ionize the fine liquid droplet and generate positively charged ions. Once the ions are generated in the plasma, they are directed into the mass spectrometer by the interface region. This interface region consists of two metallic cones called the sampler and skimmer cones, each with a small orifice to allow ions to pass to the ion optics (a series of electrostatic lenses), where they are guided into the true mass spectrometer. The true mass-spectrometer device (mostly a quadrupole) separates ions according to their mass by charge ratio (m/z). Finally, an ion detector is used to counts and sorts the ions and relates them to their corresponding mass.

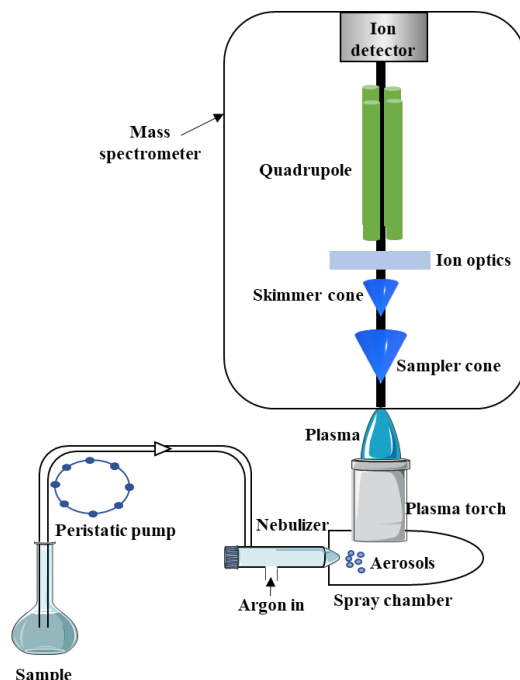


Figure 5. A schematic illustration of ICP-MS setup.

For ICP-MS quantitative analysis, element standards can be purchased commercially, and must be diluted further with nitric acid to prepare different concentrations in order to obtain a calibration curve, which will allow to determine the unknown concentration of the sample.

In this work the M(II)/Al(III) molar ratios of LDH powders and films were measured by Induced Couple Plasma Mass Spectroscopy (ICP-MS Agilent-7800). LDH NPs and films were dissolved into 1% HNO₃, and the calibration range was set as 10 to 3000 ppb. The detected isotopes were: ²⁷Al, ⁶⁶Zn, ⁶³Cu, ⁶⁰Ni, ⁵⁹Co, ²⁶Mg. ICP-MS was also used to determine the partial dissolution profiles of LDHs in Lysogeny Broth (LB) and Tryptic Soy Broth (TSB) bacterial growth media.

The partial dissolution profiles of LDH powders into their constituents divalent and trivalent metals was also evaluated by dispersing 10 mg/mL of LDHs in both Lysogeny Broth (LB) and Tryptic Soy Broth (TSB). After a given incubation time of 48 or 24 hours at 37°C, the supernatants were collected by centrifugation. The supernatants were diluted with nitric acid in order to perform the analysis. Control partial dissolution experiments were also done in Milli-Q water under the same experimental conditions.

4.2. X-ray diffraction

X-ray diffraction (XRD) is a structural non-destructive technique used to characterize crystal structures that consist, ideally, of an infinite repetition of identical structural units in space.

X-rays are short-wavelength electromagnetic radiations produced when electrically charged particles of sufficient energy are decelerated. They are produced in an X-ray vacuum tube comprising both anode and cathode (usually a tungsten filament) electrodes. The cathode is heated to provoke an electron emission and a high voltage is applied between both electrodes to accelerate the movement of electrons from the cathode to the anode, thus inducing the emission of X-ray radiation from the anode compartment. When a sample is irradiated by an X-ray beam, each atom emits radiation of the same wavelength in all directions. The scattering created by the material in certain directions depends on the characteristics of the crystal lattice (constructive interference). The detected intensity is thus recorded as a function of the deviation angle (2θ) which depends on the interplanar spacing d_{hkl} of the different crystalline planes by application of Bragg's law:

$$2d \sin(\theta) = n \lambda \quad (4)$$

Where d represents interplanar spacing (\AA), θ is the angle of incidence of X-rays (rad), n is an integer representing the order of the diffraction phenomenon and λ the wavelength of the X-ray beam (\AA).

Since the majority of crystalline materials have a unique diffraction pattern, they can thus be recognized using a database of diffraction patterns. A diffraction pattern can be used to identify and refine the lattice parameters of a crystal structure as well as the purity of the tested sample.

A basic X-ray diffractometer (**Figure 6**) involves a monochromatic radiation source engulfed in an X-ray tube and an X-rays detector on the circumference of a graduated circle centered on the sample specimen. A divergent slit is present between the X-ray source and the sample. A receiving slit is also placed between the detector and the sample to limit non-diffracted scattered radiations and to reduce background noise. It should be noted that the detector and sample holder should be mechanically coupled using a goniometer fixed at a 2/1 ratio, in order to keep the rotation of the detector ($2 \times$ degrees) in conjunction with the rotation of the sample (x degrees).

XRD makes it possible to determine different information on the studied material, including:

- The calculation of the lattice parameters from the interplanar spacings (d_{hkl})
- Confirmation of the phases: by comparing the experimental results on the basis of the JCPDS file reference data
- The calculation of the average crystallite size using the Scherrer formula:

$$D = \frac{K \lambda}{\beta \cos \theta} \quad (5)$$

Where K is the Scherrer constant (0.9), λ is incident ray wavelength, β is the full width at half maximum in radians, and θ is the Bragg angle (rad) [8].

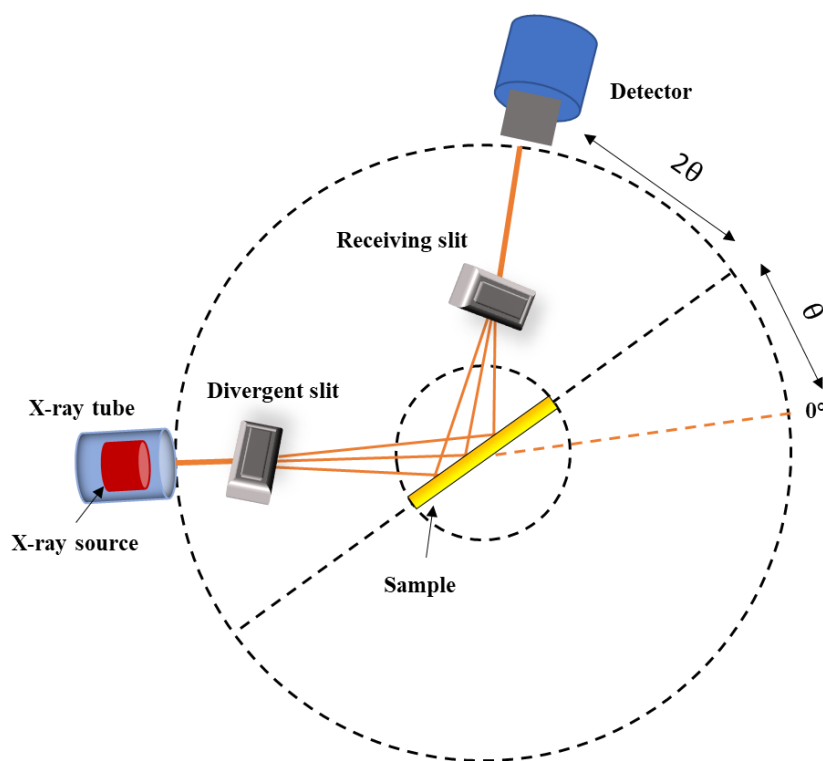


Figure 6. A schematic illustration of X-ray diffraction setup.

In this study, XRD characterization of LDH powders and films were performed at room temperature by a Panalytical X'Pert Pro MPD diffractometer in reflection geometry using a Cu radiation ($K\alpha_1 = 1.5406 \text{ \AA}$), a Ge(111) incident-beam monochromator, Soller slits of 0.02 rad, programmable divergence and anti-scatter slits. The irradiated area was fixed to 10mm x 10mm, and an X'Celerator detector was used. Data were collected with a sample holder spinner and continuous rotation of sample to improve statistical representation of the samples. All diffraction

data were collected using the same procedure, *i.e.*, at the same scattering angle range (between 5 and 70°) with a 0.0167°step and a speed of 1°/min.

4.3. Infra-red spectroscopy

Infrared (IR) spectroscopy is a chemical analytical technique used to characterize, identify and also quantify several substances by measuring the infrared intensity vs wavenumber of light. The vibration characteristics of chemical functional groups in a sample can be detected through IR spectroscopy by interacting an infrared light with the matter where the chemical bonds of the sample will stretch, contract or bend. As a result, a chemical functional group adsorbs infrared radiation in a specific wavenumber. Therefore, the correlation between the band wavenumber position and the chemical structure of substances is used to identify a functional group in a sample using IR spectroscopy [9].

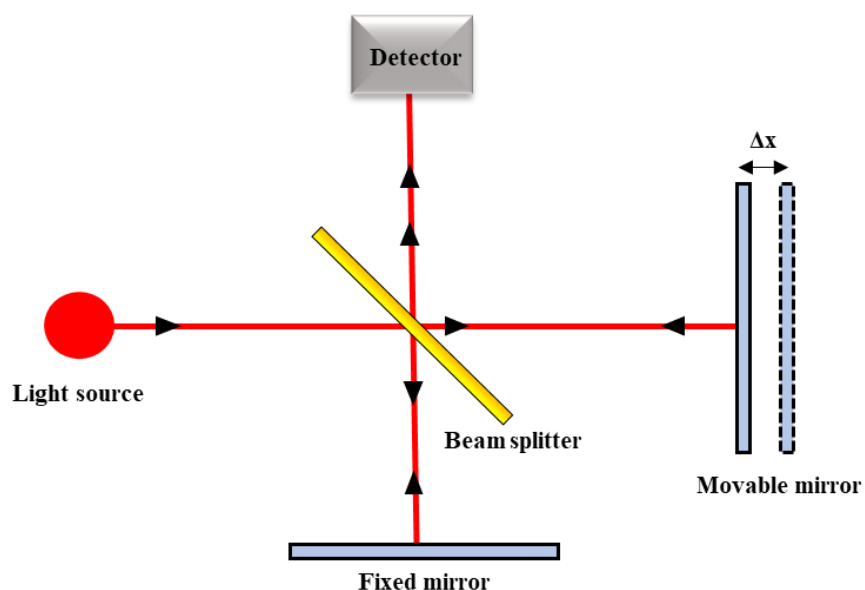


Figure 7. A schematic illustration of Michelson interferometer adopted for FT-IR system.

The intensity of the IR bands is presented in function of the wavenumber of the radiation, (reciprocal of the wavelength, cm^{-1}). The measurement of the signal intensity as a function of the wavenumber is obtained with the aid of a Michelson interferometer (**Figure 7**). When the light is radiated from the source, it passes through the beam splitter which transmit half of the light and reflect the other half. The reflected light reaches a fixed mirror, from which it is after reflected back to the beam splitter, whereas the transmitted part passes to another mirror subjected to a slow

move (movable mirror). The movement of the mirror (Δx) changes the path distance of the reflected beam, meaning that the amplitude of recombined beams changes as a function of mirror movement distance. The amplitude is maximized when both beams travel in the same direction and is minimized when the beams cancel each other, intermediately giving a sinusoidal curve on the detector. The changes in the amplitude of recombined beams are recorded by the detector as a function of mirror displacement [10]. The Fourier transform (FT) mathematical equation translate this function into a new one expressing signal intensity as a function of wavenumber. The use of FT-IR enables fast spectra recording while a good resolution is maintained.

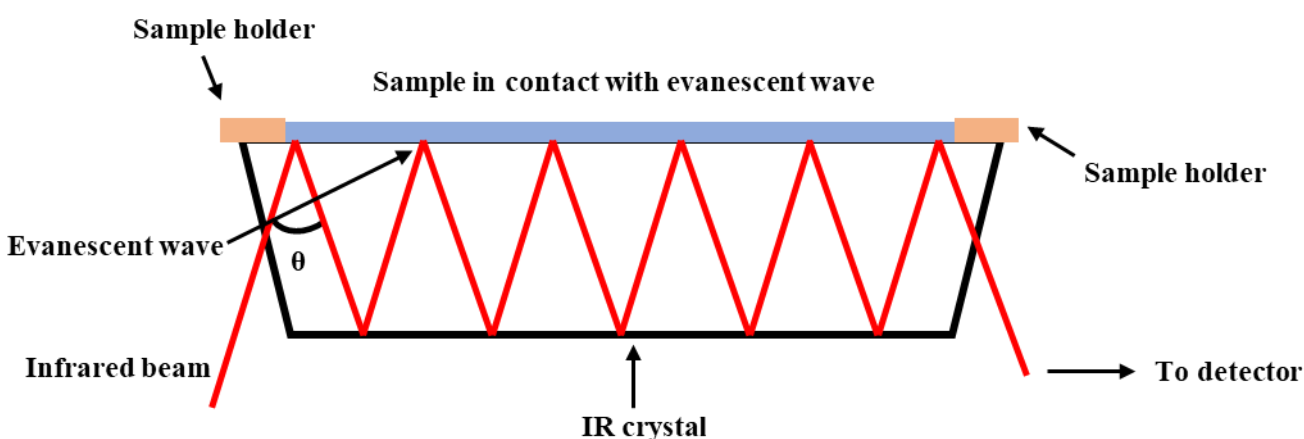


Figure 8. A schematic illustration of a multiple reflection ATR system.

Attenuated Total Reflectance infrared spectroscopy (ATR-IR) uses a property of total internal reflection resulting in an evanescent wave. One important advantage of ATR-FTIR, is that no sample preparation is needed for analyzing bulk materials or films. By pressing the sample into an intimate optical (**Figure 8**) in contact with the top surface of a crystal (Zinc selenide (ZnSe), Germanium (Ge), or diamond), the IR radiation beam is directed toward the crystal by enter the crystal and reflects through it at least once off the internal surface in contact with the sample. This reflection forms the evanescent wave which penetrates and extends into the sample. At the output end of the crystal, the beam is directed out of the crystal and back into the normal beam path of the spectrometer and collected by a detector [11].

In order to obtain internal reflectance, the incident beam must be reflected with an angle (θ) exceeding the critical angle (θ_c) which is related to the refractive indices of both the sample and the ATR crystal by the following:

$$\theta_c = \sin^{-1} \left(\frac{n_2}{n_1} \right) \quad (6)$$

where n_2 is the refractive index of the sample and n_1 is the refractive index of the crystal.

The electric field amplitude of the produced evanescent wave decays exponentially with the distance from the crystal surface. The penetration depth, d_p , of the evanescent wave is defined as the distance at which the evanescent wave drops to e^{-1} times its intensity through the following equation:

$$d_p = \frac{\lambda}{\left\{ 2\pi n_1 \left[\sin^2 \theta - \left(\frac{n_2}{n_1} \right)^2 \right] \right\}} \quad (7)$$

where λ is the wavelength of the incident radiation, n_1 is the refractive index of the crystal, n_2 is the refractive index of the sample in contact with the crystal, and θ is the angle of incidence.

Therefore, the signal intensity in ATR IR is determined by several factors including the wavelength of the used IR beam, the refractive index of the IR crystal, number of reflections, and quantity of the sample in contact with the ATR crystal.

In this work, IR spectra of LDH powders were recorded in the mid-infrared range on a Bruker Vertex 70v spectrometer equipped with a KBr beam-splitter and a deuterated triglycine sulfate (DTGS) detector. An attenuated total reflection (ATR) accessory (Platinum ATR with a single reflection diamond crystal, Bruker) was used for acquiring spectra of the LDH powders. The spectral resolution was 4 cm^{-1} and the accumulation time was 1 min (100 scans). Compartments containing the detector and the ATR accessory were under vacuum ($<1 \text{ hPa}$).

Infrared spectra of LDH films were recorded under nitrogen flow in a transmission mode on a FTIR Nicolet 8700 spectrometer equipped with a KBr beam splitter and a DTGS thermal detector. The reference was the aluminum coated silicon wafer. LDH films spectra were recorded and processed using OMNIC 8.1.0.10 software (Thermo Fisher Scientific Inc.).

ATR-FTIR spectra of *S. aureus* bacterial suspensions with and without Zn(II)Al(III) LDH nanoparticles in dark and UVA light conditions (exposure for 4 h) were recorded between 4000 and 800 cm^{-1} on a Bruker Tensor 27 spectrometer equipped with a KBr beam splitter and a DTGS detector, and driven by the OPUS 7.5 software. The resolution of the single beam spectra was 4 cm^{-1} . A nine-reflection diamond ATR accessory (DurasamplIR™, SensIR Technologies,

incidence angle: 45°) was used for acquiring spectra. The number of bidirectional double-sided interferogram scans was 200, which corresponds to a 2 min accumulation. All interferograms were Fourier processed using the Mertz phase correction mode and a Blackman-Harris three-term apodization function. No ATR correction was performed, and the shown spectra in this manuscript are those between 4000 and 800 cm^{-1} (bacteria fingerprint regions) highlighting the most useful information. Measurements were performed at room temperature in an air-conditioned room. A drop of $50\text{ }\mu\text{L}$ of the bacterial suspensions in their culture media was put on the ATR crystal. The used spectral background was the supernatant of bacterial suspensions which was obtained by centrifugation at 10000 rpm for 5 min . Four measurements were carried on each sample, separated by a time interval of 5 mins to allow the bacterial/LDH suspensions to accumulate on the crystal, thus enhancing the intensity. Water vapor subtraction was performed when necessary.

4.4. Raman spectroscopy

Raman spectroscopy is based on light scattering phenomenon which occurs due to collisions between photons and molecules in a sample. In Raman spectroscopy, a monochromatic source of light with an energy $E_0 = h\nu_0$ strikes at a sample, where it scatters in all directions after interacting with the molecules of the sample molecules. Much of this scattered radiation does not change its energy after the collision (elastic collision), where it has a frequency equal to that of incident radiation and constitutes Rayleigh scattering. On the other hand, only a small fraction of scattered radiation has a frequency different from that of the incident radiation (inelastic collision) which resembles Raman scattering. If the frequency of the scattered radiation is lower than incident radiation thus having an energy of $E = h\nu_0 - h\nu$, the scattering is called “Stokes Raman Scattering”. In the case where the frequency of the scattered radiation is higher than incident radiation ($E = h\nu + h\nu_0$), “anti-Stokes Raman Scattering” take place [12].

Figure 9 illustrates Stokes and anti-Stokes Raman scattering. Stokes Raman scattering is due to the interaction between a photon and a molecule that is in the ground state, while anti-Stokes Raman scattering arises from the interaction between a photon and a molecule in the excited state. Due to the fact that molecules are normally present in the ground vibrational state, Stokes Raman scattering occurs far more easily and frequently, which is the reason why Stokes Raman scattering is evaluated in Raman spectroscopy analysis. The frequency shift between the incident light and

the scattered ones is attributable to the Raman effect and is called ‘‘Raman shift’’. Intensity of scattered radiation in function of Raman shift constitutes a Raman spectrum which is known to be unique for each individual substance.

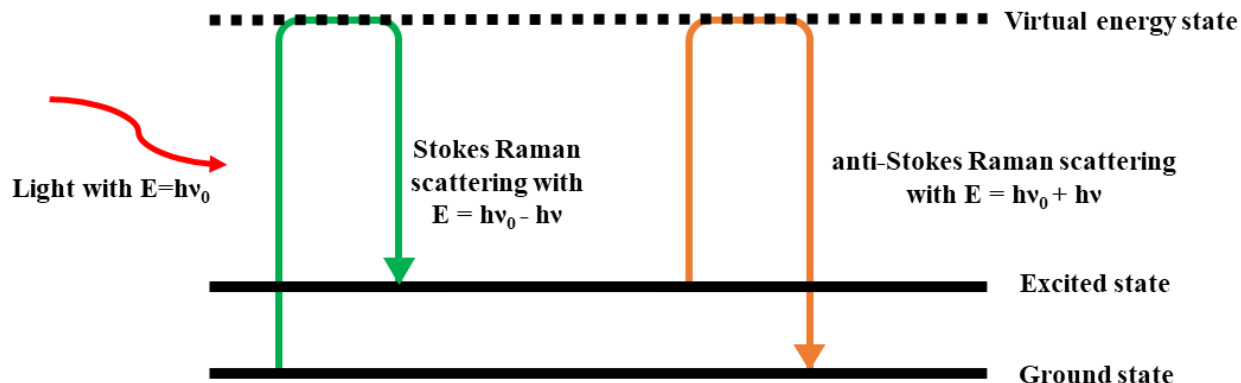


Figure 9. A schematic illustration of Stokes and anti-Stokes Raman scattering.

In general, the light source used in a Raman spectrometer is a laser with a specific wavelength. The wavelength of the laser can be Ultraviolet, visible or near-Infrared, depending on the sample being tested. The light beam is focused on a dichroic filter (Notch filter) which reflects the light to the sample at a right angle (**Figure 10**). The resulting Raman scattering is focused back to the dichroic filter which now serves as band-stop filter whereby the incident light from the light source is almost completely attenuated, and only Raman scattered light can pass the filter unaltered. This light is then reflected by a mirror to reach a monochromator which uses grating to diffract the beam into a narrow band of wavelengths. The photo current from each wavelength section is then measured at a charge-coupled device which serves as a detector.

In this work, Raman spectroscopy characterizations for LDH powders were performed using a confocal Raman microscope (inVia® Qontor with a Peltier-cooled charge-coupled device (CCD) camera, Renishaw, Wotton-under-Edge, UK) equipped with a 532 nm laser, a 50x objective with 0.55 of numerical aperture, and a 2400 lines/mm grating. The spectral resolution was 3 cm^{-1} (10 acquisitions of 5 seconds). Each sample was analyzed at different points to check the uniformity of the studied hydroxides. The laser power was changed in the range of 50 to 1 mW depending on the type of LDH sample and the spectra were recorded in the $400\text{ to }4000\text{ cm}^{-1}$ wavenumber range.

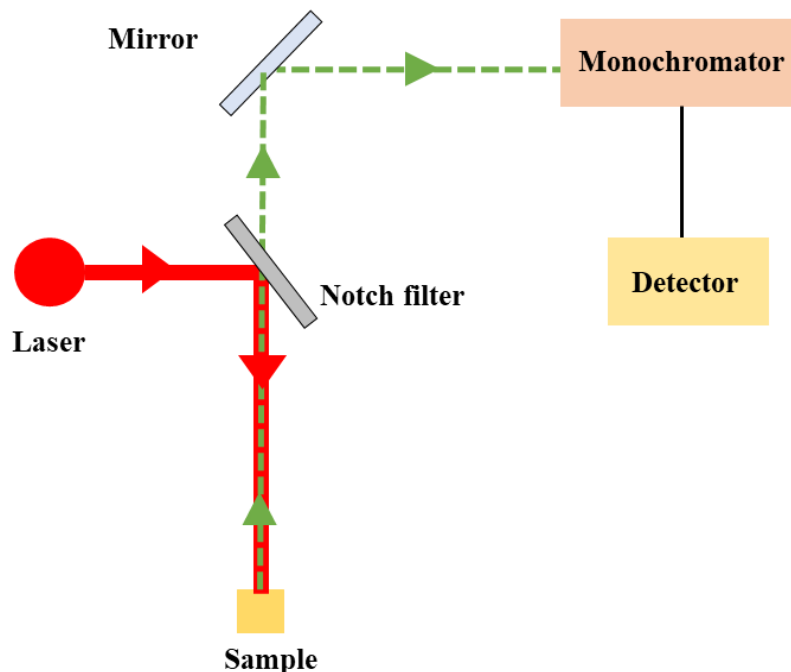


Figure 10. A schematic illustration of Raman spectroscopy set up. The red arrows represent the direction of incident light beam from the laser, whereas the green ones represent the direction of the diffused light out of the sample.

4.5. X-ray photoelectron spectroscopy

X-ray photoelectron spectroscopy (XPS) is a surface-sensitive semi quantitative technique that determines the elemental composition, chemical state and electronic state of the elements that exist within a material. An XPS spectrum is obtained by irradiating a material with a beam of X-rays while simultaneously measuring the kinetic energy and number of electrons that escape from the up to 10 nm of the sample being analyzed.

The principle of XPS is based on the photoelectric effect. An atom ideally has a core electron with the characteristic binding energy that is theoretically, but not strictly, equal to the ionization energy of an electron [13]. When a sample is subjected to an X-ray radiation, the energy of the X-ray photon is adsorbed by the core electron of an atom. If the photon energy of the X-ray radiation ($h\nu$) is large enough, the core electron referred to as “photoelectron” is escaped and emitted out of the surface with a kinetic energy “ E_k ”.

The binding energy (B.E) of the core electron is derived from the Einstein relationship:

$$h\nu = B.E + E_k + \phi \quad (8)$$

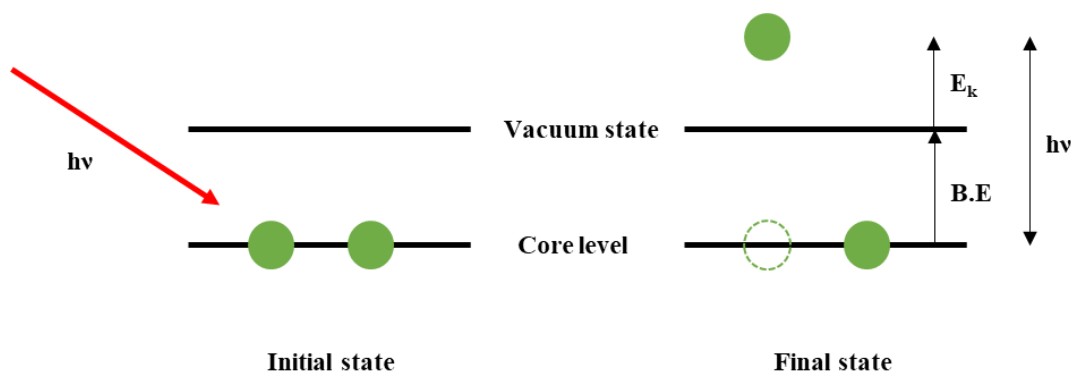


Figure 11. A schematic view of the photoemission process during an XPS experiment.

where $h\nu$ is the X-ray photon energy, E_k is the kinetic energy of photoelectron, which is measured by the energy analyzer; and ϕ is the work function induced by the analyzer ($\sim 4\text{-}5$ eV).

In fact, the work function (ϕ) is a constant which can be compensated artificially. Therefore, the binding energy can be considered as a direct measure of the energy required to remove the core electron from its initial level to the vacuum level (**Figure 11**), and it can be simply expressed as follows:

$$B.E = h\nu - E_k \quad (9)$$

A basic X-ray photoelectron spectrometer comprise the following elements (**Figure 12**): (i) an X-ray source of fixed energy radiation, (ii) an electron energy analyzer used to sort the emitted electrons according to their kinetic energy, (iii) a high vacuum environment allowing the analysis of the emitted electrons without any interference from gas phase collision and avoiding contamination of the sample surface.

In this work, a photoelectron spectrometer (Kratos Axis Ultra DLD, Manchester, Royaume-Uni) equipped with a degassing chamber under ultra-vacuum, a storage room and an analysis chamber UHV under ultra-vacuum was used to obtain the XPS spectra of LDH powders. Samples were deposited on a conductive copper belt, inserted on the transfer bar, introduced into a degassing chamber and then to the analysis chamber which is equipped with a monochromatic X-ray source Al $K\alpha$ emission at 1486.6 eV. Electron counting and detection were performed by a delay line detector DLD (Delay-Line Detector, 115 channels). Spectra were recorded at a normal angle (90°) between the surface of the sample and the direction of ejected electrons. The acquisition of low-

resolution spectra has been carried out with pass energy of 160 eV at steps of 1 eV and the high-resolution spectra with pass energy of 20 eV at steps of 0.5 eV. The analyzed area for all samples was fixed at $0.3 \times 0.7 \text{ mm}^2$. Samples were corrected for charging effects using the C 1s peak. The spectra were adjusted by the Shirley baseline by two models of peak compounds: 70 % of Gaussian function and 30 % of Lorentzian function.

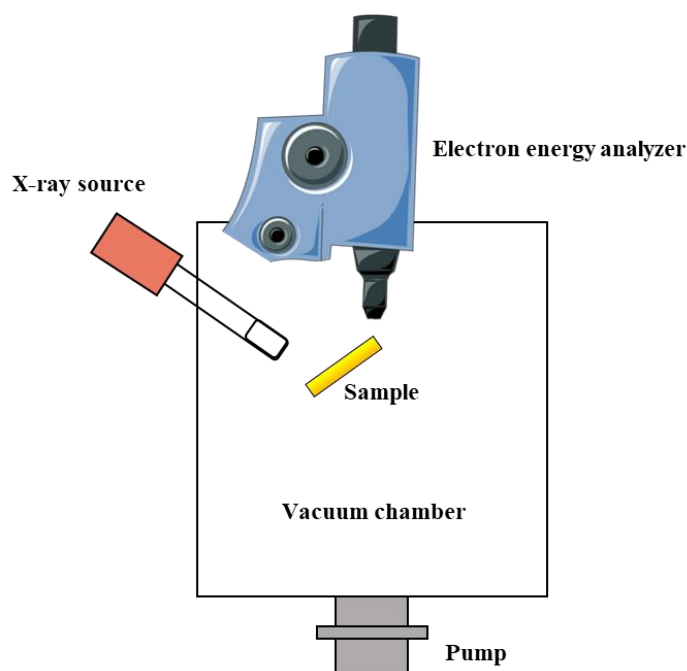


Figure 12. A schematic illustration of XPS system.

4.6. Energy dispersive X-ray spectroscopy

Energy dispersive X-ray spectroscopy (EDS) is a non-destructive standard method for identifying and quantifying elemental compositions of solid samples. EDS systems are generally coupled to an electron microscopy instrument such as scanning electron microscopy (SEM) which will be described in details in the next section (**Section 5.1**). In a properly equipped SEM, the atoms on a sample surface are excited by an electron beam, emitting specific characteristic X-rays. Because characteristic X-rays have specific energy corresponding to each element, elements of a sample can be identified from the peak energy position, whereas the quantification of elements are derived from the integrated intensity of the peak [14].

When an X-ray electron beam hits the surface of a sample, characteristic X-ray photons are emitted. An energy dispersive detector is used to sort and analyze these emitted X-ray photons. Finally, an EDS spectrum displaying the peaks correlated to the elemental composition of the investigated sample is obtained. EDS is capable to detect minor elements in a sample (~ 0.1% weight for bulk materials). However, this technique is limited to the identification of elements having an atomic number $Z > 11$.

Due to its ability to determine the elemental composition of very small solid samples, an electron-dispersive X-ray spectrometer combined to an SEM (JEOL, model JSM-6490LV) was employed to determine the chemical composition of LDH films and LDH-functionalized AFM tips used in this work.

5. Morphological characterization

5.1. Scanning electron Microscopy

Scanning electron microscopy (SEM) is a type of electron microscope that scans surfaces of materials using a beam of low energy. Electron microscopes use very short wavelengths in comparison to the light microscopes which enables better resolution power.

SEM works on the principle produces signals by applying kinetic energy through emitted electrons which interact with a certain sample. This interaction takes place only if the sample is relatively conductive, otherwise, the sample should be coated with a conductive material such as carbon or gold. When high energy electrons reach the sample, several electron signals are generated. These electrons could be secondary electrons, backscattered electrons, and diffracted backscattered electrons which are used to view crystallized phases. Secondary and backscattered electron signals produce an image. The secondary electrons are emitted from the specimen play the primary role of detecting the morphology and topography of the specimen, whereas backscattered electrons show contrast in the composition of the elements of the sample.

In a SEM microscope, the electron source (usually a tungsten filament lamp or field emission gun) is placed at the top of the column. After applying thermal energy to the electron source (a voltage of 1-40 kV), electrons are emitted and transferred toward several condenser lenses which focus the beam of electrons from the source through the column (**Figure 13**). The electron beam then

penetrates through an aperture toward a scanning coil which deflects the beam over an objective lens to reach the sample surface. When the electrons reach the sample, the surface emit different type of electrons, *e.g.*, secondary, backscattered electrons, and diffracted backscattered electrons, which are then trapped by a special detector apparatus made up of several detectors that are able to differentiate different electron types. For most imaging purposes, only a secondary electron detector is used, since secondary electrons are the main contributors for detecting the morphology and topography. An amplifier is used to amplify the signal obtained from the detector, which allows obtaining an image that looks like a television picture.

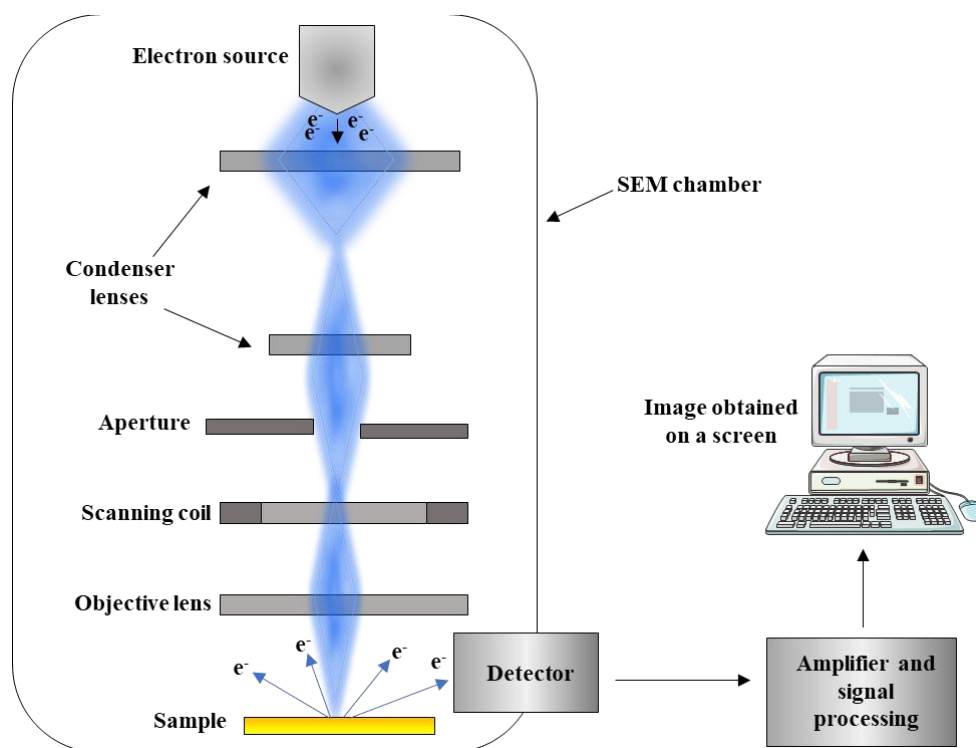


Figure 13. A schematic illustration of an SEM instrument.

The morphology of LDH powders, films and LDH-functionalized AFM tips was examined by Scanning Electron Microscopy (SEM) performed on a JEOL JSM-IT500HR, with a Field Emission Gun (FEG) and a voltage of analysis situated in between 2kV and 5 kV. The analysis was performed under high vacuum, and 60 μ m diaphragm aperture was settled. Secondary Electron Detector (SED) was used for imaging.

5.2. Laser diffraction granulometry

Laser diffraction is a widely technique for determining particle size distribution of materials ranging from hundreds of nanometers up to several millimeters in size. Laser diffraction measures particle size distributions by evaluating the angular deviation of the scattered light by a dispersed particulate a sample. As a laser beam passes through a sample, large particles scatter light at small angles relative to the laser beam, whereas small particles scatter light at larger angles. The angular scattering intensity data is then analyzed to calculate the different particle sizes of the sample responsible for creating the scattering pattern. The particle size is reported as a volume equivalent sphere diameter. Using light scattering technique, one could obtain information about the particle size distribution of a sample by calculating several parameters as the volume median diameter (D_{v50}) which divides the population exactly into two equal halves, and the volume-surface average diameter ($D_{[3,2]}$) which is more relevant when specific surface area is importantly determined, *e.g.*, bioavailability, reactivity and dissolution [15].

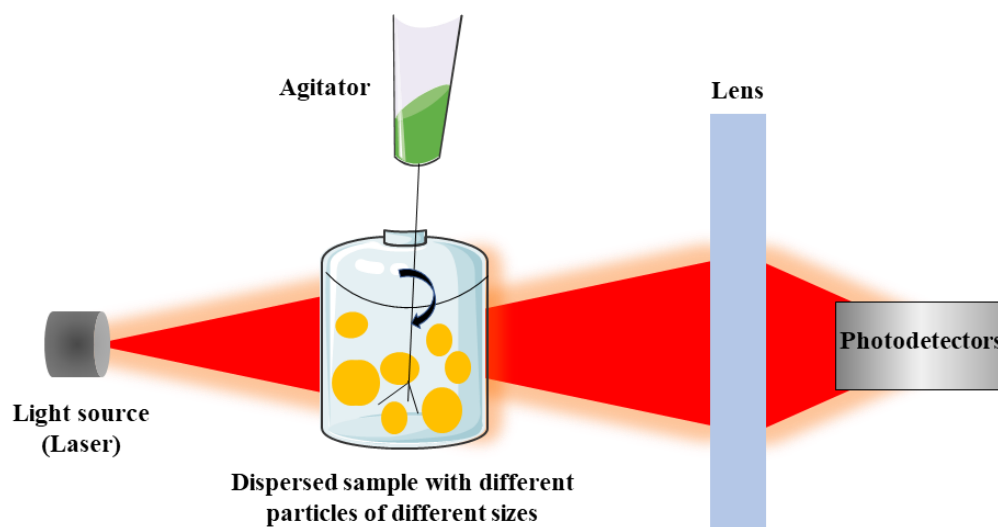


Figure 14. A schematic illustration of laser diffraction granulometry particle size analyzer.

In a typical laser diffraction granulometry analyzer, light from a laser is radiated on a sample suspended in a liquid or gas dispersant (**Figure 14**). Most of the times, an agitator is used to ensure the dispersing of powder samples in liquid dispersant. The particles of the sample scatter the light in different angles according to their size. A lens is placed between the sample and the

photodetectors, causing only the surrounding laser diffraction to reach the detectors. Detected angling of diffracted light are finally processed by a mathematical model in order to generate the particle size distribution in terms of the tested sample.

In this work, particle size distribution (PSD) of LDH powder prepared by low supersaturation slow coprecipitation was determined by Laser Diffraction using a Diffraction Mastersizer 3000 equipment from Malvern Instruments. 50 mg of dry powder was dispersed in 100 mL water using dispersion unit Hydro 2000 also from Malvern Instruments. Control tests were done in LB and TSB media for one LDH sample, and the PSD of this sample was the same as that done in distilled water, thus all other tests were conducted in distilled water for easier manipulation, time and economy saving.

5.3. Brunauer-Emmett-Teller Specific Area

Brunauer-Emmett-Teller (BET) theory explains the physical adsorption of gas molecules on a solid surface and serves as the basis for an important analysis technique for the measurement of the specific surface area of materials. BET theory applies to systems of multilayer gas adsorption. These gases that do not chemically react with material surfaces, which makes them an ideal adsorbate for BET specific area measurements. A standard BET analysis is carried out using nitrogen (N₂) as an adsorbate gas, and the experiment is thus conducted at the boiling temperature of N₂ [16].

BET equation is used to determine the adsorbed monolayer gas volume (V_m):

$$\frac{1}{v[(p_0-p)-1]} = \frac{c-1}{V_m c} \left(\frac{p}{p_0}\right) + \frac{1}{V_m c} \quad (10)$$

Where v is the adsorbed gas volume, p₀ is the saturation pressure of adsorbate, p is the equilibrium pressure of adsorbate and c is the BET constant.

The specific surface area can then be from the monolayer absorbed gas volume (V_m) through the following equation:

$$S_{BET} = \frac{V_m N_s}{V_a} \quad (11)$$

Where N is the Avogadro's number (6.02×10^{23} molecules/mol), V is the molar volume of N_2 (22.4 L/mol), s is the cross-sectional area of N_2 ($16.2 \text{ \AA}^2/\text{molecule}$ of Nitrogen), and a is the mass of the sample.

For an accurate measurement, the sample must first be degassed in a vacuum at high temperatures to remove adsorbing water molecules and other contaminants. After that, the degassed sample must be measured accurately and placed in a glass cell supported by glass rods to minimize the dead space in the cell (**Figure 15**). Dewar of liquid nitrogen are used to cool the sample and maintain it at a constant temperature. Nitrogen gas acting as an adsorbate is then injected into the sample cell with a calibrated piston, whereas helium (He) is used as a carrier inert gas. The partial pressure of the adsorbate is determined by the gas flow meter, whereas the adsorbed gas amount could be determined by a potentiometer and data is collected using a certain data collector.

In this work, specific surface area analysis of LDH powders were performed using the Brunauer-Emmet-Teller (BET) approach using a BELSORP MAX analyzer at 77K in N_2 . The solids were degassed at 120°C prior to the measurements to remove any adsorbed water molecules.

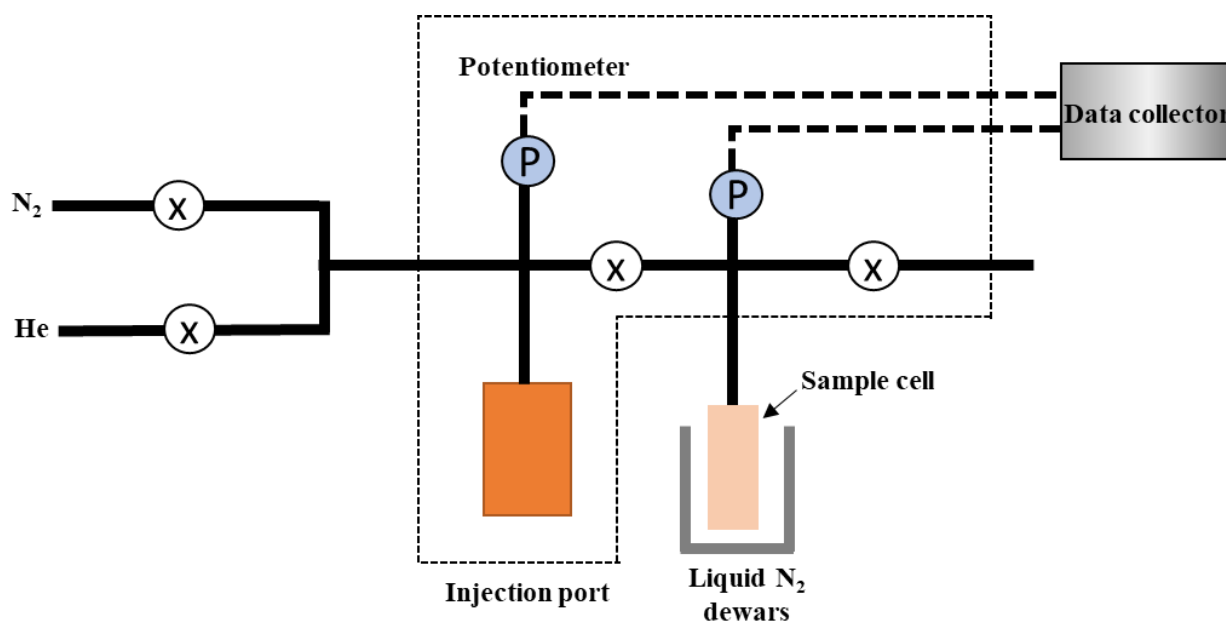


Figure 15. A schematic illustration of BET instrument.

6. Atomic force microscopy

6.1. Topographical characterization of LDHs and bacteria

Atomic force microscopy (AFM) is a commonly used technique used to obtain three-dimensional images of a surface at a nanometer scale. The principle of operation of the atomic force microscope is illustrated in **Figure 16**. A sharp tip used for measurements, attached to the end of a flexible cantilever arrives at the surface of the sample. The scanner moves the substrate under the tip in both x and y directions to scan areas ranging from nm^2 to μm^2 . The difference in height profiles present on the surface of the sample induce a deviation of the cantilever in the z-direction. This deviation is controlled by an optical detection system located inside the head of the microscope. The detection system consists of a laser beam from a 4-quadrant photodiode. The photodiode detects any variation in the incident beam, *e.g.*, any deviation in the cantilever through the z-piezo. Thus, information about the surface topography of a sample could be obtained by detecting the fluctuation in the bending cantilever [17].

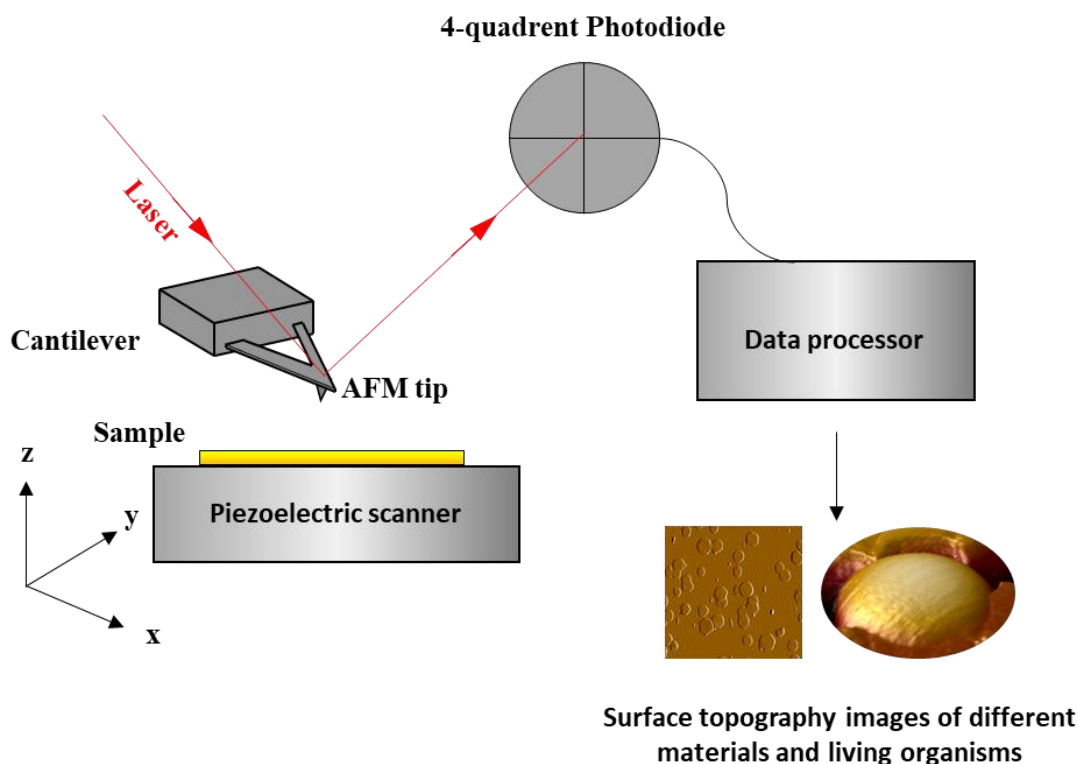


Figure 16. A schematic illustration of atomic force microscopy set up and principle to perform surface topography imaging.

Images are usually recorded in constant or dynamic (tapping) modes. In contact mode, the tip is brought into contact with the sample where the deflection of the cantilever remains constant during scanning, thus recording sample surface topography as a function of vertical motion. In tapping mode, the cantilever is vibrated near its resonance frequency causing the tip to oscillate, thus recording sample surface topography in function of height. Unlike contact mode, tapping mode allows coming into close contact with the surface intermittently. This limits frictional forces between the sample surface and the probe associated sample damage, thus making tapping mode more suitable for imaging soft samples. On the other hand, more acquisition time is needed to obtain high-resolution image using tapping mode in comparison to contact mode.

One great advantage of AFM over other imaging techniques is that it performed not only in air but also in liquid conditions, thus mimicking physiological conditions for living organisms as microorganisms [18].

In this work, LDH nanoparticles immobilized on silicon substrates and LDH films were imaged in peak-force tapping mode using SNL-C tips (Bruker corporation) in air. LDH NPs were dispersed in an ethanol solution, sonicated for 30 min and deposited on clean silicon substrates and dried at 30°C overnight.

For topography images on *S. aureus*, cells were cultivated alone (untreated) or with (treated) the minimum inhibitory concentration LDH NPs during 24 h in Tryptic Soy Broth at 37°C. For imaging in MOPS ((3-(N-morpholino)propane sulfonic acid) buffer solution, stationary phase cultures of *S. aureus* were centrifuged, washed twice in MOPS and filtered into porous polycarbonate membranes (pore size = 0.8 µm). After filtration and rough rinsing, a 1 x 1 cm² piece of membrane was cut and attached with double sided adhesive tape at the bottom of a Petri dish and immersed in MOPS. The roughness parameter Rq (root mean square of the heights) of the cells was calculated using the commercial Nanoscope analysis (Bruker) from AFM images performed on the top of bacteria at a high magnification of 400 × 400 nm² scanning areas using the following formula:

$$Rq = \sqrt{\frac{\sum Z_i^2}{N}} \quad (12)$$

Where Rq is derived using the software and considered as standard deviation of the Z values within the box cursor, Z_i is the current Z value, and N is the number of points within the box cursor.

For imaging in air, cells were centrifuged, washed twice and resuspended in ultra-pure distilled water then deposited on mica substrates. After 2 hours, substrates were gently rinsed in ultrapure distilled water and dried overnight at 30 °C. For both air and liquid conditions, images were acquired in peak-force tapping mode using SNL-C tips.

6.2. Force spectroscopy

Mechanical forces between AFM probes and different samples could be probed by force spectroscopy mode. These forces are derived from the cantilever deflection according to Hooke's law:

$$F = -k_c d \quad (13)$$

where k_c is the spring constant of the cantilever and d is the extension of the cantilever bend.

At the initial stage, the tip and the sample are separated by a large distance meaning that no interaction is present between them and the cantilever remains in a noninteracting equilibrium state. As the tip approaches the sample, it is brought in contact with the sample at a fixed rate and the interaction begins. The probe is then withdrawn from the sample surface presenting one or multiple interaction sites (retraction curve peaks) which are characteristics of the force created due to the interaction between the probe and the sample surface (**Figure 17**). The maximum distance at which the probe interacts with the sample (rupture length) can be identified by the z scale of the piezoelectric scanner which regulates the distance at which the interaction occurs.

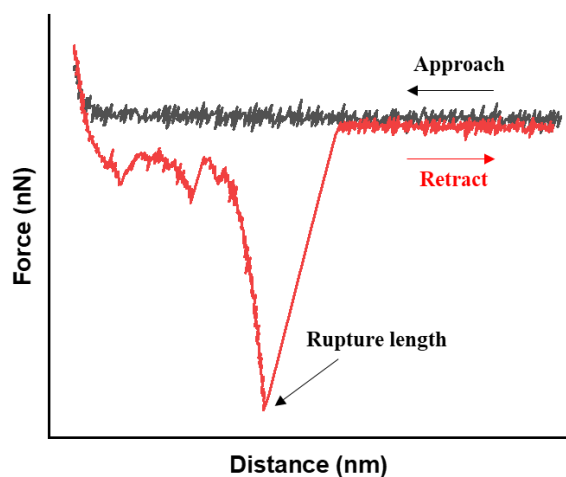


Figure 17. An example of force-distance curves obtained during approach/retract process of AFM-based force spectroscopy.

In this work, AFM tips were functionalized with LDH films using the procedure described in **Section 3.4**. These functionalized tips were used to probe the interactions between LDHs and living *S. aureus* cells trapped in porous membranes by means of AFM-based force spectroscopy.

First, bare MLCT-C tips were used to localize and image individual cells. Then, the tips were replaced by aluminum-coated tips, MgAl and ZnAl LDH-functionalized tips. Adhesion force maps and histograms were obtained by recording 32×32 force–distance curves on areas of $400 \times 400 \text{ nm}^2$ on cells surfaces, calculating the adhesion force of the last adhesion peak for each force curve, and displaying the value as a grey pixel on adhesion maps. All curves were recorded using a maximum applied force of 250 pN, a contact time of 250 ms, and constant approach and retraction speeds of $1 \text{ }\mu\text{m/s}$. Data were processed using the commercial Nanoscope analysis (Bruker) and MATLAB (The MathWorks, Natick, MA) softwares.

7. Antibacterial activity tests

7.1. Bacterial strains and culture conditions

Two bacterial strains were used as tested microorganisms in this study: Gram-positive *Staphylococcus aureus* strain 187 (HER 1239, provided by Félix d'Hérelle Reference Center for Bacterial Viruses from the Université Laval; Québec, Canada) and E2146 strain of *Escherichia coli* (provided from Institut Pasteur; Paris, France).

S. aureus is a round-shaped bacterium, a member of the *Bacillota*, which could be commonly found in the upper respiratory tract of human and on the skin. Although *S. aureus* usually acts as a commensal of the human microbiota, it can also become an opportunistic pathogen, being a major cause of food poisoning, respiratory and skin infections [19].

E. coli is an anaerobic, rod-shaped bacterium of the genus *Escherichia* which is naturally present in the lower intestine of human and animals. However, some *E. coli* strains are pathogenic, leading to different diseases associated with intestinal and extra-intestinal infections [20].

Bacterial strains used in this work for the antibacterial activity tests were cultivated in Tryptic Soy Broth (TSB) for *S. aureus* and Lysogeny Broth (LB) for *E. coli*. Initial stocks were stored at -80°C (*S. aureus* in TSB with 20 % (v/v) of glycerol, *E. coli* in LB with 25 % (v/v) of glycerol).

The working stocks were obtained at 37°C following the growth of bacteria on TSB agar or LB agar within 24 hours for *S. aureus* and *E. coli*, respectively.

7.2. Agar disc diffusion test

Agar disk diffusion is a routinely used method for antimicrobial susceptibility testing in most clinical microbiology laboratories [21]. This antibacterial test relies on inoculating agar plates with a standardized inoculum of the tested microorganisms in question, then placing filter paper discs (about 6 mm in diameter) containing the test compound at a desired concentration on specified spots of the agar spots. Then, Petri plates are incubated under suitable temperature and time conditions according to the type and strain of the tested microorganism. In general, antimicrobial agents diffuse to the agar and inhibit the growth of the test microorganisms, thus generating inhibition zones known as antibiograms. According to the measured diameter of the generated inhibition zones, one can classify bacterial pathogens as susceptible, intermediate, or resistant to the tested microbial agent. It is important to mention that this method express a long-range antibacterial effect depending on the diffusion of coefficient of the tested antibacterial agent.

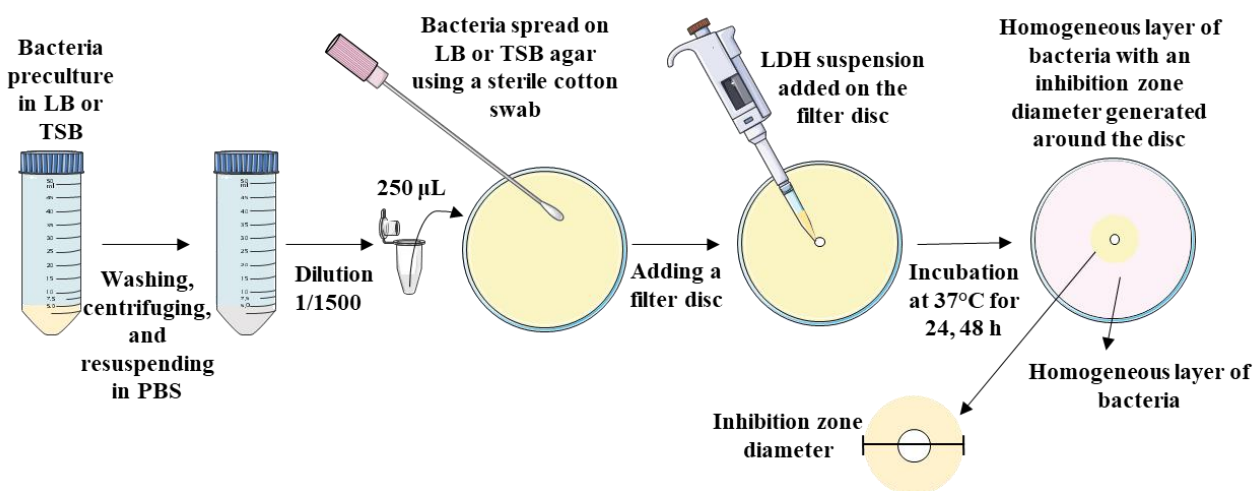


Figure 18. A schematic illustration of the experimental protocol used to determine inhibition zone diameters of LDH suspensions against *S. aureus* and *E. coli*.

In this work, antibacterial activity of LDH powders was evaluated against *E. coli* and *S. aureus* using agar disc diffusion assay. The followed experimental protocol for this antibacterial activity tests is illustrated in **Figure 18**. All experiments were repeated three times to ensure their

reproducibility. First, *E. coli* and *S. aureus* were precultured overnight in 5 mL of LB and TSB respectively. LB and TSB agar plates were prepared, sterilized and solidified. Then, 250 μL of bacterial suspension were diluted to 1/1500 in sterile phosphate buffer saline (PBS) and spread on LB and TSB agar plates using a sterile cotton swab to prepare bacterial lawns homogeneous layers. Antibiotic filter discs of 6 mm were placed on these plates and 20 μL of LDH dispersions (10 mg/mL) were loaded on the respective discs. The plates were then incubated at 37°C for 24 or 48 h. Afterwards, bacterial inhibition zones were observed around the discs. The diameter of the circular zones was measured using a centimeter ruler and mean values of three repeated trials for each microorganism were recorded and represented in millimeters. A similar procedure was followed to investigate the antimicrobial activity of divalent metallic salts having a molar concentration similar to that released out of their LDHs counterparts.

7.3. Broth micro- and macro-dilution tests

Broth dilution methods are one of the earliest antimicrobial susceptibility tests. Using these methods, two-fold dilutions of the antimicrobial agent (*e.g.*, 1, 2, 4, 8, 16, 32 and 64 mg/mL) are prepared in liquid growth medium dispensed in tubes with a minimum volume of 1 mL for macro-dilution or with 96-well microtitration plate for microdilution [22]. The antibacterial agent containing tubes or wells are inoculated with a standardized bacterial suspension of known optical density. After well mixing, the tubes or the microtitration plate are incubated under appropriate time and temperature conditions. Broth dilution tests are considered very suitable ones for the determination of the minimum inhibitory concentration (MIC) because they offer the great advantage of estimating the exact concentration of the antibacterial agent in question [21]. Following the incubation, the tubes or the wells are examined for either visible bacterial growth evidenced by turbidity or using optical density spectrometer devices.

Broth microdilution turbidimetric method was used to determine the MIC of LDH powders. *E. coli* and *S. aureus* were precultured in 5 mL of LB and TSB, respectively. An inoculum of each of strain was prepared and diluted to obtain an optical density of 0.1 at $\lambda = 600 \text{ nm}$ ($\text{OD}_{600}=0.1$). LDH powders were dispersed in broth culture media (LB or TSB), and two-fold dilution series were then prepared in a 96-well micro-titer plate (**Figure 19**). Each well included 25 μL of the diluted LDH powder and 175 μL of bacterial inoculum. Un-inoculated broth wells containing the different

used LDH dispersion concentrations were used as a negative standard growth control. As a positive control, 12 wells were prepared with 175 μL of bacterial inoculum and 25 μL of broth culture media. The micro-titer plate was then sealed and incubated at 37°C under agitation for 24 or 48 hours. The MIC value for each LDH sample was recognized as the lowest concentration that had no visible turbidity. A similar protocol but with larger volumes (125 μL of the diluted LDH powder + 875 μL of bacterial inoculum with a total volume of 1 mL) was followed to perform broth macro-dilution tests in Eppendorf tubes. The obtained volumes in broth macro-dilution were used to analyze bacterial samples using AFM and FT-IR spectroscopy.

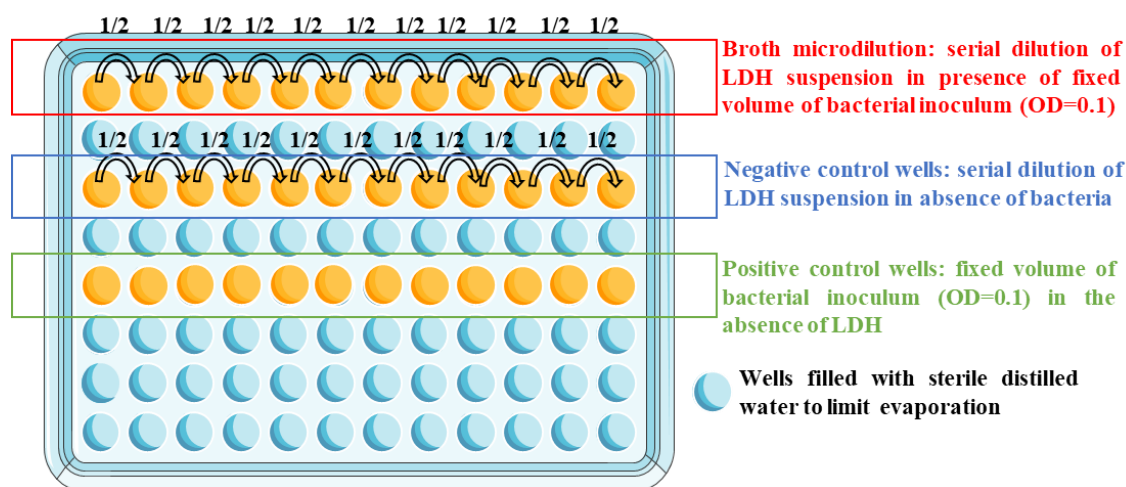


Figure 19. A schematic representation of 96-well micro-titer plate used to determine the minimum inhibitory concentration of LDHs against *S. aureus* and *E. coli* using broth microdilution method.

7.4. Colony forming unit count

Colony forming unit (CFU) count is a measure of viable bacterial cells. This method relies on spreading the bacteria and determining their growth as colonies on a nutrient medium. A serial dilution of a culture containing bacteria and the antibacterial agent in question is added to the plate and usually spread using sterilized beads. After a certain incubation time and under suitable bacterial growth conditions, bacterial colonies become visible to the naked eye and the number of colonies on a plate can be counted. The results of CFU count experiments are usually reported in CFU/mL (colony forming unit/mL):

$$CFU/mL = \frac{Nd}{v} \quad (14)$$

Where N is the number of colonies formed on the plate, d is the dilution factor and v is the volume of the of the initial bacterial inoculum at a defined OD.

Since CFU count is only accounted for viable bacterial cells, bactericidal efficiency of a certain antibacterial agent could also be determined through the following formula:

$$\% \text{ bactericidal efficiency} = \frac{N_c - N_A}{N_c} \times 100 \quad (15)$$

Where N_C is the number of bacterial colonies in a control group in the absence of the antibacterial agent and N_A is the number of bacterial colonies found in the presence of the tested antibacterial agent.

The bactericidal rate at each defined data point could also be calculated as follows:

$$\text{Bactericidal rate} = \frac{N_0 - N_t}{N_0 t} \times 100 \quad (16)$$

Where N_0 is the number of colonies formed in a certain experimental condition at $t=0$, N_t is the number of colonies formed at a defined time point, and t is the defined time point.

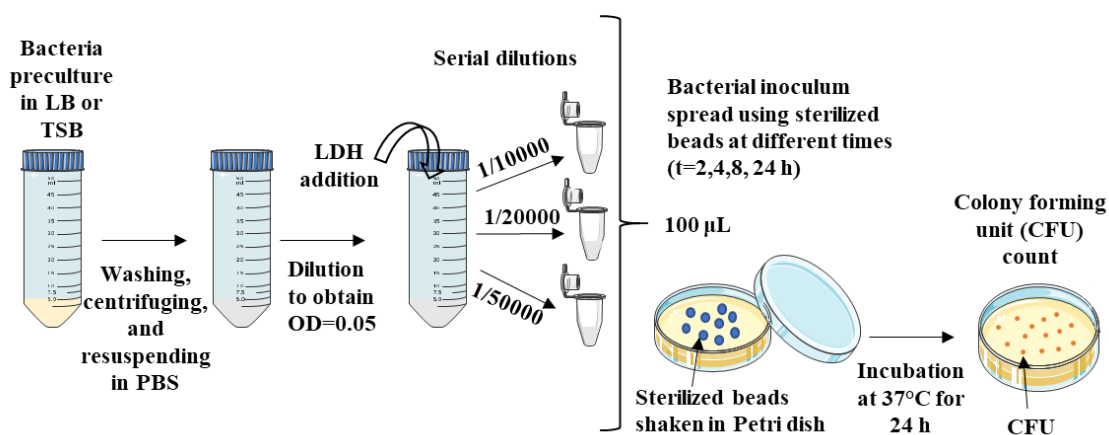


Figure 20. A schematic representation of CFU count experiments.

In this work, the antibacterial activity of Zn(II)Al(III) LDH nanoparticles in dark and UVA light conditions (exposure for 4 h) was examined against *S. aureus* using CFU count method (**Figure 6**). 1 mL of bacterial suspension having an optical density of 0.05 with and without LDH nanoparticles in dark and UVA conditions were deposited on 12-well plates and gently agitated at 37 °C. At defined time points (0 h, 2 h, 4 h, 8 h and 24 h), 100 µL were pipetted, serially diluted (1/10000, 1/20000, 1/50000) and spread on TSB agar Petri dishes using sterilized beads. The plates

were then incubated at 37 °C to determine bacterial viability by counting the number of colonies formed on the Petri dish.

References

- [1] A. Di Bitetto, Étude structurale et dynamique d'hydroxydes doubles lamellaires : du matériau carbonaté aux hybrides organo-minéraux, 2017.
- [2] N. Iyi, H. Yamada, T. Sasaki, Deintercalation of carbonate ions from carbonate-type layered double hydroxides (LDHs) using acid–alcohol mixed solutions, *Appl. Clay Sci.* 54 (2011) 132–137.
- [3] Z.P. Xu, G.S. Stevenson, C.-Q. Lu, G.Q. (Max) Lu, P.F. Bartlett, P.P. Gray, Stable Suspension of Layered Double Hydroxide Nanoparticles in Aqueous Solution, *J. Am. Chem. Soc.* 128 (2006) 36–37.
- [4] Z.P. Xu, G. Stevenson, C.-Q. Lu, G.Q. (Max) Lu, Dispersion and Size Control of Layered Double Hydroxide Nanoparticles in Aqueous Solutions, *J. Phys. Chem. B.* 110 (2006) 16923–16929.
- [5] M.A. Iqbal, L. Sun, A.T. Barrett, M. Fedel, Layered Double Hydroxide Protective Films Developed on Aluminum and Aluminum Alloys: Synthetic Methods and Anti-Corrosion Mechanisms, *Coatings.* 10 (2020) 428.
- [6] F. Zhang, L. Zhao, H. Chen, S. Xu, D.G. Evans, X. Duan, Corrosion Resistance of Superhydrophobic Layered Double Hydroxide Films on Aluminum, *Angew. Chem. Int. Ed.* 47 (2008) 2466–2469.
- [7] R. Thomas, *Practical Guide to ICP-MS: A Tutorial for Beginners*, Second Edition, 2nd ed., CRC Press, 2008.
- [8] B.D. Cullity, *Elements of x-ray diffraction*, 2d ed, Addison-Wesley Pub. Co, Reading, Mass, 1978.
- [9] D. Steele, *Infrared Spectroscopy: Theory*, in: J.M. Chalmers, P.R. Griffiths (Eds.), *Handb. Vib. Spectrosc.*, John Wiley & Sons, Ltd, Chichester, UK, 2006: p. s0103.
- [10] B.H. Stuart, *Analytical Techniques in Materials Conservation*, John Wiley & Sons, Ltd, Chichester, UK, 2007.
- [11] B. Schrader, ed., *Tools for infrared and Raman spectroscopy*, in: *Infrared Raman Spectrosc.*, Wiley-VCH Verlag GmbH, Weinheim, Germany, 1995: pp. 63–188.
- [12] Y. Ozaki, S. ai, *Introduction to Raman Spectroscopy*, in: S. ai (Ed.), *Pharm. Appl. Raman Spectrosc.*, John Wiley & Sons, Inc., Hoboken, NJ, USA, 2007: pp. 1–28.
- [13] S. Hüfner, *Introduction and Basic Principles*, in: *Photoelectron Spectrosc.*, Springer Berlin Heidelberg, Berlin, Heidelberg, 2003: pp. 1–60.
- [14] D. Shindo, T. Oikawa, *Energy Dispersive X-ray Spectroscopy*, in: *Anal. Electron Microsc. Mater. Sci.*, Springer Japan, Tokyo, 2002: pp. 81–102.
- [15] A. Rawle, *The Basic Principles of Particle Size Analysis*, *Surf. Coat. Int. Part Coat. J.* 86 (2003) 58–65.
- [16] A. Trewin, *Analyzing the Surface Area Properties of Microporous Materials*, in: B. Pignataro (Ed.), *Mol. Work*, 1st ed., Wiley, 2012: pp. 71–95.
- [17] B. Voigtländer, *Atomic Force Microscopy*, Springer International Publishing, Cham, 2019.
- [18] V.J. Morris, A.R. Kirby, A.P. Gunning, *Atomic Force Microscopy for Biologists*, 2nd ed., IMPERIAL COLLEGE PRESS, 2009.
- [19] S. Peacock, *Staphylococcus aureus*, in: S.H. Gillespie, P.M. Hawkey (Eds.), *Princ. Pract. Clin. Bacteriol.*, John Wiley & Sons, Ltd, Chichester, UK, 2006: pp. 73–98.

- [20] J.B. Kaper, J.P. Nataro, H.L.T. Mobley, Pathogenic *Escherichia coli*, *Nat. Rev. Microbiol.* 2 (2004) 123–140.
- [21] T.L. Gavan, *In Vitro Antimicrobial Susceptibility Testing: Clinical Implications and Limitations*, *Med. Clin. North Am.* 58 (1974) 493–503.
- [22] M. Balouiri, M. Sadiki, S.K. Ibsouda, *Methods for in vitro evaluating antimicrobial activity: A review*, *J. Pharm. Anal.* 6 (2016) 71–79.

Antibacterial activity of pristine layered double hydroxides by divalent metal ions release

Table of figures	106
Table of tables.....	108
1. Context	109
2. Synthesis of LDH powders.....	110
2.1. Carbonate-intercalated LDHs	110
2.2. Chloride-, nitrate- and perchlorate-intercalated Zn(II)Al(III) LDHs.....	111
3. Characterization of LDH powders	112
3.1. Structural characterization.....	112
3.1.1. M(II)/Al(III) molar ratio determination by inductively coupled plasma mass spectroscopy	112
3.1.2. Powder X-ray diffraction	112
3.1.3. InfraRed and Raman spectroscopies	115
3.2. Morphological and textural characterizations	117
4. Influence of different physicochemical parameters on the constituent divalent metal release from LDHs in broth culture media.....	121
4.1. Influence of the nature constituent divalent metal on the release profile of M^{2+}_{aq}	123
4.2. Influence of crystallinity on the release profile of Zn^{2+}_{aq}	125
4.3. Influence of Zn(II)/Al(III) molar ratio on the release profile of Zn^{2+}_{aq}	125
4.4. Influence of intercalated-anion on the release profile of Zn^{2+}_{aq}	126

5. LDH structure after exposition to culture media	128
6. Antibacterial activity of LDHs	129
6.1. Influence of the nature of divalent metal on the antibacterial activity of LDHs	131
6.2. Difference in antibacterial activity among the tested M(II)Al(III) LDHs	133
6.3. Correlating the antibacterial activity of LDHs to their divalent metal ions release profile 133	
7. Conclusion.....	135
References	137

Table of figures

Figure 1. A schematic illustration of the systematic study aimed at studying the different physico-chemical parameters affecting the antibacterial activity of pristine LDHs mediated by the mechanism of divalent metal release.	110
Figure 2. PXRD patterns of the different prepared LDH samples: a) $Zn_2Al:CO_3$ -hyd, b) $Zn_2Al:CO_3$ -cop, c) $Zn_3Al:CO_3$, d) $Zn_2Al:Cl$, e) $Zn_2Al:NO_3$, f) $Zn_2Al:ClO_4$, g) $Mg_2Al:CO_3$, h) $Cu_2Al:CO_3$, i) $Ni_2Al:CO_3$, j) $Co_2Al:CO_3$	113
Figure 3. a) InfraRed spectra of carbonate-intercalated LDHs: (a) $Zn_2Al:CO_3$ -hyd, (b) $Zn_2Al:CO_3$ -cop, (c) $Zn_3Al:CO_3$, (d) $Mg_2Al:CO_3$, (e) $Cu_2Al:CO_3$, (f) $Ni_2Al:CO_3$, (g) $Co_2Al:CO_3$. b) InfraRed spectra of chloride-, nitrate- and perchlorate intercalated LDHs. (a) $Zn_2Al:Cl$, (b) $Zn_2Al:NO_3$, (c) $Zn_2Al:ClO_4$	116
Figure 4. a) Raman spectra of carbonate-intercalated LDHs: (a) $Zn_2Al:CO_3$ -hyd, (b) $Zn_2Al:CO_3$ -cop, (c) $Zn_3Al:CO_3$, (d) $Mg_2Al:CO_3$, (e) $Cu_2Al:CO_3$, (f) $Ni_2Al:CO_3$, (g) $Co_2Al:CO_3$. b) Raman spectra of chloride-, nitrate- and perchlorate intercalated LDHs: (a) $Zn_2Al:Cl$, (b) $Zn_2Al:NO_3$, (c) $Zn_2Al:ClO_4$	116
Figure 5. SEM micrographs of: a,b) $Zn_2Al:CO_3$ -hyd, c,d) $Zn_2Al:CO_3$ -cop, e,f) $Zn_3Al:CO_3$	117
Figure 6. SEM micrographs of: a) $Zn_2Al:Cl$, b) $Zn_2Al:NO_3$, c) $Zn_2Al:ClO_4$	118
Figure 7. SEM micrographs of $Cu_2Al:CO_3$ LDH.	118
Figure 8. Particle Size Distribution (PSD) curves in water dispersion of: a) $Zn_2Al:CO_3$ -hyd, b) $Zn_2Al:CO_3$ -cop, c) $Zn_3Al:CO_3$, d) $Zn_2Al:Cl$, e) $Zn_2Al:NO_3$, and f) $Zn_2Al:ClO_4$	120
Figure 9. Partial dissolution profiles of all synthesized LDH samples into M^{2+} in LB and TSB media, in terms of average percentage compared to the initial amount present in the LDH.	121
Figure 10. Kinetic dissolution profiles of $Zn_2Al:CO_3$ -hyd and $Zn_2Al:CO_3$ -cop into Zn^{2+} in LB and TSB media.	123
Figure 11. PXRD diffraction patterns of: a) $Zn_2Al:CO_3$, b) $Zn_2Al:Cl$, c) $Zn_2Al:NO_3$ and d) $Zn_2Al:ClO_4$ LDHs, before and after being exposed to TSB for 48 h.....	128
Figure 12. SEM micrographs of: a) $Zn_2Al:Cl$, b) $Zn_2Al:NO_3$, c) $Zn_2Al:ClO_4$, after being exposed to TSB medium for 48 h.....	129
Figure 13. Antibacterial agar disk diffusion tests against: a) <i>S. aureus</i> control, b) <i>S. aureus</i> using $Zn_2Al:CO_3$ -hyd (top), $Zn_2Al:CO_3$ -cop (bottom left) and $Zn_3Al:CO_3$ (bottom right), c) <i>S. aureus</i>	

using $Zn_2Al:Cl$ (top), $Zn_2Al:NO_3$ (bottom left) and $Zn_2Al:ClO_4$ (bottom right), d) *E. coli* control, e) *E. coli* using $Zn_2Al:CO_3$ -hyd (top), $Zn_2Al:CO_3$ -cop (bottom left) and $Zn_3Al:CO_3$ (bottom right), f) *E. coli* using $Zn_2Al:Cl$ (top), $Zn_2Al:NO_3$ (bottom left) and $Zn_2Al:ClO_4$ (bottom right). 130

Figure 14. Antimicrobial activity of LDH samples and metal ion solutions against *S. aureus* and *E. coli* in terms of mean zone of inhibition generated in agar disc diffusion tests. 131

Figure 15. Evolution of antimicrobial activity in terms of LDH MIC against *S. aureus* and *E. coli* as a function of average concentration of Zn^{2+} released from of $Zn(II)Al(III)$ LDH samples. ... 134

Table of tables

Table 1. Experimental conditions for the synthesis of M(II)Al(III) LDH powders together with their respective M(II)/Al(III) molar ratio determined by ICP-MS.	111
Table 2. Unit cell lattice parameters, interlamellar distance (d), $L_{(003)}$ and $L_{(110)}$ of the prepared LDH samples.	114
Table 3. Specific surface area determined by BET , D_{v50} and $D_{[3, 2]}$ determined by PSD for the different prepared Zn(II)Al(III) LDH samples.	119
Table 4. Partial dissolution profiles of all synthesized LDH samples into M^{2+} in distilled water, in terms of average percentage compared to the initial amount present in the LDH.....	122
Table 5. pK_{sp} values for $M(OH)_2$ reported by [56].	124
Table 6. MIC values of different LDH samples against <i>E. coli</i> and <i>S. aureus</i>	130

1. Context

Nowadays, the fabrication of different materials avoiding biofouling or pathogenic bacteria proliferation is highly demanded [1]. Under this aspect, LDH and LDH-composite materials were utilized in different antimicrobial applicational fields as water purification [2,3], food packaging [4,5], wound healing dressings [6], and textile industries [7].

In fact, many surveys showed that LDHs possess high potential as carriers of biological antibiotics due to their controlled release rate [8–10]. Antibiotics can treat bacterial infections, however, the excessive use of antibiotic had led to emergence and spread of new antimicrobials of resistant strains [11,12], where the World Health Organization (WHO) estimates 700,000 global deaths per year due to antimicrobial resistance phenomenon [13].

Some recent studies proved that unmodified pristine LDHs could act as efficient antibiotic-free antimicrobial materials [3,14–20]. As previously suggested in **Chapter 1**, the antibacterial mechanism of pristine LDHs could be explained by the following three mechanisms; **(1)** direct contact between LDHs and bacteria leading to membrane and cell wall damage, **(2)** release of divalent metals inducing serious changes in bacterial membrane permeability thus leading to their damage, **(3)** generation of reactive oxygen species (ROS) which are well known to be toxic for the bacteria. Despite the fact these hypotheses were proposed to explain the antimicrobial effect of pristine LDHs the followed antibacterial mechanism is still not well understood.

Therefore, the partial dissolution of pristine LDHs into their constituents M^{2+} aqueous ions might constitute one possible explanation to their antibacterial activities (**Mechanism 2**) [14,18,19]. Although such antimicrobial mode of action was suggested, no real experimental set up was designed to validate it and no proof of experimental evidence was previously reported. Moreover, these studies did not provide systematic approaches to determine in depth how to tune the physicochemical parameters of pristine LDHs to enhance the desired antimicrobial effect mediated by dissolution and release of constituent divalent metals.

In this context, this chapter is dedicated to evaluate systematically the influence of different parameters (crystallinity, M(II)/Al(III) molar ratio, type of intercalated anion $\{CO_3^{2-}, Cl^-, NO_3^-, ClO_4^-\}$ and nature of M(II) cations) on the solubility of pristine LDHs in broth media contributing to their antimicrobial effect (**Figure 1**). The properties of Zn(II)-based LDHs had been

systematically analyzed due to their relatively well-established antimicrobial behavior. The dissolution properties of the prepared M(II)Al(III) LDHs were studied in growth media of *Escherichia coli* and *Staphylococcus aureus* bacteria, *i.e.*, Lysogeny Broth (LB) and Tryptic Soy Broth (TSB), respectively. Finally, the relationship between the solubility and physicochemical properties of the LDHs and their antimicrobial activity was determined and subsequently the antimicrobial mechanism of pristine LDHs by divalent metal ions release was validated.

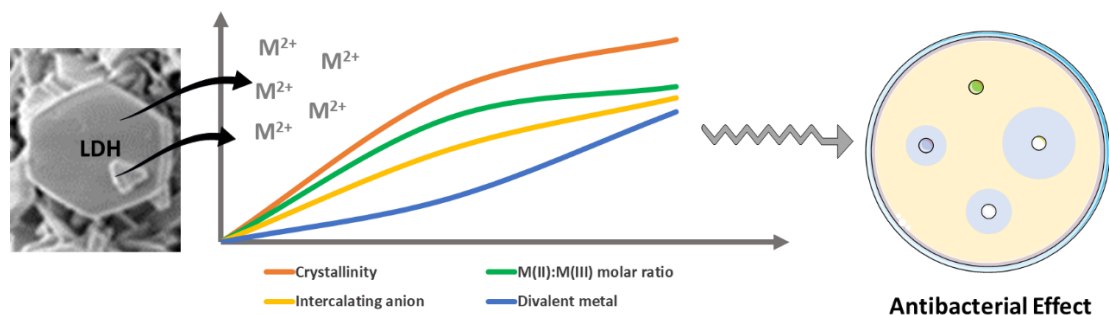


Figure 1. A schematic illustration of the systematic study aimed at studying the different physico-chemical parameters affecting the antibacterial activity of pristine LDHs mediated by the mechanism of divalent metal release.

The content of this chapter is published in *Applied Clay Science* ([Annex I](#)).

2. Synthesis of LDH powders

2.1. Carbonate-intercalated LDHs

Carbonate-intercalated LDHs marked as $M_2Al:CO_3$ ($M= Zn, Cu, Ni, Co, Mg$) and $M_3Al:CO_3$ ($M= Zn$) were synthesized by low supersaturation coprecipitation method [21]. First a 0.05 mol/L ammonium/ammonia solution was prepared then the pH of the solution was fixed to a value of 10 using a solution of 1% HNO_3 . A solution of 0.4 mol/L M(II) and Al(III) nitrate salts having a molar ratio M(II)/Al(III) of 2/1 or 3/1 was added slowly using a peristaltic pump operated at 0.3 mL/min into the ammonia solution. The pH was kept constant at 10 by an automatic titrator using a solution of 1 mol/L NaOH and 0.25 mol/L Na_2CO_3 . For most of the synthesis, this was followed by a hydrothermal treatment in an autoclave at 80°C for 24 hours to enhance the crystallinity, then the solids were washed for 4 times in deionized water and collected by centrifugation. Finally, the obtained LDH solids were dried in air at 80°C for 24 hours. Only one LDH sample, denoted as

$Zn_2Al:CO_3$ -cop, was not exposed to hydrothermal treatment, where the solid obtained directly after coprecipitation was washed and dried without any further treatment.

2.2. Chloride-, nitrate- and perchlorate-intercalated $Zn(II)Al(III)$ LDHs

$Zn_2Al:Cl$, $Zn_2Al:NO_3$ and $Zn_2Al:ClO_4$ LDHs were prepared by anion-exchange reactions of $Zn_2Al:CO_3$ -hyd in presence of acid-alcohol mixed solutions following the method adapted by Iyi *et al.* [22]. Briefly, 1 mmol of $Zn_2Al:CO_3$ was dispersed in 30 mL ethanol, then 1.986 mmol of strong acid (HCl, HNO_3 , $HClO_4$) present in 20 mL of ethanol solution was added, to avoid brutal contact between the solid and the acid thus limiting the dissolution of the LDHs. The whole exchange process was allowed to take place at 50°C for 1 hour under vigorous stirring and nitrogen (N_2) flow to promote a total exchange. The samples were then filtered on a Buchner funnel, washed with distilled water and finally dried in air at 80°C. The experimental conditions for these LDHs as well as those obtained by coprecipitation are reported in **Table 1**.

Table 1. Experimental conditions for the synthesis of M(II)Al(III) LDH powders together with their respective M(II)/Al(III) molar ratio determined by ICP-MS.

LDH sample	M(II)/Al(III) (theoretical)	Synthesis method	Hydrothermal treatment	M(II)/Al(III) determined by ICP
$Zn_2Al:CO_3$ -hyd	2	Coprecipitation	Yes	1.9
$Zn_2Al:CO_3$ -cop	2		No	1.9
$Zn_3Al:CO_3$	3	Coprecipitation	Yes	2.9
$Cu_2Al:CO_3$	2	Coprecipitation	Yes	2
$Ni_2Al:CO_3$	2	Coprecipitation	Yes	1.9
$Co_2Al:CO_3$	2	Coprecipitation	Yes	2
$Mg_2Al:CO_3$	2	Coprecipitation	Yes	2.1
$Zn_2Al:Cl$	2	Anion- exchange	-	1.9
$Zn_2Al:NO_3$	2	Anion- exchange	-	1.9
$Zn_2Al:ClO_4$	2	Anion- exchange	-	1.8

3. Characterization of LDH powders

3.1. Structural characterization

3.1.1. M(II)/Al(III) molar ratio determination by inductively coupled plasma mass spectroscopy

The M(II)/Al(III) molar ratios of all the prepared LDH powders evaluated by ICP-MS, were found to be very close to the expected values (**Table 1**). This implies that almost all the Al(III) ions are co-precipitated with the M(II) ions to obtain a solid with the stoichiometry of two or three M(II) atoms for each Al(III) atom, thus corresponding potentially to ideal arrangements of the M(II) and Al(III) cations in the brucite-like sheets [23].

3.1.2. Powder X-ray diffraction

Powder X-ray diffraction (PXRD) was performed on the different synthesized LDH samples in order to examine their structural features and to determine their crystallite sizes, expressed in terms of XRD coherent domains through the following Scherrer equation:

$$L = \frac{K \lambda}{\beta \cos\theta} \quad (1)$$

Where K is the Scherrer constant (0.9), λ is incident ray wavelength, β is the full width at half maximum in radians, and θ is the Bragg angle (rad) [24].

Figure 2 shows the PXRD patterns of the prepared LDH samples having the characteristic reflections of layered double hydroxides exhibiting a hexagonal lattice with rhombohedral 3R symmetry [25]. The low angle peak situated in the 2θ range 10° and 12° depending on the type of LDH is indexed to the (003) basal reflection, whereas the peak located at 2θ of approximately 60° is indexed to the (110) reflection. The unit cell lattice parameters a and c can be calculated from the position of these two peaks, with $a = 2d_{(110)}$ and $c = 3d_{(003)}$ [26].

The obtained parameters as well as the crystallite sizes $L_{(003)}$ and $L_{(110)}$, calculated as XRD coherent domains in directions perpendicular to the (003) and (110) planes respectively using Scherrer's formula (**Equation 1**), are presented in **Table 2**.

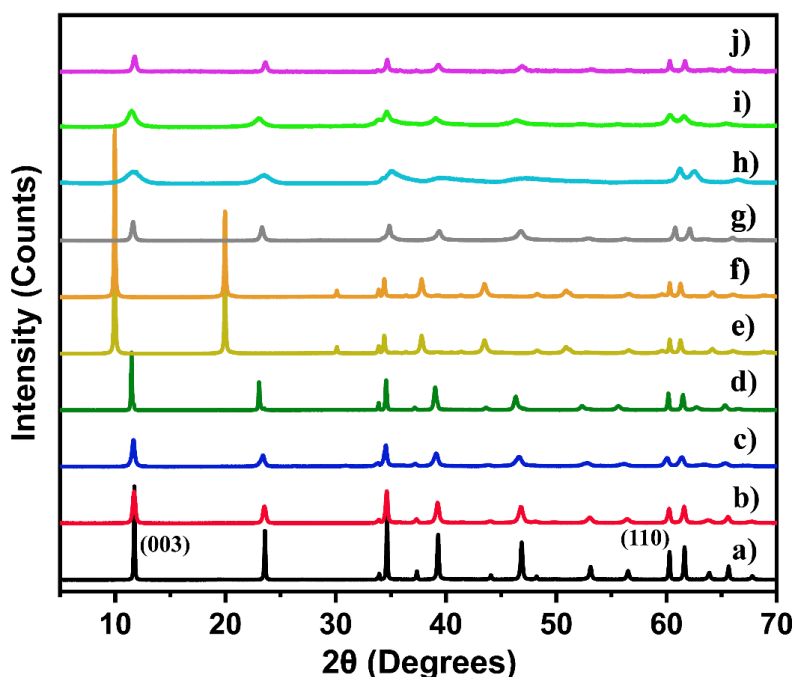


Figure 2. PXRD patterns of the different prepared LDH samples: a) $\text{Zn}_2\text{Al}:\text{CO}_3\text{-hyd}$, b) $\text{Zn}_2\text{Al}:\text{CO}_3\text{-cop}$, c) $\text{Zn}_3\text{Al}:\text{CO}_3$, d) $\text{Zn}_2\text{Al}:\text{Cl}$, e) $\text{Zn}_2\text{Al}:\text{NO}_3$, f) $\text{Zn}_2\text{Al}:\text{ClO}_4$, g) $\text{Mg}_2\text{Al}:\text{CO}_3$, h) $\text{Cu}_2\text{Al}:\text{CO}_3$, i) $\text{Ni}_2\text{Al}:\text{CO}_3$, j) $\text{Co}_2\text{Al}:\text{CO}_3$.

Slightly different lattice parameters of carbonate-intercalated LDH samples may be due to the different atomic radii of their constituent metals and their orientation within the LDH structure [27]. The values of the crystallite sizes $L_{(003)}$ and $L_{(110)}$ show that the prepared LDHs exhibit a relatively good crystallinity, with the exception for $\text{Cu}_2\text{Al}:\text{CO}_3$ sample. This was also shown in the PXRD pattern of $\text{Cu}_2\text{Al}:\text{CO}_3$ (presented in blue in **Figure 2**) which exhibited broader less intense diffraction peaks at (003) and (110) reflections caused by poor long-range ordering [28]. Such decrease in crystallinity could be actually attributed to the Jahn-Teller distortion effect of copper present in octahedral coordination [29].

The c parameter of carbonate-intercalated $\text{Zn}^{\text{II}}\text{-Al}^{\text{III}}$ LDHs were found to be very close to that found in the literature [30,31]. A slight difference could be noted between $\text{Zn}_2\text{Al}:\text{CO}_3\text{-hyd}$ and $\text{Zn}_2\text{Al}:\text{CO}_3\text{-cop}$. A similar change in c lattice parameter was reported by Kovanda *et al.*[32] and Benito *et al.*[33] who assigned the decrease in the interlamellar space of the LDH after exposing it to hydrothermal treatment to the strengthening of the interaction between the interlayer anions and the hydroxide layers. As suggested by **Figure 2**, the application of hydrothermal treatment had also resulted in an increase of the integral intensity of (003) and (110) diffraction lines. This

was associated with larger $L_{(003)}$ and $L_{(110)}$ crystallite sizes (**Table 2**), which also indicates an enhancement in the crystallinity of LDH phase in the treated sample and further ordering of the LDH crystal structure [32]. Such an effect of hydrothermal treatment on the crystallinity of the LDH samples is expected, where the application of hydrothermal treatment on hydrotalcites is mainly aimed to : (i) transform the small crystallites of the powders into larger more crystallized ones, (ii) transform amorphous precipitates into crystalline LDHs [25], or (iii) induce crystal rearrangement, thus decreasing the number of defects present in the crystals [34]. Miyata *et al.* had also reported a dramatic effect on the crystallite size induced by hydrothermal treatment of hydrotalcite compounds [35]. Actually, thermal treatment promotes the continuous dissolving of a significant part of the less thermodynamically stable particles obtained during the coprecipitation step, *i.e.*, small particles with high surface energy and amorphous phases, while the resulting dissolved species recrystallize again adding to and forming more stable crystals [36].

Table 2. Unit cell lattice parameters, interlamellar distance (d), $L_{(003)}$ and $L_{(110)}$ of the prepared LDH samples.

Sample	a (Å)	c (Å)	d (Å)	$L_{(003)}$ * (nm)	$L_{(110)}$ * (nm)
Zn ₂ Al:CO ₃ -hyd	3.06	22.59	7.53	69	60
Zn ₂ Al:CO ₃ -cop	3.07	22.65	7.55	27	32
Zn ₂ Al:Cl	3.07	23.1	7.7	46	32
Zn ₂ Al:NO ₃	3.07	26.61	8.87	45	31
Zn ₂ Al:ClO ₄	3.08	27.45	9.15	47	37
Zn ₃ Al:CO ₃	3.08	22.86	7.62	25	35
Cu ₂ Al:CO ₃	3.03	22.77	7.59	6	15
Ni ₂ Al:CO ₃	3.05	22.59	7.59	13	23
Co ₂ Al:CO ₃	3.05	22.56	7.52	23	37
Mg ₂ Al:CO ₃	3.06	22.77	7.59	25	29

* Crystallite sizes calculated as XRD coherent domains in directions perpendicular to (003) or (110) planes using Scherrer's formula.

Similarly, upon increasing the molar ratio of Zn(II)/Al(III) from 2 to 3, an increase in the lattice parameters a and c was observed (**Table 2**). The first is related to the larger ionic radius of zinc compared to that of aluminum resulting in lattice expansion along the ab -plane, whereas the second is attributed to the reduction of layer electrostatic charge in the Zn₃Al:CO₃ LDH leading to wider interlayer distance along the c -axis [37]. Moreover, the crystallite sizes $L_{(003)}$ and $L_{(110)}$ had town down by 3 and 2 times, respectively. In fact, it had been previously reported that an increase in

M(II)/M(III) molar ratio is usually associated with a reduction in crystallinity degree due to a decrease in layer charges [38].

Moreover, upon exchanging carbonate anions in $\text{Zn}_2\text{Al}:\text{CO}_3$ with other anions, the type of XRD patterns was unchanged, indicating that the product still kept the rhombohedral 3R symmetry [39]. However, the (003) peak was shifted to lower 2θ values compared with $\text{Zn}_2\text{Al}:\text{CO}_3$ LDH, revealing an increase in the crystal layer spacing c , following the order:



The evolution of the c lattice parameter with the change in nature of intercalated anion is in agreement with those reported for hydrotalcite-like compounds [40,41], thus indicating the success of the anion exchange reactions. The interlamellar distance is actually related to the size, charge and orientation of the corresponding intercalated anions within the layers [26].

The effect of anion exchange of CO_3^{2-} with the other intercalating anions on the crystallinity of Zn_2Al LDHs had been also investigated. The results shown in **Table 2** provide an evidence about the sensitivity of the crystallinity of LDHs toward anion exchange reactions, where the crystallite sizes $L_{(003)}$ and $L_{(110)}$, had decreased by almost 1.5 times upon exchanging carbonate anions with chloride, nitrate and perchlorate. However, no remarkable difference between the crystallite sizes of LDHs intercalated with Cl^- , NO_3^- and ClO_4^- was detected. We can thus assume that the exchange reactions of carbonate-intercalated LDHs, had led to a reduced crystallinity as a result of mechanical fragmentation of the crystallites rather than dissolution/recrystallization [42]. In fact, anion exchange reactions in layered double hydroxides may involve the breakage of the electrostatic interactions as well as the hydrogen bonds between the hydroxide layers and the outgoing anion and the reformation of these bonds with the incoming anions [43]. This maybe a reasonable explanation of the reduced crystallite sizes for Zn(II)Al(III) LDHs obtained from anion-exchange reactions.

3.1.3. InfraRed and Raman spectroscopies

The purity of all the carbonate-intercalated LDH powders was also checked out by InfraRed (IR) and Raman spectroscopies, where no additional vibration bands assigned to amorphous phases have been detected (**Figure 3** and **Figure 4**).

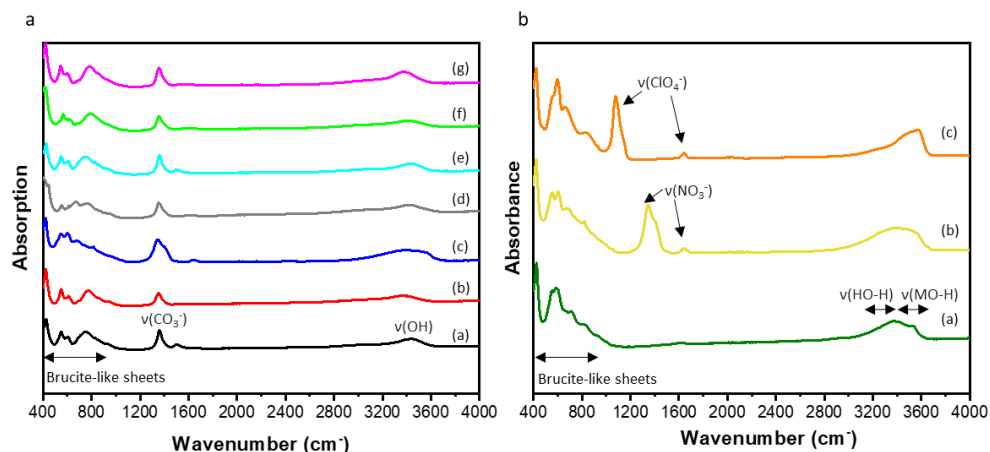


Figure 3. a) InfraRed spectra of carbonate-intercalated LDHs: (a) $\text{Zn}_2\text{Al}:\text{CO}_3\text{-hyd}$, (b) $\text{Zn}_2\text{Al}:\text{CO}_3\text{-cop}$, (c) $\text{Zn}_3\text{Al}:\text{CO}_3$, (d) $\text{Mg}_2\text{Al}:\text{CO}_3$, (e) $\text{Cu}_2\text{Al}:\text{CO}_3$, (f) $\text{Ni}_2\text{Al}:\text{CO}_3$, (g) $\text{Co}_2\text{Al}:\text{CO}_3$. b) InfraRed spectra of chloride-, nitrate- and perchlorate intercalated LDHs. (a) $\text{Zn}_2\text{Al}:\text{Cl}$, (b) $\text{Zn}_2\text{Al}:\text{NO}_3$, (c) $\text{Zn}_2\text{Al}:\text{ClO}_4$.

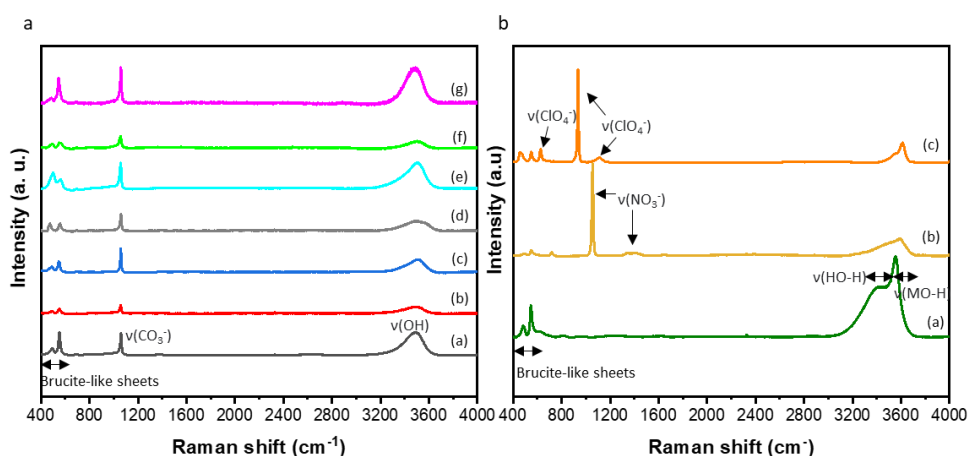


Figure 4. a) Raman spectra of carbonate-intercalated LDHs: (a) $\text{Zn}_2\text{Al}:\text{CO}_3\text{-hyd}$, (b) $\text{Zn}_2\text{Al}:\text{CO}_3\text{-cop}$, (c) $\text{Zn}_3\text{Al}:\text{CO}_3$, (d) $\text{Mg}_2\text{Al}:\text{CO}_3$, (e) $\text{Cu}_2\text{Al}:\text{CO}_3$, (f) $\text{Ni}_2\text{Al}:\text{CO}_3$, (g) $\text{Co}_2\text{Al}:\text{CO}_3$. b) Raman spectra of chloride-, nitrate- and perchlorate intercalated LDHs: (a) $\text{Zn}_2\text{Al}:\text{Cl}$, (b) $\text{Zn}_2\text{Al}:\text{NO}_3$, (c) $\text{Zn}_2\text{Al}:\text{ClO}_4$.

The successful intercalation of Cl^- , NO_3^- and ClO_4^- could also be affirmed by examining the IR and Raman spectroscopy spectra of $\text{Zn}_2\text{Al}:\text{Cl}$, $\text{Zn}_2\text{Al}:\text{NO}_3$ and $\text{Zn}_2\text{Al}:\text{ClO}_4$ (Figure 3b and Figure 4b), which comes in good agreement with the XRD results.

3.2. Morphological and textural characterizations

3.2.1. Scanning electron microscopy

Scanning electron microscopy (SEM) was used to determine the morphology and the average lateral particle sizes of Zn(II)Al(III) and Cu(II)Al(III) LDH samples.

As shown in **Figure 5**, Zn₂Al:CO₃-hyd and Zn₂Al:CO₃-cop as well as Zn₃Al:CO₃ LDH samples adopt a “cauliflower-like” morphology, very similar to that reported by Scarpellini *et al.* [44]. The scaled samples exhibited distinct platelet-like particles in a high degree of agglomeration, which is a well-known characteristic of LDHs [45].

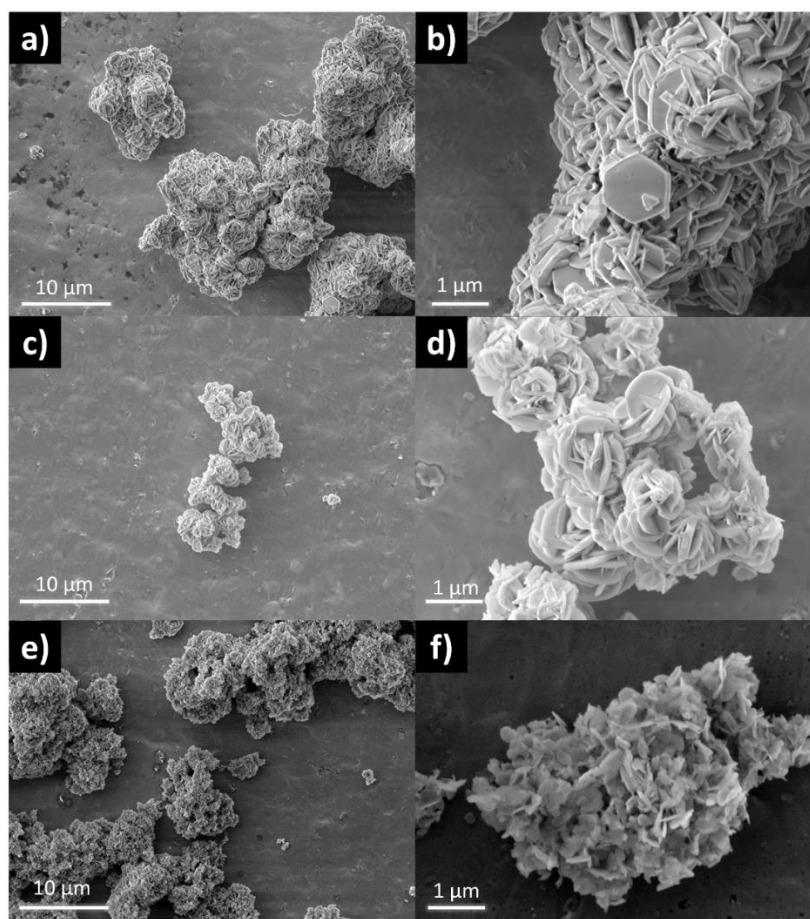


Figure 5. SEM micrographs of: a,b)Zn₂Al:CO₃-hyd, c,d) Zn₂Al:CO₃-cop, e,f) Zn₃Al:CO₃.

In the absence of any hydrothermal treatment, the platelets hexagonal geometry of Zn₂Al:CO₃-cop was less sharp and defined (**Figure 5c, d**) than that of Zn₂Al:CO₃-hyd. This highlights the lower crystallinity of the particles of Zn₂Al:CO₃ unexposed to any hydrothermal treatment. However, the

lateral particle size of hydrothermally treated $\text{Zn}_2\text{Al}:\text{CO}_3$ (1050 ± 130 nm) was only slightly larger than that of the hydrothermally untreated sample (821 ± 112 nm). Thus, the larger crystallite size for $\text{Zn}_2\text{Al}:\text{CO}_3$ -hyd did not lead to significant changes on the particle size at the micrometric range. In fact, it has been previously reported that the lateral size of LDHs prepared directly by coprecipitation without further hydrothermal treatment was almost the same as that of LDHs subsequently exposed to hydrothermal treatment, although their coherent crystallite domains were more than two times greater that of hydrothermally treated LDH [46].

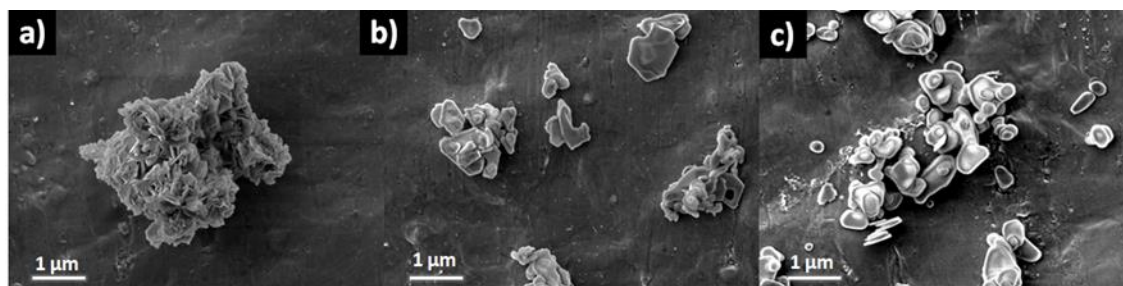


Figure 6. SEM micrographs of: a) $\text{Zn}_2\text{Al}:\text{Cl}$, b) $\text{Zn}_2\text{Al}:\text{NO}_3$, c) $\text{Zn}_2\text{Al}:\text{ClO}_4$.

On the other hand, the SEM micrographs of $\text{Zn}_3\text{Al}:\text{CO}_3$ hexagonal platelets having an average lateral size of 415 ± 45 nm, was much smaller and the particles were less defined than those of $\text{Zn}_2\text{Al}:\text{CO}_3$. In this case, the reduction in the average lateral size is in good agreement with the reduced coherent size of $\text{Zn}_3\text{Al}:\text{CO}_3$ (**Table 2**).

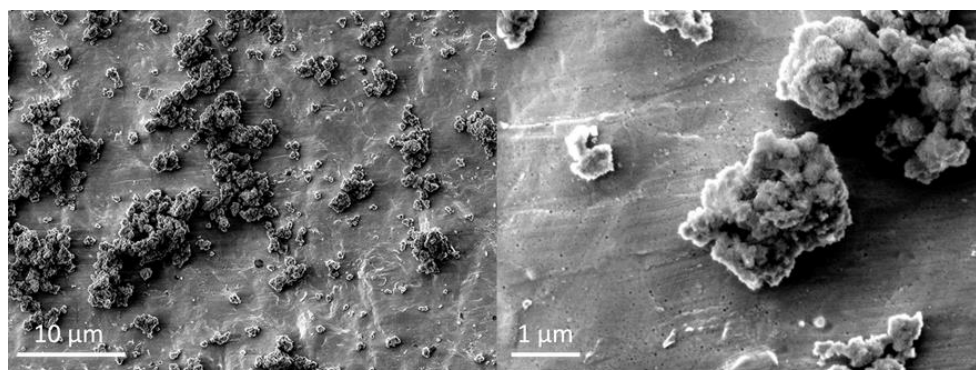


Figure 7. SEM micrographs of $\text{Cu}_2\text{Al}:\text{CO}_3$ LDH.

Upon exchanging carbonate anions in $\text{Zn}_2\text{Al}:\text{CO}_3$ -hyd with chloride, nitrate and perchlorate anions a remarkable change in the morphology and aggregate size was observed (**Figure 6**). The generation of defects in anion-exchanged powders, especially for $\text{Zn}_2\text{Al}:\text{NO}_3$ and $\text{Zn}_2\text{Al}:\text{ClO}_4$, comes in line with the reduced crystallite sizes (**Table 2**), and suggests again the occurrence of

mechanical fragmentation of the crystallites in an ion exchange reaction rather than dissolution/recrystallization [42].

Figure 7 shows the morphology of $\text{Cu}_2\text{Al}:\text{CO}_3$ exhibiting small globular distorted crystallites with uncertain length, similar to that of CuMgAl LDH obtained by Oliveira *et al.* [19]. In general, the synthesis of LDH containing Cu(II) as the only divalent metal is somehow difficult due to the Jahn teller distortion phenomena [47] which may had led to a distortion and presence of defects in its structure, as suggested by its PXRD pattern (**Figure 2(h)**).

3.2.2. Specific surface area and particle size distribution

The dissolution behavior of LDHs is considered as a surface-controlled reaction which is expected to be highly determined by their particle size [48]. For this reason, the specific surface area and particle size distribution of the synthesized different Zn(II)Al(III) LDHs were studied by BET approach and Laser Diffraction, respectively.

Table 3. Specific surface area determined by BET , D_{v50} and $D_{[3, 2]}$ determined by PSD for the different prepared Zn(II)Al(III) LDH samples.

Sample	S_{BET} (m^2/g)	D_{v50} (μm)	$D_{[3, 2]}$ (μm)
$\text{Zn}_2\text{Al}:\text{CO}_3\text{-hyd}$	6.2	13.7	13.2
$\text{Zn}_2\text{Al}:\text{CO}_3\text{-cop}$	19	9.6	5.2
$\text{Zn}_3\text{Al}:\text{CO}_3$	13.3	9.4	7.3
$\text{Zn}_2\text{Al}:\text{Cl}$	16.7	8.4	6.4
$\text{Zn}_2\text{Al}:\text{NO}_3$	22.5	3.1	2.6
$\text{Zn}_2\text{Al}:\text{ClO}_4$	24.8	1.7	1.5

Brunauer–Emmett–Teller theory (BET) provides a suitable method to measure specific surface area of LDH powders which is directly linked to their sizes. Moreover, particle size distribution (PSD) also gives information about the LDH particle sizes, which usually are aggregates of crystallites [49]. The D_{v50} is the volume median diameter which divides the population exactly into two equal halves, whereas the $D_{[3, 2]}$ is the surface area mean diameter, which is more relevant when specific surface area is important, *e.g.*, bioavailability, reactivity and dissolution [50]. The specific surface areas of ZnIIAl(III) LDHs determined by BET (S_{BET}), D_{v50} and $D_{[3, 2]}$ values are reported in **Table 3**.

Compared to $\text{Zn}_2\text{Al}:\text{CO}_3\text{-hyd}$ LDH sample, which showed a monomodal narrow size distribution of particle aggregates having a median diameter of $13.7\ \mu\text{m}$ (**Figure 8a**), $\text{Zn}_2\text{Al}:\text{CO}_3\text{-cop}$ showed a bimodal size distribution composed of both individual particles and aggregates with broader size distribution having an average median size of $9.6\ \mu\text{m}$ (**Figure 8b**). The larger size and narrow particle distribution of $\text{Zn}_2\text{Al}:\text{CO}_3\text{-hyd}$ sample could be explained by the aging in hydrothermal conditions which leads to recrystallization and Ostwald ripening processes [48]. Additionally, the larger S_{BET} and smaller $D_{[3, 2]}$ for $\text{Zn}_2\text{Al}:\text{CO}_3\text{-cop}$ supported such results. The reduction of the surface area of LDHs subsequently exposed to a hydrothermal treatment could be attributed to the recrystallization of small crystallites and amorphous particles and subsequent increase of the LDH crystallite size [32], which is also confirmed by our XRD and SEM results presented in **Figure 2** and **Figure 5**, respectively.

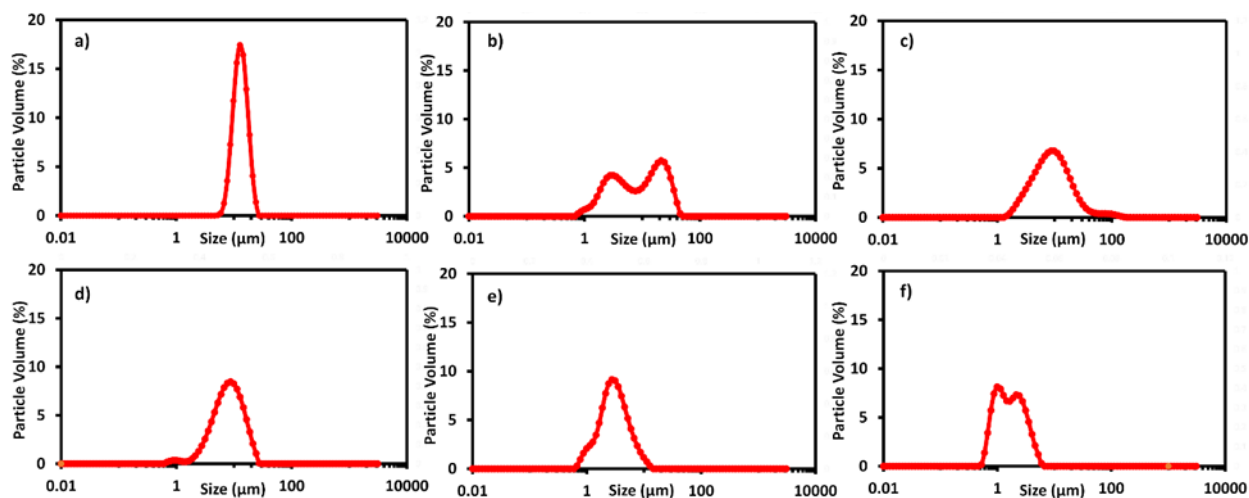


Figure 8. Particle Size Distribution (PSD) curves in water dispersion of: a) $\text{Zn}_2\text{Al}:\text{CO}_3\text{-hyd}$, b) $\text{Zn}_2\text{Al}:\text{CO}_3\text{-cop}$, c) $\text{Zn}_3\text{Al}:\text{CO}_3$, d) $\text{Zn}_2\text{Al}:\text{Cl}$, e) $\text{Zn}_2\text{Al}:\text{NO}_3$, and f) $\text{Zn}_2\text{Al}:\text{ClO}_4$.

On the other hand, upon increasing the molar ratio of $\text{Zn(II)}/\text{Al(III)}$ from 2 to 3, the LDH powder showed a broader particle size distribution. $\text{Zn}_3\text{Al}:\text{CO}_3$ exhibited a monomodal distribution similar to that of $\text{Zn}_2\text{Al}:\text{CO}_3$, yet with a short arm located at around $100\ \mu\text{m}$ and a smaller aggregated particles fraction ($\sim 27\%$) in the range of $1.5\text{-}5\ \mu\text{m}$ (**Figure 8c**), which was absent in the case of $\text{Zn}_2\text{Al}:\text{CO}_3\text{-hyd}$.

Similarly, upon exchanging carbonate anions in $\text{Zn}_2\text{Al}:\text{CO}_3$ with other intercalating anions, *i.e.*, Cl^- , NO_3^- , and ClO_4^- , a significant fraction of smaller agglomerates and/or individual particles appeared (**Figure 8d,e,f**). Such decrease in agglomeration degree imposed by anionic exchange

reactions could also be seen through the SEM micrographs presented in **Figure 6**. This was also associated with a remarkable increase in S_{BET} and smaller D_{V50} and $D_{[3,2]}$ sizes, especially for the nitrate and perchlorate intercalated samples (**Table 2**).

4. Influence of different physicochemical parameters on the constituent divalent metal release from LDHs in broth culture media

The partial dissolution of all the synthesized LDH powders (10 mg/ml) into Al^{3+} and their constituent divalent metals (M^{2+}) was studied after 48 h of incubation at $37^{\circ}C$, in Lysogeny Broth (LB, pH= 6.7) and Tryptic Soy Broth (TSB, pH= 7), growth media of Gram-negative *Escherichia coli* and Gram-positive *Staphylococcus aureus* bacteria, respectively.

The negative blanc tests of pure LB and TSB media ensured that the media where the study had taken place did not contain any amounts of Al^{3+} or any other divalent metal included in the study, *i.e.*, Zn^{2+} , Cu^{2+} , Ni^{2+} , Co^{2+} , Mg^{2+} , prior to the addition of LDH powders.

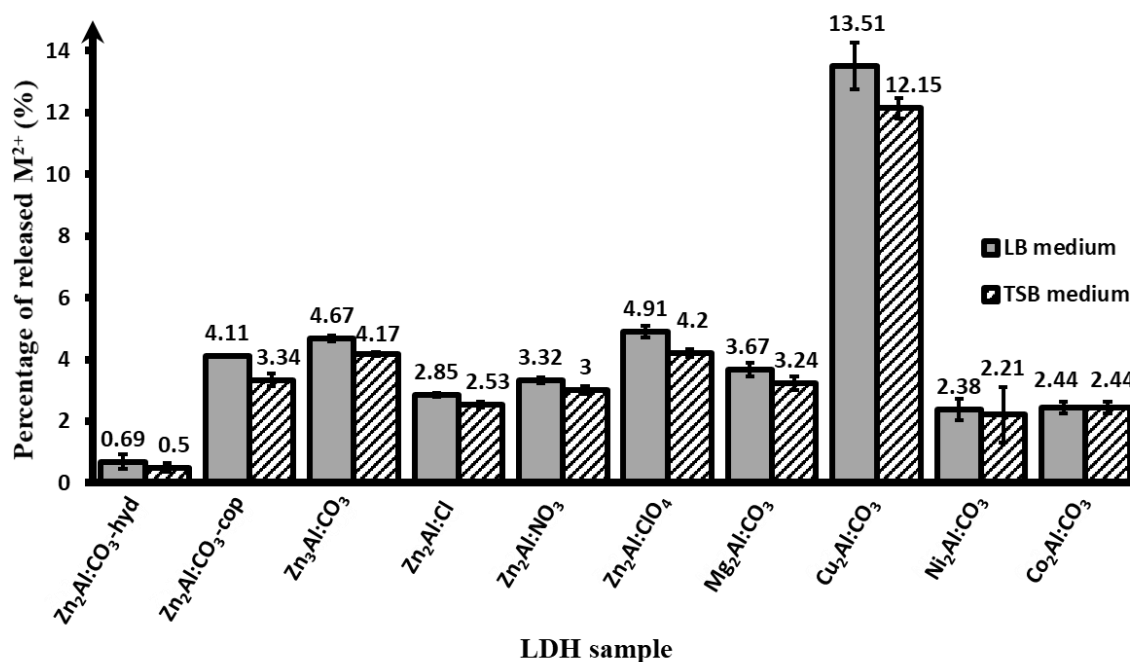


Figure 9. Partial dissolution profiles of all synthesized LDH samples into M^{2+} in LB and TSB media, in terms of average percentage compared to the initial amount present in the LDH.

In this study, the dissolution of LDHs into their constituent divalent metals was uniquely considered, since the dissolution of Al^{3+} in both LB and TSB media was below the detection point for all the tested samples. In fact, Peng *et al.* had previously shown that only divalent cations were released from LDH powders into the biological α -Minimum Essential Medium (α -MEM), whereas soluble trivalent cations (Al^{3+} and Fe^{3+}) were not released [14]. Jobbágy *et al.* also reported that the dissolution of Al^{3+} out of chloride-intercalated Mg(II)Al(III) LDH was below the limit of detection in the pH range of 5-9, and only leaching of Mg^{2+} was observed [51].

Table 4. Partial dissolution profiles of all synthesized LDH samples into M^{2+} in distilled water, in terms of average percentage compared to the initial amount present in the LDH.

LDH sample	Percentage of released M^{2+} (%)
$\text{Zn}_2\text{Al:CO}_3\text{-hyd}$, $\text{Zn}_2\text{Al:CO}_3\text{-cop}$, $\text{Zn}_3\text{Al:CO}_3$, $\text{Zn}_2\text{Al:Cl}$, $\text{Zn}_2\text{Al:NO}_3$, $\text{Zn}_2\text{Al:ClO}_4$, $\text{Cu}_2\text{Al:CO}_3$, $\text{Ni}_2\text{Al:CO}_3$, $\text{Co}_2\text{Al:CO}_3$, $\text{Mg}_2\text{Al:CO}_3$	Below detection point

Therefore, the percentage of the released divalent metal ions in LB and TSB media relative to the amount of constituent divalent metal initially present in the LDH powders was evaluated by ICP-MS (Figure 9). The average percentage of M^{2+} out of M(II)Al(III) LDHs was calculated as the mean value obtained for at least 3 independent experiments.

Control partial dissolution experiments of the synthesized LDH powders were also done in Milli-Q distilled water having a pH of 6.98 very close to that of LB and TSB, where the release of both divalent and trivalent metals was below the detection point for all the LDH samples (Table 4). Such behavior could provide an evidence that the chemical species contained in LB and TSB broth are able to increase the solubility of LDHs by the formation of complex species with their constituent divalent metal. In fact, several studies have previously shown that the solubility and metal release from zinc oxide (ZnO) powders was greatly enhanced in biological complex media as LB, TSB and MH (Mueller Hinton) broths, which may be due to the ability of zinc present in the powder to react with amino acids and proteins to form complex organometallic compounds [52–54]. In the present case, proteins and amino acids present in LB and TSB liquid broths were probably the chemical species that might formed complexes with M^{2+} ions and provided a superior dissolution of the powders compared to that obtained in distilled water.

Furthermore, in order to ensure that thermodynamic equilibrium was reached within 48 hours of LDH dispersion incubation, the evolution of Zn^{2+} released from $Zn_2Al:CO_3$ -hyd and $Zn_2Al:CO_3$ -cop was monitored over time. As suggested by **Figure 10**, thermodynamic equilibrium was reached for $Zn_2Al:CO_3$ -hyd and $Zn_2Al:CO_3$ -cop within 8 and 6 hours, respectively. The faster release profile in $Zn_2Al:CO_3$ -cop was probably due to the presence of a significant fraction of smaller particles/agglomerates (**Figure 8**) which had provided a larger exposed surface area in contact with the dissolution media, thus promoting greater release of Zn^{2+} in aqueous broth solutions [48].

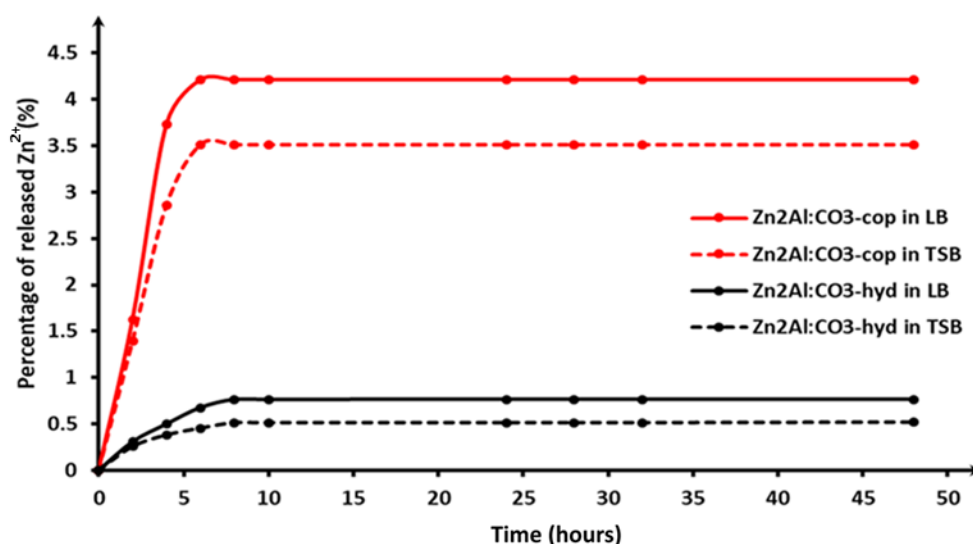


Figure 10. Kinetic dissolution profiles of $Zn_2Al:CO_3$ -hyd and $Zn_2Al:CO_3$ -cop into Zn^{2+} in LB and TSB media.

4.1. Influence of the nature constituent divalent metal on the release profile of M^{2+}_{aq}

In order to examine the relationship between the constituent divalent metal M(II) of carbonate-intercalated LDHs and their dissolution properties, different LDHs having a molar ratio of M(II)/Al(III) of 2 were synthesized coprecipitation method followed by a hydrothermal treatment at 80°C for 24 hours. The intercalated anion in all these LDH samples was CO_3^{2-} , and the divalent metal was changed accordingly: M(II)= Zn, Mg, Cu, Ni, or Co.

According to **Figure 9**, the partial dissolution profile of $M_2Al:CO_3$ LDHs into M^{2+} in both LB and TSB media followed the following trend:



Table 5 provides the relative pK_{sp} values of the different divalent metal hydroxides counterparts of the different synthesized LDH samples. In fact, Bocclair *et al.* had previously related the relative stabilities of LDHs to their corresponding metal hydroxides [55]. That is for a given M^{2+} cation, the higher the solubility of $M(\text{OH})_2$, the less stable its corresponding LDH is. Thus, the partial dissolution profiles of $M(\text{II})\text{Al}(\text{III})$ LDHs into M^{2+} in LB and TSB media was correlated to that of their $M(\text{OH})_2$ counterparts.

Table 5. pK_{sp} values for $M(\text{OH})_2$ reported by [56].

Metal hydroxide	pK_{sp}
Zn(OH) ₂	15.7
Cu(OH) ₂	18.6
Ni(OH) ₂	14.7
Co(OH) ₂	14.8
Mg(OH) ₂	10.8

Our results agreed well with the proposed hypothesis by Bocclair *et al.*, by which lower dissolution is observed with increasing $M(\text{OH})_2$ pK_{sp} values. The dissolution driving force is dictated by thermodynamics, and the solubility of LDHs varies according to the nature of the constituent metal ions. One sole exception was noted in the case of $\text{Cu}_2\text{Al}:\text{CO}_3$ LDH which seemed to be highly unstable thus generating an amplified release of Cu^{2+} although $\text{Cu}(\text{OH})_2$ exhibited lower solubility compared to those of the other studied divalent metals. This surprising result, may be attributed to the poor crystallinity of $\text{Cu}_2\text{Al}:\text{CO}_3$ (**Figure 2(h)**), very small crystallite sizes ($L_{(003)} \approx 6\text{nm}$ and $L_{(110)} \approx 15\text{nm}$), and its distorted very irregular structure revealed by its SEM micrographs (**Figure 7**), thus indicating the presence of defects due to Jahn Teller distortion phenomena. Another possible explanation could be the behavior of copper LDHs in the broth media itself. The solubility values obtained previously for LDHs refer to the dissolution behavior of LDHs in distilled water. The experiments done here are performed in LB and TSB biological broth culture media having a complex compositional structure. Therefore, the enhanced release of Cu^{2+} out of $\text{Cu}_2\text{Al}:\text{CO}_3$ LDH sample may be related to its tendency to form complex organometallic compounds with component of the broth culture media.

4.2. Influence of crystallinity on the release profile of $\text{Zn}^{2+}_{\text{aq}}$

The application of a post-synthetic hydrothermal treatment is an important step evaluated in this study for obtaining Zn_2AlCO_3 LDH samples having different crystallinities: $\text{Zn}_2\text{Al:CO}_3\text{-hyd}$ and $\text{Zn}_2\text{Al:CO}_3\text{-cop}$. Both samples were prepared using the same experimental procedures, where the only difference was the application of a hydrothermal treatment for $\text{Zn}_2\text{Al:CO}_3\text{-hyd}$, while $\text{Zn}_2\text{Al:CO}_3\text{-cop}$ was not exposed to any post-synthetic treatment procedure. Subsequently, the two LDHs possessed different structural and textural properties, where $\text{Zn}_2\text{Al:CO}_3\text{-cop}$ exhibited lower crystallinity revealed by their smaller crystallite sizes (**Table 2**), larger surface area, smaller median size and surface area mean of agglomerates (**Table 3**) than those of the treated one.

The crystallinity effect on the stability and dissolution properties of LDHs was studied by evaluating the amount of released Zn^{2+} from hydrothermally treated and untreated $\text{Zn}_2\text{Al:CO}_3$ LDH samples in LB and TSB media. It could be noticed from **Figure 9**, that the dissolution of Zn^{2+} in both samples was slightly higher in LB medium than TSB. This might be simply attributed to the difference in nature and composition of the biological growth media, in addition to the slightly lower pH of LB (6.63) compared to that of TSB (6.97), where it is known that the solubility of LDHs is highly pH-dependent and their dissolution accelerates with increasing acidity [57].

In both media, the amount of the leached Zn^{2+} out of $\text{Zn}_2\text{Al:CO}_3\text{-cop}$ was enhanced by almost 6 times in comparison to that of $\text{Zn}_2\text{Al:CO}_3\text{-hyd}$. Such result is consistent with that of Hibino, who found out that the release of Mg^{2+} out of lower crystallinity Mg(II)Al(III) LDH directly obtained after co-precipitation higher than that of the same LDH subsequently exposed to hydrothermal treatment [46].

Therefore, the lower crystallinity of Zn(II)Al(III) LDH as well as their smaller aggregated sizes and larger surface area promotes the release of more Zn^{2+} ions in broth culture media.

4.3. Influence of Zn(II)/Al(III) molar ratio on the release profile of $\text{Zn}^{2+}_{\text{aq}}$

The impact of M(II)/M(III) molar ratio on divalent metal dissolution capacity of LDHs was another important parameter investigated in our study. Such influence was examined by comparing the partial dissolution profiles of Zn^{2+} of the two prepared LDH samples: $\text{Zn}_2\text{Al:CO}_3\text{-hyd}$ and

$\text{Zn}_3\text{Al}:\text{CO}_3$ having a Zn(II)/Al(III) molar ratio of 2 and 3, respectively. The two samples were prepared using a similar coprecipitation experimental procedure followed by a hydrothermal treatment at 80°C .

As shown in **Figure 9**, the partial dissolution profiles of Zn^{2+} increases significantly by about 7 and 8 times in LB and TSB media respectively, when the molar ratio of Zn(II)/Al(III) was increased from 2 to 3.

It is worth mentioning here that the crystallinity of these samples and the particles/agglomerates sizes as well their surface areas were not the same for these two samples. The crystallite sizes determined by XRD (**Table 2**) were reduced by at least two times upon increasing the Zn(II)/Al(III) molar ratio. It was actually noticed in the previous section that the crystallinity of LDHs could play an important role on their dissolution behavior, where the solubility of LDHs in aqueous solutions was expected to be enhanced as their crystallinity decreases (**Section 4.2**).

Thus, the higher dissolution behavior presented in $\text{Zn}_3\text{Al}:\text{CO}_3$ could be either assigned to its higher zinc content initially present in the structure, or to its lower crystallinity, or to the combined effect of these two factors.

4.4. Influence of intercalated-anion on the release profile of $\text{Zn}^{2+}_{\text{aq}}$

The influence of intercalating four different interlayer anions: CO_3^{2-} , Cl^- , NO_3^- and ClO_4^- in Zn(II)Al(III) LDH layers, on their partial dissolution into Zn^{2+} ions was investigated. The partial dissolution profiles of these LDHs (**Figure 9**), prove that changes in the nature and composition of the anion in the hydrotalcite interlayer region exhibited an important effect on the solubility of Zn(II)Al(III) LDHs. For instance, the release of Zn^{2+} increases by about 4 times in LB medium upon exchanging carbonate anions with chloride and nitrate ones, and 6 times in case of perchlorate compared to carbonate intercalated sample within the same LB medium.

Another important point to note here is that the difference in the dissolution behavior in LB and TSB media, having slightly different pH, is more pronounced in case of carbonate intercalated Zn_2Al LDH than other samples having other intercalated anions. This could be explained by the urge to protonate both hydroxyl groups and carbonate anions in order for the dissolution to occur

in carbonate intercalated LDH [46], thus making $Zn_2Al:CO_3$ LDH sample more sensitive to the pH of the aqueous media.

It is also remarkable that the increasing solubility of LDHs here followed the same trend as that of the value of c parameter obtained by XRD (**Section 3.1.2**), and the opposite trend to that of the order of affinity of LDHs toward intercalating anions previously described in the literature [58,59]:



Thus, one could conclude that the lower the affinity of the intercalated anion toward the Zn_2Al LDH structure, the lower the stability of the LDH in broth media.

In fact, some previous studies showed that the dissolution of LDHs was strongly dependent on the type of intercalated anion, where Baek *et al.* reported that chloride intercalated $Mg(II)Al(III)$ LDH was less stable and released more magnesium ions than carbonate intercalated $Mg(II)Al(III)$ LDH in simulated body conditions [60]. Other theoretical thermodynamic study had also shown that NO_3^- intercalated hydrotalcites were more soluble than CO_3^{2-} intercalated ones and even small amounts of carbonate could change the solubility of a nitrate phase by several orders of magnitude [61].

However, one important parameter neglected by these studies [60,61], is the difference in crystallinity and the structure of the LDHs having different intercalated anions. As previously mentioned in **Section 3.1.2**, exchanging carbonate anions in Zn_2Al LDHs with other anions less favored by the LDH structure promoted a remarkable decrease in the crystallinity of the latter associated with a decrease in aggregate sizes (**Table 2**) and generation of defects in the structure (**Figure 6**).

Therefore, the poor crystallinity and presence of defects is a first explanation for the higher dissolution of LDHs obtained by anion exchange. The second one is the nature of intercalated anion itself, which may weaken the binding between the metal cations and the layers, thus promoting higher dissolution behavior.

5. LDH structure after exposition to culture media

As compared to distilled water, the partial dissolution of LDHs into their constituent divalent metals was much more pronounced. Therefore, it is of great importance to assure that the LDH structure is conserved when LDHs are present in such culture media during the tested exposition time (48h). LB and TSB media are rich in different components including proteins, amino acids and phosphates. Thus, it is also important to determine whether the intercalated anion in the LDH is exchanged during the exposition period (48 h) with other anions, *e.g.*, phosphates, contained in the culture media. Moreover, it is well known that LDHs have higher affinities toward intercalating carbonate anions, thus it is also essential to determine that chloride-, nitrate- and perchlorate- anions are not exchanged with carbonates anions as well. For these reasons, XRD analysis was carried out on Zn(II)Al(III) LDHs after the powders were recovered from the exposition to TSB medium for 48 h.

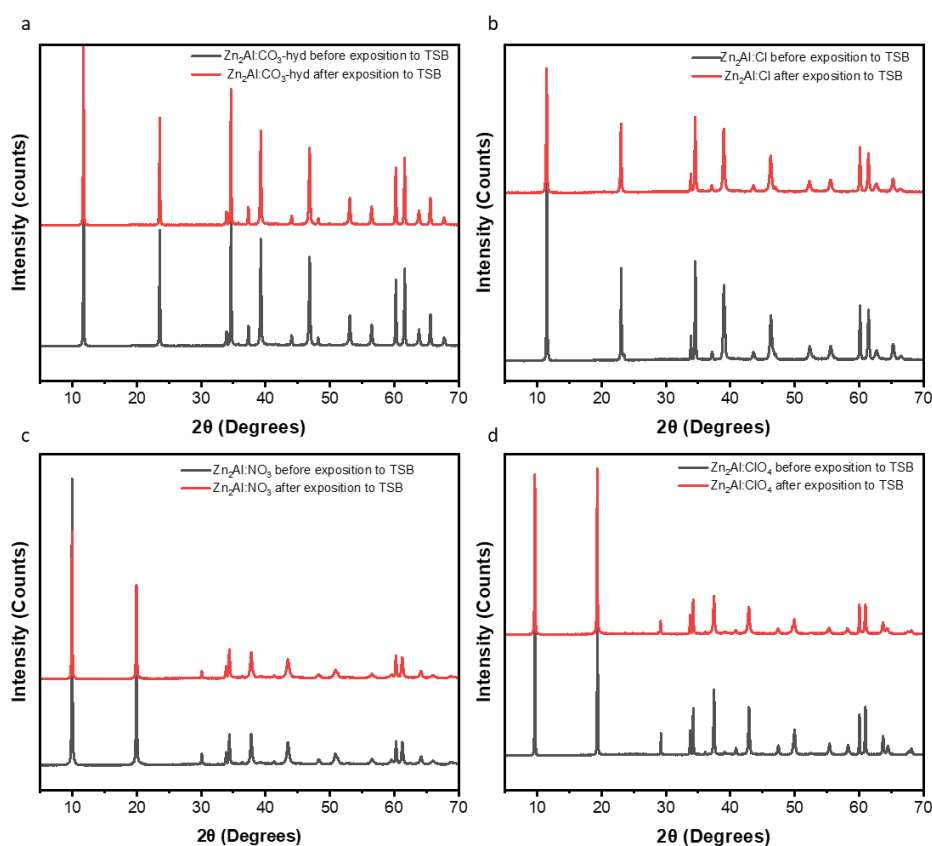


Figure 11. PXRD diffraction patterns of: a) $\text{Zn}_2\text{Al}:\text{CO}_3$, b) $\text{Zn}_2\text{Al}:\text{Cl}$, c) $\text{Zn}_2\text{Al}:\text{NO}_3$ and d) $\text{Zn}_2\text{Al}:\text{ClO}_4$ LDHs, before and after being exposed to TSB for 48 h.

No remarkable difference was observed for LDH samples after being exposed to TSB culture medium for 48 h (**Figure 11**), suggesting that the LDH structure is conserved in broth culture media. Additionally, the intercalating anion inside the LDH interlayer was conserved as well. This indicates that no anion-exchange reaction took place in broth media neither with the compositional anions present in TSB media nor with carbonate anions. The morphology of the chloride-, nitrate- and perchlorate-intercalated Zn(II)Al(III) LDHs after being exposed to TSB medium (**Figure 12**) was also similar to the initial one observed before the exposition (**Figure 6**), thus supporting the results of XRD obtained after incubation in TSB after 48 h. Such findings assure that the enhanced release behavior of Zn^{2+} out of $Zn_2Al:Cl$, $Zn_2Al:NO_3$ and $Zn_2Al:ClO_4$ is not related to the possibility of any change in structure imposed by the exposition in broth media, but rather to their initial physico-chemical properties, *i.e.*, stability of LDHs in accordance to the nature of intercalating anion, crystallinity and particle/agglomerate sizes.

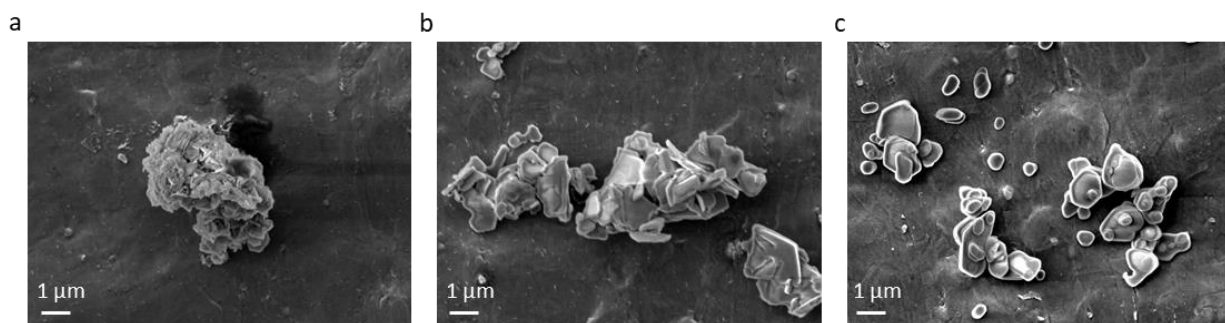


Figure 12. SEM micrographs of: a) $Zn_2Al:Cl$, b) $Zn_2Al:NO_3$, c) $Zn_2Al:ClO_4$, after being exposed to TSB medium for 48 h.

6. Antibacterial activity of LDHs

The antibacterial activities of the different prepared LDH samples were tested against both Gram-positive and Gram-negative bacterial strains, *S. aureus* and *E. coli* respectively, using the agar disk diffusion method. Bacterial inoculums were spread on TSB and LB Petri agar dishes to obtain a homogeneous continuous layer of bacteria. After that, LDH suspensions (10 mg/mL) were loaded on a filter disc placed on defined areas on the Petri dish. The diameter of the generated inhibition zone induced by the LDH suspension was then measured using a centimeter rule to determine the bacterial inhibition efficiency by the tested LDHs (**Figure 13**). A similar procedure was followed to investigate the antimicrobial activity of metallic salts counterparts having a molar concentration

similar to the average released concentration of metallic cations out of their LDH samples counterparts. The obtained inhibition zone diameters for the all the synthesized LDH samples and ion salts counterparts against *S. aureus* and *E. coli* are presented in **Figure 14**.

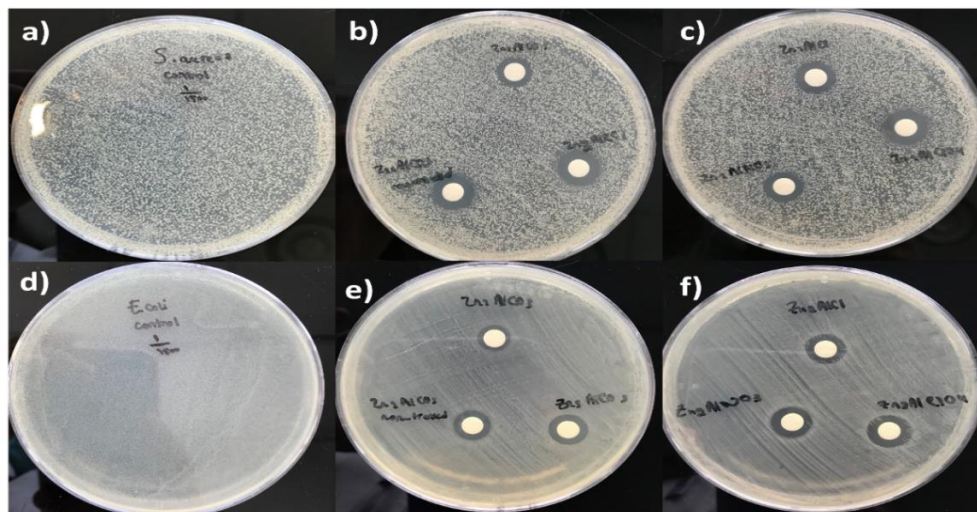


Figure 13. Antibacterial agar disk diffusion tests against: a) *S. aureus* control, b) *S. aureus* using Zn₂Al:CO₃-hyd (top), Zn₂Al:CO₃-cop (bottom left) and Zn₃Al:CO₃ (bottom right), c) *S. aureus* using Zn₂Al:Cl (top), Zn₂Al:NO₃ (bottom left) and Zn₂Al:ClO₄ (bottom right), d) *E. coli* control, e) *E. coli* using Zn₂Al:CO₃-hyd (top), Zn₂Al:CO₃-cop (bottom left) and Zn₃Al:CO₃ (bottom right), f) *E. coli* using Zn₂Al:Cl (top), Zn₂Al:NO₃ (bottom left) and Zn₂Al:ClO₄ (bottom right).

The minimum inhibitory concentration (MIC) of the prepared LDHs was also evaluated using the microdilution turbidimetric method, where LDHs were added in different concentrations (diluted in two-fold) into a bacterial inoculum of fixed optical density (OD₆₀₀=0.1). The MIC value for each LDH sample was recognized as the lowest concentration that had no visible turbidity. The obtained MIC samples are reported in **Table 6**.

Table 6. MIC values of different LDH samples against *E. coli* and *S. aureus*.

LDH sample	Tested bacteria	
	<i>E. coli</i>	<i>S. aureus</i>
	MIC (mg/mL)	
Zn ₂ Al:CO ₃ -hyd	12	6
Zn ₂ Al:CO ₃ -cop	1.5	0.75
Zn ₃ Al:CO ₃	0.75	0.375
Zn ₂ Al:Cl	3	1.5
Zn ₂ Al:NO ₃	3	1.5
Zn ₂ Al:ClO ₄	1.5	0.75

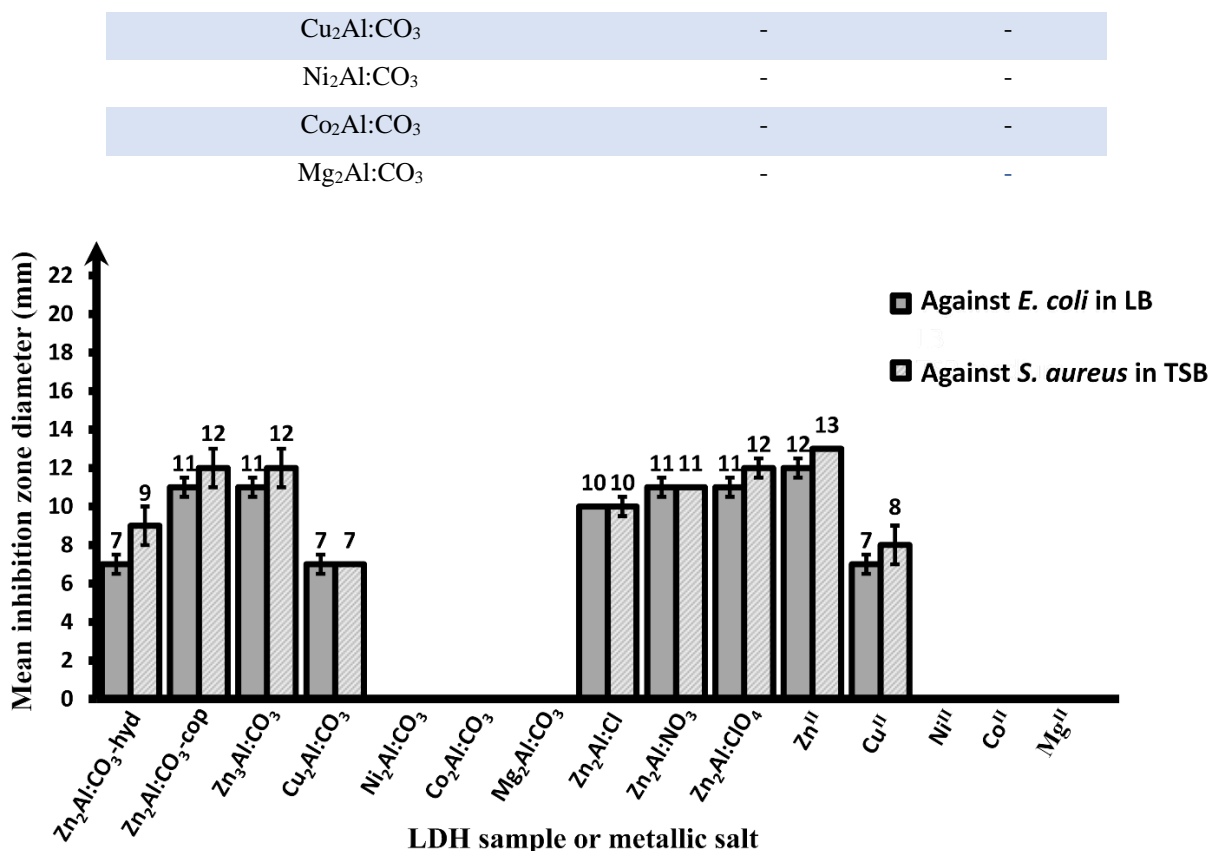


Figure 14. Antimicrobial activity of LDH samples and metal ion solutions against *S. aureus* and *E. coli* in terms of mean zone of inhibition generated in agar disc diffusion tests.

6.1. Influence of the nature of divalent metal on the antibacterial activity of LDHs

As suggested by **Figure 14**, only Zn(II) and Cu(II)-based LDHs were able to impose an antimicrobial effect against *E. coli* and *S. aureus* using agar disc diffusion tests. Zn(II)-based LDHs provided inhibition zone diameters ranging from 7 to 13 mm depending on the type of LDH and the amount of zinc ions released. The obtained values were similar to those of pristine LDHs found in the literature [20,21]. However, other studies reported greater inhibition zone diameters induced by Zn(II)-based LDHs [3,15]. Such difference in the antimicrobial performance may be related to the different physico-chemical properties of the tested LDHs, the different tested bacterial strains, the employed LDH dosage in the test as well as to the different experimental protocols used to carry out the antimicrobial agar diffusion assay.

Similarly, turbidimetric microdilution antibacterial test used to determine the MIC values of LDHs also showed that only Zn(II)-based LDHs were antibacterial toward *S. aureus* and *E. coli* (**Table 6**). The obtained MIC values fall within the range of the obtained MIC values reported for most pristine antimicrobial LDHs found in the literature with some differences depending on the experimental protocol for MIC determination and the physico-chemical properties of tested LDHs [16,27,62].

In contrary to the agar disc diffusion test, the turbidimetric microdilution antibacterial test assay showed that Cu₂Al:CO₃ LDH sample do not impose an antibacterial activity toward neither *S. aureus* nor *E. coli* (no MIC value was detected). Therefore, the antibacterial activity of Cu(II)-based LDHs could be related to the amplified amount of copper released in broth media (**Figure 9**) which was more expressed in agar disc diffusion test, probably because it is more dependent on the diffusion phenomena in the agar gel.

In fact, previous reports validated the antibacterial activity of pristine Zn(II)-based LDH powders [3,14]. Another recent study demonstrated that unmodified Cu(II)-based hydroxalcalites could exhibit an antibacterial effect that was expected to be related to the amount of released Cu²⁺ ions [19].

Therefore, the antibacterial activity of pristine LDHs is primarily dependent on the nature of constituent divalent metals where Zn(II)-based LDHs performed best in both agar disk diffusion and microdilution turbidimetric test assays, despite the fact that they showed minimal release profiles of M²⁺ compared to other M(II)Al(III) LDH samples.

It is also remarkable here to mention that the antibacterial activity of Zn(II)Al(III) LDH samples varied according to the type of tested bacteria. Although the release profile of Zn²⁺ was higher in LB medium than in TSB (**Figure 9**), the antibacterial efficiency of Zn(II)-based samples was more pronounced in case of *S. aureus* (cultivated in TSB) than *E. coli* (cultivated in LB). This can be explained by the unlike cell structures of the tested bacteria and the fact that antimicrobial agents possess a specific response toward a certain bacterial species. For examples, *E. coli* are Gram-negative bacteria with an outer membrane and a thick cell wall which is not present in the case of Gram-positive *S. aureus* bacteria [63].

6.2. Difference in antibacterial activity among the tested M(II)Al(III) LDHs

The fact that Zn(II)-based LDHs were able to establish a superior antibacterial activity to those of other LDHs, even at low Zn²⁺ release profile as is the case for Zn₂AlCO₃-hyd, could be attributed to the nature of the divalent metal present in the LDH itself. In fact, Zn(II) ions salt also showed an enhanced antibacterial activity to that Cu(II) ions salt as well as other M(II) ions salt (**Figure 13**). This highlights again the specificity of the antimicrobial activity of pristine LDHs toward the nature of their constituent divalent metal.

Indeed, both Zn²⁺ and Cu²⁺ metal ions possess similar antibacterial mode of action by which they can induce serious disruption to the bacterial membrane permeability through blocking the transport of nutrients and substances in and out the membrane, or through binding to bacterial intracellular DNA leading to their denaturation [14,64,65]. However, the difference in the antimicrobial activity among different divalent metals, is actually related to several factors, including the role each metal plays in normal metabolism and the presence of specific membrane binding sites for each metal [64]. Therefore, bacteria may be more sensitive to one metal ion more than the other [66], *i.e.*, in this case *E. coli* and *S. aureus* were more sensitive to Zn²⁺ than Cu²⁺ and other tested constituent divalent metal ions of the tested M(II)Al(III) LDHs (Mg²⁺, Co²⁺, Ni²⁺).

6.3. Correlating the antibacterial activity of LDHs to their divalent metal ions release profile

Based on the proposed antibacterial mechanisms of LDHs found in the literature, the antimicrobial activity of LDHs may be due to: (1) direct contact between LDHs and bacteria, (2) release of antimicrobial divalent metal ions, (3) generation of biological toxic reactive oxygen reactive species (ROS).

The similar inhibition zone diameters generated by M(II)Al(III) LDHs and their M(II) salts counterparts (**Figure 14**) can thus be justified by taking into consideration the suggested mechanism of divalent metal release into consideration (mechanism 2). Therefore, the inability of Ni₂Al:CO₃, Co₂Al:CO₃ and Mg₂Al:CO₃ LDHs to demonstrate an antibacterial activity in agar disc diffusion test may be explained by the lower release profiles of their corresponding constituent divalent

metals (M^{2+}). Their respective metallic salts were also not able to impose the desired antimicrobial effect at a concentration similar to that of the released ones. Whereas in case of Cu_2AlCO_3 , the release profile of Cu^{2+} was remarkably high thus providing a sufficient concentration to inhibit the growth of *E. coli* and *S. aureus* in LB and TSB, respectively.

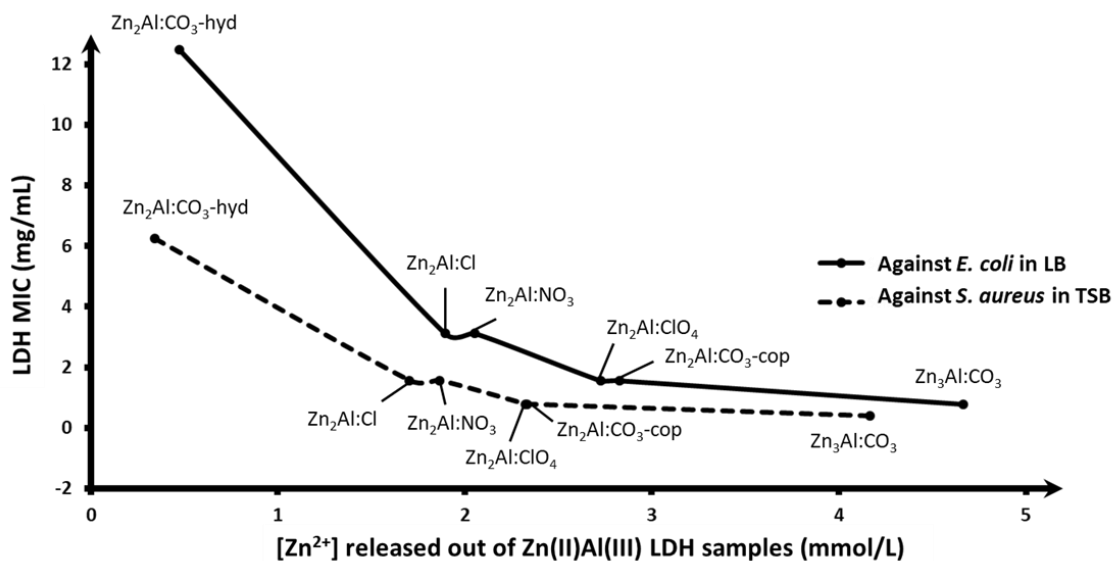


Figure 15. Evolution of antimicrobial activity in terms of LDH MIC against *S. aureus* and *E. coli* as a function of average concentration of Zn^{2+} released from of Zn(II)Al(III) LDH samples.

In order to further support the antibacterial mechanism of pristine LDH by divalent metal release (**Mechanism 2**), the relationship between the partial release profile of Zn^{2+} out of Zn(II)Al(III) LDH samples in bacterial growth media was established. The evolution of MIC values of Zn(II)-based LDH samples determined in liquid LB and TSB broths, was studied in function of the concentration of released Zn^{2+} out of these samples, *i.e.*, $Zn_2Al:CO_3$ -hyd, $Zn_2Al:CO_3$ -cop, $Zn_3Al:CO_3$, $Zn_2Al:Cl$, $Zn_2Al:NO_3$ and $Zn_2Al:ClO_4$, prepared using different experimental procedures.

The obtained MIC values for Zn(II)Al(III) LDHs (ranging from 1.5 to 12 mg/mL and 6 to 0.375 mg/mL for *E. coli* and *S. aureus*, respectively) was dependent on the concentration of zinc ions released from the samples. As presented in **Figure 15**, the MIC values of Zn(II)-based LDHs decreased significantly depending on the amount of released Zn^{2+} in broth media. This points out the impact of the divalent metal release phenomena (dissolution of M^{2+}) of pristine Zn(II)Al(III) LDH powders on their antibacterial efficiency. In other words, the antimicrobial activity is

enhanced with increasing concentration of divalent metal released out of LDHs. This finding supports the possible mechanism of the antibacterial activity of LDHs induced by the release of their constituent divalent metal ions (**Mechanism 2**).

In other words, Zn(II)-based LDHs release Zn^{2+} , acting as an antibiotic-free antibacterial agent, thus inhibiting the growth of *S. aureus* and *E. coli*. Zn^{2+} soluble species then may damage the bacterial membrane function through changing its charge distribution and permeability or else by binding to nucleic acids leading to bacterial proliferation inhibition [14].

On the other hand, the dependence of antibacterial activity of LDHs in terms of MIC values did not change linearly with increasing concentrations of Zn^{2+} released out of Zn(II)Al(III). This non-linear relation gives a sign of the contribution of other possible mechanisms contributing to the antibacterial activity of pristine LDHs, *e.g.*, direct contact with bacteria and ROS generation by LDHs.

The role of direct contact antibacterial mechanism of LDHs will be discussed further in **Chapter 4**, where we limit the number of tested LDH samples to simplify the study, and the antibacterial of bulk LDHs used in this chapter (agglomerated with larger particle size) are compared to well-dispersed smaller particles LDHs (LDH nanoparticles). The comparison between the latter two (having similar chemical composition) will allow us to determine precisely the influence of direct contact mechanism pronounced by smaller LDH particle sizes thus leading to greater area of contact between LDHs and bacteria.

Moreover, antibacterial activity tests presented in this chapter were carried out in an incubator in the absence of light. Therefore, the contribution of ROS generation by LDHs could be eliminated. However, the possible enhancement of LDHs antibacterial activity in presence of light promoting oxidative stress will be evaluated in **Chapter 5**.

7. Conclusion

The dissolution of constituent divalent metal ion (M^{2+}) from pristine LDH powders in broth culture media was strongly dependent on their different physicochemical properties, *e.g.*, nature of constituent divalent metal (M(II)), crystallinity, M(II)/Al(III) molar ratio as well as the nature of intercalated anion in the interlayer space (A^{n-}).

The dissolution properties of different M(II)Al(III) LDHs into M^{2+} in broth bacterial culture media was related to the thermodynamic stability of their $M(OH)_2$ hydroxide counterparts. One exception was revealed for Cu(II)-based LDHs which released a great amount of Cu^{2+} , probably due to its very poor crystallinity and irregular structure presenting defects or due to its great affinity to form organometallic complex compounds with the broth culture components.

Lower crystallinity $Zn_2Al:CO_3$ LDH unexposed to hydrothermal treatment showed more defects and small aggregated particles and thus released more zinc ions in broth media. Similarly, increasing M(II)/Al(III) ratio in Zn(II)-based LDH samples also led an enhanced release of Zn^{2+} ions in broth media, probably due to the greater amount of zinc ions initially present in the LDH structure and/or due to the reduction in crystallinity. Moreover, the crystallinity and structure of the powders were also influenced by the anionic exchange reactions which aimed at eliminating carbonate anions from Zn(II)Al(III) and exchanging them with other intercalating anions (chloride, nitrate and perchlorate). The powders resulted from anion-exchange reaction presented a more defected structure with smaller crystallite sizes and agglomerates, thus leading to an amplified release of zinc ions as well.

The antibacterial activity of the tested pristine M(II)Al(III) LDHs was determined, where only Zn(II) and Cu(II)-based LDHs were able to establish an inhibitory effect against *E. coli* and *S. aureus*. The superior antimicrobial activity of Zn(II)Al(III) LDHs compared to other M(II)Al(III) LDH samples, even when lower amount of M^{2+} was released out of them, was related to the nature of their constituent divalent metal, *i.e.*, Zn(II). In addition, the antibacterial inhibitory effect of M(II)Al(III) LDHs, evaluated using agar disc diffusion tests, was similar to that of their corresponding M(II) salts counterparts, thus supporting the antibacterial mechanism of pristine LDHs by the release of divalent metals (**Mechanism 2**). Such hypothesis was further validated by the decrease in the minimum inhibitory concentration (MIC) of Zn(II)Al(III) LDH with increasing concentrations of released Zn^{2+} , which was initially controlled by the different studied physicochemical parameters. Although such findings provide insightful explanations of the antibacterial mode of action of pristine LDHs, this does not eliminate the possibility of the contribution of other suggested antimicrobial mechanisms which will further be discussed in the manuscript, *i.e.*, direct surface contact interactions and ROS generation.

References

- [1] C. Forano, F. Bruna, C. Mousty, V. Prevot, Interactions between Biological Cells and Layered Double Hydroxides: Towards Functional Materials, *Chem. Rec.* 18 (2018) 1150–1166.
- [2] W. Kamal, W.M.A. El Rouby, A.O. El-Gendy, A.A. Farghali, Bimodal applications of LDH-chitosan nanocomposite: water treatment and antimicrobial activity, *IOP Conf. Ser. Mater. Sci. Eng.* 464 (2018) 012005.
- [3] S.A.A. Moaty, A.A. Farghali, R. Khaled, Preparation, characterization and antimicrobial applications of Zn-Fe LDH against MRSA, *Mater. Sci. Eng. C.* 68 (2016) 184–193.
- [4] H.-M. Cheng, X.-W. Gao, K. Zhang, X.-R. Wang, W. Zhou, S.-J. Li, X.-L. Cao, D.-P. Yan, A novel antimicrobial composite: ZnAl-hydroxalcalite with *p*-hydroxybenzoic acid intercalation and its possible application as a food packaging material, *New J. Chem.* 43 (2019) 19408–19414.
- [5] L. Tamaro, V. Vittoria, V. Bugatti, Dispersion of modified layered double hydroxides in Poly(ethylene terephthalate) by High Energy Ball Milling for food packaging applications, *Eur. Polym. J.* 52 (2014) 172–180.
- [6] W. Zhang, Y. Zhao, W. Wang, J. Peng, Y. Li, Y. Shanguan, G. Ouyang, M. Xu, S. Wang, J. Wei, H. Wei, W. Li, Z. Yang, Colloidal Surface Engineering: Growth of Layered Double Hydroxides with Intrinsic Oxidase-Mimicking Activities to Fight Against Bacterial Infection in Wound Healing, *Adv. Healthc. Mater.* 9 (2020) 2000092.
- [7] S. Mallakpour, Z. Radfar, C.M. Hussain, Current advances on polymer-layered double hydroxides/metal oxides nanocomposites and bionanocomposites: Fabrications and applications in the textile industry and nanofibers, *Appl. Clay Sci.* 206 (2021) 106054.
- [8] Y. Wang, D. Zhang, Synthesis, characterization, and controlled release antibacterial behavior of antibiotic intercalated Mg–Al layered double hydroxides, *Mater. Res. Bull.* 47 (2012) 3185–3194.
- [9] M.A. Djebbi, A. Elabed, Z. Bouaziz, M. Sadiki, S. Elabed, P. Namour, N. Jaffrezic-Renault, A.B.H. Amara, Delivery system for berberine chloride based on the nanocarrier ZnAl-layered double hydroxide: Physicochemical characterization, release behavior and evaluation of antibacterial potential, *Int. J. Pharm.* 515 (2016) 422–430.
- [10] Y. Salguero, L. Valenti, R. Rojas, M.C. García, Ciprofloxacin-intercalated layered double hydroxide-in-hybrid films as composite dressings for controlled antimicrobial topical delivery, *Mater. Sci. Eng. C.* 111 (2020) 110859.
- [11] A.A.G. El-Shahawy, F.I. Abo El-Ela, N.A. Mohamed, Z.E. Eldine, W.M.A. El Rouby, Synthesis and evaluation of layered double hydroxide/doxycycline and cobalt ferrite/chitosan nanohybrid efficacy on gram positive and gram negative bacteria, *Mater. Sci. Eng. C.* 91 (2018) 361–371.
- [12] O. Williams, I. Clark, R.L. Gomes, T. Pehinec, J.L. Hobman, D.J. Stekel, R. Hyde, C. Dodds, E. Lester, Removal of copper from cattle footbath wastewater with layered double hydroxide adsorbents as a route to antimicrobial resistance mitigation on dairy farms, *Sci. Total Environ.* 655 (2019) 1139–1149.
- [13] WHO, New report calls for urgent action to avert antimicrobial resistance crisis, World Health Organization, 2019. <https://www.who.int/news/item/29-04-2019-new-report-calls-for-urgent-action-to-avert-antimicrobial-resistance-crisis>.

- [14] F. Peng, D. Wang, D. Zhang, H. Cao, X. Liu, The prospect of layered double hydroxide as bone implants: A study of mechanical properties, cytocompatibility and antibacterial activity, *Appl. Clay Sci.* 165 (2018) 179–187.
- [15] S. Dutta, T.K. Jana, S.K. Halder, R. Maiti, A. Dutta, A. Kumar, K. Chatterjee, Zn₂Al-CO₃ Layered Double Hydroxide: Adsorption, Cytotoxicity and Antibacterial Performances, *ChemistrySelect.* 5 (2020) 6162–6171.
- [16] M. Lobo-Sánchez, G. Nájera-Meléndez, G. Luna, V. Segura-Pérez, J.A. Rivera, G. Fetter, ZnAl layered double hydroxides impregnated with eucalyptus oil as efficient hybrid materials against multi-resistant bacteria, *Appl. Clay Sci.* 153 (2018) 61–69.
- [17] H.A. Tabti, M. Adjdir, A. Ammam, B. Mdjahed, B. Guezzen, A. Ramdani, C.K. Bendedouche, N. Bouchikhi, N. Chami, Facile synthesis of Cu-LDH with different Cu/Al molar ratios: application as antibacterial inhibitors, *Res. Chem. Intermed.* 46 (2020) 5377–5390.
- [18] A.M. León-Vallejo, F.D. Velázquez-Herrera, Á. Sampieri, G. Landeta-Cortés, G. Fetter, Study of layered double hydroxides as bactericidal materials against *Corynebacterium ammoniagenes*, a bacterium responsible for producing bad odors from human urine and skin infections, *Appl. Clay Sci.* 180 (2019) 105194.
- [19] G. Rocha Oliveira, L.J. Dias do Amaral, M. Giovanela, J. da Silva Crespo, G. Fetter, J.A. Rivera, A. Sampieri, P. Bosch, Bactericidal Performance of Chlorophyllin-Copper Hydrotalcite Compounds, *Water. Air. Soil Pollut.* 226 (2015) 316.
- [20] M. Li, L. Li, S. Lin, Efficient antimicrobial properties of layered double hydroxide assembled with transition metals via a facile preparation method, *Chin. Chem. Lett.* 31 (2020) 1511–1515.
- [21] S. Kim, J. Fabel, P. Durand, E. André, C. Carteret, Ternary Layered Double Hydroxides (LDHs) Based on Co-, Cu-Substituted ZnAl for the Design of Efficient Photocatalysts: Ternary Layered Double Hydroxides (LDHs) Based on Co-, Cu-Substituted ZnAl for the Design of Efficient Photocatalysts, *Eur. J. Inorg. Chem.* 2017 (2017) 669–678.
- [22] N. Iyi, H. Yamada, T. Sasaki, Deintercalation of carbonate ions from carbonate-type layered double hydroxides (LDHs) using acid–alcohol mixed solutions, *Appl. Clay Sci.* 54 (2011) 132–137.
- [23] R.M.A. Lieth, ed., *Preparation and Crystal Growth of Materials with Layered Structures*, Springer Netherlands, Dordrecht, 1977.
- [24] B.D. Cullity, *Elements of x-ray diffraction*, 2d ed, Addison-Wesley Pub. Co, Reading, Mass, 1978.
- [25] F. Cavani, F. Trifirò, A. Vaccari, Hydrotalcite-type anionic clays: Preparation, properties and applications., *Catal. Today.* 11 (1991) 173–301.
- [26] F.Z. Mahjoubi, A. Khalidi, M. Abdennouri, N. Barka, Zn–Al layered double hydroxides intercalated with carbonate, nitrate, chloride and sulphate ions: Synthesis, characterisation and dye removal properties, *J. Taibah Univ. Sci.* 11 (2017) 90–100.
- [27] M. Li, L. Li, S. Lin, Efficient antimicrobial properties of layered double hydroxide assembled with transition metals via a facile preparation method, *Chin. Chem. Lett.* 31 (2020) 1511–1515.
- [28] J. Li, S. Zhang, Y. Chen, T. Liu, C. Liu, X. Zhang, M. Yi, Z. Chu, X. Han, A novel three-dimensional hierarchical CuAl layered double hydroxide with excellent catalytic activity for degradation of methyl orange, *RSC Adv.* 7 (2017) 29051–29057.

- [29] S. Kannan, V. Rives, H. Knözinger, High-temperature transformations of Cu-rich hydrotalcites, *J. Solid State Chem.* 177 (2004) 319–331.
- [30] J. Zhang, F. Zhang, L. Ren, D.G. Evans, X. Duan, Synthesis of layered double hydroxide anionic clays intercalated by carboxylate anions, *Mater. Chem. Phys.* 85 (2004) 207–214.
- [31] I. Crespo, Intercalation of iron hexacyano complexes in Zn,Al-hydrotalcite, *Solid State Ion.* 101–103 (1997) 729–735.
- [32] F. Kovanda, T. Rojka, P. Bezdička, K. Jiráťová, L. Obalová, K. Pacultová, Z. Bastl, T. Grygar, Effect of hydrothermal treatment on properties of Ni–Al layered double hydroxides and related mixed oxides, *J. Solid State Chem.* 182 (2009) 27–36.
- [33] P. Benito, F.M. Labajos, V. Rives, Microwave-treated layered double hydroxides containing Ni²⁺ and Al³⁺: The effect of added Zn²⁺, *J. Solid State Chem.* 179 (2006) 3784–3797.
- [34] C.-C. Wang, J.Y. Ying, Sol–Gel Synthesis and Hydrothermal Processing of Anatase and Rutile Titania Nanocrystals, *Chem. Mater.* 11 (1999) 3113–3120.
- [35] S. Miyata, Physico-Chemical Properties of Synthetic Hydrotalcites in Relation to Composition, *Clays Clay Miner.* 28 (1980) 50–56.
- [36] T.L.P. Galvão, C.S. Neves, A.P.F. Caetano, F. Maia, D. Mata, E. Malheiro, M.J. Ferreira, A.C. Bastos, A.N. Salak, J.R.B. Gomes, J. Tedim, M.G.S. Ferreira, Control of crystallite and particle size in the synthesis of layered double hydroxides: Macromolecular insights and a complementary modeling tool, *J. Colloid Interface Sci.* 468 (2016) 86–94.
- [37] J.-Y. Lee, G.-H. Gwak, H.-M. Kim, T. Kim, G.J. Lee, J.-M. Oh, Synthesis of hydrotalcite type layered double hydroxide with various Mg/Al ratio and surface charge under controlled reaction condition, *Appl. Clay Sci.* 134 (2016) 44–49.
- [38] A.A.A. Ahmed, Z.A. Talib, M.Z. Hussein, Influence of Metallic Molar Ratio on the Electron Spin Resonance and Thermal Diffusivity of Zn–Al Layered Double Hydroxide, *J. Nanomater.* 2013 (2013) 1–9.
- [39] Y. Liu, Z. Yang, Intercalation of sulfate anions into a Zn–Al layered double hydroxide: their synthesis and application in Zn–Ni secondary batteries, *RSC Adv.* 6 (2016) 68584–68591.
- [40] J.T. Klopogge, D. Wharton, L. Hickey, R.L. Frost, Infrared and Raman study of interlayer anions CO₃²⁻, NO₃⁻, SO₄²⁻ and ClO₄⁻ in Mg/Al-hydrotalcite, *Am. Mineral.* 87 (2002) 623–629.
- [41] R.P. Bontchev, S. Liu, J.L. Krumhansl, J. Voigt, T.M. Nenoff, Synthesis, Characterization, and Ion Exchange Properties of Hydrotalcite Mg₆Al₂(OH)₁₆(A)_x(A')_{2-x}·4H₂O (A, A' = Cl⁻, Br⁻, I⁻, and NO₃⁻, 2 ≥ x ≥ 0) Derivatives, *Chem. Mater.* 15 (2003) 3669–3675.
- [42] A.N. Salak, J. Tedim, A.I. Kuznetsova, M.L. Zheludkevich, M.G.S. Ferreira, Anion exchange in Zn–Al layered double hydroxides: In situ X-ray diffraction study, *Chem. Phys. Lett.* 495 (2010) 73–76.
- [43] A.V. Radha, P. Vishnu Kamath, C. Shivakumara, Mechanism of the anion exchange reactions of the layered double hydroxides (LDHs) of Ca and Mg with Al, *Solid State Sci.* 7 (2005) 1180–1187.
- [44] D. Scarpellini, C. Falconi, P. Gaudio, A. Mattoccia, P.G. Medaglia, A. Orsini, R. Pizzoferrato, M. Richetta, Morphology of Zn/Al layered double hydroxide nanosheets grown onto aluminum thin films, *Microelectron. Eng.* 126 (2014) 129–133.
- [45] I. Clark, R.L. Gomes, C. Crawshaw, L. Neve, R. Lodge, M. Fay, C. Winkler, M. Hull, E. Lester, Continuous synthesis of Zn₂Al–CO₃ layered double hydroxides: a comparison of bench, pilot and industrial scale syntheses, *React. Chem. Eng.* 4 (2019) 663–666.

- [46] T. Hibino, Acid Treatment of Layered Double Hydroxides Containing Carbonate: Acid Treatment of Layered Double Hydroxides Containing Carbonate, *Eur. J. Inorg. Chem.* 2014 (2014) 5311–5321.
- [47] H. Liu, Q. Jiao, Y. Zhao, H. Li, C. Sun, X. Li, Mixed oxides derived from Cu–Co layered double hydroxide nanorods: Preparation, characterization and their catalytic activities, *J. Alloys Compd.* 496 (2010) 317–323.
- [48] R. Rojas, Effect of particle size on copper removal by layered double hydroxides, *Chem. Eng. J.* 303 (2016) 331–337.
- [49] M. Herrero, F. Labajos, V. Rives, Size control and optimisation of intercalated layered double hydroxides, *Appl. Clay Sci.* (2008) S0169131708001336. ht
- [50] A. Rawle, The Basic Principles of Particle Size Analysis, *Surf. Coat. Int. Part Coat. J.* 86 (2003) 58–65.
- [51] M. Jobbágy, A.E. Regazzoni, Dissolution of nano-size Mg–Al–Cl hydrotalcite in aqueous media, *Appl. Clay Sci.* 51 (2011) 366–369.
- [52] S. Liu, E. Killen, M. Lim, C. Gunawan, R. Amal, The effect of common bacterial growth media on zinc oxide thin films: identification of reaction products and implications for the toxicology of ZnO, *RSC Adv.* 4 (2014) 4363–4370.
- [53] L. Esteban-Tejeda, F. Palomares, B. Cabal, R. López-Píriz, A. Fernández, D. Sevillano, L. Alou, R. Torrecillas, J. Moya, Effect of the Medium Composition on the Zn²⁺ Lixiviation and the Antifouling Properties of a Glass with a High ZnO Content, *Materials.* 10 (2017) 167.
- [54] J. Pasquet, Y. Chevalier, J. Pelletier, E. Couval, D. Bouvier, M.-A. Bolzinger, The contribution of zinc ions to the antimicrobial activity of zinc oxide, *Colloids Surf. Physicochem. Eng. Asp.* 457 (2014) 263–274.
- [55] J.W. Boclair, P.S. Braterman, Layered Double Hydroxide Stability. 1. Relative Stabilities of Layered Double Hydroxides and Their Simple Counterparts, *Chem. Mater.* 11 (1999) 298–302.
- [56] J.F. Blais, Z. Djedidi, R.B. Cheikh, R.D. Tyagi, G. Mercier, Metals Precipitation from Effluents: Review, *Pract. Period. Hazard. Toxic Radioact. Waste Manag.* 12 (2008) 135–149.
- [57] Q. Zheng, Y. Hao, P. Ye, L. Guo, H. Wu, Q. Guo, J. Jiang, F. Fu, G. Chen, A pH-responsive controlled release system using layered double hydroxide (LDH)-capped mesoporous silica nanoparticles, *J. Mater. Chem. B.* 1 (2013) 1644.
- [58] S.V. Prasanna, P.V. Kamath, Anion-Exchange Reactions of Layered Double Hydroxides: Interplay between Coulombic and H-Bonding Interactions, *Ind. Eng. Chem. Res.* 48 (2009) 6315–6320.
- [59] M. Pavlovic, Ion specific effects on the stability of layered double hydroxide colloids, *Soft Matter.* (2016) 10.
- [60] M. Baek, I.-S. Kim, J. Yu, H.E. Chung, J.-H. Choy, S.-J. Choi, Effect of Different Forms of Anionic Nanoclays on Cytotoxicity, *J. Nanosci. Nanotechnol.* 11 (2011) 1803–1806.
- [61] R. k. Allada, Thermochemistry and Aqueous Solubilities of Hydrotalcite-Like Solids, *Science.* 296 (2002) 721–723.
- [62] Z. Wang, H. Yu, K. Ma, Y. Chen, X. Zhang, T. Wang, S. Li, X. Zhu, X. Wang, Flower-like Surface of Three-Metal-Component Layered Double Hydroxide Composites for Improved Antibacterial Activity of Lysozyme, *Bioconjug. Chem.* 29 (2018) 2090–2099.
- [63] Y. Qiao, Q. Li, H. Chi, M. Li, Y. Lv, S. Feng, R. Zhu, K. Li, Methyl blue adsorption properties and bacteriostatic activities of Mg–Al layer oxides via a facile preparation method, *Appl. Clay Sci.* 163 (2018) 119–128.

- [64] G. Borkow, J. Gabbay, Copper as a Biocidal Tool, *Curr. Med. Chem.* 12 (2005) 2163–2175.
- [65] S. Mittapally, R. Taranum, S. Parveen, Metal ions as antibacterial agents, *J. Drug Deliv. Ther.* 8 (2018) 411–419.
- [66] M.R. Bruins, S. Kapil, F.W. Oehme, Microbial Resistance to Metals in the Environment, *Ecotoxicol. Environ. Saf.* 45 (2000) 198–207.

Antibacterial activity of Zn(II)-based layered double hydroxide nanoparticles by direct surface interactions

Table of figures	144
Table of tables.....	147
1. Context	148
2. Synthesis and characterization of LDH NPs	150
2.1. Synthesis.....	150
2.2. Structural characterization.....	151
2.3. Textural and morphological characterization	153
3. Antibacterial activity of LDH NPs	155
4. Effect of LDH NPs treatment on the morphology of <i>S. aureus</i> cells	157
5. Synthesis and characterization of LDH films and LDH-functionalized tips.....	161
5.1. Synthesis.....	161
5.2. Structural characterization.....	162
5.3. Textural and morphological characterization	163
6. Force spectroscopy measurements between LDH-functionalized tips and <i>S. aureus</i> cells .	166
6.1. Force spectroscopy using ZnAl-functionalized tips	166
6.2. FS comparison of ZnAl-, MgAl- and Al-functionalized tips	168
6.3. FS using ZnAl-functionalized tips in presence of Zn ²⁺	171

Chapter 4: Antibacterial activity of Zn(II)-based layered double hydroxide nanoparticles by direct surface interactions

7. Conclusion.....172
References174

Table of figures

Figure 1. A schematic illustration of the interactions probed between single living <i>S. aureus</i> cells and LDH-functionalized AFM tips.	150
Figure 2. LDH NPs structural characterization. (a) XRD patterns of MgAl and ZnAl NPs. (b) FT-IR spectra of MgAl and ZnAl NPs.....	151
Figure 3. XPS spectra of MgAl LDH NPs. (a) Full spectrum. (b) Al 2p region. (c) O 1s region. (d) Mg 2p region.	152
Figure 4. XPS spectra of MgAl LDH NPs. (a) Full spectrum. (b) Al 2p region. (c) O 1s region. (d) Zn 2p region.	153
Figure 5. LDH NPs characterization. (a,c) SEM images of MgAl (a) and ZnAl (c) NPs (scale bar = 200 nm). (b,d) AFM height images of MgAl (b) and ZnAl (d) NPs (scale bar = 200 nm, insets are deflection images showing the NPs surface ultra-structure) together with height profiles of single particles. Dashed lines marked on the height images represent the sections used to determine the height profiles.....	154
Figure 6. NPs antibacterial activity against <i>S. aureus</i> . (a) Agar disk diffusion test using 10 mg/mL ZnAl and MgAl NPs suspensions (scale bar = 5 mm). (b) Mean zone of inhibition of MgAl, ZnAl NPs and micron-sized ZnAl LDH calculated as the average inhibition diameters of three repetitive trials. (c) MIC values for MgAl, ZnAl NPs and micron-sized ZnAl LDH calculated as the average MIC of three repetitive trials. *Data for micron-sized ZnAl LDH are obtained from Chapter 3	155
Figure 7. AFM deflection images of <i>S. aureus</i> in liquid (scale bar = 250 nm). (a) Untreated <i>S. aureus</i> cells. (b) <i>S. aureus</i> cells treated with MgAl LDH NPs at MIC value of ZnAl LDH NPs. (c) <i>S. aureus</i> cells treated with ZnAl LDH NPs at MIC.....	158
Figure 8. AFM deflection images of <i>S. aureus</i> cells in air (scale bar = 500 nm). (a) Untreated <i>S. aureus</i> cells. (b) <i>S. aureus</i> cells treated with MgAl LDH NPs at MIC value of ZnAl LDH NPs. (c) <i>S. aureus</i> cells treated with ZnAl LDH NPs at MIC. White arrows point to enlarged swelled cells. Red arrows point to distorted cells. Yellow arrows point to cell debris.	159
Figure 9. AFM height images of <i>S. aureus</i> cells in air (scale bar = 500 nm) together with the height profiles of three cells taken along the dashed lines marked on their AFM height images. (a)	

Untreated *S. aureus* cells. (b) *S. aureus* cells treated with MgAl LDH NPs at MIC value of ZnAl LDH NPs. (c) *S. aureus* cells treated with ZnAl LDH NPs at MIC. 160

Figure 10. LDH films structural characterization. (a) XRD patterns of MgAl and ZnAl LDH films. (b) FT-IR spectra of MgAl and ZnAl LDH films. 162

Figure 11. SEM images of LDH films on silicon wafers and AFM tips (scale bar = 1 μm). (a) MgAl LDH film grown on silicon wafer. (b) ZnAl LDH film grown on silicon wafer. (c) Bare silicon nitride AFM tip. (d) Al-functionalized silicon nitride AFM tip. (e) MgAl LDH-functionalized silicon nitride AFM tip. (f) ZnAl LDH-functionalized silicon nitride AFM tip. 163

Figure 12. EDS spectra of LDH films grown on silicon wafers. (a) MgAl LDH film. (b) ZnAl LDH film. The peak appearing at 0 keV is attributed to the noise from the EDS detector. 164

Figure 13. SEM and AFM images used to determine the average thickness of the LDH films. (a,c) SEM cross-sectional images of MgAl (a) and ZnAl (c) LDH films (scale bar = 250 nm). (b,d) AFM height images of MgAl (b) and ZnAl (d) LDH films interfaces with silicon substrates revealed by a scratch (scale bar = 2 μm) together with their height profiles. The dashed lines marked on the height images represent the sections used to determine the height profiles of the films. 165

Figure 14. EDS spectra of LDH-functionalized tips performed on the apex of the probe. (a) MgAl LDH-functionalized tip. (b) ZnAl LDH-functionalized. 166

Figure 15. FS on live *S. aureus* cells with ZnAl-functionalized AFM tips. (a) Adhesion maps (400 x 400 nm^2) recorded on *S. aureus* cells (insets are AFM deflection images of probed cells, scale bar = 250 nm) with ZnAl-functionalized AFM tips. White/grey pixel correspond to adhesive events and black pixels correspond to non-adhesive events (scale 0-1000 pN). (b, c) Corresponding adhesion force (b) and rupture length (c) histograms together with representative force-distance curves. Data were obtained from four independent experiments using different tips and independent cell cultures. 167

Figure 16. FS with functionalized tips reveals specific interactions for ZnAl tips. (a) Topography images of *S. aureus* cells trapped in porous membranes (scale bar = 250 nm) and probed with functionalized AFM tips. (b,c,d) Adhesion force histograms and adhesion force maps (insets, 400 x 400 nm^2) obtained on the top of cells using ZnAl-functionalized AFM tip (b) MgAl-functionalized AFM tip (c) Al-functionalized AFM tip (d). White/grey pixel correspond to adhesive events and black pixels correspond to non-adhesive events (scale 0-1000 pN). Data were

obtained from four independent experiments using different tips and independent cell cultures. 169

Figure 17. SEM images of LDH functionalized-AFM tips after being used in force measurement experiments (scale bar = 1 μm). (a) MgAl-functionalized silicon nitride AFM tip. (b) ZnAl-functionalized silicon nitride AFM tip. 170

Figure 18. FS on live *S. aureus* cells with ZnAl-functionalized AFM tips before (black histograms) and after addition of Zn^{2+} salt (red histograms). (a) Topography images of *S. aureus* cells trapped in porous membranes (scale bar = 250 nm) and probed with ZnAl-functionalized AFM tips. (b,c) Corresponding adhesion force (b) and rupture length (c) histograms. Data were obtained from four independent experiments using different tips and independent cell cultures. 171

Figure 19. A schematic illustration of the proposed antibacterial mechanism of pristine LDHs through direct surface interactions between LDHs and bacteria (**Mechanism 1**). Scale is adjusted to clarify the illustration. 172

Table of tables

Table 1. Roughness parameter Rq of <i>S. aureus</i> cells untreated and treated with ZnAl and MgAl LDH NPs.	157
Table 2. M(II)/A(III) molar ratio in LDH films grown on silicon wafers and LDH-functionalized AFM tips.....	163

1. Context

In the previous chapter, we confirmed the contribution of the amount of released Zn^{2+} ions out of Zn(II)-based LDHs to their antibacterial activity (**Mechanism 2**). Although our findings supported the first suggested antibacterial mode of action of pristine LDHs by release of divalent ions, this does not eliminate the possibility of the contribution of the other two suggested mechanisms, particularly membrane and cell wall damages by direct interactions with bacterial surfaces.

Bacterial adhesion to LDHs was previously investigated using standard adsorption isotherm, density-gradient separation techniques as well as scanning and tunneling electron microscopy imaging [1–5]. Although these investigations admitted the presence of direct surface interactions between LDHs and bacteria, almost none of them correlated such interactions to the antibacterial activity of LDHs, as no antibacterial tests were carried out. In other words, adsorption or adhesion cannot solely explain antibacterial activity. Moreover, only few adhesion forces between bacteria and antibacterial clay materials or inorganic nanoparticles (NPs) were successfully measured using atomic force microscopy (AFM) technique [6,7], and as far as our knowledge none of them was performed to particularly decipher the antibacterial mechanisms of LDHs.

AFM is considered advantageous compared to other high-resolution techniques, because it allows analysis of samples in liquid, thus mimicking physiologically relevant conditions [8]. Thanks to the development of AFM-based force spectroscopy (FS) approaches, AFM was not only limited to be a powerful tool for high resolution imaging of bacterial cells but also used to probe bacterial adhesion at the single particle level [9,10]. In this context, AFM provides a quantitative evaluation of adhesion interactions between bacteria and Zn(II)-based antimicrobial LDHs and a potential correlation to their antibacterial properties.

In order to measure LDH NPs interactions with bacterial walls using AFM-based FS, two contact surfaces need to be created: an immobilized NPs-functionalized AFM probe surface, and a bacterial substrate surface to be probed. In fact, some studies reported the attachment of NPs on AFM probes using commercial glue adhesives [11]. However, if LDH NPs were to be attached to AFM probe using any type of glue, contamination may take place due to the possibility of glue adsorption on the surface thus leading to false adhesion force measurements. Another way to fix NPs on AFM tips is by chemical covalent functionalization using covalent linkers [12–14].

However, these chemical modifications may alter the LDHs chemical nature and thus may in turn influence their interactions with bacteria. *In-situ* deposition of NPs on the tips under electron beam irradiation, evanescent wave illumination and short current-limited bias voltage were also reported [15–17]. Nevertheless, the advanced devices required in such approaches may not be readily available, which hamper their generalization.

Therefore, a new suitable method to functionalize AFM tips with LDHs is necessary to probe their interactions with bacteria and to understand their antibacterial mechanism. For this purpose, we designed an original approach to fabricate LDH-functionalized AFM tips by *in-situ* growth of LDH films directly on the surface of AFM tips. These LDH-functionalized tips were used to probe adhesion interactions with *S. aureus* bacteria.

Since Zn(II)-based LDHs possessed the best antibacterial activity among all the other tested M(II)Al(III) LDHs, we intended to synthesize nitrate-intercalated LDH NPs of smaller particle sizes by a fast co-precipitation synthesis method. The antibacterial performance of smaller-sized ZnAl LDH NPs were compared to the nitrate-intercalated micron-sized LDHs obtained in **Chapter 3**. Moreover, Mg(II)Al(III) LDH NPs were also prepared to serve as control non-antibacterial LDH NPs.

The antimicrobial activity of ZnAl LDH NPs against *S. aureus* bacteria was determined using agar disk diffusion and broth microdilution methods and compared to the effect of MgAl LDH NPs and micron-sized Zn(II)-based LDHs. The comparison between the antibacterial properties of nano-sized and micron-sized Zn(II)-based LDHs showed that the antibacterial properties of the NPs go beyond the simple dissolution of Zn^{2+} ions, where it was also related to surface contact interactions. Furthermore, AFM imaging revealed that growth inhibition by Zn(II)-based LDH NPs was associated to severe morphological cell wall changes.

Then, we took advantage of our original approach to grow LDH films *in situ* on AFM tips and to probe the interaction between LDHs and living *S. aureus* cells using AFM-based FS approach (**Figure 1**). The physico-chemical characterizations based on X-ray diffraction (XRD) and Fourier-Transfer InfraRed (FT-IR) spectroscopy revealed that LDH films presented properties comparable to those of LDH NPs. As compared to the controls, the FS adhesion maps recorded with ZnAl LDH-functionalized tips presented strong adhesion (hundreds of pN) at high frequency

which suggest that the antimicrobial effect of Zn(II)-based LDH NPs is at least partly due to specific and direct interactions with the bacterial cell wall, thus validating the first suggested antibacterial mechanism of pristine LDHs by direct surface interactions.

The content of this chapter is published in *Nanoscale* (**Annex I**).

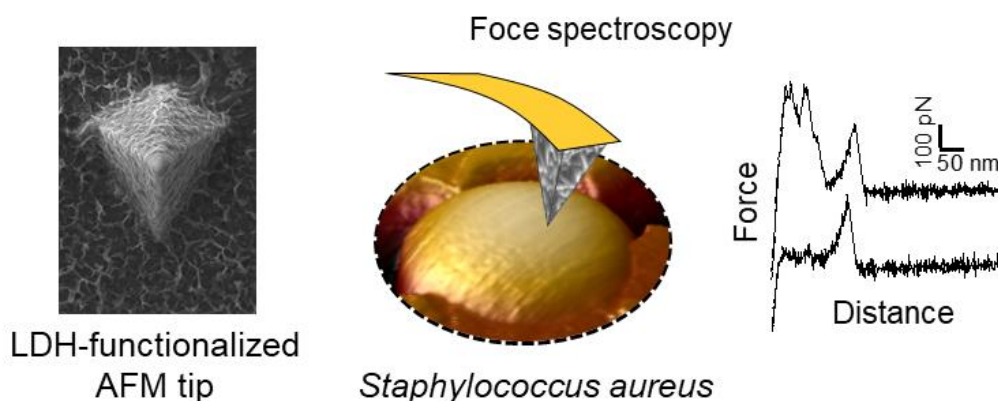


Figure 1. A schematic illustration of the interactions probed between single living *S. aureus* cells and LDH-functionalized AFM tips.

2. Synthesis and characterization of LDH NPs

2.1. Synthesis

Nitrate-intercalated Zn(II)Al(III) and Mg(II)Al(III) LDHs were synthesized by a fast coprecipitation-hydrothermal method, adapted from Xu *et al.* [18]. Briefly, a mixture of 2 mmol $M(\text{NO}_3)_2 \cdot 6\text{H}_2\text{O}$ ($M=\text{Zn}, \text{Mg}$) and 1 mmol $\text{Al}(\text{NO}_3)_3 \cdot 9\text{H}_2\text{O}$ was very quickly added to a 0.15 M NaOH solution, under nitrogen atmosphere and vigorous stirring for 20 minutes. The LDH slurry was obtained by centrifugation, washed and dispersed again in decarbonated water. The resultant suspension was then transferred to a stainless-steel autoclave with a Teflon lining and heated at 80°C for 24 h. LDH NPs powders were then obtained by centrifugation and air drying at 80 °C. The obtained LDH NPs are denoted in the manuscript as ZnAl and MgAl LDH NPs.

2.2. Structural characterization

2.2.1. M(II)/Al(III) molar ratio determination

The M(II)/Al(III) molar ratio of ZnAl and MgAl LDH NPs evaluated using inductively coupled plasma mass spectroscopy (ICP-MS) analysis were found to be 1.94 and 1.97, respectively. Such obtained values were very close to the expected value of 2, thus corresponding potentially to ideal arrangements of the M(II) and Al(III) cations in the brucite-like sheets [19].

2.2.2. X-ray diffraction

Figure 2a shows the XRD patterns of the prepared MgAl and ZnAl LDH NPs, both having the characteristic reflections of LDH materials exhibiting a hexagonal lattice with rhombohedral 3R symmetry and no further crystalline impurities [20]. The interlayer spacing of both LDH NPs extracted from diffraction peaks at (003) and (006) basal reflections was 0.89 ± 0.01 nm, which is in good agreement with the interlayer spacing values for nitrate-intercalated LDHs [21,22].

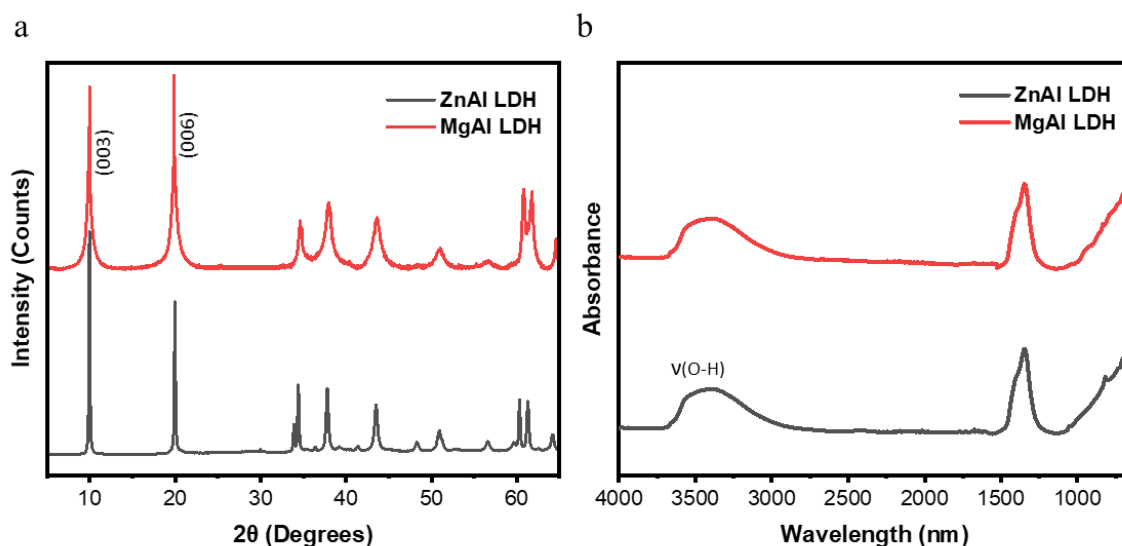


Figure 2. LDH NPs structural characterization. (a) XRD patterns of MgAl and ZnAl NPs. (b) FT-IR spectra of MgAl and ZnAl NPs.

2.2.3. Fourier-Transform InfraRed spectroscopy

The Fourier-Transform InfraRed (FT-IR) spectra of both LDH NPs showed characteristic peaks of nitrate-intercalated LDHs corresponding to O-H stretching vibrations at 3446 cm^{-1} and NO_3^-

vibration at 1350 cm^{-1} (Figure 2b) [23]. No additional vibration bands which could be assigned to amorphous impurity phases had been detected, suggesting the high purity of our prepared NPs.

2.2.4. X-ray photoelectron spectroscopy

XPS spectroscopy was further used to confirm the chemical composition and bonding states of MgAl and ZnAl LDH NPs (Figure 3 and Figure 4).

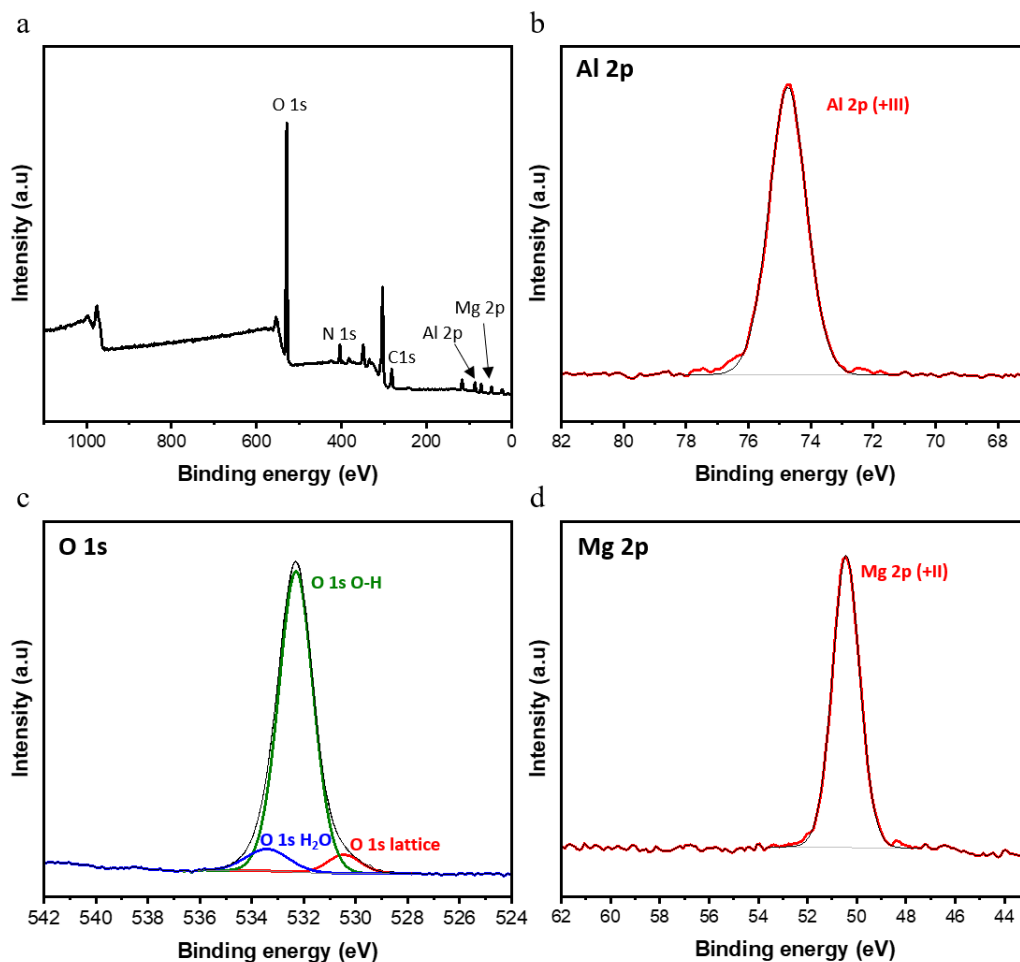


Figure 3. XPS spectra of MgAl LDH NPs. (a) Full spectrum. (b) Al 2p region. (c) O 1s region. (d) Mg 2p region.

N 1s, Al 2p, and O 1s peaks located respectively at about 406.5, 74.5 and 532 eV, were found in both MgAl and ZnAl LDH NPs (Figure 3a and Figure 4a). The presence of N 1s peak is ascribed to spin-orbit characteristics of NO_3^- , accounting for nitrate intercalated anions [24]. The Al 2p region (Figure 3b and Figure 4b) illustrates the presence of Al(III) species in the both samples [25]. The O1s signal peak can be separated into three peaks located at about 530 eV, 532 eV and

533 eV (Figure 3c and Figure 4c), which are attributed to the lattice oxygen, hydroxyl groups and water molecules, respectively [25–27]. Moreover, the XPS spectra of MgAl NPs shows the presence of Mg 2p peak at ~50.5 eV (Figure 3d) accounting for the constituent Mg(II) divalent metal [28]. On the other hand, the presence of Zn(II) constituent divalent metals in ZnAl NPs was confirmed by the presence of Zn 2p_{1/2} and Zn 2p_{3/2} located at ~1044 and ~1021 eV respectively (Figure 4d) [24]. Therefore, such configurations accounts for typical MgAl and ZnAl LDH structures as suggested by the XRD and FT-IR analysis.

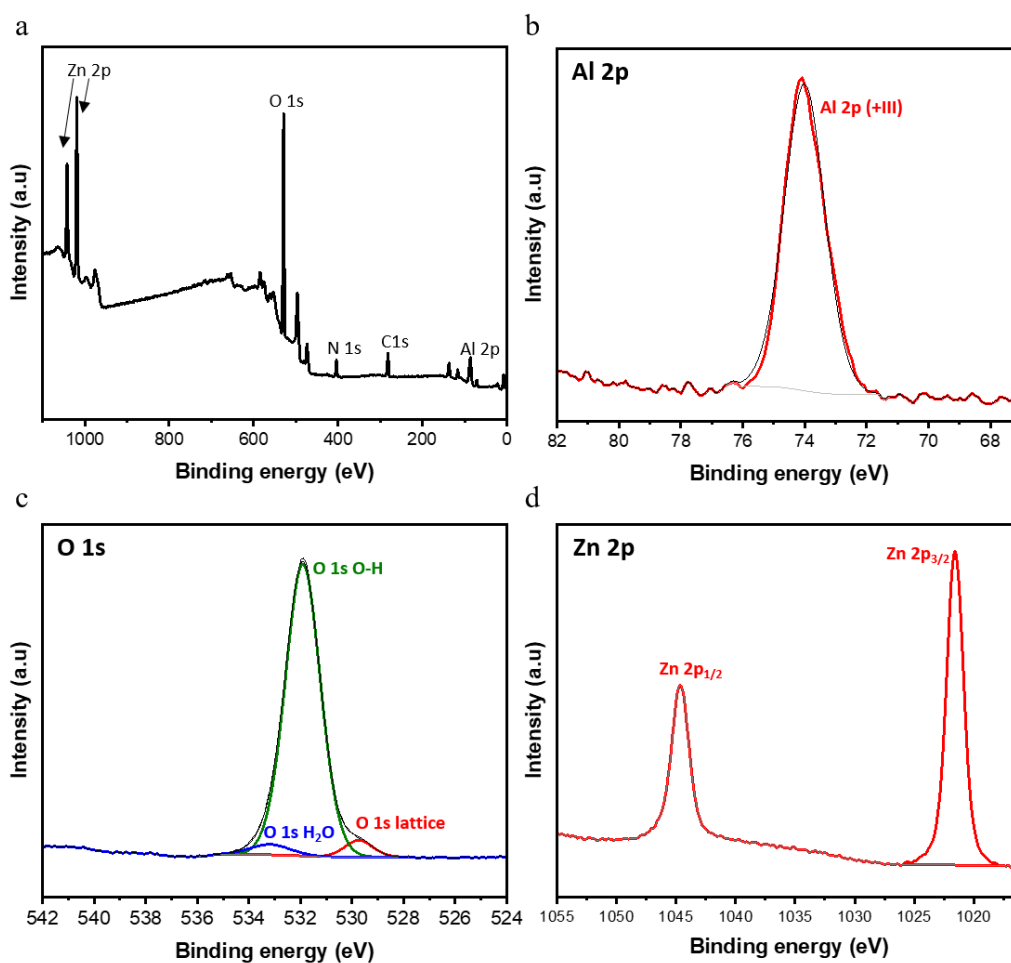


Figure 4. XPS spectra of MgAl LDH NPs. (a) Full spectrum. (b) Al 2p region. (c) O 1s region. (d) Zn 2p region.

2.3. Textural and morphological characterization

Both MgAl and ZnAl NPs presented a hexagonal lamellar structure as revealed by their SEM and AFM images (Figure 5). Both NPs also possessed similar average particle sizes (obtained as an

average particle size of 100 LDH NPs) extracted from their SEM images (172 ± 31 nm and 176 ± 44 nm, for MgAl and ZnAl NPs, respectively). Similar average particle size values (obtained as an average particle size of 100 LDH NPs) of 169 ± 35 nm for MgAl NPs and 171 ± 38 nm for ZnAl NPs were obtained from their AFM height images as well.

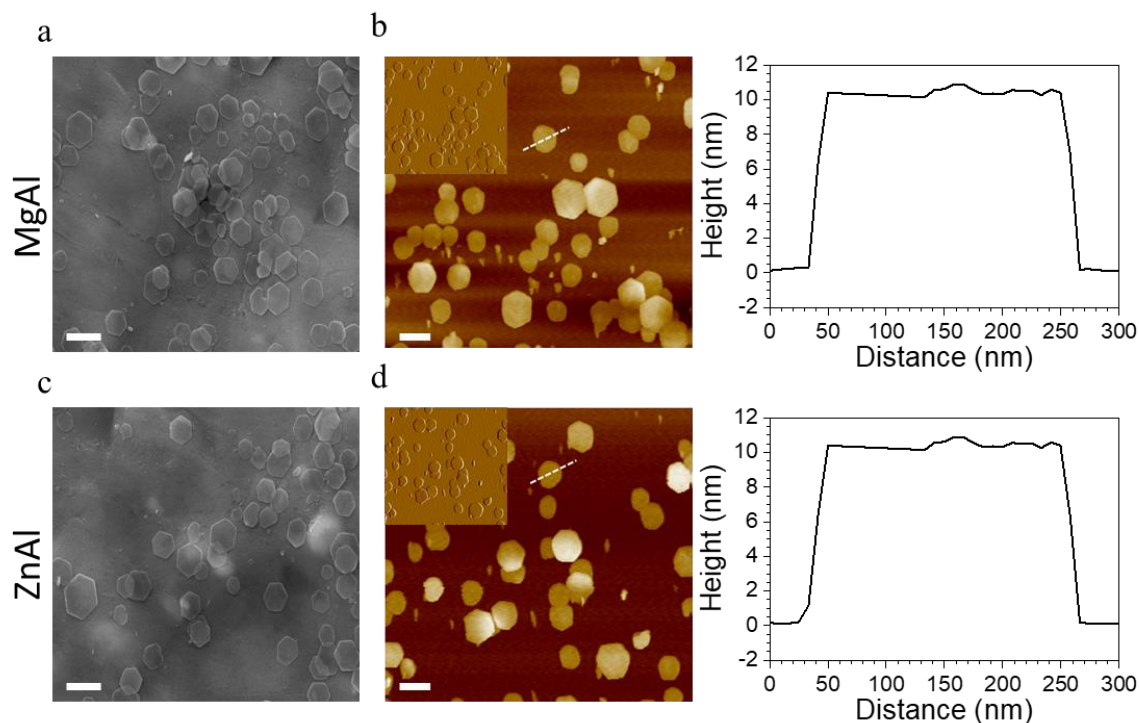


Figure 5. LDH NPs characterization. (a,c) SEM images of MgAl (a) and ZnAl (c) NPs (scale bar = 200 nm). (b,d) AFM height images of MgAl (b) and ZnAl (d) NPs (scale bar = 200 nm, insets are deflection images showing the NPs surface ultra-structure) together with height profiles of single particles. Dashed lines marked on the height images represent the sections used to determine the height profiles.

The height profiles revealed that our synthesized NPs also had a similar average whole thickness (obtained as an average thickness of 100 LDH NPs) of 10.6 ± 0.4 and 10.4 ± 0.7 , respectively. The theoretical thickness of the LDH sheet is 0.48 nm [29,30]. Possible adsorption of anions on the surface may account for the deviation of ~ 0.30 nm. Van der Waals radius of hydrogen atoms (0.12 nm) may also be responsible for this deviation [29]. Therefore, such a thickness unambiguously implied the multilamellar nature (~ 12 layers) of the synthesized NPs [29,31].

3. Antibacterial activity of LDH NPs

The antibacterial activity of ZnAl and MgAl LDH NPs against *S. aureus* was first evaluated using agar disk diffusion method. The generated inhibition zone diameters and their mean values obtained from three repetitive trials are presented in **Figure 6a** and **b**. Broth microdilution turbidimetric tests were also carried out to determine the minimum inhibitory concentration (MIC) required to inhibit the growth of *S. aureus* by ZnAl and MgAl LDHs (**Figure 6c**).

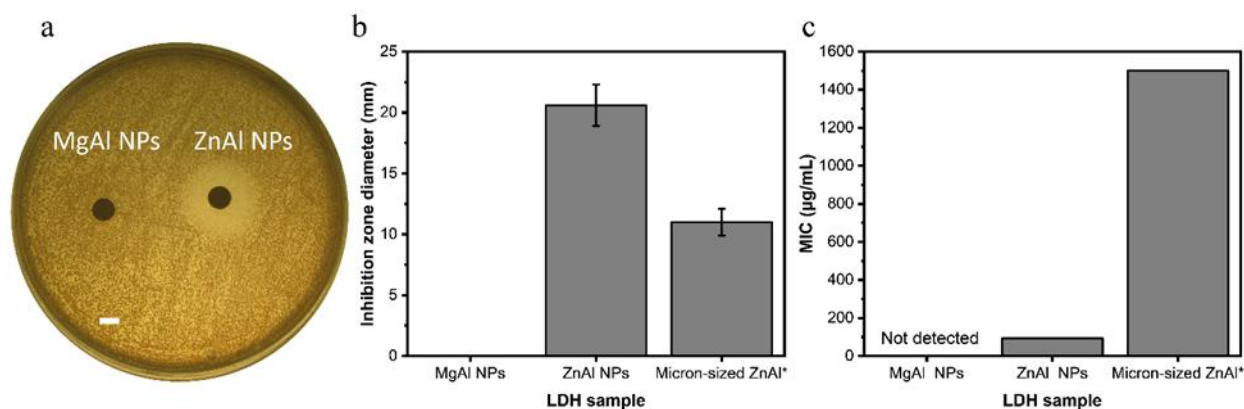


Figure 6. NPs antibacterial activity against *S. aureus*. (a) Agar disk diffusion test using 10 mg/mL ZnAl and MgAl NPs suspensions (scale bar = 5 mm). (b) Mean zone of inhibition of MgAl, ZnAl NPs and micron-sized ZnAl LDH calculated as the average inhibition diameters of three repetitive trials. (c) MIC values for MgAl, ZnAl NPs and micron-sized ZnAl LDH calculated as the average MIC of three repetitive trials. *Data for micron-sized ZnAl LDH are obtained from **Chapter 3**.

ZnAl LDH NPs showed an efficient antibacterial effect against *S. aureus* with an average inhibition zone diameter of 20.6 mm and MIC value of 93.8 µg/mL. On the other hand, MgAl LDH NPs did not provide any antibacterial activity revealed by any of the two antibacterial tests, and thus played the role of a negative control in this case.

The superior antibacterial activity of ZnAl LDH NPs could be attributed to the nature of their constituent divalent metal, *i.e.*, Zn²⁺. In fact, we have already proved that Zn(II)-based LDHs possessed a superior antibacterial activity toward *S. aureus* in comparison to other M(II)-based LDHs (M(II) = Mg, Co, Ni, Co). Moreover, it was also previously reported that Zn(II)-based NPs have a strong antibacterial effect toward a broad range of bacteria [32]. Such an effect may be achieved by adhering to bacteria, changing its charge distribution and blocking the transport of nutrients in and out of the membrane, or else by binding to bacterial intracellular DNA leading to their denaturation [32–34].

The antibacterial activity of the prepared ZnAl LDH NPs against *S. aureus* was slightly higher than those reported by Dutta *et al.* for ~250 nm-sized ZnAl LDHs having a MIC value of 200 µg/mL against *S. aureus* [35], yet remarkably superior to those of micron-sized Zn(II)-based LDHs prepared by Lobo-Sanchez *et al.* (MIC value of 10,000 µg/mL) [36]. On the other hand, Zn(II)-based LDH NPs having a particle size ~50 nm reported by Moaty *et al.* presented a MIC value of 15.6 µg/mL against the same bacterial strain, which is superior to that of our ZnAl LDH NPs [37]. Such a difference in the antibacterial activity should be interpreted very cautiously, since many parameters play a role in the antibacterial properties of LDHs including their different physicochemical properties, the different tested strains and to the different followed experimental procedures used to demonstrate the antibacterial test assays.

In this chapter, we performed the antibacterial activity tests with identical experimental procedures reported in **Chapter 3**. We showed that the antibacterial activity of micron-sized ZnAl LDHs (particle size ~ 1 µm) was related to released Zn²⁺ ions (**Mechanism 2**) which was found to be 3.3% relative to the total amount of metal zinc ions initially present in the nitrate-intercalated ZnAl LDHs. Consequently, the tested LDH sample showed an inhibition zone diameter of 11 mm. On the other hand, the partial dissolution profile Zn²⁺ released out of ZnAl LDH NPs (particle size ~ 167 nm) used in this study was found to be 6.8%. Interestingly, the increase in inhibition zone diameters for ZnAl LDH NPs used in this study was almost in the same order (~2 times) of the increased amount of released zinc ions. The fact that these augmentations fall in the same range indicates that the enhanced antibacterial performance for ZnAl NPs in agar disk diffusion test can be related to Zn²⁺ release in broth media. As we have previously discussed in **Chapter 1**, inhibition zones are related to the diffusion phenomena, which agrees with such finding.

On the contrary, the MIC value can be impacted by all the antimicrobial mechanisms, *e.g.*, surface interactions and ROS generation. In this case, the MIC of ZnAl LDH NPs (93.8 µg/mL) used in this study was almost 16 times greater than that obtained previously for micron-sized ZnAl LDH (MIC = 1500 µg/mL). Taking into consideration that similar antibacterial tests assay protocols against the same strain were adopted in both studies, the increase in Zn²⁺ release by a factor of 2 cannot by itself explain the enhanced antibacterial activity of ZnAl LDH NPs. In fact, this seems to be more related to the lateral crystal size of LDHs which was reduced by almost 6 times in the case of ZnAl NPs compared to micron-sized LDHs used previously. Additionally, the great

difference in MIC values between micron-sized particles and our newly synthesized NPs could also be related to the ability of NPs to provide a stable mobile suspension in solution, whereas micron-sized LDH particles were sedimented.

This provides an evidence concerning the role of surface interactions in the antibacterial effect of LDHs (**Mechanism 1**). In this context, smaller size LDHs were able to induce an enhanced antibacterial effect due to their larger surface area (in this case, the surface is 36 times greater for the NPs) and a higher mobility of the NPs in a stable suspension promoting more accessible surface and contact with the tested *S. aureus* bacteria [38–40].

Finally, it is important to mention that the contribution of ROS generation to the antibacterial activity of our ZnAl LDH NPs (**Mechanism 3**) could be eliminated since all experiments were performed inside an incubator in the absence of light and the production of ROS by LDHs is only pronounced in the presence of a suitable light source.

4. Effect of LDH NPs treatment on the morphology of *S. aureus* cells

AFM imaging was used to visualize the surface topography of *S. aureus* cells before and after treatment with ZnAl and MgAl LDH NPs at concentration of 93.8 $\mu\text{g/mL}$, corresponding to MIC value of ZnAl LDH NPs. Additionally, the roughness parameter Rq (root mean square of the heights) was obtained from AFM images performed on the top of bacteria at a high magnification of $400 \times 400 \text{ nm}^2$ scanning areas. The measured roughness parameter for all treated/untreated cells was performed on a similar area to that of the high magnification AFM images, *i.e.*, $400 \times 400 \text{ nm}^2$ (512 samples/line; 262,144 data points).

Table 1. Roughness parameter Rq of *S. aureus* cells untreated and treated with ZnAl and MgAl LDH NPs.

<i>S. aureus</i> cells	Rq (nm)
Untreated	15.9 ± 0.6
Treated with MgAl	16.8 ± 0.8
Treated with ZnAl	49.5 ± 0.7

As shown in **Figure 7a** and **b**, untreated cells as well as those treated with non-antibacterial MgAl LDH NPs presented regular spheroid morphologies and smooth surfaces with quite similar roughness values (**Table 1**). The obtained Rq values seemed to be greater than those previously obtained in the literature [41,42], probably due to the different selected measurement area and/or used AFM imaging conditions (liquid/air).

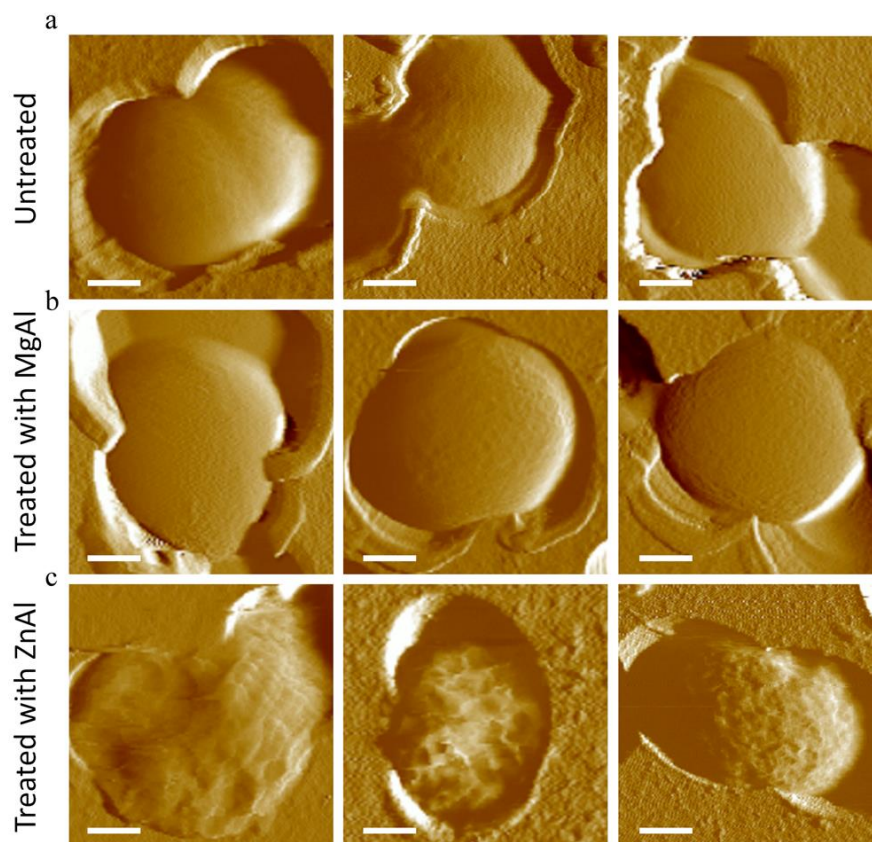


Figure 7. AFM deflection images of *S. aureus* in liquid (scale bar = 250 nm). (a) Untreated *S. aureus* cells. (b) *S. aureus* cells treated with MgAl LDH NPs at MIC value of ZnAl LDH NPs. (c) *S. aureus* cells treated with ZnAl LDH NPs at MIC.

On the other hand, cells treated with antibacterial ZnAl LDH NPs were completely distorted with highly corrugated surfaces presenting hollows and crests (**Figure 7c**). Similar cells damage observations were previously reported [42–45]. Moreover, cells treated with ZnAl LDH NPs were found to have 3 times rougher surfaces than untreated and MgAl NPs treated cells (**Table 1**). The increase in surface roughness of bacteria suggests the existence of cell wall damages induced by ZnAl LDH NPs [41,42], which could eventually be followed by cell lysis and subsequent leakage of intracellular components [45].

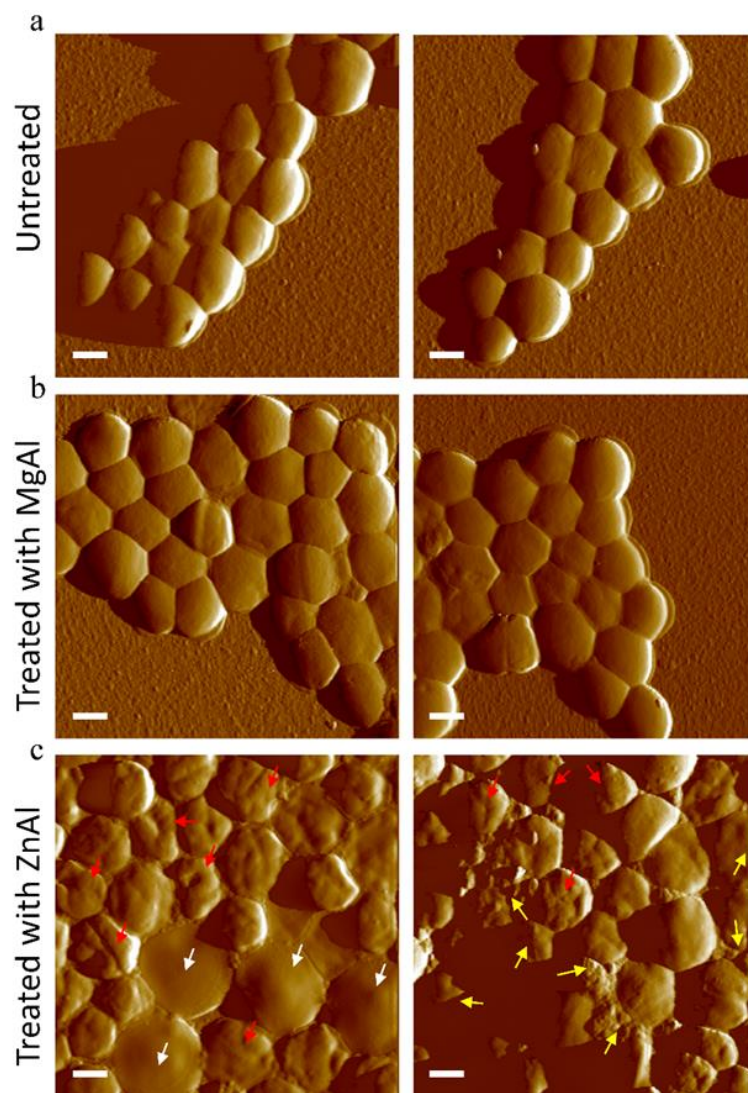


Figure 8. AFM deflection images of *S. aureus* cells in air (scale bar = 500 nm). (a) Untreated *S. aureus* cells. (b) *S. aureus* cells treated with MgAl LDH NPs at MIC value of ZnAl LDH NPs. (c) *S. aureus* cells treated with ZnAl LDH NPs at MIC. White arrows point to enlarged swelled cells. Red arrows point to distorted cells. Yellow arrows point to cell debris.

To examine the morphological impacts of antibacterial ZnAl LDH on a greater fraction of cells, *S. aureus* were immobilized on mica substrates and imaged in air. Although imaging in air is not physiologically relevant, it can enhance morphological features and help to differentiate topographical differences between cells [46].

Untreated and MgAl NPs treated *S. aureus* cells appeared on the mica surface as grape-like clusters of round cocci with homogeneous cellular shapes and regular surfaces (**Figure 8a** and **b**). The

diameter of cells observed in clusters varied from 600 to 1080 nm and the average value was 752 ± 115 nm, typical for this type of microorganism [47,48].

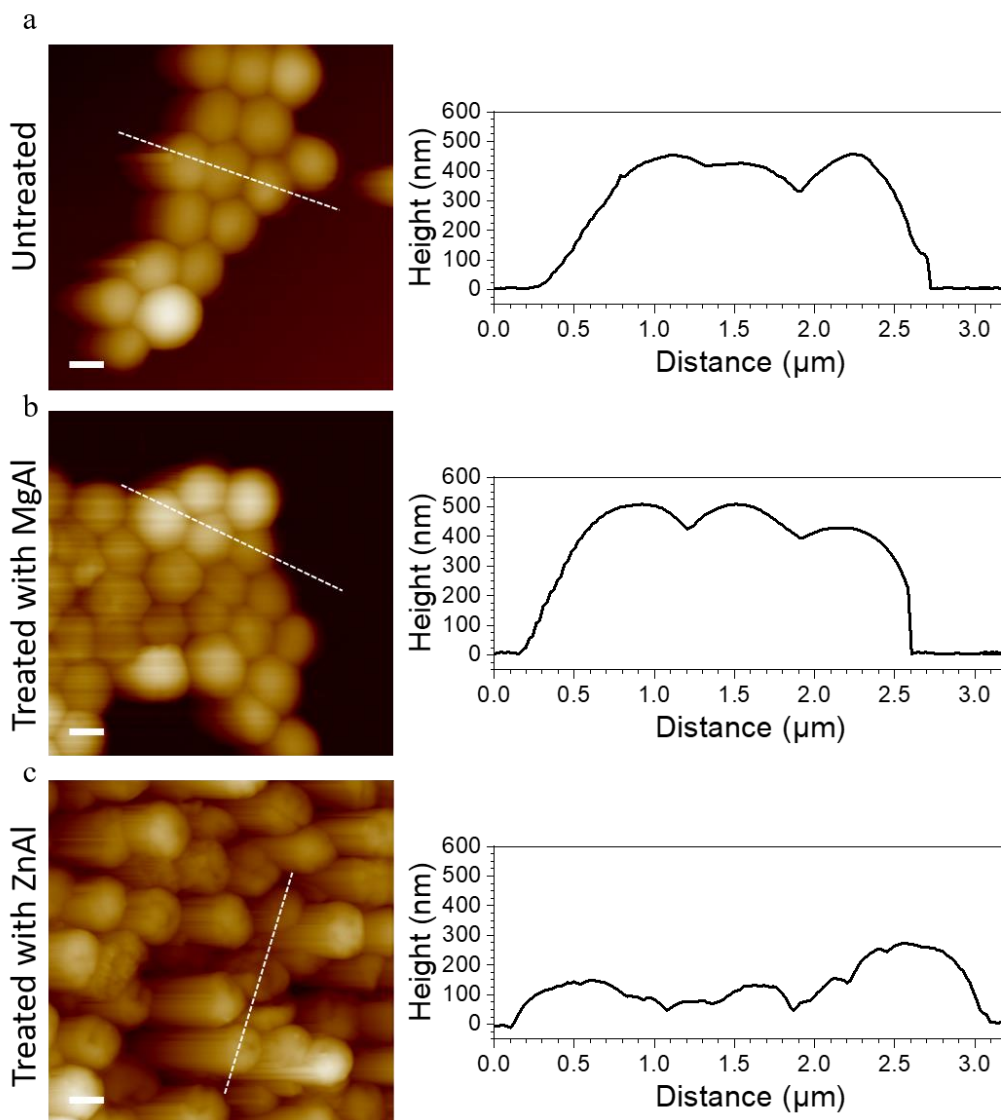


Figure 9. AFM height images of *S. aureus* cells in air (scale bar = 500 nm) together with the height profiles of three cells taken along the dashed lines marked on their AFM height images. (a) Untreated *S. aureus* cells. (b) *S. aureus* cells treated with MgAl LDH NPs at MIC value of ZnAl LDH NPs. (c) *S. aureus* cells treated with ZnAl LDH NPs at MIC.

Upon treating *S. aureus* with antibacterial ZnAl LDH NPs, nearly all cells presented abnormal shapes and irregular surfaces (**Figure 8**). Some cells were enlarged in diameter (~ 1400 nm) suggesting cellular swelling due to ZnAl NPs treatment. Other cells appeared completely distorted

with deep grooves, crests, hollows and even some split surfaces. Finally, some cells were completely disrupted or lysed leaving behind some cell debris covering the mica substrate.

The corresponding height profiles of bacterial cells immobilized on mica substrate were also determined (**Figure 9**). Cells treated with MgAl NPs showed a height profile of 480 ± 45 nm quite similar to that of healthy untreated cells (445 ± 19 nm). In contrary, *S. aureus* cells treated with ZnAl LDH NPs presented a lower height profile (180 ± 77 nm), suggesting their collapse. Consequently, cells treated with antibacterial ZnAl LDH NPs did not only exhibit a different morphology than those of healthy untreated ones but also different height profiles. Similar effect was previously noted for damaged *Escherichia coli* cells [45].

All these observations suggest that ZnAl LDH NPs induce an antibacterial effect on *S. aureus* cells by targeting their cell wall leading to their damage, swelling or collapse, leakage of intercellular components and subsequently to the death of the microorganism [42–45].

5. Synthesis and characterization of LDH films and LDH-functionalized tips

Surface interactions occurring at the interface between bacteria and ZnAl LDH NPs are probably a main contributor to their antibacterial effect. In order to decipher the role of surface interactions in the antibacterial activity of ZnAl LDH NPs by AFM-based FS, AFM tips were functionalized with LDHs. This was performed by growing LDH films directly on the surface of silicon nitride AFM tips. However, since it is quite difficult to perform LDH characterizations directly on AFM tips, the characterization was done on LDH films initially grown on silicon wafers.

5.1. Synthesis

ZnAl and MgAl LDH films were synthesized on silicon wafers by *in-situ* growth method adapted from Zhang *et al.* [49]. First, silicon wafers were cleaned with Piranha solution and coated with a thin layer of aluminum (~10 nm) by plasma sputtering. The aluminum coated silicon substrate was then placed in a Teflon-lined autoclave containing a solution of ammonium nitrate (NH_4NO_3) acting as pH regulator and divalent metal ion salt to provide a source of the divalent metal for the

LDH film ($M(\text{NO}_3)_2 \cdot 6\text{H}_2\text{O}$; $M = \text{Zn}, \text{Mg}$). The pH of the solutions was initially fixed at 6.5 and 7.5 for ZnAl and MgAl LDH films, respectively and the synthesis was carried out at 80°C for 24h.

5.2. Structural characterization

The obtained M(II)/Al(III) molar ratios evaluated by ICP-MS analysis for ZnAl and MgAl LDH films were 2.1 and 2.05, respectively. These values correspond again very well to the expected M(II)/Al(III) molar ratio of 2, similar to those for nano-sized and micron-sized ZnAl and MgAl LDHs.

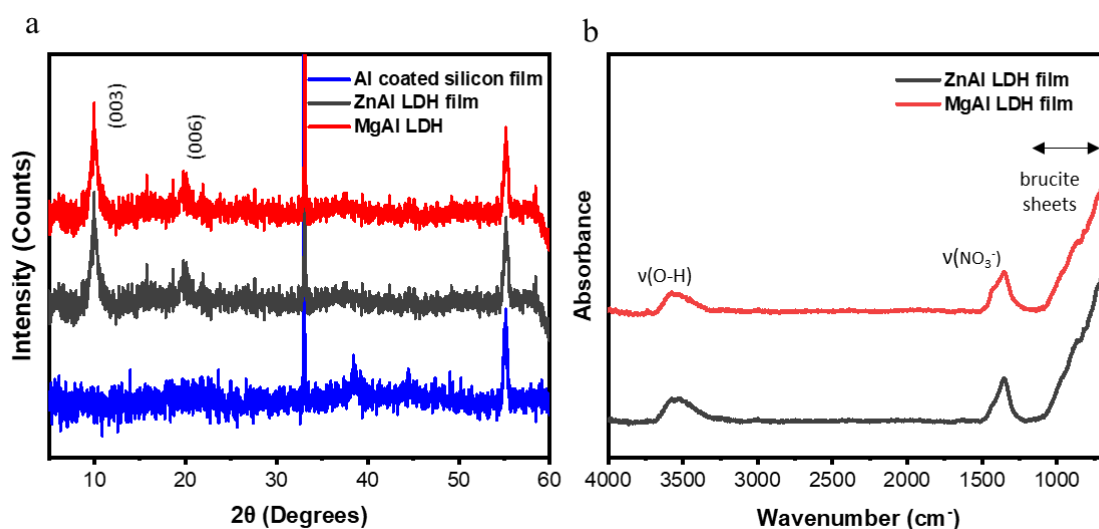


Figure 10. LDH films structural characterization. (a) XRD patterns of MgAl and ZnAl LDH films. (b) FT-IR spectra of MgAl and ZnAl LDH films.

The XRD patterns of the synthesized ZnAl and MgAl LDH films exhibited the characteristic (003) and (006) basal reflections of the LDH structure, which confirmed the formation of the LDH film on the silicon substrate (**Figure 10a**). The interlayer spacing of both LDH films was 0.89 ± 0.01 nm, which is in perfect agreement with the interlayer spacing values for nitrate-intercalated LDHs and their previously synthesized NPs counterparts [21,22]. The quasi-absence of non-basal reflections at high angles implied the *c*-oriented growth of LDH crystallites in the films [50,51]. Similarly, the FT-IR spectra of ZnAl and MgAl films also confirmed the successful growth of nitrate-intercalated LDH films without any amorphous impurity phases (**Figure 10b**).

5.3. Textural and morphological characterization

The morphology of the LDH films and LDH-functionalized AFM tips were examined by SEM imaging. As shown in **Figure 11a** and **b**, MgAl and ZnAl LDH films were successfully grown on the surface of silicon wafer with their *c*-axes mostly perpendicular to the substrate.

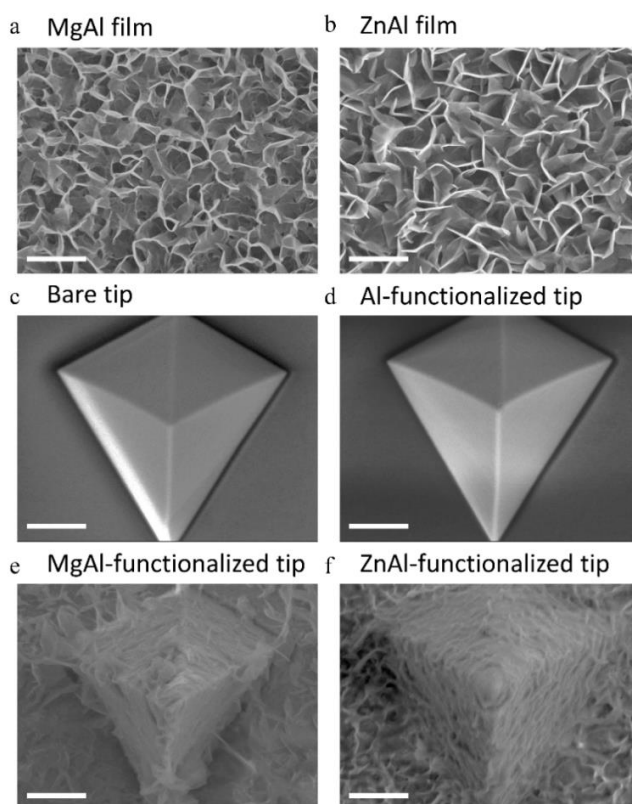


Figure 11. SEM images of LDH films on silicon wafers and AFM tips (scale bar = 1 μm). (a) MgAl LDH film grown on silicon wafer. (b) ZnAl LDH film grown on silicon wafer. (c) Bare silicon nitride AFM tip. (d) Al-functionalized silicon nitride AFM tip. (e) MgAl LDH-functionalized silicon nitride AFM tip. (f) ZnAl LDH-functionalized silicon nitride AFM tip.

Table 2. M(II)/A(III) molar ratio in LDH films grown on silicon wafers and LDH-functionalized AFM tips.

Sample	M(II)/Al(III) determined by EDS analysis
MgAl LDH films grown on silicon wafer	1.99
ZnAl LDH films grown on silicon wafer	2.02
MgAl LDH-functionalized tips	1.97
ZnAl LDH functionalized tips	2.1

The morphology of the observed structures showed a “cauliflower-like” shape, very similar to that reported by other groups [52,53], using comparable *in-situ* growth wet-chemistry synthesis method. Electron dispersive X-ray spectroscopy (EDS) was further performed on the LDH films (Figure 12) which ensured the growth of LDH films on silicon wafers with a M(II)/Al(III) molar ratio similar to that determined by ICP analysis, *i.e.*, ~2 (Table 2).

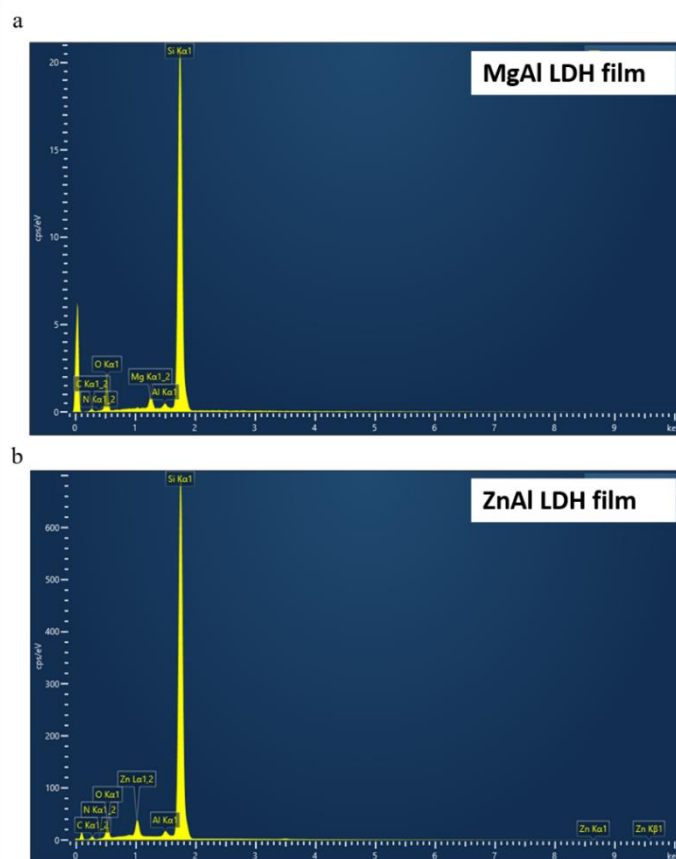


Figure 12. EDS spectra of LDH films grown on silicon wafers. (a) MgAl LDH film. (b) ZnAl LDH film. The peak appearing at 0 keV is attributed to the noise from the EDS detector.

The thickness of the formed films was determined by cross-sectional SEM imaging and was found to be 312 ± 24 nm and 315 ± 25 nm for MgAl film and ZnAl LDH films, respectively (Figure 13a and c). Scratch method was also used to determine the thickness of the obtained films by AFM imaging and the obtained values (314 ± 10 nm and 316 ± 12 nm for MgAl film and ZnAl LDH films, respectively) were in good agreement with those found by SEM imaging (Figure 13b and d).

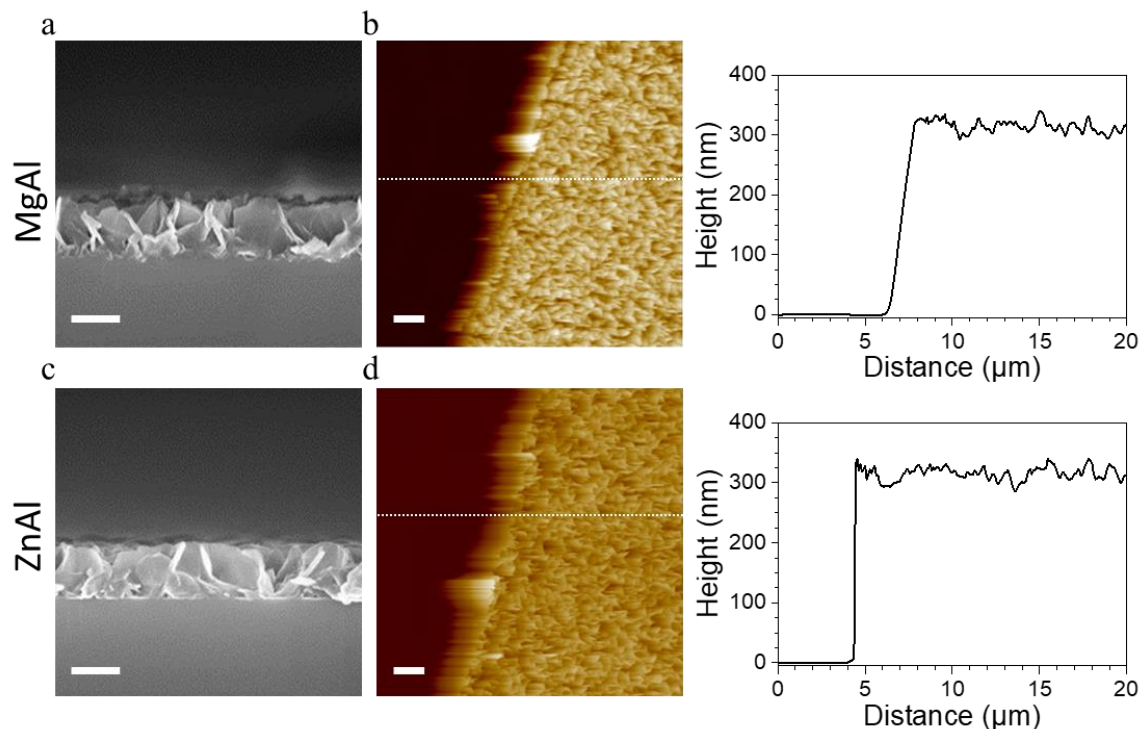


Figure 13. SEM and AFM images used to determine the average thickness of the LDH films. (a,c) SEM cross-sectional images of MgAl (a) and ZnAl (c) LDH films (scale bar = 250 nm). (b,d) AFM height images of MgAl (b) and ZnAl (d) LDH films interfaces with silicon substrates revealed by a scratch (scale bar = 2 μm) together with their height profiles. The dashed lines marked on the height images represent the sections used to determine the height profiles of the films.

Similar synthesis conditions were adapted to grow LDH films on silicon nitride AFM tips, where bare silicon nitride tip (**Figure 11c**) was first coated with aluminum (**Figure 11d**). ZnAl and MgAl LDH films were then grown directly on the surface of aluminum-coated tips (**Figure 11e** and **f**). The morphology of LDH films grown on the tips was similar to those grown on silicon wafers, however, the hexagonal particles in this case seemed to be less defined probably due to the pyramidal geometry of tip. The successful functionalization of AFM tips with MgAl and ZnAl LDH films with a M(II)/Al(III) molar ratio ~ 2 similar to that obtained on LDH films grown on silicon wafers was also confirmed by EDS analysis (**Figure 14** and **Table 2**). However, the greater nitrogen content in LDH-functionalized tips compared to LDH films grown on silicon wafer (**Figure 12**) is due to the chemical composition of the tips which is made up of silicon nitride materials.

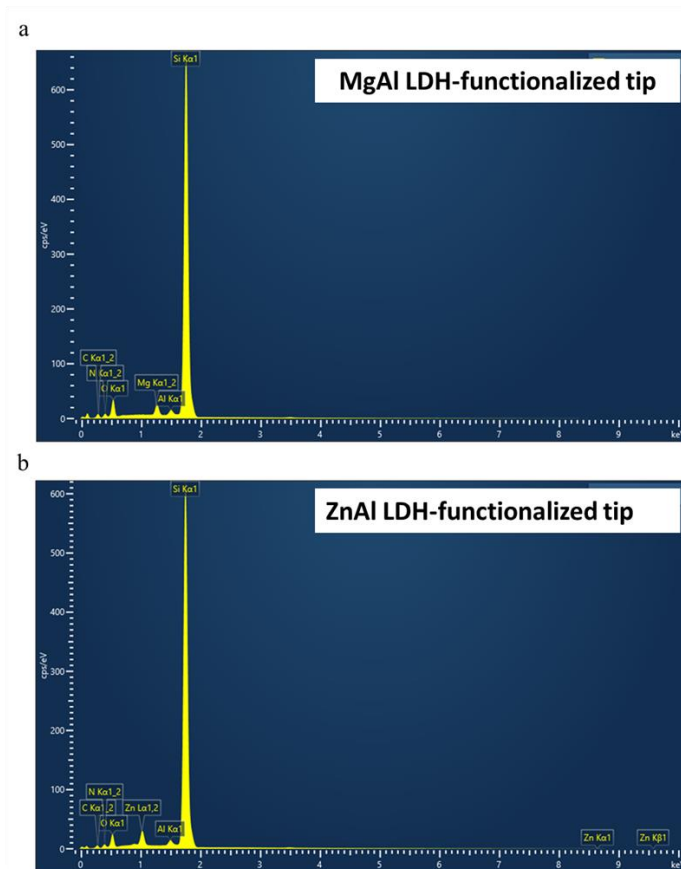


Figure 14. EDS spectra of LDH-functionalized tips performed on the apex of the probe. (a) MgAl LDH-functionalized tip. (b) ZnAl LDH-functionalized.

6. Force spectroscopy measurements between LDH-functionalized tips and *S. aureus* cells

6.1. Force spectroscopy using ZnAl-functionalized tips

Single living *S. aureus* cells were probed by ZnAl-functionalized tips using AFM-based FS. **Figure 15a-c** and **Figure 16b** and show adhesion maps, adhesion force and rupture length histograms as well as representative force-distance (FD) curves obtained between different *S. aureus* cells and ZnAl tips.

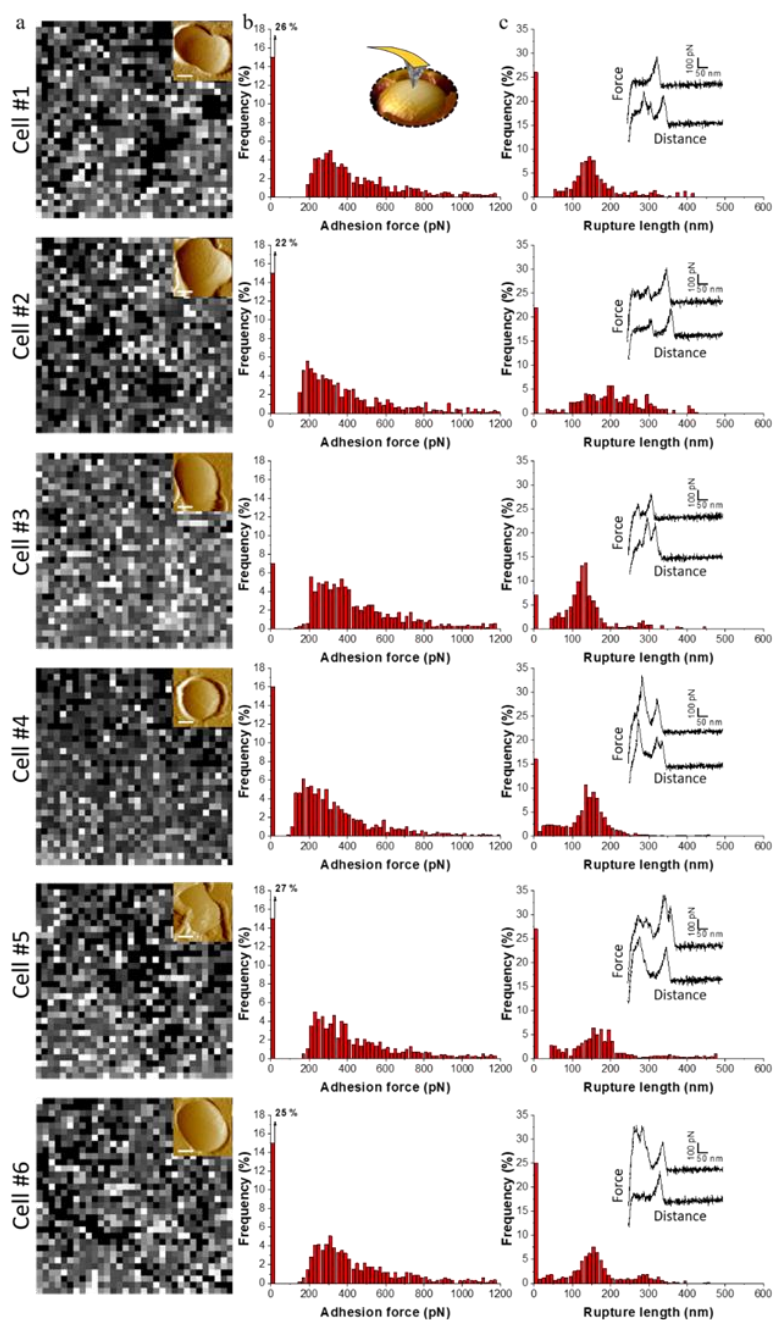


Figure 15. FS on live *S. aureus* cells with ZnAl-functionalized AFM tips. (a) Adhesion maps ($400 \times 400 \text{ nm}^2$) recorded on *S. aureus* cells (insets are AFM deflection images of probed cells, scale bar = 250 nm) with ZnAl-functionalized AFM tips. White/grey pixel correspond to adhesive events and black pixels correspond to non-adhesive events (scale 0-1000 pN). (b, c) Corresponding adhesion force (b) and rupture length (c) histograms together with representative force-distance curves. Data were obtained from four independent experiments using different tips and independent cell cultures.

Adhesive pixels were randomly distributed on the maps suggesting the homogeneous adhesion of ZnAl LDH to the host cell surface. Most recorded FD curves showed an adhesion signature with

a frequency ranging from 63 to 93% (**Figure 15b** and **Figure 16b**). The variation in adhesion frequencies among the probed cells may be attributed to the slight heterogeneity in cell wall microarchitecture and composition or else to the position of ZnAl-functionalized AFM tips during measurements. Measured adhesion forces of all cells mainly ranged from 180 to 1000 pN with rupture lengths ranging between 10 and 300 nm (**Figure 15c**). Such finding indicates that ZnAl tips were able to recognize *S. aureus* cell wall with high adhesion frequency, thus suggesting the presence of surface interactions occurring at the interface between ZnAl LDHs and bacterial cell wall.

6.2. FS comparison of ZnAl-, MgAl- and Al-functionalized tips

To determine whether the presented surface interactions between ZnAl LDH and *S. aureus* are specifically related to their antibacterial properties, the adhesion behavior of ZnAl-functionalized tips was compared to that of control Al-coated tips as well as to that of non-antibacterial MgAl-functionalized ones. For this purpose, individual living *S. aureus* cells trapped in porous membranes (**Figure 16a**) were probed using the three different AFM tips, *i.e.*, ZnAl-functionalized, MgAl-functionalized and Al-functionalized tips.

Upon probing the same cells using Al-functionalized tips, no considerable adhesion between Al-functionalized tips and *S. aureus* was noticed, where the adhesion frequencies and force magnitudes did not exceed 11% and 280 pN (**Figure 16d**), respectively. This indicates that constituent aluminum trivalent metal ions do not contribute to the observed adhesion surface interactions between ZnAl LDHs and the cell wall of *S. aureus*.

MgAl-functionalized tips adopting quite similar morphologies to those of ZnAl-functionalized ones (**Figure 11**) were also used to probe the cell surfaces of *S. aureus*. This was actually done for two main reasons. First, to eliminate the possibility of the contribution of the LDH-functionalized tips morphology to the reliability of our force measurements. Second, to determine whether the observed surface interactions between the cell wall of *S. aureus* and ZnAl LDHs are specific to Zn-based LDHs and to further link them to their demonstrated antibacterial properties.

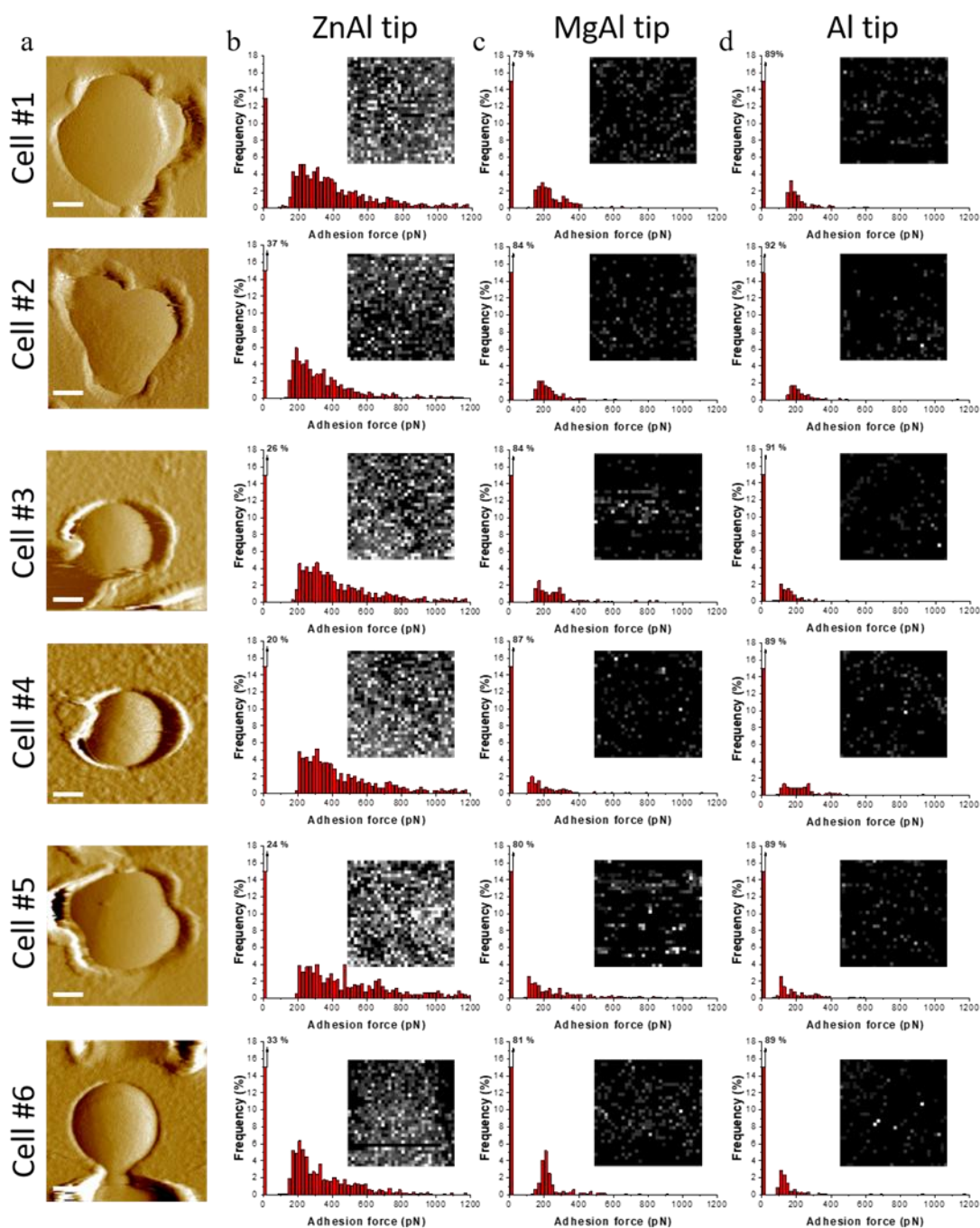


Figure 16. FS with functionalized tips reveals specific interactions for ZnAl tips. (a) Topography images of *S. aureus* cells trapped in porous membranes (scale bar = 250 nm) and probed with functionalized AFM tips. (b,c,d) Adhesion force histograms and adhesion force maps (insets, 400 x 400 nm²) obtained on the top of cells using ZnAl-functionalized AFM tip (b) MgAl-functionalized AFM tip (c) Al-functionalized AFM tip (d). White/grey pixel correspond to adhesive events and black pixels correspond to non-adhesive events (scale 0-1000 pN). Data were obtained from four independent experiments using different tips and independent cell cultures.

Although cells probed with MgAl-functionalized tips showed slightly higher adhesion frequencies (13-21%) and force magnitudes (150-300 pN) in comparison to Al-functionalized tips, their adhesion behavior in terms of both adhesion frequencies and force magnitudes were remarkably weaker than those of ZnAl-functionalized tips (**Figure 16**). This indicates that our LDH functionalization protocol did not impose critical complications to the consistency of our force measurements even when the morphology of the AFM tip was modified.

At the end of each experiment, both LDH-functionalized tips were washed with ethanol, dried with nitrogen and imaged again using SEM. The functionalized tips seemed to be intact after being in contact with the bacteria during the experiments (**Figure 17**) thus confirming the robust functionalization protocol used.

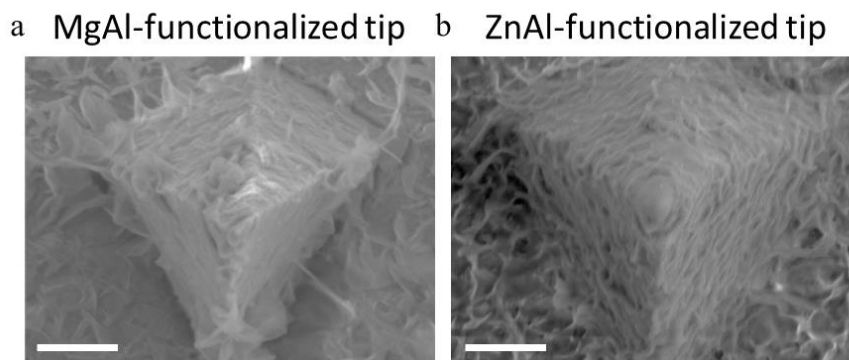


Figure 17. SEM images of LDH functionalized-AFM tips after being used in force measurement experiments (scale bar = 1 μm). (a) MgAl-functionalized silicon nitride AFM tip. (b) ZnAl-functionalized silicon nitride AFM tip.

We had previously established in this chapter that ZnAl LDH NPs possessed specific and superior antibacterial properties in comparison to non-antibacterial MgAl LDH NPs, which was validated by *S. aureus* growth inhibition (**Figure 6**) and imposing serious morphological impacts to their cell walls (**Figure 7** and **Figure 8**). Therefore, the specific adhesion interactions observed for antibacterial ZnAl LDHs provided a first insight about the contribution of direct contact interactions to the antibacterial activity of Zn-based LDHs (**Mechanism 2**). In fact, the sensitivity of microorganisms to different divalent metals-based materials is actually dependent on several factors, including the role each metal plays in normal metabolism, and the presence of specific binding sites for each metal [54,55]. *S. aureus* cells were highly sensitive to ZnAl LDHs probably due to the antibacterial role played by their constituent zinc components where they showed strong surface adhesion interactions with the tested bacterial membranes. In this context, ZnAl LDH NPs

were specifically able to recognize and adhere to *S. aureus* cells thus imposing serious damages to their cell walls by direct surface interactions.

6.3. FS using ZnAl-functionalized tips in presence of Zn^{2+}

In order to further investigate the behavior of specific surface interactions between Zn(II)-based LDHs and *S. aureus* cells in presence of released Zn^{2+} metal ions (**Mechanism 2**), the adhesion behavior of ZnAl-functionalized tips before and after one hour of the addition of Zn^{2+} ion salt (in a concentration similar to that released out of ZnAl LDH NPs, *i.e.*, 4.1 mmol/L) were compared.

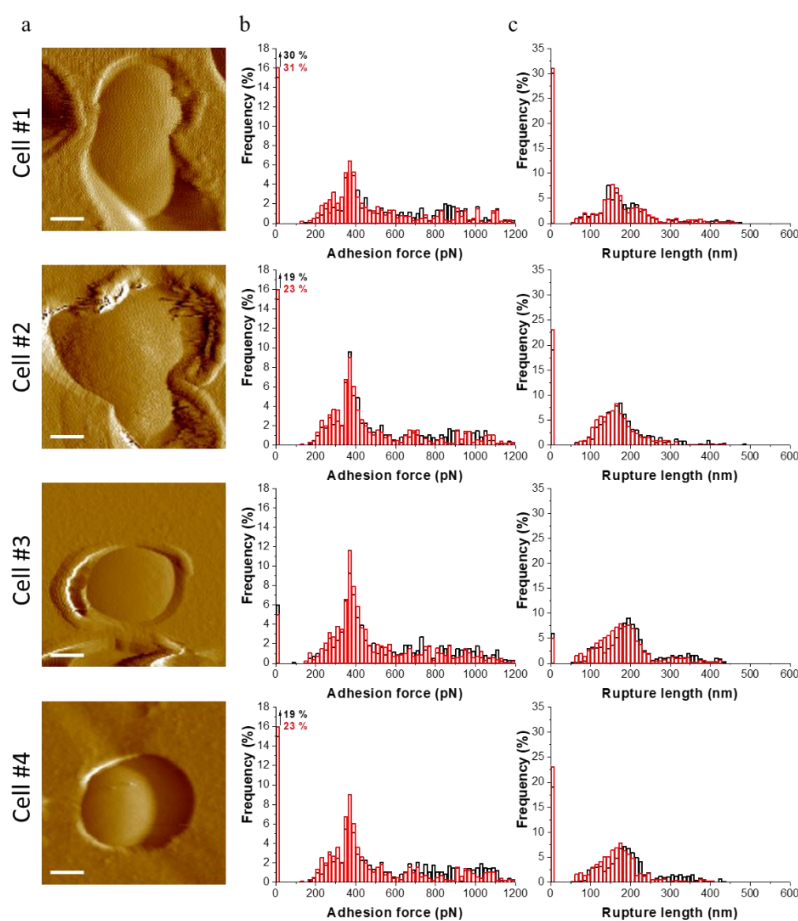


Figure 18. FS on live *S. aureus* cells with ZnAl-functionalized AFM tips before (black histograms) and after addition of Zn^{2+} salt (red histograms). (a) Topography images of *S. aureus* cells trapped in porous membranes (scale bar = 250 nm) and probed with ZnAl-functionalized AFM tips. (b,c) Corresponding adhesion force (b) and rupture length (c) histograms. Data were obtained from four independent experiments using different tips and independent cell cultures.

Upon probing the same cells (**Figure 18a**) using ZnAl-functionalized tips, no remarkable differences was observed neither in adhesion frequency nor in rupture length values were noticed

(Figure 18b and b) after the addition of Zn^{2+} ion salts. This indicates that released Zn^{2+} ions out of Zn(II)-based LDHs does not actually compete or affect the direct surface interactions occurring between ZnAl NPs and *S. aureus*. Therefore, the occurrence of antibacterial of LDHs mediated by release of divalent metal ions (Mechanism 2) does not suppress the action of antibacterial mechanism by direct surface interactions (Mechanism 1). A decent rigid comparison between these two different mechanisms will further be addressed in Chapter 6 where we will determine the contribution of each mechanism to the antibacterial activity of Zn(II)-based LDH NPs.

7. Conclusion

In this chapter, the role of surface interactions in the antibacterial activity of ZnAl LDH NPs was studied. ZnAl LDH NPs exhibited specific antibacterial activity against *S. aureus* in comparison to non-antibacterial MgAl LDH.

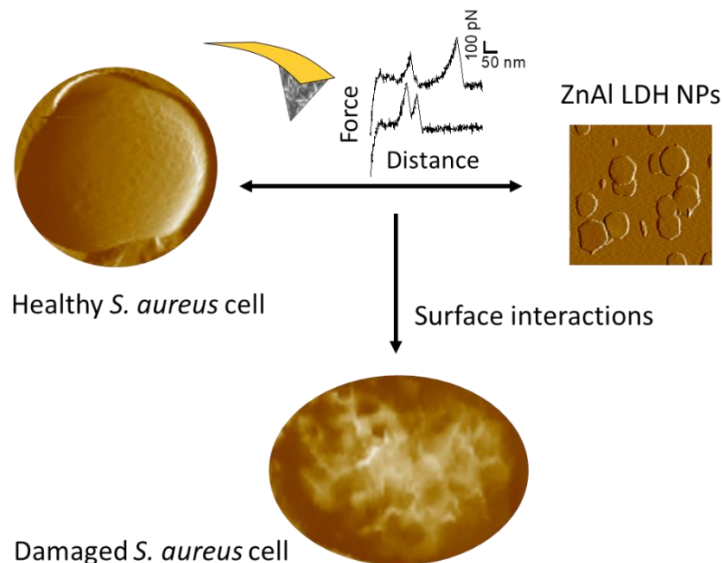


Figure 19. A schematic illustration of the proposed antibacterial mechanism of pristine LDHs through direct surface interactions between LDHs and bacteria (Mechanism 1). Scale is adjusted to clarify the illustration.

An evidence of the contribution of surface interactions to the antibacterial activity of LDHs was pronounced by the superior antibacterial activity of nano-sized ZnAl LDH NPs compared to micron-sized ZnAl LDHs. For similar quantities, agar disk diffusion showed an inhibition zone two times larger and broth microdilution antibacterial assays showed that the MIC was 16 times lower for ZnAl NPs, showing an effect beyond the simple dissolution into Zn^{2+} antibacterial ions.

Therefore, direct contact interactions have to be considered, which is evidenced by serious morphological impacts including membrane distortion, swelling and dissociation into cell debris which were observed on the surface of *S. aureus* cells upon being treated with ZnAl LDH NPs at MIC.

In addition, LDH-functionalized AFM tips were prepared and used to probe surface adhesion interactions between the cell surface and LDHs using AFM-based FS. ZnAl-functionalized AFM tips were able to recognize the cell wall of *S. aureus* cells with high adhesion frequencies. Additionally, comparison of the adhesion behavior of three different AFM tips, *i.e.*, Al-coated, MgAl functionalized and ZnAl-functionalized tips, indicated the presence of specific surface interactions between ZnAl LDHs and *S. aureus* cells. Such finding suggested the presence of a strong correlation between the specific ability of zinc-based LDHs to adhere and damage bacterial cell walls, thus supporting the previously suggested antibacterial mechanism of pristine LDHs by direct surface interactions (**Mechanism 1, Figure 19**).

References

- [1] W. Zhang, Y. Zhao, W. Wang, J. Peng, Y. Li, Y. Shanguan, G. Ouyang, M. Xu, S. Wang, J. Wei, H. Wei, W. Li, Z. Yang, Colloidal Surface Engineering: Growth of Layered Double Hydroxides with Intrinsic Oxidase-Mimicking Activities to Fight Against Bacterial Infection in Wound Healing, *Adv. Healthc. Mater.* 9 (2020) 2000092.
- [2] S. Jin, P.H. Fallgren, J.M. Morris, Q. Chen, Removal of bacteria and viruses from waters using layered double hydroxide nanocomposites, *Sci. Technol. Adv. Mater.* 8 (2007) 67–70.
- [3] J. Liu, C. Duan, J. Zhou, X. Li, G. Qian, Z.P. Xu, Adsorption of bacteria onto layered double hydroxide particles to form biogranule-like aggregates, *Appl. Clay Sci.* 75–76 (2013) 39–45.
- [4] T. Alekseeva, V. Prevot, M. Sancelme, C. Forano, P. Besse-Hoggan, Enhancing atrazine biodegradation by *Pseudomonas* sp. strain ADP adsorption to Layered Double Hydroxide bionanocomposites, *J. Hazard. Mater.* 191 (2011) 126–135.
- [5] D. Wang, F. Peng, J. Li, Y. Qiao, Q. Li, X. Liu, Butyrate-inserted Ni–Ti layered double hydroxide film for H₂O₂-mediated tumor and bacteria killing, *Mater. Today*. 20 (2017) 238–257.
- [6] W. Zhang, A.G. Stack, Y. Chen, Interaction force measurement between *E. coli* cells and nanoparticles immobilized surfaces by using AFM, *Colloids Surf. B Biointerfaces*. 82 (2011) 316–324.
- [7] Q. Huang, H. Wu, P. Cai, J.B. Fein, W. Chen, Atomic force microscopy measurements of bacterial adhesion and biofilm formation onto clay-sized particles, *Sci. Rep.* 5 (2015) 16857.
- [8] A. Beaussart, C. Feuillie, S. El-Kirat-Chatel, The microbial adhesive arsenal deciphered by atomic force microscopy, *Nanoscale*. 12 (2020) 23885–23896.
- [9] A. Beaussart, S. El-Kirat-Chatel, Microbial adhesion and ultrastructure from the single-molecule to the single-cell levels by Atomic Force Microscopy, *Cell Surf.* 5 (2019) 100031.
- [10] S.A. James, N. Hilal, C.J. Wright, Atomic force microscopy studies of bioprocess engineering surfaces - imaging, interactions and mechanical properties mediating bacterial adhesion, *Biotechnol. J.* 12 (2017) 1600698.
- [11] Q.K. Ong, I. Sokolov, Attachment of nanoparticles to the AFM tips for direct measurements of interaction between a single nanoparticle and surfaces, *J. Colloid Interface Sci.* 310 (2007) 385–390.
- [12] X. Liu, Interactions of Silver Nanoparticles Formed in Situ on AFM Tips with Supported Lipid Bilayers, *Langmuir*. 34 (2018) 10774–10781.
- [13] I.U. Vakarelski, S.C. Brown, B.M. Moudgil, K. Higashitani, Nanoparticle—terminated scanning probe microscopy tips and surface samples, *Adv. Powder Technol.* 18 (2007) 605–614.
- [14] I.U. Vakarelski, K. Higashitani, Single-Nanoparticle-Terminated Tips for Scanning Probe Microscopy, *Langmuir*. 22 (2006) 2931–2934.
- [15] O. Sqalli, I. Utke, P. Hoffmann, F. Marquis-Weible, Gold elliptical nanoantennas as probes for near field optical microscopy, *J. Appl. Phys.* 92 (2002) 1078–1083.
- [16] T. Okamoto, I. Yamaguchi, Photocatalytic deposition of a gold nanoparticle onto the top of a SiN cantilever tip, *J. Microsc.* 202 (2001) 100–103.
- [17] H.-W. Cheng, Y.-C. Chang, S.-N. Tang, C.-T. Yuan, J. Tang, F.-G. Tseng, Characterization of single 1.8-nm Au nanoparticle attachments on AFM tips for single sub-4-nm object pickup, *Nanoscale Res. Lett.* 8 (2013) 482.

- [18] Z.P. Xu, G. Stevenson, C.-Q. Lu, G.Q. (Max) Lu, Dispersion and Size Control of Layered Double Hydroxide Nanoparticles in Aqueous Solutions, *J. Phys. Chem. B.* 110 (2006) 16923–16929.
- [19] R.M.A. Lieth, ed., *Preparation and Crystal Growth of Materials with Layered Structures*, Springer Netherlands, Dordrecht, 1977.
- [20] F. Cavani, F. Trifirò, A. Vaccari, Hydrotalcite-type anionic clays: Preparation, properties and applications., *Catal. Today.* 11 (1991) 173–301.
- [21] S. Marappa, S. Radha, P.V. Kamath, Nitrate-Intercalated Layered Double Hydroxides – Structure Model, Order, and Disorder, *Eur. J. Inorg. Chem.* 2013 (2013) 2122–2128.
- [22] F.Z. Mahjoubi, A. Khalidi, M. Abdennouri, N. Barka, Zn–Al layered double hydroxides intercalated with carbonate, nitrate, chloride and sulphate ions: Synthesis, characterisation and dye removal properties, *J. Taibah Univ. Sci.* 11 (2017) 90–100.
- [23] R. Zhu, X. Zhu, Y. Zhu, Z. Wang, X. He, Z. Wu, L. Xue, W. Fan, R. Huang, Z. Xu, X. Qi, W. Xu, Y. Yu, Y. Ren, C. Li, Q. Cheng, L. Ling, S. Wang, L. Cheng, Immunomodulatory Layered Double Hydroxide Nanoparticles Enable Neurogenesis by Targeting Transforming Growth Factor- β Receptor 2, *ACS Nano.* 15 (2021) 2812–2830.
- [24] W. Bao, H. Tian, Y. Jiang, K. Zhu, R. Zhang, Y. Tan, W. Li, Z. Yu, L. Wang, Controlled preparation of Ni–Al LDH–NO₃ by a dual-anion intercalating process for supercapacitors, *Ionics.* 25 (2019) 3859–3866.
- [25] Z. Zhang, Z. Hua, J. Lang, Y. Song, Q. Zhang, Q. Han, H. Fan, M. Gao, X. Li, J. Yang, Eco-friendly nanostructured Zn–Al layered double hydroxide photocatalysts with enhanced photocatalytic activity, *CrystEngComm.* 21 (2019) 4607–4619.
- [26] B. Xiao, W. Zhu, Z. Li, J. Zhu, X. Zhu, G. Pezzotti, Tailoring morphology of cobalt–nickel layered double hydroxide via different surfactants for high-performance supercapacitor, *R. Soc. Open Sci.* 5 (2018) 180867.
- [27] P. Li, Y. Jiao, S. Yao, L. Wang, G. Chen, Dual role of nickel foam in NiCoAl-LDH ensuring high-performance for asymmetric supercapacitors, *New J. Chem.* 43 (2019) 3139–3145.
- [28] S. Kundu, M.K. Naskar, Carbon-layered double hydroxide nanocomposite for efficient removal of inorganic and organic based water contaminants – unravelling the adsorption mechanism, *Mater. Adv.* 2 (2021) 3600–3612.
- [29] L. Li, R. Ma, Y. Ebina, N. Iyi, T. Sasaki, Positively Charged Nanosheets Derived via Total Delamination of Layered Double Hydroxides, *Chem. Mater.* 17 (2005) 4386–4391.
- [30] T. Hibino, Delamination of Layered Double Hydroxides Containing Amino Acids, *Chem. Mater.* 16 (2004) 5482–5488.
- [31] Z. Liu, R. Ma, M. Osada, N. Iyi, Y. Ebina, K. Takada, T. Sasaki, Synthesis, Anion Exchange, and Delamination of Co–Al Layered Double Hydroxide: Assembly of the Exfoliated Nanosheet/Polyanion Composite Films and Magneto-Optical Studies, *J. Am. Chem. Soc.* 128 (2006) 4872–4880.
- [32] F. Peng, D. Wang, D. Zhang, H. Cao, X. Liu, The prospect of layered double hydroxide as bone implants: A study of mechanical properties, cytocompatibility and antibacterial activity, *Appl. Clay Sci.* 165 (2018) 179–187.
- [33] M. Sharma, P. Prasher, *Metallic Nanoparticles at the Biointerface*, in: C. Bhargava, A. Sachdeva (Eds.), *Nanotechnology*, 1st ed., CRC Press, 2020: pp. 261–276.
- [34] G. Vimbela, S.M. Ngo, C. Frazee, L. Yang, D.A. Stout, Antibacterial properties and toxicity from metallic nanomaterials, *Int. J. Nanomedicine.* Volume 12 (2017) 3941–3965.

- [35] S. Dutta, T.K. Jana, S.K. Halder, R. Maiti, A. Dutta, A. Kumar, K. Chatterjee, Zn₂Al-CO₃ Layered Double Hydroxide: Adsorption, Cytotoxicity and Antibacterial Performances, *ChemistrySelect*. 5 (2020) 6162–6171.
- [36] M. Lobo-Sánchez, G. Nájera-Meléndez, G. Luna, V. Segura-Pérez, J.A. Rivera, G. Fetter, ZnAl layered double hydroxides impregnated with eucalyptus oil as efficient hybrid materials against multi-resistant bacteria, *Appl. Clay Sci.* 153 (2018) 61–69.
- [37] S.A.A. Moaty, A.A. Farghali, R. Khaled, Preparation, characterization and antimicrobial applications of Zn-Fe LDH against MRSA, *Mater. Sci. Eng. C.* 68 (2016) 184–193.
- [38] G. Mishra, B. Dash, S. Pandey, D. Sethi, Ternary layered double hydroxides (LDH) based on Cu- substituted Zn Al for the design of efficient antibacterial ceramics, *Appl. Clay Sci.* 165 (2018) 214–222.
- [39] J. Awassa, D. Cornu, C. Ruby, S. El-Kirat Chatel, Direct contact, dissolution and generation of reactive oxygen species: How to optimize the antibacterial effects of layered double hydroxides, *Chemistry*, 2022.
- [40] G. Mishra, B. Dash, S. Pandey, P.P. Mohanty, Antibacterial actions of silver nanoparticles incorporated Zn–Al layered double hydroxide and its spinel, *J. Environ. Chem. Eng.* 1 (2013) 1124–1130.
- [41] J. Wu, Z. Chu, Z. Ruan, X. Wang, T. Dai, X. Hu, Changes of Intracellular Porphyrin, Reactive Oxygen Species, and Fatty Acids Profiles During Inactivation of Methicillin-Resistant *Staphylococcus aureus* by Antimicrobial Blue Light, *Front. Physiol.* 9 (2018) 1658.
- [42] H. Li, Q. Chen, J. Zhao, K. Urmila, Enhancing the antimicrobial activity of natural extraction using the synthetic ultrasmall metal nanoparticles, *Sci. Rep.* 5 (2015) 11033.
- [43] K. Sahu, H. Bansal, C. Mukherjee, M. Sharma, P.K. Gupta, Atomic force microscopic study on morphological alterations induced by photodynamic action of Toluidine Blue O in *Staphylococcus aureus* and *Escherichia coli*, *J. Photochem. Photobiol. B.* 96 (2009) 9–16.
- [44] J.-W. Liou, Y.-J. Hung, C.-H. Yang, Y.-C. Chen, The Antimicrobial Activity of Gramicidin A Is Associated with Hydroxyl Radical Formation, *PLOS ONE*. 10 (2015) e0117065.
- [45] M. Mathelié-Guinlet, C. Grauby-Heywang, A. Martin, H. Février, F. Moroté, A. Vilquin, L. Béven, M.-H. Delville, T. Cohen-Bouhacina, Detrimental impact of silica nanoparticles on the nanomechanical properties of *Escherichia coli*, studied by AFM, *J. Colloid Interface Sci.* 529 (2018) 53–64.
- [46] F. Quilès, I. Accoceberry, C. Couzigou, G. Francius, T. Noël, S. El-Kirat-Chatel, AFM combined to ATR-FTIR reveals *Candida* cell wall changes under caspofungin treatment, *Nanoscale*. 9 (2017) 13731–13738.
- [47] E.B. Tatlybaeva, H.N. Nikiyan, A.S. Vasilchenko, D.G. Deryabin, Atomic force microscopy recognition of protein A on *Staphylococcus aureus* cell surfaces by labelling with IgG–Au conjugates, *Beilstein J. Nanotechnol.* 4 (2013) 743–749.
- [48] A. Beaussart, C. Retourney, F. Quilès, R. Dos Santos Morais, C. Gaiani, H.-P. Fiérobe, S. El-Kirat-Chatel, Supported lysozyme for improved antimicrobial surface protection, *J. Colloid Interface Sci.* 582 (2021) 764–772.
- [49] F. Zhang, L. Zhao, H. Chen, S. Xu, D.G. Evans, X. Duan, Corrosion Resistance of Superhydrophobic Layered Double Hydroxide Films on Aluminum, *Angew. Chem. Int. Ed.* 47 (2008) 2466–2469.
- [50] L. Wang, C. Li, M. Liu, D.G. Evans, X. Duan, Large continuous, transparent and oriented self-supporting films of layered double hydroxides with tunable chemical composition, *Chem Commun.* (2007) 123–125.

- [51] X. Guo, F. Zhang, S. Xu, D.G. Evans, X. Duan, Preparation of layered double hydroxide films with different orientations on the opposite sides of a glass substrate by in situ hydrothermal crystallization, *Chem. Commun.* (2009) 6836.
- [52] D. Scarpellini, C. Falconi, P. Gaudio, A. Mattocchia, P.G. Medaglia, A. Orsini, R. Pizzoferrato, M. Richetta, Morphology of Zn/Al layered double hydroxide nanosheets grown onto aluminum thin films, *Microelectron. Eng.* 126 (2014) 129–133.
- [53] J. Liu, X. Huang, Y. Li, K.M. Sulieman, X. He, F. Sun, Facile and Large-Scale Production of ZnO/Zn–Al Layered Double Hydroxide Hierarchical Heterostructures, *J. Phys. Chem. B.* 110 (2006) 21865–21872.
- [54] G. Borkow, J. Gabbay, Copper as a Biocidal Tool, *Curr. Med. Chem.* 12 (2005) 2163–2175.
- [55] M.R. Bruins, S. Kapil, F.W. Oehme, Microbial Resistance to Metals in the Environment, *Ecotoxicol. Environ. Saf.* 45 (2000) 198–207.

Enhancing the antibacterial activity of Zn(II)-based layered double hydroxide nanoparticles in the presence of UVA light

Table of figures	179
Table of tables.....	181
1. Context	182
2. Antibacterial activity of Zn(II)-based LDH NPs against <i>S. aureus</i> in dark and UVA conditions 183	183
2.1. Agar disc diffusion assay and broth macro-dilution turbidimetric tests for MIC determination.....	184
2.2. CFU count experiments.....	186
2.3. CFU count experiments in presence of histidine	189
3. Surface topography of <i>S. aureus</i> cells treated with Zn(II)-based LDH NPs in dark and UVA conditions	191
4. FT-IR spectroscopy analysis of <i>S. aureus</i> cells treated with Zn(II)-based LDH NPs in dark and UVA conditions.....	194
4.1. Generalities on the FTIR spectra of <i>S. aureus</i> cells and ZnAl LDH NPs in TSB	194
4.2. Influence of ZnAl LDH NPs treatment in dark and UVA conditions on the biochemical structure of <i>S. aureus</i> cells evidenced by FT-IR spectroscopy	197
5. Conclusion.....	200
References	201

Table of figures

Figure 1. A schematic illustration of the topographical and biochemical damages and alterations of *S. aureus* cells induced by Zn(II)-based LDH NPs in dark and UVA conditions. 183

Figure 2. Absorbance spectra of Eppendorf tubes and ZnAl LDH NPs. (a) Absorbance spectrum of an Eppendorf tube (cut in half and flattened as possible) in the range of 200-400 nm. (b) UV-visible absorbance spectrum of ZnAl LDH NPs in the range of 200-800 nm. 185

Figure 3. Antibacterial activity of Zn(II)-based NPs against *S. aureus* in dark and UVA conditions. (a) Mean zone of inhibition calculated as the average inhibition diameters of three repetitive trials of agar disc diffusion tests. (c) MIC values calculated as the average MIC of three repetitive trials of broth macro-dilution turbidimetric tests..... 186

Figure 4. CFU count experiments in presence and absence of LDH NPs under dark and UVA conditions. (a) Concentration of *S. aureus* (CFU/mL). (b) Bactericidal rate of LDH NPs (%/h). 187

Figure 5. CFU count experiments in UVA conditions, in presence and absence of different amounts of histidine. (a) Concentration of *S. aureus* (CFU/mL). (b) Bactericidal rate of LDH NPs (%/h)..... 189

Figure 6. AFM deflection images of *S. aureus* in liquid (scale bar = 250 nm). (a) Untreated *S. aureus* cells in dark conditions. (b) Untreated *S. aureus* cells in UVA conditions. (c) *S. aureus* cells treated with ZnAl LDH NPs at MIC in dark conditions. (d) *S. aureus* cells treated with ZnAl LDH NPs at MIC in UVA conditions. 192

Figure 7. AFM deflection images of *S. aureus* in air (scale bar = 500 nm). (a) Untreated *S. aureus* cells in dark conditions. (b) Untreated *S. aureus* cells in UVA conditions. (c) *S. aureus* cells treated with ZnAl LDH NPs at MIC in dark conditions. (d) *S. aureus* cells treated with ZnAl LDH NPs at MIC in UVA conditions. 193

Figure 8. General IR spectra of *S. aureus* and LDH NPs. (a) *S. aureus* in TSB at different accumulation times on the ATR crystal. (b) *S. aureus* in TSB under dark and UVA condition at t = 15 min of accumulation on the ATR crystal. (c) LDH NPs in water and TSB under dark and UVA conditions at t = 15 min of accumulation on the ATR crystal. Corresponding supernatants from centrifugation were used to obtain the reference spectra. Offsets of spectra are used when

necessary for clarity. P = proteins, PS = polysaccharides, NA = nucleic acids, PL = phospholipids.

..... 195

Figure 9. PXRD diffraction pattern of ZnAl LDH NPs before and after exposition to TSB medium for 24 h. 197

Figure 10. Influence of ZnAl LDH NPs treatment on the IR spectrum of *S. aureus*. (a) IR spectra of treated and untreated *S. aureus cells* with ZnAl LDH NPs at MIC under dark conditions. (b) IR spectra of treated and untreated *S. aureus cells* with ZnAl LDH NPs at MIC under UVA conditions. (c) Difference in IR spectra of *S. aureus cells* treated with ZnAl LDH NPs at MIC under dark and UVA conditions. Corresponding supernatants from centrifugation were used to obtain the reference spectra. Offsets of spectra are used for clarity. 199

Table of tables

Table 1. Bactericidal efficiency (%) of LDH NPs under dark and UVA conditions in presence and absence of different amounts of histidine.....	188
Table 2. Average roughness parameter Rq of <i>S. aureus</i> cells treated and not with LDH NPs at MIC under dark and UVA conditions.	191
Table 3. Common peaks observed in the IR spectra of <i>S. aureus</i> [25].	196

1. Context

As previously reported in this manuscript, the generation of reactive oxygen species (ROS) inducing oxidative stress is another possible mechanism explaining the antibacterial action of pristine layered double hydroxides (**Mechanism 3**). In fact, exogenous generated-ROS provide an efficient antibacterial effect by damaging bacterial membranes, proteins, lipids, and DNA through imposing oxidative stress [1–3].

When a suitable light source irradiates LDH nanoparticles (NPs), an electron (\bar{e}) and a hole (h^+) are created which could subsequently generate ROS as hydroxyl ($\text{OH}\cdot$), superoxide ($\text{O}_2\cdot^-$), hydrogen superoxide ($\text{HOO}\cdot$) radicals as well as hydrogen peroxide (H_2O_2) [4,5]. These generated ROS are thus expected to enhance the antibacterial activity of LDHs.

Previous reports proved that the antibacterial activity of zinc oxide nanoparticles could be enhanced by the generation of ROS in the presence of a UV or visible light source with a suitable wavelength [6–8]. However, no proof of evidence was reported concerning the antibacterial activity of Zn(II)-based LDHs by ROS-induced oxidative stress.

In the previous two chapters, we have already investigated the antibacterial activity of Zn(II)-based LDHs by the release of Zn^{2+} and direct contact with the bacterial cell wall in the absence of light (no generated ROS). However, it is of great interest as well to determine whether the antibacterial activity of Zn(II)-based LDHs could further be enhanced through the generation of ROS in the presence of light.

In this chapter, we will present our newly results concerning the enhancement of antibacterial activity of Zn(II)-based LDH nanoparticles (NPs) used in **Chapter 4** in the presence of UVA light ($\lambda = 365 \text{ nm}$). To avoid repetition, we will skip details of NPs synthesis and characterization since they are found in the previous chapter. Therefore, the antibacterial activity of Zn(II)Al(III) LDH NPs against *Staphylococcus aureus* in UVA conditions will be compared to that found in dark conditions. Such comparison will be achieved through evaluating the minimum inhibitory concentration (MIC) and bactericidal efficiency in both dark and UVA conditions. It is true that the generation of ROS need to be further validated by fluorescence spectroscopy and/or electron spin resonance (ESR) spectroscopy. However, as primary evidence of ROS generation, the

antibacterial activity of ZnAl NPs will be determined in presence of histidine, a well-known ROS scavenger [9–11].

Finally, the surface topography and structural composition of *S. aureus* treated with Zn(II)-based NPs in dark and UVA conditions will also be investigated using atomic force microscopy imaging and Fourier-Transform InfraRed (FT-IR) spectroscopy, respectively. Our preliminary findings suggest that the antibacterial efficiency of Zn(II)-based LDH NPs is enhanced in presence of UVA, by which the bactericidal efficiency could reach 100%, the surface topography and biochemical structure of bacteria is completely altered probably due to the generation of ROS by the LDH NPs in response to UVA light irradiation (Figure 1).

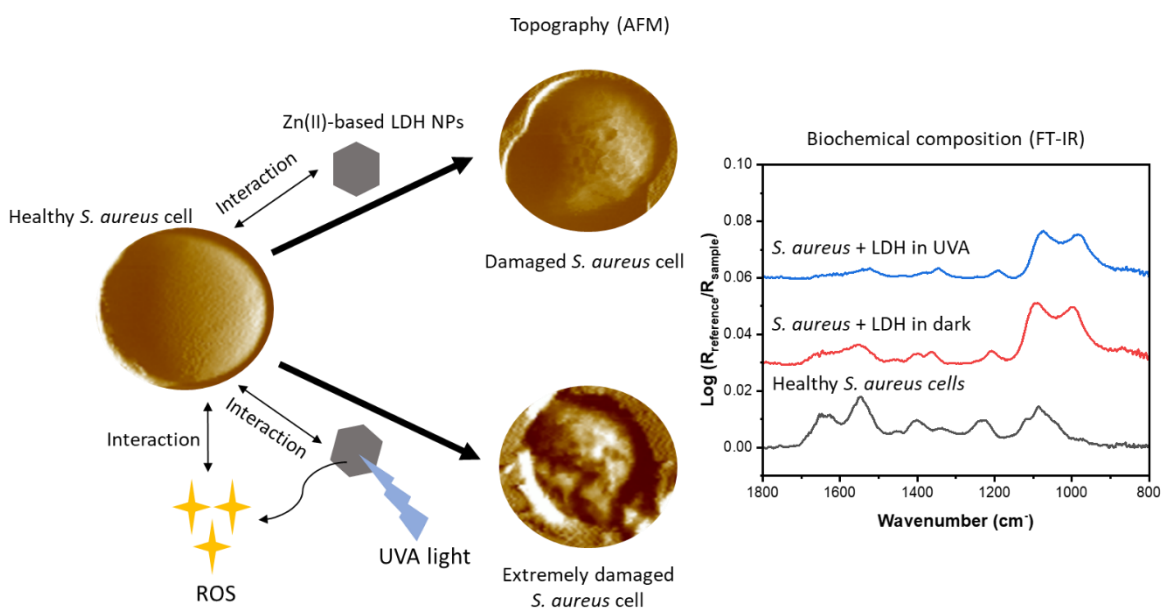


Figure 1. A schematic illustration of the topographical and biochemical damages and alterations of *S. aureus* cells induced by Zn(II)-based LDH NPs in dark and UVA conditions.

2. Antibacterial activity of Zn(II)-based LDH NPs against *S. aureus* in dark and UVA conditions

The antibacterial activity of Zn(II)-based NPs used in Chapter 4 was investigated in presence of UVA light (irradiated only during the first 4 h of the experiment) using agar disc diffusion test and broth macro-dilution test aimed at determining the minimum inhibitory concentration (MIC). Moreover, bactericidal efficiency against *S. aureus* was also determined using colony forming unit

(CFU) count experiments in both dark and UVA conditions. The irradiation time period was set for only the first 4 h of the experiments in order to determine the antibacterial effect obtained after turning off the light.

2.1. Agar disc diffusion assay and broth macro-dilution turbidimetric tests for MIC determination

The inhibitory diameter of Zn(II)-based NPs against *S. aureus* was evaluated using agar disc diffusion test in both dark and UVA conditions. An inoculum of *S. aureus* was spread on a TSB agar Petri dish to obtain a homogeneous continuous layer of bacteria and a 10 mg/mL of LDH suspension was added to round filter disc (6 mm). The Petri dishes were then placed in an incubator in dark and under UVA illumination at 37°C for 24 h. Control experiments were carried out using UVA light in the absence of LDH NPs, and no inhibitory zones were detected ensuring that UVA light does not induce any antibacterial effect by itself.

The antibacterial effect of LDH NPs was also evaluated through broth macro-dilution tests aimed at determining their MIC. These tests were performed in Eppendorf tubes made of polypropylene allowing UVA light to be transmitted into the LDH-bacterial suspension (**Figure 2a**) [12]. Indeed, the transmission of the UV light at 365 nm is large and one can expect that the part that is not transmitted to the detector is diffused and still collected in the Eppendorf tube. A bacterial inoculum of fixed optical density ($OD_{600} = 0.1$) and volume was added to different LDH suspensions (diluted in two-fold). The Eppendorf tubes were then placed in an incubator at 37 °C for 24 h in both dark and UVA conditions (applied only during the first 4 hours of the experiment). The MIC value for the LDH NPs was recognized as the lowest concentration that had no visible turbidity in each condition. Control experiments with UVA illumination in the absence of LDH NPs were also carried out, and no decrease in turbidity nor optical density was noticed compared to dark conditions over 24 h.

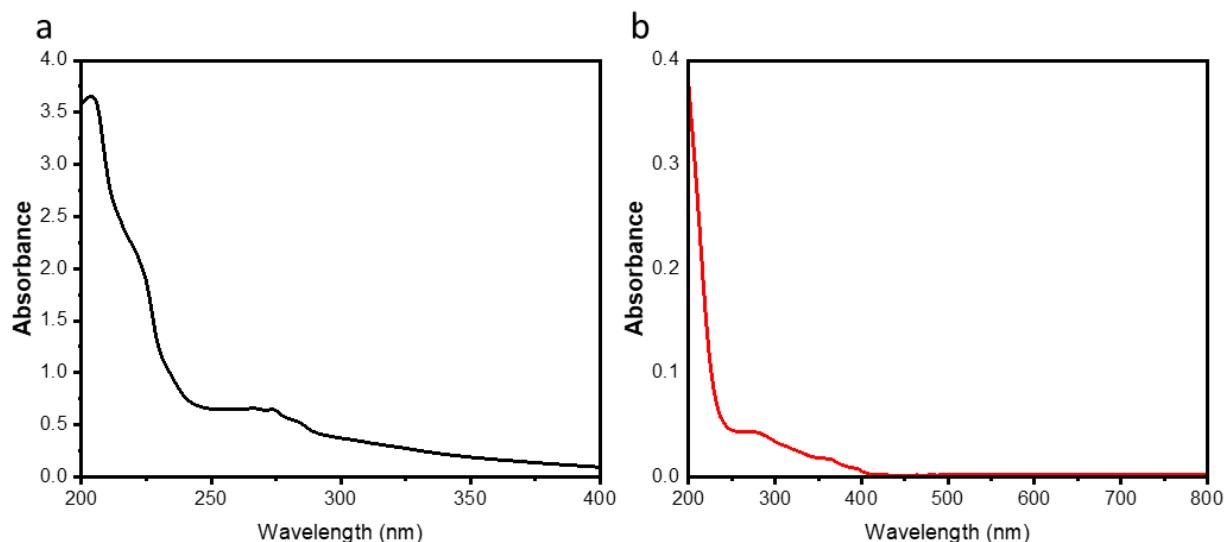


Figure 2. Absorbance spectra of Eppendorf tubes and ZnAl LDH NPs. (a) Absorbance spectrum of an Eppendorf tube (cut in half and flattened as possible) in the range of 200-400 nm. (b) UV-visible absorbance spectrum of ZnAl LDH NPs in the range of 200-800 nm.

No remarkable change was detected in the inhibitory zone diameter upon irradiating ZnAl LDH NPs in UVA light. This suggests that UVA light does not improve the antibacterial activity of these LDH NPs in agar gel (**Figure 3a**). On the contrary, the MIC of Zn(II)-based NPs against *S. aureus* was two times decreased in UVA conditions compared to dark conditions (**Figure 3b**). Considering that UVA light does not contribute to any inhibitory effect by itself, the antibacterial activity of Zn(II)-based LDHs in liquid TSB was remarkably enhanced in presence of UVA light.

Taking into consideration the suggested antibacterial mechanism of LDHs by the generation of ROS under a suitable light source irradiation, the enhanced antibacterial activity of ZnAl LDH NPs may be explained by ROS generation in response to UVA radiation.

In this context, the inability of generated ROS to provide any improvement to the antibacterial activity in the agar disc diffusion tests may be related to their short lifespan. In fact, the average lifetime of free radicals is 10^{-9} - 10^{-6} sec [13], thus limiting their diffusion into the agar gel. On the other hand, generated ROS are in direct contact with the bacteria during MIC experiments, which makes them more accessible to *S. aureus* cells in liquid environment.

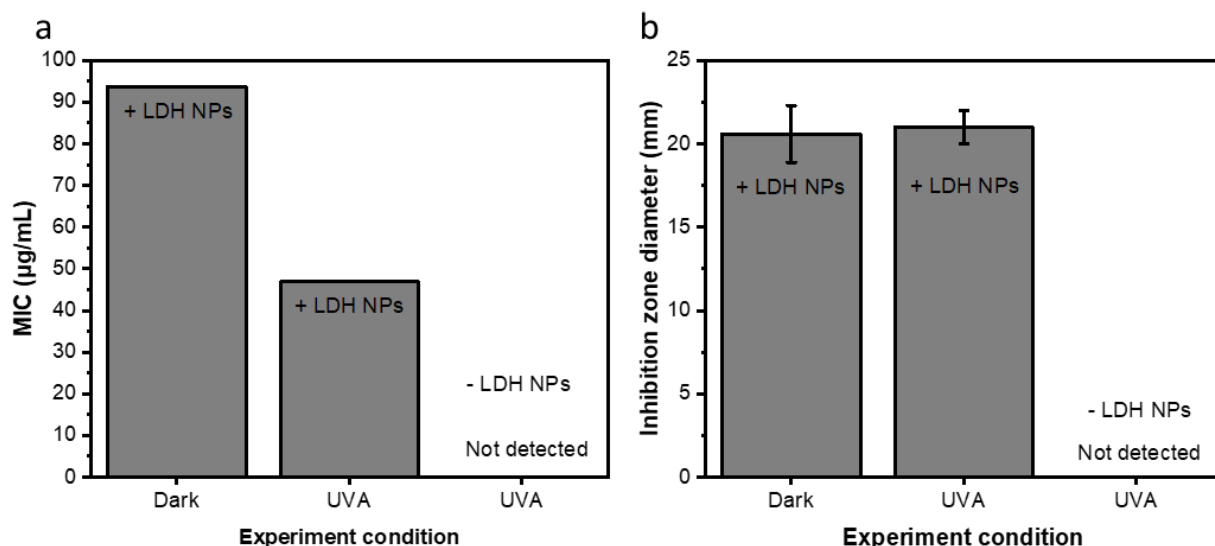


Figure 3. Antibacterial activity of Zn(II)-based NPs against *S. aureus* in dark and UVA conditions. (a) Mean zone of inhibition calculated as the average inhibition diameters of three repetitive trials of agar disc diffusion tests. (c) MIC values calculated as the average MIC of three repetitive trials of broth macro-dilution turbidimetric tests.

2.2. CFU count experiments

The antibacterial activity of Zn(II)-based LDH NPs in dark and UVA light conditions (exposure for first 4 h) was also examined against *S. aureus* using CFU count method. A Tris-buffered saline (TBS) buffer suspension of *S. aureus* ($OD_{600} = 0.05$) in presence and absence of LDH NPs (93.8 µg/mL) in both dark and UVA conditions was prepared. At different defined time points (0 h, 2 h, 4 h, 8 h and 24 h), a fixed volume (100 µL) of this suspension (diluted to 1/10000, 1/20000 and 1/50000) was spread on Tryptic Soy Broth (TSB) agar Petri plates. The plates were then incubated at 37 °C for 24 h to determine bacterial viability by counting the number of colonies formed. Each experiment was repeated three times, and the average concentration of viable cells, the concentration of viable cells (CFU/mL), the bactericidal efficiency after 24 h and bactericidal rate at each defined time point were determined through the following formulas:

$$CFU/mL = \frac{Nd}{v} \quad (1)$$

$$\% \text{ bactericidal efficiency} = \frac{N_c - N_A}{N_c} \times 100 \quad (2)$$

$$\text{Bactericidal rate} = \frac{N_0 - N_t}{N_0 t} \times 100 \quad (3)$$

Where N is the number of colonies formed on the plate, d is the dilution factor, v is the volume of the of the initial bacterial inoculum, N_C is the number of bacterial colonies in a control group in the absence of LDH, N_A is the number of bacterial colonies found in the presence of LDH, N_0 is the number of colonies formed in a certain experimental condition at $t=0$, N_t is the number of colonies formed at a defined time point, and t is the defined time point.

Control experiments were also carried out in dark and UVA conditions at each time point to determine the concentration of viable cells in the absence of LDH NPs.

No remarkable decrease in the concentration of *S. aureus* was noted in the absence of LDH NPs over 24 hours neither in dark conditions nor upon irradiating the bacterial suspension with UVA during the first 4 hours of the experiment (Figure 4a). This ensures that the number of bacteria was maintained constant in TBS buffer and that UVA light by itself does not impose any antibacterial activity as suggested by the agar disc diffusion and broth macro-dilution tests.

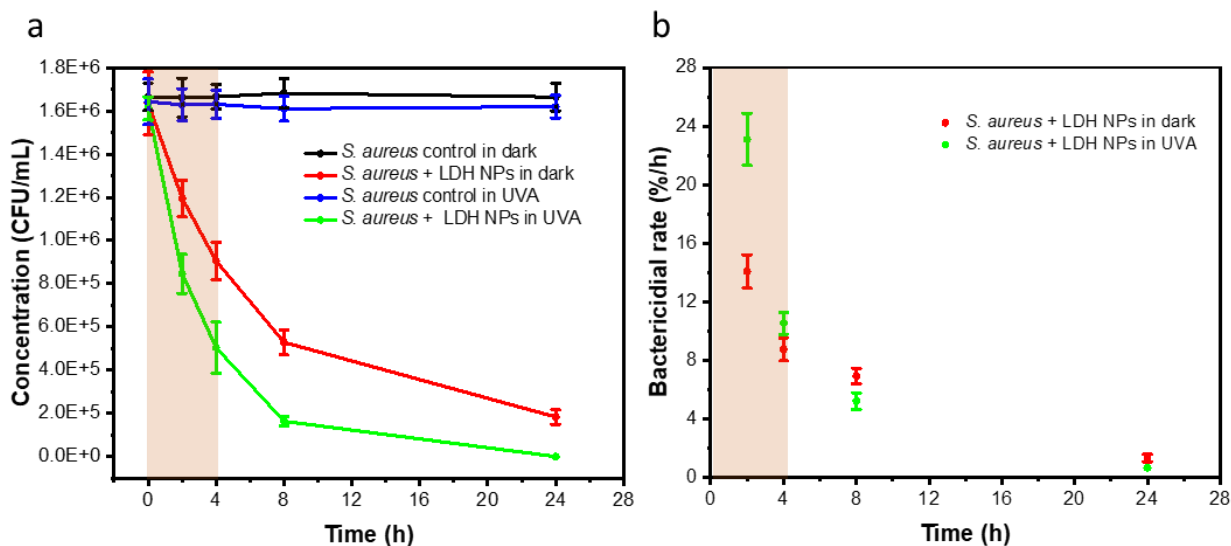


Figure 4. CFU count experiments in presence and absence of LDH NPs under dark and UVA conditions. (a) Concentration of *S. aureus* (CFU/mL). (b) Bactericidal rate of LDH NPs (%/h).

Upon adding ZnAl NPs to the bacterial suspension cultured in dark conditions, the concentration of *S. aureus* significantly decreased (Figure 4a) reaching an average bactericidal efficiency of 88.9% after 24 h (Table 1). The bactericidal efficiency of ZnAl LDH NPs was further enhanced in UVA conditions where the decrease in the bacterial concentration was more pronounced (Figure 4a) reaching a bactericidal efficiency of 100% after 24 h. Similar findings were previously

observed by Nocchetti *et al.* who reported a remarkable enhancement in the bactericidal efficiency of AgCl NPs-loaded ZnAl LDHs by the generation of ROS upon being irradiating with a source of light ($\lambda > 350$ nm) for 3 hours [14]. Therefore, ZnAl LDH NPs are able to kill a great portion of bacteria without the generation of ROS. However, the generation ROS which is a possible explanation of the enhanced antibacterial activity, could further aid in the observed bactericidal effect leading to the death of all the present *S. aureus* cells.

Another important factor highlighting the remarkable antibacterial properties of ZnAl LDH NPs in presence of UVA light is the bactericidal rate. **Figure 4b** shows the rate of bactericidal efficiency of Zn(II)-based LDH NPs at different time points in both dark and UVA conditions. The bactericidal rates in UVA conditions during the first 4 h of the experiment were remarkably higher than those obtained in dark conditions, suggesting that the possible generated ROS do not only enhance the antibacterial activity but also increase the rate of bacterial killing. On the other hand, the bactericidal rate in dark conditions after 4 h without any exposition to UVA light was slightly greater than in obtained after 4h UVA exposition. The lower bactericidal rate observed in UVA conditions after 4 hours of exposure is due to the lower number of remaining bacteria alive accessible for the LDH NPs to kill.

Table 1. Bactericidal efficiency (%) of LDH NPs under dark and UVA conditions in presence and absence of different amounts of histidine.

Condition	dark		UVA				
	LDH + <i>S. aureus</i>	<i>S. aureus</i> + 160 mg histidine	LDH + <i>S. aureus</i>	LDH + <i>S. aureus</i> + 20 mg histidine	LDH + <i>S. aureus</i> + 40 mg histidine	LDH + <i>S. aureus</i> + 80 mg histidine	LDH + <i>S. aureus</i> + 160 mg histidine
Bactericidal efficiency (%)	88.9 ± 1.9	0	100	96.6 ± 0.9	94.5 ± 1.1	92.5 ± 1	92.7 ± 1.3

The observed bactericidal rate enhancement during the first 4 hours can be explained by the fact that UVA light was used only during the first 4 hours of the experiment, and ROS were therefore generated only during this period of time. After turning off the UVA light and returning to dark conditions, the possible generated ROS are recombined/decayed and the LDH NPs continued to impose the antibacterial activity alone.

2.3. CFU count experiments in presence of histidine

In the previous section, we have suggested that the enhanced bactericidal efficiency of ZnAl LDH NPs is due to the generation of ROS by LDHs under UVA irradiation. According to the UV-visible spectrum of ZnAl LDH NPs, it is not clear whether LDH NPs absorb light at 365 nm to be able to generate ROS (**Figure 2b**) because the lower transmission observed can be related to the diffusion of light. Therefore, a suitable method should be adapted to establish the ability of our Zn(II)-NPs to produce ROS in presence of the used UVA light. In fact, ROS generation could be evaluated using different methods including fluorescence spectroscopy using fluorescent dye probes, ESR and chromatography methods [15].

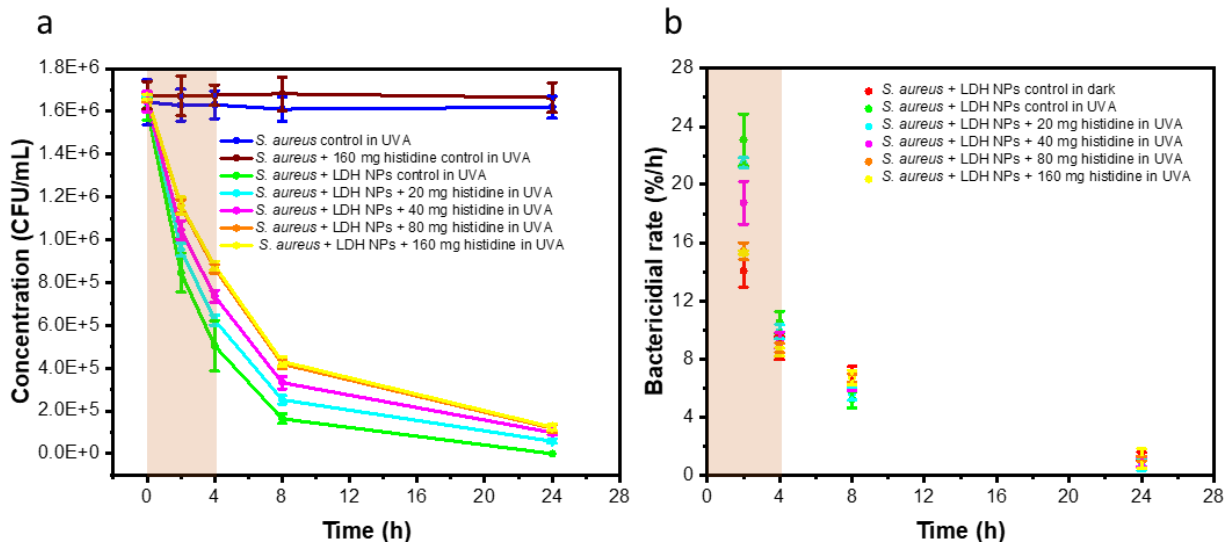


Figure 5. CFU count experiments in UVA conditions, in presence and absence of different amounts of histidine. (a) Concentration of *S. aureus* (CFU/mL). (b) Bactericidal rate of LDH NPs (%/h).

As a primary evidence of ROS generation by our ZnAl LDH NPs, we aimed to determine their bactericidal efficiency under UVA conditions in presence of histidine. Histidine is a well-known ROS scavenger with remarkable antioxidative properties [9–11]. Therefore, the antibacterial activity of ZnAl LDH NPs was investigated using CFU count in a similar procedure as reported before (**Section 2.2**) in presence different amounts of histidine (20 mg, 40 mg, 80 mg, 160 mg) under UVA irradiation.

As a first step, we ensured that our ROS scavenger, *e.g.*, histidine, does not impose by itself any antibacterial effect against *S. aureus* in both UVA (**Figure 5a**) and dark conditions (**Table 1**). Upon adding increasing amounts of histidine from 20 to 80 mg to the suspension of *S. aureus* and LDH NPs irradiated by UVA, the final achieved bactericidal efficiency after 24 h was also lower in presence of increasing amounts histidine up to 80 mg (**Table 1**). Moreover, bacterial concentration in presence of different concentrations of histidine in UVA conditions was greater than that obtained in the absence of histidine in the same conditions for each time point (**Figure 5a**).

Such results fall in good agreement with those of Dutta *et al.* who noted a decrease in bactericidal efficiency of ZnO NPs in presence of increasing amounts of histidine [16]. Indeed, the authors performed fluorescence dye measurements and ensured that histidine was able to scavenge generated ROS up to a certain limit. Histidine is an efficient ROS scavenger, however, its scavenging action is limited to hydroxyl and singlet oxygen radicals [17], while hydrogen peroxide which is also a possible generated ROS by LDHs might not be scavenged by histidine. In this context, the inability of histidine to completely suppress the action of possible produced ROS could be explained by its incapability to scavenge all types of generated ROS. This can also be a reasonable explanation of the limit of the amount of ROS to provide a suppressing effect after 80 mg. In other words, after adding 80 mg of histidine, a plateau of its scavenging action is obtained.

It is also remarkable that the suppressing effect of histidine toward possible generated ROS was more pronounced during the first 4 hours of the experiment (irradiation time period). As suggested by **Figure 5b**, the rate of bactericidal efficiency in presence of histidine was remarkably lower in presence of increasing amount of histidine than that found in UVA in the absence of histidine during the first 4 hours. This is probably due to suppression of possible generated ROS produced only during UVA irradiation period. After that, the rate in presence of increasing amounts of histidine was greater than that found in UVA conditions (without histidine), which could be explained by the greater number of bacteria still present after 4 h in case of histidine addition.

On the contrary, the bactericidal efficiency in presence of increasing amounts of histidine under UVA conditions was still higher than that in dark conditions during the whole 24 hours of the experiment. This could be because not all the possible generated ROS were scavenged by histidine, and therefore the action of ROS on increasing the bactericidal rate was not completely suppressed

during the first four hours. After turning off the UVA light at $t = 4$ h, generated ROS are probably recombined/decayed, and therefore the bactericidal rate of LDHs alone depends on the concentration of bacteria present which was greater in dark conditions.

3. Surface topography of *S. aureus* cells treated with Zn(II)-based LDH NPs in dark and UVA conditions

AFM imaging was used to visualize the influence of ZnAl LDH NPs (93.8 $\mu\text{g}/\text{mL}$, corresponding to MIC value obtained in dark conditions) in dark and UVA conditions on the surface topography of *S. aureus* cells. For this purpose, untreated and ZnAl LDH NPs-treated cells were trapped in porous membranes and imaged in TSB buffer liquid. The roughness parameter R_q (root mean square of the heights, calculated as an average of 15 cells) was also obtained from AFM images performed on the top of bacteria at a high magnification of $400 \times 400 \text{ nm}^2$ scanning areas.

As shown in **Figure 6a** and **b**, untreated cells in dark and UVA conditions presented regular spheroid morphologies and smooth surfaces with a similar R_q roughness parameter (**Table 2**). Such observation suggests that UVA light alone does not impose any damage to the cell wall of *S. aureus* cells.

Table 2. Average roughness parameter R_q of *S. aureus* cells treated and not with LDH NPs at MIC under dark and UVA conditions.

<i>S. aureus</i> cells	R_q (nm)
Untreated in dark conditions	15.3 ± 0.9
Untreated in UVA conditions	15.8 ± 1.3
Treated with MIC of LDH in dark conditions	49.7 ± 2.9
Treated with MIC of LDH in UVA conditions	59.4 ± 1.1

As previously reported in **Chapter 2**, cells treated with ZnAl LDH NPs in dark conditions were seriously damaged as they appeared distorted with highly corrugated surfaces showing several hollows and crests (**Figure 6c**). The increase of roughness of the cells treated with ZnAl LDH NPs in dark conditions (~ 3 times rougher surfaces) was similar to that reported in the previous chapter. The cell wall damages imposed by ZnAl LDH NPs were even more pronounced in UVA conditions. Most treated cells in UVA conditions lost their spheroid morphology and showed

deeper grooves (Figure 6d) as well as an increase in of ~20% surface roughness (Table 2) compared to treated cells in dark conditions.

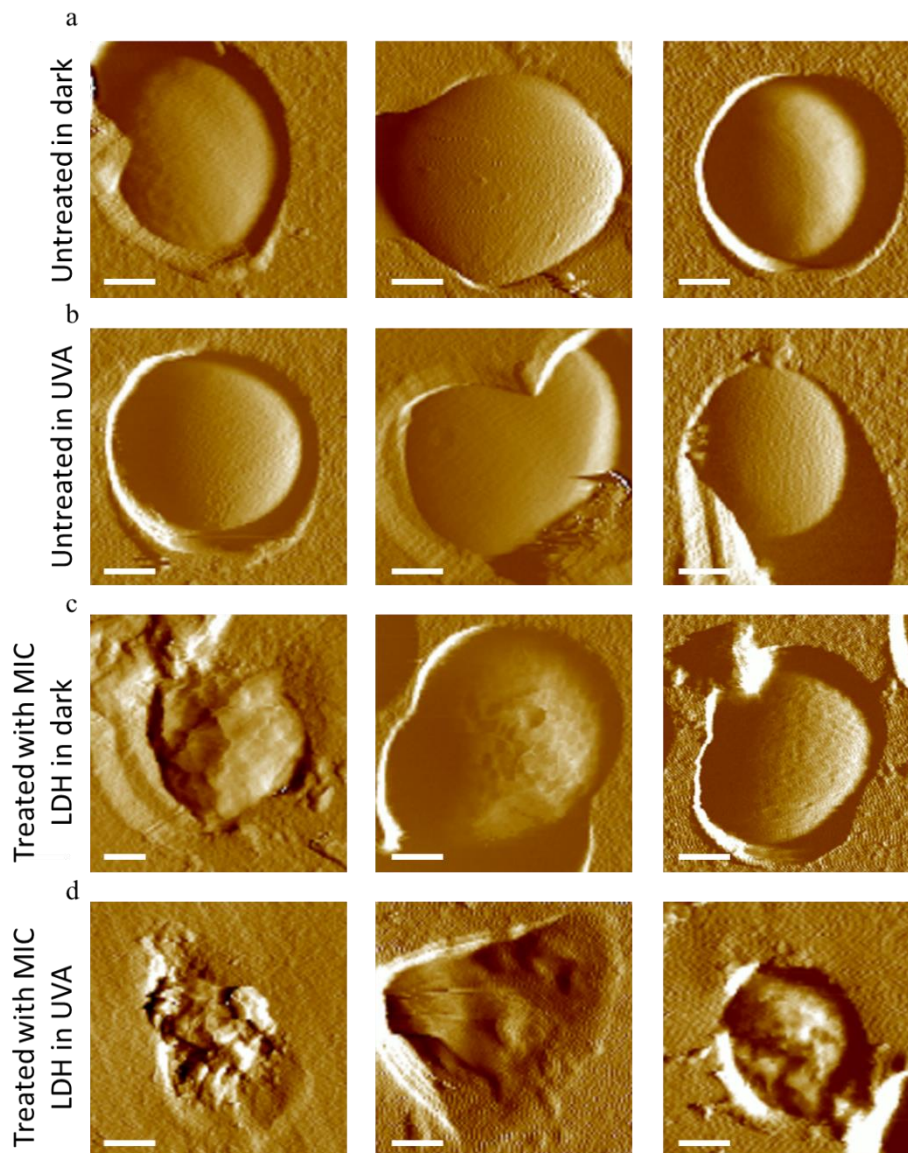


Figure 6. AFM deflection images of *S. aureus* in liquid (scale bar = 250 nm). (a) Untreated *S. aureus* cells in dark conditions. (b) Untreated *S. aureus* cells in UVA conditions. (c) *S. aureus* cells treated with ZnAl LDH NPs at MIC in dark conditions. (d) *S. aureus* cells treated with ZnAl LDH NPs at MIC in UVA conditions.

Cell imaging in air was also performed in order to examine the morphological impacts of ZnAl LDH NPs treatment in dark and UVA conditions on a greater fraction of cells immobilized on mica substrates. Cells imaging in air can also help to better differentiate topographical differences between treated cells [18], in dark and UVA conditions.

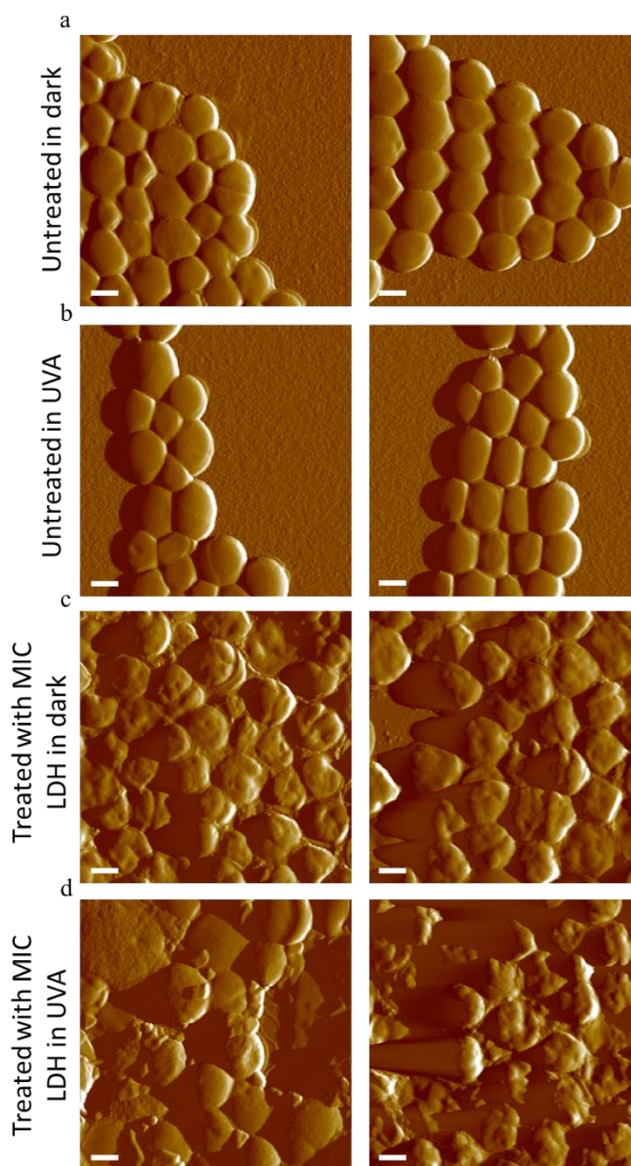


Figure 7. AFM deflection images of *S. aureus* in air (scale bar = 500 nm). (a) Untreated *S. aureus* cells in dark conditions. (b) Untreated *S. aureus* cells in UVA conditions. (c) *S. aureus* cells treated with ZnAl LDH NPs at MIC in dark conditions. (d) *S. aureus* cells treated with ZnAl LDH NPs at MIC in UVA conditions.

Untreated *S. aureus* cells in both dark and UVA conditions showed homogeneous cellular shapes with a spheroid geometry and regular surfaces, typical for this type of bacteria [19,20]. However, cells treated with ZnAl LDH NPs in dark conditions were completely distorted showing deep grooves, crests, hollows and even some split surfaces, leaving behind some cell debris. On the other hand, only lysed cells and cell debris were observed for those treated in UVA conditions.

Such observation comes in line with our CFU count experiments, by which we reported a 100 % bactericidal efficiency of ZnAl NPs in UVA conditions ensuring that all cells were killed.

The more pronounced cells damage of *S. aureus* treated with ZnAl LDH NPs (observed in both liquid and air imaging environments) in UVA conditions is probably to the dual antibacterial effect of Zn(II)-based LDH NPs and the possible generated ROS under UVA irradiation.

4. FT-IR spectroscopy analysis of *S. aureus* cells treated with Zn(II)-based LDH NPs in dark and UVA conditions

As the bacterial cell wall properties are defined by their biochemical composition [18], we aimed to determine which compositional changes of *S. aureus* cells were associated with the antibacterial effect of ZnAl LDH NPs which was previously evidenced by a high bactericidal efficiency and serious cell wall damages. Attenuated Total Reflectance Fourier-Transform Infrared Spectroscopy (ATR-FTIR) was used to establish the biochemical fingerprints of *S. aureus* cells treated or not with ZnAl LDH NPs (93.8 µg/mL, corresponding to MIC value obtained in dark conditions) in both dark and UVA conditions. *S. aureus* cells (OD₆₀₀ = 0.1) were cultured in TSB with and without LDH NPs for 24 h at 37°C. A certain volume of the suspension obtained after 24 h was centrifuged to obtain a supernatant (free of bacteria and LDH NPs) which was used as a reference for the recorded spectra of *S. aureus* cells in TSB. Four measurements were carried on each sample, separated by a time interval of 5 mins to allow the bacterial/LDH suspensions to accumulate on the ATR crystal in purpose on enhancing the recorded intensity.

4.1. Generalities on the FTIR spectra of *S. aureus* cells and ZnAl LDH NPs in TSB

Before moving directly to investigating the influence of ZnAl LDH NPs on the biochemical structure of *S. aureus* cells, it is important to define the general biochemical components of this bacteria and to determine effect of the culture media, *i.e.*, TSB, on the IR spectrum of ZnAl NPs.

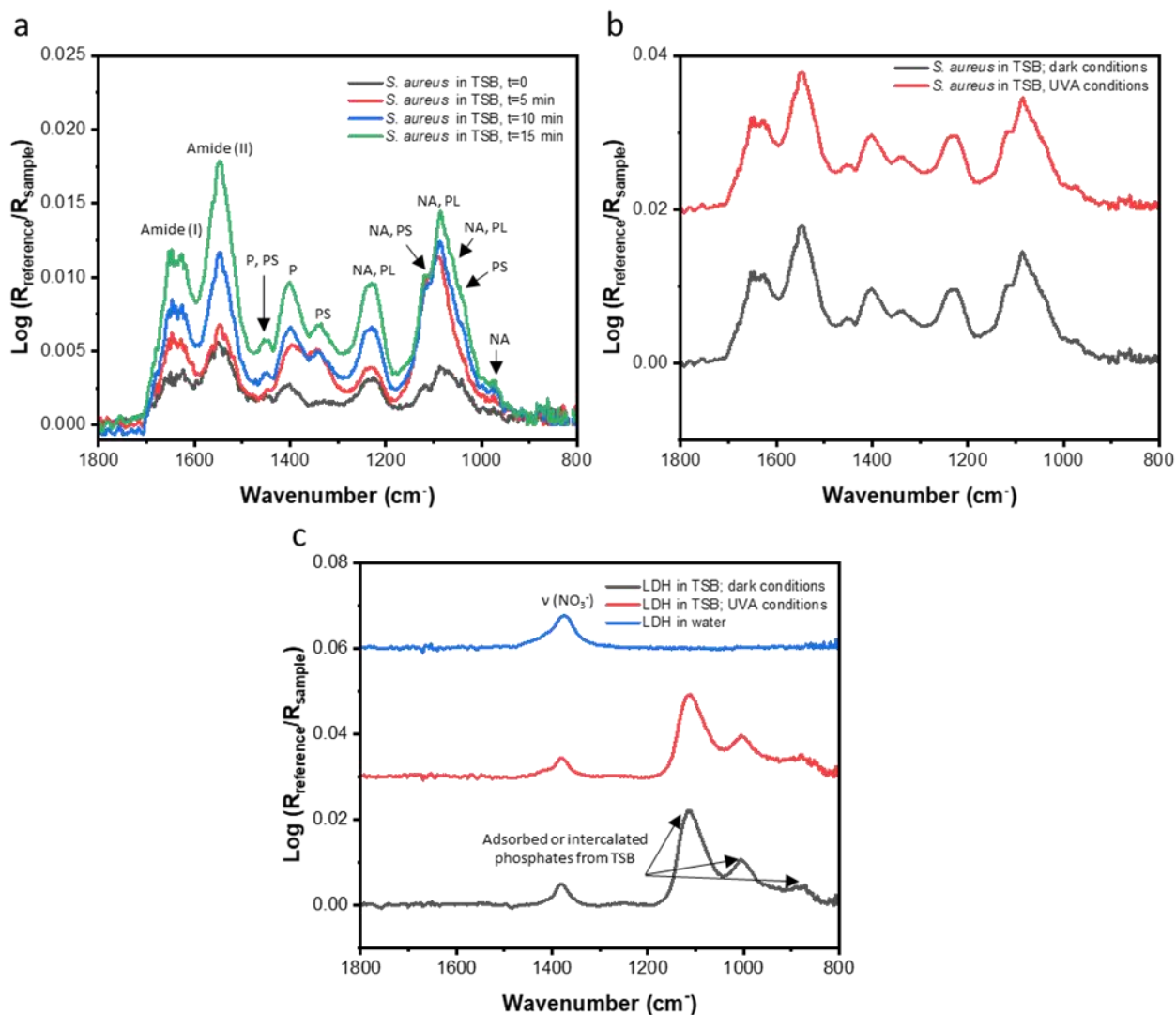


Figure 8. General IR spectra of *S. aureus* and LDH NPs. (a) *S. aureus* in TSB at different accumulation times on the ATR crystal. (b) *S. aureus* in TSB under dark and UVA condition at $t = 15$ min of accumulation on the ATR crystal. (c) LDH NPs in water and TSB under dark and UVA conditions at $t = 15$ min of accumulation on the ATR crystal. Corresponding supernatants from centrifugation were used to obtain the reference spectra. Offsets of spectra are used when necessary for clarity. P = proteins, PS = polysaccharides, NA = nucleic acids, PL = phospholipids.

Figure 8a shows the obtained FTIR spectra of *S. aureus* cells recorded during different time intervals. The spectrum recorded after 15 min showed the most intense peaks due to the time needed by the bacterial suspension to accumulate on the ATR crystal. Therefore, all other FTIR spectra provided will be the ones recorded after a time interval of 15 min relative to the initial time of suspension deposition on the crystal. The spectral features of *S. aureus* cells were typical to those reported previously in the literature (**Table 3**) [21]. The spectral region situated between

1800 and 1500 cm^{-1} arises mainly from the vibration of amide I and amide II bonds (proteins). Whereas the region located between 1500 and 1170 cm^{-1} was governed by the vibrations of functional compounds attributed to proteins, polysaccharides, phospholipids and nucleic acids. Finally, the region between 1170 and 800 cm^{-1} was dominated by vibrations of nucleic acids, polysaccharides and phospholipids functional groups. As suggested by **Figure 8b**, no remarkable peak shift or intensity change was observed upon irradiating cells with UVA light, ensuring that UVA light does not impose significant structural change to the biochemical composition of *S. aureus* cells, as previously suggested by the antibacterial activity tests and AFM imaging.

Table 3. Common peaks observed in the IR spectra of *S. aureus* [21].

Peak position (cm^{-1})	Vibration	Possible assignment
1638	Amide I	Proteins
1548	Amide II	Proteins
1452	$\delta(\text{CH}_3)$, $\delta(\text{CH}_2)$	Proteins, polysaccharides, lipids
1394	$\nu_s(\text{COO}^-)$	Proteins
1335	$\delta(\text{CH})$	Polysaccharides
1240	$\nu_a(\text{PO}_2)$	Nucleic acids, phospholipids
1117	$\nu(\text{C-C})$, $\nu(\text{C-O})$, $\nu(\text{P-O-C})$	Nucleic acids, polysaccharides
1082	$\nu_s(\text{PO}_2)$	Nucleic acids, phospholipids
1057, 1032, 965	$\nu(\text{C-O-C})$, $\nu(\text{C-C})$, $\nu(\text{C-O})$	Nucleic acids, phospholipids, polysaccharides

The FTIR spectrum of ZnAl LDH NPs was strongly influenced by the TSB culture media (**Figure 8c**). Two strong vibration bands were noticed at $\sim 1110 \text{ cm}^{-1}$ and $\sim 988 \text{ cm}^{-1}$ which were absent in the spectrum recorded in distilled water. These peaks maybe assigned to vibration bands of adsorbed or intercalated phosphate groups [22–25], *e.g.*, H_2PO_4^- and HPO_4^{2-} present in a pH range of 7.2–12 [26]. These adsorbed/intercalated phosphate groups arise from the chemical composition of TSB culture media.

The XRD powder diffractogram of LDH NPs exposed to TSB medium for 24 h did not show any significant change neither in the intensity nor in the position of the (00n) basal diffraction peaks (**Figure 9**) which are affected by ionic exchange, as they are linked to the size of the intercalated anion. The possibility of a massive exchange of anion to intercalate phosphate groups has to be excluded. However, the IR spectra of LDH NPs in TSB media (**Figure 8c**) suggests the exchange

(or the adsorption) of a small portion of nitrate anions with phosphates ones. This could actually be derived by the slight change in chemical environment and decrease in the intensity of intercalated nitrate anions in TSB media compared to that found in water which suggests the exchange of a small portion of nitrate anions with phosphates ones.

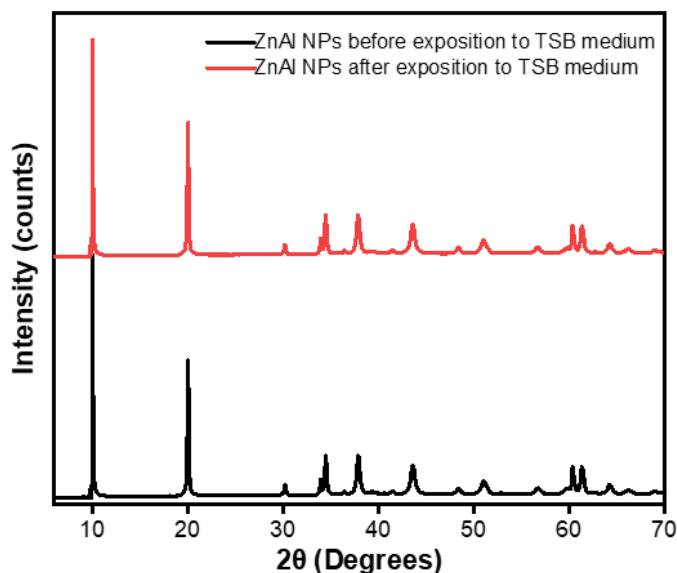


Figure 9. PXRD diffraction pattern of ZnAl LDH NPs before and after exposition to TSB medium for 24 h.

4.2. Influence of ZnAl LDH NPs treatment in dark and UVA conditions on the biochemical structure of *S. aureus* cells evidenced by FT-IR spectroscopy

Several remarkable changes in the biochemical structure were noted upon treating *S. aureus* cells with ZnAl LDH NPs in dark conditions and UVA conditions (Figure 10a and b). In the region between 1800 and 1500 cm^{-1} , the intensities of the amide I, amide II and proteins bands located at around 1638, 1550, respectively, were reduced for ZnAl NPs-treated *S. aureus* cells in dark conditions. This decrease in intensity of these bands was even more pronounced and associated with a downshift in amide II peak from 1548 to $\sim 1539 \text{ cm}^{-1}$ in case the cells were treated with ZnAl NPs in UVA conditions (Figure 10b and c). Such decrease in intensity may be attributed in to the decrease in biomass production leading to bacterial growth inhibition. Such inhibition maybe due to the suppression of transpeptidation process [27], the reaction that leads to the cross-linkage of two glycan-linked peptide chains. As a result, a newly synthesized bacterial cell wall will no

longer be cross-linked and cannot maintain its strength [27–29], leading to the death of *S. aureus* cells as previously observed in our CFU count experiments. Furthermore, the downshift in wavenumber for amide II peak for treated cells in UVA conditions indicates that the population of proteins underwent a significant structural modification. Most probably, denaturation associated with the destruction of the cell wall of *S. aureus* as suggested by the AFM imaging of treated cells in UVA conditions (**Figure 6d**).

In the region of 1500 to 1170 cm^{-1} , the most remarkable change was observed for the phospholipids and nucleic acids bands located at $\sim 1240 \text{ cm}^{-1}$ corresponding to the vibration of (PO_2) groups. In both treated samples in dark and UVA conditions the band (**Figure 10a and b**) disappeared completely, suggesting that bacterial membrane phospholipids were destroyed by LDH treatment. A new peak also appeared in both treated samples at around 1208 cm^{-1} belonging to organo-phosphorous compounds [30], which may be attributed to the synthesis of new phosphorous compounds by the bacteria in response to the antibacterial effect induced by ZnAl LDH NPs in dark and UVA conditions. In fact, it was previously reported that alterations in membrane phosphorous compounds take place in response to environmental stress [31]. Cell lysis and formation of cell debris (**Figure 7c and d**) may be another explanation of the appearance of the new phosphorous compounds, where cell lysis results in the release of phosphorus-containing cell components and active enzymes that could persist after the lysis process [32]. Additionally, a significant decrease was observed in the intensities of proteins and polysaccharide peaks in the range of 1477 and 1290 cm^{-1} for both treated samples (dark and UVA conditions), with a more pronounciation in case of ZnAl NPs-treated cells under UVA conditions. This highlights again the efficiency of ZnAl LDH NPs in UVA conditions to suppress the production of these essential cell compounds. Finally, the peak located at $\sim 1360 \text{ cm}^{-1}$ is assigned to nitrate intercalated anions previously observed in the ZnAl LDH control spectra in TSB medium.

In the region between 1170 and 800 cm^{-1} , the spectral fingerprints of *S. aureus* were unfortunately masked by the adsorbed/intercalated groups on the LDH in case of ZnAl LDH NPs-treated samples in dark and UVA conditions (**Figure 10a and b**). However, we can clearly notice that shape and the intensity of the peaks in this region were not exactly similar to that of pure LDH NPs in TSB. This suggests that intense peaks located around ~ 1091 and $\sim 995 \text{ cm}^{-1}$ might be attributed not only to adsorbed/intercalated phosphate groups on the LDHs but also to the

biochemical bacterial composition, *e.g.*, nucleic acids, phospholipids and polysaccharides. Yet, it is still difficult to detect changes induced by the NPs in this region due to the overlapping with peaks coming from the LDHs in contact with TSB medium.

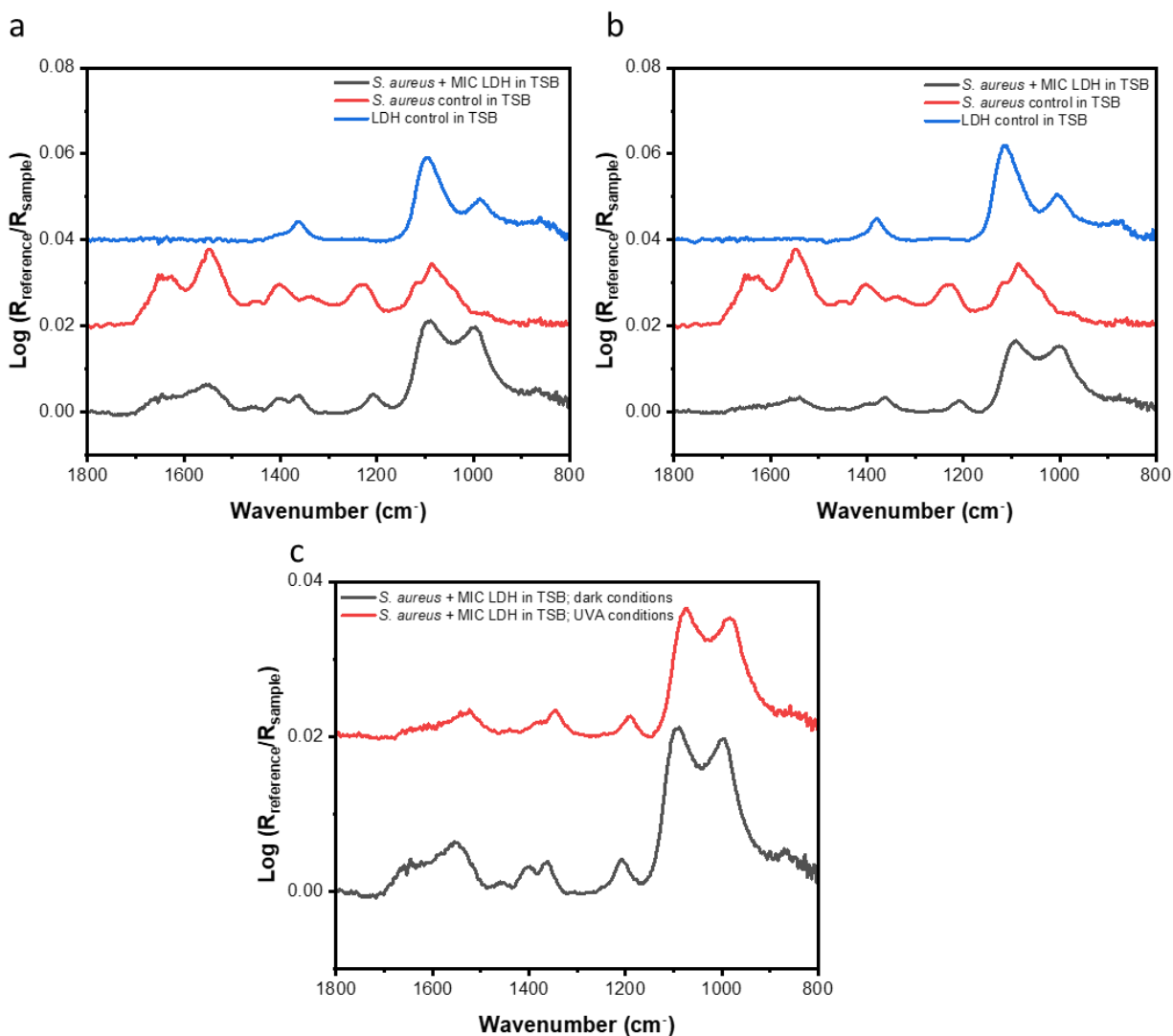


Figure 10. Influence of ZnAl LDH NPs treatment on the IR spectrum of *S. aureus*. (a) IR spectra of treated and untreated *S. aureus* cells with ZnAl LDH NPs at MIC under dark conditions. (b) IR spectra of treated and untreated *S. aureus* cells with ZnAl LDH NPs at MIC under UVA conditions. (c) Difference in IR spectra of *S. aureus* cells treated with ZnAl LDH NPs at MIC under dark and UVA conditions. Corresponding supernatants from centrifugation were used to obtain the reference spectra. Offsets of spectra are used for clarity.

We can thus ensure that ZnAl LDH NPs impose serious alterations to the biochemical structure of *S. aureus*. This impact was more definite in UVA conditions probably due the generation of ROS by the LDHs in response to the illumination. In this context, when UVA light irradiates ZnAl LDH

NPs, their antibacterial activity is enhanced due to the dual effect of the NPs themselves and the possible generated ROS, thus inducing a more efficient bactericidal effect against *S. aureus* cells by causing serious damages to their cell wall composition and structure.

5. Conclusion

In summary, bactericidal efficiency of ZnAl LDH NPs against *S. aureus* was enhanced from a partial bactericidal effect in dark condition (88.9%) to a complete killing effect (100%) in UVA light probably due to the generation of ROS by the LDHs in response to the irradiation. This was also associated with an increase in the rate of killing the bacteria during the irradiation time period. The bactericidal activity of the suggested produced ROS was less pronounced in presence of histidine acting as a ROS scavenger. Such finding provided a primary evidence concerning the generation of ROS by ZnAl LDH NPs in presence of UVA light. Moreover, FTIR spectroscopy revealed remarkable changes in the structural components of the cells imposed by ZnAl LDH NPs treatment in both dark and UVA conditions with more pronounced alterations in the latter. The impacts of such alterations were highlighted in the morphology and textural features of *S. aureus* cells exposed to LDH NPs treatment, by which they seemed completely distorted possessing rough surfaces, especially those treated in UVA conditions. All these findings suggest the presence of a dual effect between ZnAl LDH NPs and generated ROS to provide an amplified antibacterial effect.

Therefore, alongside the antibacterial activity of Zn(II)-based LDHs mediated by direct contact (**Mechanism 1**) and release of Zn^{2+} ions (**Mechanism 2**), the antibacterial activity of these LDHs may further be improved by the generation of ROS (**Mechanism 3**) in the presence of a suitable light source. Despite the fact that our findings suggest the production of ROS in presence of UVA light, a suitable method should be adapted to experimentally measure ROS, *e.g.*, fluorescence spectroscopy using fluorescent dye probes, ESR or chromatography methods.

References

- [1] B. Ezraty, A. Gennaris, F. Barras, J.-F. Collet, Oxidative stress, protein damage and repair in bacteria, *Nat. Rev. Microbiol.* 15 (2017) 385–396.
- [2] R. Mittler, ROS Are Good, *Trends Plant Sci.* 22 (2017) 11–19.
- [3] H. Li, X. Zhou, Y. Huang, B. Liao, L. Cheng, B. Ren, Reactive Oxygen Species in Pathogen Clearance: The Killing Mechanisms, the Adaption Response, and the Side Effects, *Front. Microbiol.* 11 (2021) 622534.
- [4] H. Abdolmohammad-Zadeh, M. Zamani-Kalajahi, In situ generation of H₂O₂ by a layered double hydroxide as a visible light nano-photocatalyst: Application to bisphenol A quantification, *Microchem. J.* 158 (2020) 105303.
- [5] Z. Zhang, Z. Hua, J. Lang, Y. Song, Q. Zhang, Q. Han, H. Fan, M. Gao, X. Li, J. Yang, Eco-friendly nanostructured Zn–Al layered double hydroxide photocatalysts with enhanced photocatalytic activity, *CrystEngComm.* 21 (2019) 4607–4619.
- [6] B. Abebe, E.A. Zereffa, A. Tadesse, H.C.A. Murthy, A Review on Enhancing the Antibacterial Activity of ZnO: Mechanisms and Microscopic Investigation, *Nanoscale Res. Lett.* 15 (2020) 190.
- [7] C. Bankier, Y. Cheong, S. Mahalingam, M. Edirisinghe, G. Ren, E. Cloutman-Green, L. Ciric, A comparison of methods to assess the antimicrobial activity of nanoparticle combinations on bacterial cells, *PLOS ONE.* 13 (2018) e0192093.
- [8] S.-E. Jin, J.E. Jin, W. Hwang, S.W. Hong, Photocatalytic antibacterial application of zinc oxide nanoparticles and self-assembled networks under dual UV irradiation for enhanced disinfection, *Int. J. Nanomedicine.* Volume 14 (2019) 1737–1751.
- [9] A.M. Wade, H.N. Tucker, Antioxidant characteristics of L-histidine 11The work described in this manuscript was partially sponsored and funded by Cytos Pharmaceuticals, LLC., *J. Nutr. Biochem.* 9 (1998) 308–315.
- [10] D.O. Son, H. Satsu, M. Shimizu, Histidine inhibits oxidative stress- and TNF- α -induced interleukin-8 secretion in intestinal epithelial cells, *FEBS Lett.* 579 (2005) 4671–4677.
- [11] Z. Zhao, C. Fu, Y. Zhang, A. Fu, Dimeric Histidine as a Novel Free Radical Scavenger Alleviates Non-Alcoholic Liver Injury, *Antioxidants.* 10 (2021) 1529.
- [12] N. Weiß, W. Wente, S. Topp, The Influence of UV Absorbing Substances Released from Plastic Containers, (n.d.).
- [13] I. Bokkon, EDITORIAL (Hot Topic: Recognition of Functional Roles of Free Radicals), *Curr. Neuropharmacol.* 10 (2012) 287–288.
- [14] M. Nocchetti, M. Pica, B. Ridolfi, A. Donnadio, E. Boccalon, G. Zampini, D. Pietrella, M. Casciola, AgCl-ZnAl Layered Double Hydroxides as Catalysts with Enhanced Photodegradation and Antibacterial Activities, *Inorganics.* 7 (2019) 120.
- [15] Y. Zhang, M. Dai, Z. Yuan, Methods for the detection of reactive oxygen species, *Anal. Methods.* 10 (2018) 4625–4638.
- [16] R.K. Dutta, B.P. Nenavathu, M.K. Gangishetty, A.V.R. Reddy, Studies on antibacterial activity of ZnO nanoparticles by ROS induced lipid peroxidation, *Colloids Surf. B Biointerfaces.* 94 (2012) 143–150.
- [17] G. Applerot, A. Lipovsky, R. Dror, N. Perkas, Y. Nitzan, R. Lubart, A. Gedanken, Enhanced Antibacterial Activity of Nanocrystalline ZnO Due to Increased ROS-Mediated Cell Injury, *Adv. Funct. Mater.* 19 (2009) 842–852.

- [18] F. Quilès, I. Accoceberry, C. Couzigou, G. Francius, T. Noël, S. El-Kirat-Chatel, AFM combined to ATR-FTIR reveals *Candida* cell wall changes under caspofungin treatment, *Nanoscale*. 9 (2017) 13731–13738.
- [19] E.B. Tatlybaeva, H.N. Nikiyan, A.S. Vasilchenko, D.G. Deryabin, Atomic force microscopy recognition of protein A on *Staphylococcus aureus* cell surfaces by labelling with IgG–Au conjugates, *Beilstein J. Nanotechnol.* 4 (2013) 743–749.
- [20] A. Beaussart, C. Retourney, F. Quilès, R. Dos Santos Morais, C. Gaiani, H.-P. Fiérobe, S. El-Kirat-Chatel, Supported lysozyme for improved antimicrobial surface protection, *J. Colloid Interface Sci.* 582 (2021) 764–772.
- [21] K. Kochan, E. Lai, Z. Richardson, C. Nethercott, A.Y. Peleg, P. Heraud, B.R. Wood, Vibrational Spectroscopy as a Sensitive Probe for the Chemistry of Intra-Phase Bacterial Growth, *Sensors*. 20 (2020) 3452.
- [22] C.V. Luengo, M.A. Volpe, M.J. Avena, High sorption of phosphate on Mg-Al layered double hydroxides: Kinetics and equilibrium, *J. Environ. Chem. Eng.* 5 (2017) 4656–4662.
- [23] M.A. Woo, T. Woo Kim, M.-J. Paek, H.-W. Ha, J.-H. Choy, S.-J. Hwang, Phosphate-intercalated Ca–Fe-layered double hydroxides: Crystal structure, bonding character, and release kinetics of phosphate, *J. Solid State Chem.* 184 (2011) 171–176.
- [24] Y.-H. Jiang, A.-Y. Li, H. Deng, C.-H. Ye, Y. Li, Phosphate adsorption from wastewater using ZnAl-LDO-loaded modified banana straw biochar, *Environ. Sci. Pollut. Res.* 26 (2019) 18343–18353.
- [25] M. Badreddine, A. Legrouri, A. Barroug, A. De Roy, J.-P. Besse, Influence of pH on Phosphate Intercalation in Zinc-Aluminum Layered Double Hydroxide, *Collect. Czechoslov. Chem. Commun.* 63 (1998) 741–748.
- [26] K.N. Han, Characteristics of Precipitation of Rare Earth Elements with Various Precipitants, *Minerals*. 10 (2020) 178.
- [27] N.T. Xuan Nguyen, S. Sarter, N. Hai Nguyen, P. Daniel, Detection of molecular changes induced by antibiotics in *Escherichia coli* using vibrational spectroscopy, *Spectrochim. Acta. A. Mol. Biomol. Spectrosc.* 183 (2017) 395–401.
- [28] F. Malouin, L.E. Bryan, Modification of penicillin-binding proteins as mechanisms of beta-lactam resistance, *Antimicrob. Agents Chemother.* 30 (1986) 1–5.
- [29] J. Ruiz, Mechanisms of resistance to quinolones: target alterations, decreased accumulation and DNA gyrase protection, *J. Antimicrob. Chemother.* 51 (2003) 1109–1117.
- [30] G. Socrates, Infrared and Raman characteristic group frequencies : tables and charts, in: 2001.
- [31] V.W. Rowlett, V.K.P.S. Mallampalli, A. Karlstaedt, W. Dowhan, H. Taegtmeier, W. Margolin, H. Vitrac, Impact of Membrane Phospholipid Alterations in *Escherichia coli* on Cellular Function and Bacterial Stress Adaptation, *J. Bacteriol.* 199 (2017).
- [32] A.H. Mine, M.L. Coleman, A.S. Colman, Phosphorus Release and Regeneration Following Laboratory Lysis of Bacterial Cells, *Front. Microbiol.* 12 (2021) 641700.

The contribution of direct contact and divalent metal ions release to the antibacterial activity of Zn(II)-based layered double hydroxide nanoparticles

Table of figures	204
Table of tables.....	205
1. Context	206
2. Agar disc diffusion assay and broth macro-dilution turbidimetric tests for MIC determination 207	
3. CFU count experiments.....	209
4. AFM imaging of treated cells	211
5. Conclusion.....	214
References	216

Table of figures

- Figure 1.** A schematic illustration of the contribution of direct contact (**Mechanism 1**) and release of Zn²⁺ ions (**Mechanism 2**) to the antibacterial activity of Zn(II)-based LDH NPs.206
- Figure 2.** Antibacterial activity against *S. aureus* of ZnAl NPs NPs (a) Mean zone of inhibition calculated as the average inhibition diameters of three repetitive trials of agar disc diffusion tests. (c) MIC values calculated as the average MIC of three repetitive trials of broth macro-dilution turbidimetric tests. *Zn²⁺ ions salt employed in a concentration of 4.1 mmol/L, corresponding to the average concentration of Zn²⁺ released out of ZnAl LDH NPs in agar disc diffusion test experiments.....208
- Figure 3.** CFU count experiments against *S. aureus* cells. (a) Concentration of treated and untreated *S. aureus* cells with ZnAl LDH NPs in presence and absence of EDTA. (b) Bactericidal efficiency of ZnAl LDH NPs and Zn²⁺ ions salt. * Zn²⁺ ions salt employed in a concentration of 0.04 mmol/L, corresponding to the average concentration of Zn²⁺ released out of ZnAl LDH NPs in agar disc diffusion test experiments.210
- Figure 4.** AFM deflection images of *S. aureus* in liquid (scale bar = 250 nm). (a) *S. aureus* cells treated with 41 mmol/L EDTA. (b) *S. aureus* cells treated with ZnAl LDH NPs at MIC. (c) *S. aureus* cells treated ZnAl LDH NPs at MIC and 41 mmol/L EDTA. (d) *S. aureus* cells treated with 0.04 mmol/L Zn²⁺ ions salt, corresponding to the molar concentration of released Zn²⁺ out ZnAl LDH NPs in MIC determination experiments in TSB medium.212
- Figure 5.** AFM deflection images of *S. aureus* in air (scale bar = 500 nm). (a) *S. aureus* cells treated with 41 mmol/L EDTA. (b) *S. aureus* cells treated with ZnAl LDH NPs at MIC. (c) *S. aureus* cells treated ZnAl LDH NPs at MIC and 41 mmol/L EDTA. (d) *S. aureus* cells treated with 0.04 mmol/L Zn²⁺ ions salt, corresponding to the molar concentration of released Zn²⁺ out ZnAl LDH NPs in MIC determination experiments in TSB medium.214

Table of tables

Table 1. Average concentration of release Zn^{2+} ions out of ZnAl LDH NPs in TSB medium during agar disc diffusion and broth macro-dilution turbidimetric tests.....	207
Table 2. Roughness parameter R_q of <i>S. aureus</i> cells treated and not with Zn^{2+} ion salts or LDH NPs at MIC in presence and absence of EDTA.....	213

1. Context

In the previous three chapters we have validated the existence of the three suggested antibacterial mechanisms of pristine LDHs for Zn(II)-based LDHs: (1) direct surface interactions with bacterial cell wall (**Chapter 4**), (2) release of Zn^{2+} metal ions (**Chapter 3**), (3) generation of ROS by LDHs in presence of UVA light (**Chapter 5**). In fact, we have already evaluated the influence of possibly produced ROS on the enhancement of the antibacterial activity of ZnAl LDH NPs where their bactericidal efficiency was enhanced by thus achieving a total killing effect toward *S. aureus*. However, the contribution of the other suggested mechanisms reported in the absence of any source of light, *i.e.*, direct contact and Zn^{2+} release, is still unknown. Therefore, it was of great importance to us to determine which mechanism may dominate the antibacterial activity of Zn(II)-based LDH NPs.

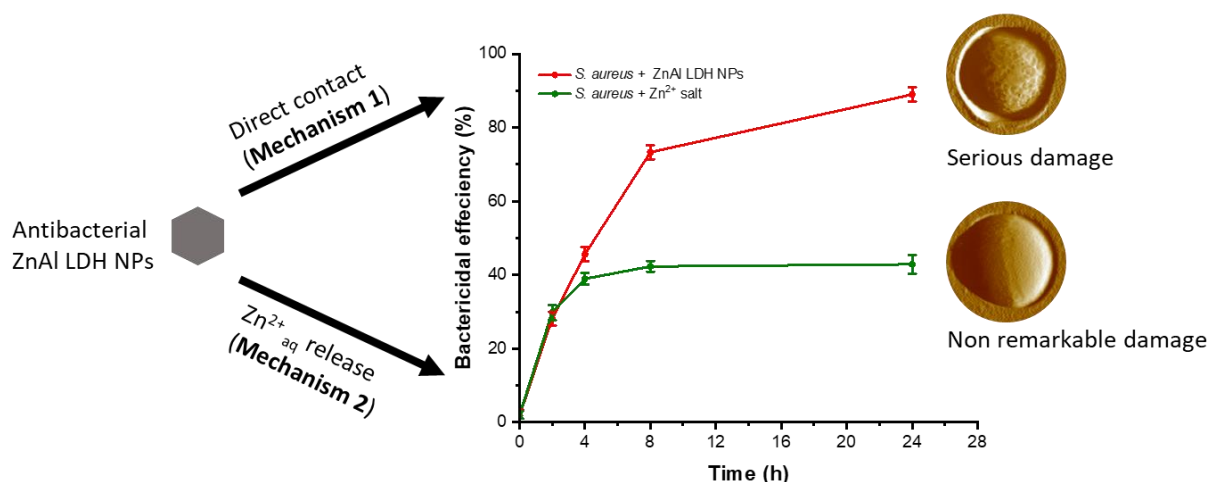


Figure 1. A schematic illustration of the contribution of direct contact (**Mechanism 1**) and release of Zn^{2+} ions (**Mechanism 2**) to the antibacterial activity of Zn(II)-based LDH NPs.

In this chapter, we will compare two antibacterial mechanisms of the previously used ZnAl LDH NPs: direct contact (**Mechanism 1**) and Zn^{2+} release (**Mechanism 2**). The comparison will be achieved by performing the antibacterial activity tests, *e.g.*, agar disc diffusion test, broth macro-dilution test for MIC determination and CFU counts experiments, as well as AFM cells imaging in presence of ethylenediamine tetraacetic acid (EDTA). EDTA is a very potent zinc-chelating agent which binds to zinc ions extremely tightly forming very strong complex with very low dissociation constant of 10^{-16} mol/L [1]. In this context, EDTA will be used as a scavenger of Zn^{2+}

released out of the ZnAl LDH NPs thus suppressing the antibacterial activity mechanism of divalent metal release. We will further notice that the release of Zn^{2+} out of Zn(II)-based LDH NPs (**Mechanism 2**) is a dominant mechanism in some antibacterial activity tests, whereas it is less pronounced in others.

Antibacterial activity tests and AFM cells imaging using zinc ions salt (zinc nitrate salt) will also be presented to differentiate between the antibacterial efficiency and mode of action of released Zn^{2+} ions and Zn(II)-based LDHs (**Figure 1**). The comparison of the antibacterial properties between the latter two will allow us to determine the advantages of using Zn(II)-based LDHs as efficient antibacterial agents due to their amplified and prolonged antibacterial effect.

2. Agar disc diffusion assay and broth macro-dilution turbidimetric tests for MIC determination

Agar disc diffusion assay and broth macro-dilution turbidimetric methods were carried out to determine the antibacterial activity of the previously synthesized ZnAl LDH NPs in presence of EDTA acting a scavenger of released Zn^{2+} out of ZnAl LDH NPs in Tryptic soy broth (TSB) media. Since the amount of ZnAl LDH NPs was different in agar disc diffusion experiments and broth macro-dilution tests, the concentration of released Zn^{2+} in each experiment was thus different as well. The concentration of released Zn^{2+} in both antibacterial assays was evaluated by ICP-MS (**Table 1**), and the concentration of added EDTA was set as at least 10 times that of released Zn^{2+} to ensure that all released ions were scavenged.

Table 1. Average concentration of release Zn^{2+} ions out of ZnAl LDH NPs in TSB medium during agar disc diffusion and broth macro-dilution turbidimetric tests.

Experiment	Concentration of employed ZnAl LDH NPs	Average concentration of released Zn^{2+} ions calculated by ICP-MS	Concentration of used EDTA
Agar disc diffusion test	10 mg/mL	4.1 ± 0.06 mmol/L	41 mmol/L
Broth macro-dilution turbidimetric test for MIC determination	93.8 μ g/mL	0.04 ± 0.01 mmol/L	41 mmol/L

The average generated inhibitory zone diameters and MIC values by ZnAl LDH NPs in presence and absence of EDTA reported in Figure 2 were obtained from three repetitive independent experiments.

Upon adding EDTA to the LDH suspension used in agar disc diffusion test, the inhibitory zone (average diameter = 20.6 mm) generated by ZnAl LDH NPs disappeared completely (Figure 2a). This indicates that when Zn^{2+}_{aq} release is suppressed in agar disc diffusion tests, ZnAl LDH NPs lose their antibacterial properties. In order to further support such finding, the antibacterial activity of Zn^{2+} ions salt was tested in a concentration similar to that released out of ZnAl LDH NPs, *i.e.*, 4.1 mmol/L. The inhibitory effect of Zn^{2+} (average inhibitory diameter = 20 mm) in the agar gel was similar to that imposed by the NPs, thus confirming that reported antibacterial activity of ZnAl LDH NPs is governed by the release of Zn^{2+} ions in agar solids environments.

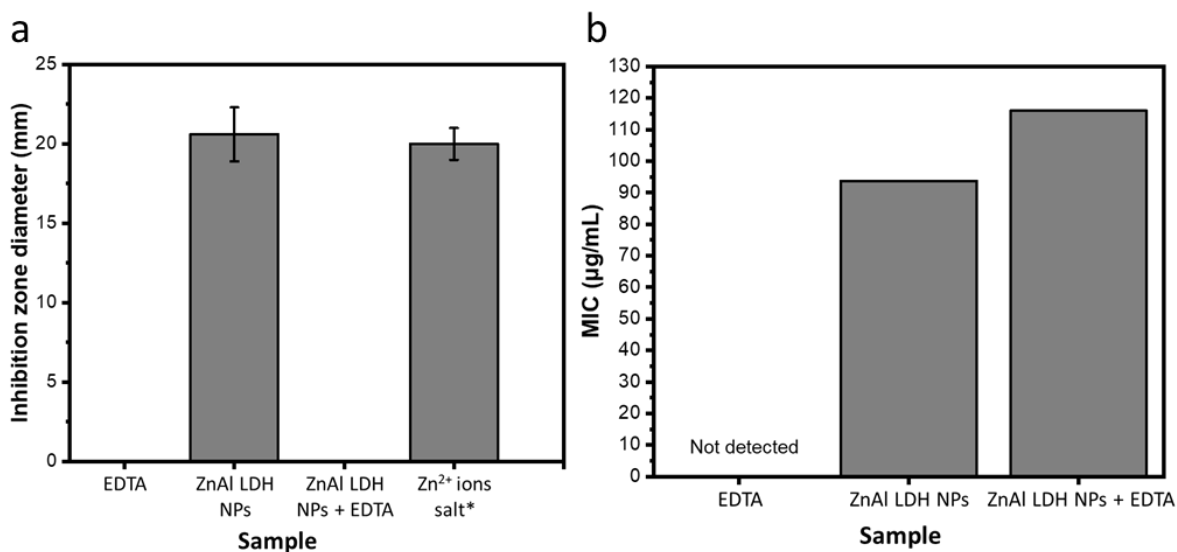


Figure 2. Antibacterial activity against *S. aureus* of ZnAl NPs (a) Mean zone of inhibition calculated as the average inhibition diameters of three repetitive trials of agar disc diffusion tests. (c) MIC values calculated as the average MIC of three repetitive trials of broth macro-dilution turbidimetric tests. * Zn^{2+} ions salt employed in a concentration of 4.1 mmol/L, corresponding to the average concentration of Zn^{2+} released out of ZnAl LDH NPs in agar disc diffusion test experiments.

Such results were actually expected, since the principle of agar disc is based on diffusion phenomena [2]. In fact, it was previously reported that the mass transfer of particles having a greater size than 70 nm can be neglected in agar gel [3]. Considering that our NPs have an average size of 176 ± 44 nm (Chapter 4), they cannot diffuse into the agar gel to inhibit bacterial growth.

Therefore, the direct contact mechanism (**Mechanism 1**) governed by surface interaction between LDH NPs and bacterial cell walls is not pronounced in agar disc diffusion tests. Moreover, we already reported in **Chapter 5** that agar disc diffusion tests are not suitable to evaluate the impact of ROS generation (**Mechanism 3**) on the antibacterial activity of ZnAl LDHs due to the very short lifespan of free radicals. In this context, the antibacterial activity of ZnAl LDH NPs observed in agar disc diffusion assay is only linked to the antibacterial mechanism mediated by $\text{Zn}^{2+}_{\text{aq}}$ release. Therefore, the release of divalent metal ions (**Mechanism 2**) is the dominating antibacterial mode of action of pristine Zn(II)-based LDHs in agar solids environments.

The MIC of ZnAl LDH NPs increase from 93.8 to 116 $\mu\text{g/mL}$ in presence of EDTA in broth macro-dilution tests. Such result suggests that the release of $\text{Zn}^{2+}_{\text{aq}}$ (**Mechanism 2**) contribute to ~24% of the achieved antibacterial effect tested by the MIC determination. In order to validate this suggestion, we evaluated the MIC concentration of Zn^{2+} ions salt using the same experimental protocol. The MIC value of Zn^{2+} ions salt, *i.e.*, zinc nitrate hexahydrate, against *S. aureus* was found to be 56.8 $\mu\text{g/mL}$ corresponding to a molar concentration of 0.191 mmol/L. The average concentration of released Zn^{2+} out of LDH NPs was 0.04 mmol/L which constitute ~21% of the recorded MIC value for Zn^{2+} ions salt. Therefore, mechanism 2 mediated by $\text{Zn}^{2+}_{\text{aq}}$ release contributes only to ~21-24% of the reported antibacterial activity of Zn(II)-based LDH NPs. Whereas the rest is attributed to the direct surface interactions between the LDH particles and bacterial cell wall (**Mechanism 1**), thus qualifying it as a dominating mechanism during MIC determination experiments.

3. CFU count experiments

CFU counts experiments were also performed in presence and absence of EDTA in order to evaluate the contribution of $\text{Zn}^{2+}_{\text{aq}}$ release to the bactericidal efficiency of ZnAl LDH NPs. A Tris-buffered saline (TBS) buffer suspension of *S. aureus* (with and without LDH NPs in presence and absence of EDTA; $\text{OD}_{600} = 0.05$; diluted to 1/10000, 1/20000 and 1/50000; 100 μL) was spread on TSB agar Petri dishes at different defined time points. The Petri plates were then incubated at 37°C for 24 h, and the concentration of live cells was obtained from the number of colonies formed on the plate. Since the experiment evaluates the bactericidal efficiency in liquid, a concentration

of LDH NPs of 93.8 $\mu\text{g/mL}$ was used, corresponding to their MIC concentration obtained in liquid environment.

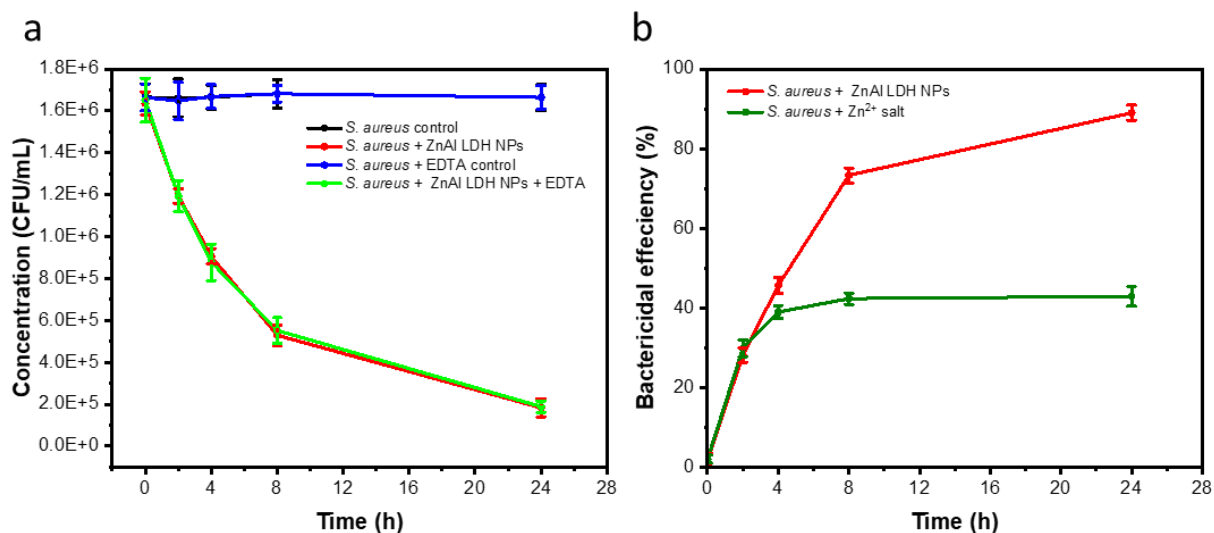


Figure 3. CFU count experiments against *S. aureus* cells. (a) Concentration of treated and untreated *S. aureus* cells with ZnAl LDH NPs in presence and absence of EDTA. (b) Bactericidal efficiency of ZnAl LDH NPs and Zn²⁺ ions salt. * Zn²⁺ ions salt employed in a concentration of 0.04 mmol/L, corresponding to the average concentration of Zn²⁺ released out of ZnAl LDH NPs in agar disc diffusion test experiments.

As the scavenging action of EDTA toward Zn²⁺ reduced the antibacterial activity of ZnAl LDHs during MIC determination experiments performed in liquid environment, an increase in the concentration of viable cells was expected. However, this was not the case. The reduction in the concentration of *S. aureus* cells induced by ZnAl LDH NPs was almost intact when EDTA was added (**Figure 3a**). Such surprising result can be explained by the fact that broth macro-dilution experiment used to evaluate the MIC value were performed in TSB where the concentration of released Zn²⁺ was 0.04 mmol/L. On the other hand, CFU count experiments were performed in TBS buffer to maintain a fixed concentration of cells which allows to determine the bactericidal efficiency. The concentration of released Zn²⁺ out of ZnAl LDH NPs in TBS buffer was actually below the detection limit of ICP. The difference in the release behavior of constituent divalent metal ions out of LDHs in different media was already addressed in **Chapter 3**. The pronounced Zn²⁺ release out of Zn(II)-based LDH NPs may be due to the tendency of zinc ions present in the powder to react to form complex organometallic compounds with proteins and amino acids present in TSB medium [4–6]. Therefore, the bactericidal efficiency of ZnAl LDH NPs (88.9%) obtained

from CFU count experiments is solely due to the direct contact mechanism, qualifying it again as a dominant mechanism in liquid environment.

In order to further differentiate between the antibacterial effect of Zn(II)-based LDHs and their metal ion salts counter parts, the bactericidal efficiency Zn²⁺ ion salts was also evaluated. Assuming that zinc nitrate salt having a water solubility value of 1.84 g/mL (~6195 mmol/L) [7], is at least as soluble in TSB buffer, a 0.04 mmol/L concentration of Zn²⁺ ion salt was added to TSB bacterial suspension, and CFU count experiments were carried out in a similar fashion described before, and the bactericidal efficiency was calculated using the following formula:

$$\% \text{ bactericidal efficiency} = \frac{N_c - N_A}{N_c} \times 100 \quad (1)$$

N_C is the number of bacterial colonies in a control group in the absence of LDH and Zn²⁺ ions salt, and N_A is the number of bacterial colonies found in the presence of ZnAl LDH NPs or Zn²⁺ ions salt.

The achieved bactericidal efficiency of Zn²⁺ ion salts did not exceed 40% (**Figure 3b**), which is remarkably lower than that induced by ZnAl LDH NPs (88.9%). The rate of bactericidal effect of Zn²⁺ ions salt increased rapidly during the first 2 hours similar to the bactericidal behavior of ZnAl NPs. After that the effect of Zn²⁺ ions salt was less pronounced for the following 6 h, after which a plateau is observed indicating that Zn²⁺ ions salt did not show any bactericidal effect after 6 h. This indicates that Zn²⁺_{aq} ions provide a “one shot” antibacterial effect. Whereas in the case of LDH NPs the antibacterial effect is extended for at least 24 hours. This highlights a clear advantage of Zn(II)-based LDHs over simple Zn²⁺ ions salt, where the former is able to provide a prolonged antibacterial effect. Such finding also highlights the advantage of direct contact mechanism (**Mechanism 1**) of ZnAl LDH NPs over the mechanism of Zn²⁺ ions release (**Mechanism 2**) due to the prolonged antibacterial followed strategy.

4. AFM imaging of treated cells

In order to determine the contribution of Zn²⁺_{aq} ions release and direct contact mechanisms to the damages imposed by ZnAl LDH NPs on *S. aureus* cell wall, AFM imaging of treated cells was performed in both liquid and air environments (**Figure 4** and **Figure 5**). The roughness parameter R_q (root mean square of the heights) was also obtained from AFM images performed on the top

of bacteria at a high magnification of $400 \times 400 \text{ nm}^2$ scanning areas (Table 2). As shown in Figure 4a, cells treated with EDTA presented regular spheroid morphologies and smooth surfaces and Rq roughness parameter similar to those of untreated normal cells (Chapters 4 and 5), ensuring that EDTA does not impose any cell wall damages to *S. aureus*.

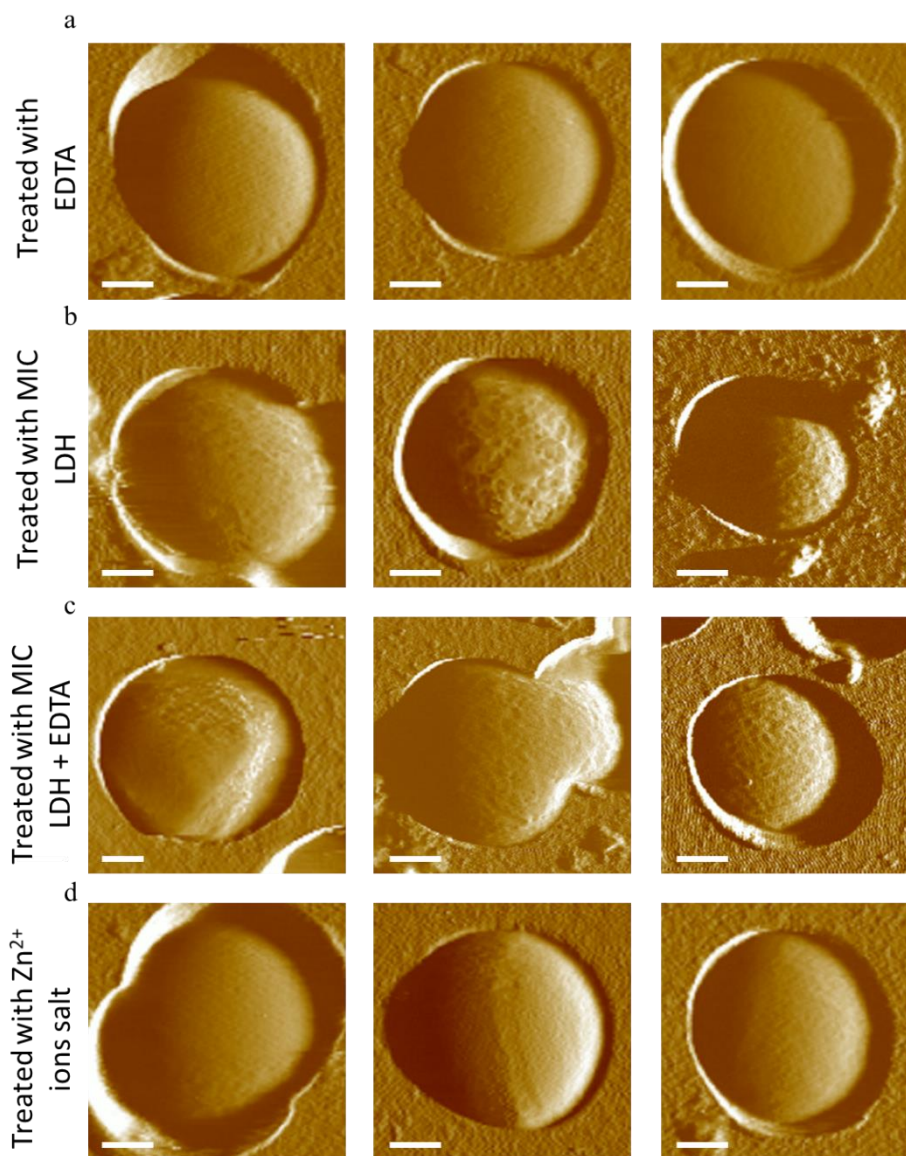


Figure 4. AFM deflection images of *S. aureus* in liquid (scale bar = 250 nm). (a) *S. aureus* cells treated with 41 mmol/L EDTA. (b) *S. aureus* cells treated with ZnAl LDH NPs at MIC. (c) *S. aureus* cells treated ZnAl LDH NPs at MIC and 41 mmol/L EDTA. (d) *S. aureus* cells treated with 0.04 mmol/L Zn^{2+} ions salt, corresponding to the molar concentration of released Zn^{2+} out ZnAl LDH NPs in MIC determination experiments in TSB medium.

The observed cell wall damages induced by ZnAl LDH NPs, *e.g.*, corrugated surfaces, hollows, crests and grooves (Figure 4b), were also found for cells treated with the NPs in presence of EDTA

(**Figure 4c**) with no remarkable change in R_q roughness parameter (**Table 2**). In addition, cells treatment with Zn^{2+} ions salt (in a concentration similar to that released out Zn^{2+} out of ZnAl LDH NPs) did not impose any serious cell wall damages to *S. aureus* as suggested by their AFM deflection images and obtained R_q roughness parameters (**Figure 4d** and **Table 2**). This indicates Zn^{2+}_{aq} ions release (**Mechanism 2**) does not contribute much to the cell wall damage effect of ZnAl LDH NPs, and these damages are primary due to direct contact interactions between the LDH surface and *S. aureus* cell wall (**Mechanism 1**). Such findings come in line with the dominance of direct contact antibacterial mechanism of ZnAl LDH NPs in liquid TSB media during MIC determination experiments (**Section 2**).

Table 2. Roughness parameter R_q of *S. aureus* cells treated and not with Zn^{2+} ion salts or LDH NPs at MIC in presence and absence of EDTA.

<i>S. aureus</i> cells	R_q (nm)
Treated with EDTA	15.4 ± 0.8
Treated with MIC of LDH NPs	49.4 ± 2
Treated with MIC of LDH NPs + EDTA	47.6 ± 1.8
Treated with Zn^{2+} ions salt*	16.8 ± 1.1

* Zn^{2+} ions salt employed in a concentration of 0.04 mmol/L, corresponding to the average concentration of Zn^{2+}_{aq} released out of ZnAl LDH NPs in MIC determination experiments.

The effect of Zn^{2+}_{aq} ions release (**Mechanism 2**) on the cell wall damages induced by ZnAl LDH NPs was also not much pronounced in case cells were imaged in air. No remarkable difference was observed among ZnAl LDH NPs-treated cells in presence and absence of EDTA (**Figure 5b** and **c**), where defected cell walls, lysed cells and cell debris persisted even in the presence of EDTA. Moreover, the majority of cells treated with Zn^{2+} ions salt (**Figure 5d**), in a concentration similar to that released out of ZnAl LDH NPs, showed homogeneous shapes with a spheroid geometry and regular surfaces similar to those of normal healthy cells (**Figure 5a**). The nearly absent effect of Zn^{2+} ions release (**Mechanism 2**) on the cell wall damages induced by ZnAl LDH NPs is probably due to the very small participation of this mechanism in liquid environments, where a concentration of 0.04 mmol/L maybe too low to impose damages. Another possible explanation could be that Zn^{2+}_{aq} ions do not impose an antibacterial effect by targeting the cell wall of the microorganism, but rather by different action modes, *e.g.*, disturbing the permeability of the membrane and binding to intracellular DNAs and proteins leading to their denaturation [8,9].

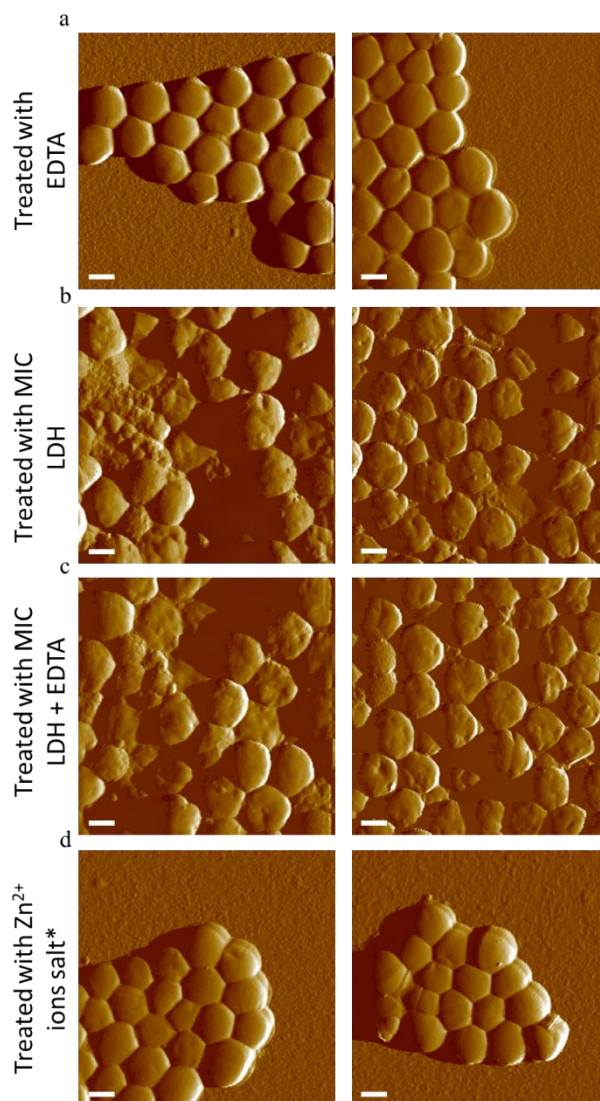


Figure 5. AFM deflection images of *S. aureus* in air (scale bar = 500 nm). (a) *S. aureus* cells treated with 41 mmol/L EDTA. (b) *S. aureus* cells treated with ZnAl LDH NPs at MIC. (c) *S. aureus* cells treated ZnAl LDH NPs at MIC and 41 mmol/L EDTA. (d) *S. aureus* cells treated with 0.04 mmol/L Zn²⁺ ions salt*, corresponding to the molar concentration of released Zn²⁺ out ZnAl LDH NPs in MIC determination experiments in TSB medium.

5. Conclusion

In summary, the contribution of divalent metal ions release and direct surface interactions to the antibacterial activity of pristine ZnAl LDH NPs was evaluated by using EDTA acting as a scavenger of Zn²⁺_{aq} ions released out of the LDH. The antibacterial properties of ZnAl LDH NPs in agar disc diffusion tests (based on diffusion phenomena) was solely attributed to the release of

Zn²⁺ ions (**Mechanism 2**), whereas the contribution of direct contact mechanism (**Mechanism 1**) was not pronounced at all due to the limit of diffusion of particles in agar gels. On the contrary, the reported antibacterial activity of ZnAl LDH NPs in MIC tests performed in liquid TSB was dominated by the direct surface interactions mechanism, whereas divalent metal ions release contributed only to 21-24% of the antibacterial activity expressed in these types of experiments. Such limited contribution was also expressed in terms of modest cell wall damages induced by the released Zn²⁺_{aq} ions. Moreover, released Zn²⁺_{aq} ions out of ZnAl NPs did not participate in the bactericidal efficiency determined by CFU count experiments due to the very low release profile of Zn²⁺_{aq} ions in TBS buffer. Therefore, the 88.9% bactericidal effect of ZnAl LDH NPs was solely due to direct contact mechanism which is responsible for the serious cell wall damages of ZnAl LDH NPs-treated *S. aureus* cells.

In summary, the released of Zn²⁺_{aq} ions (**Mechanism 2**) controls the antibacterial activity of pristine Zn(II)-based LDHs in agar solid environments. Whereas in liquid environments, the role of this mechanism 2 is less pronounced, and direct contact mechanism (**Mechanism 1**) thus dominates the antibacterial effect of LDHs. Such findings are insightful in terms of how to tune the physico-chemical properties of pristine ZnAl LDHs according to the target environment and governed antibacterial mechanism.

Finally, we would like to highlight one crucial advantage of ZnAl LDHs over simple Zn²⁺ ions salt where the former could provide a prolonged bactericidal activity unlike the latter which possess a “one-shot” bactericidal effect. Such demonstration also applies for the mechanism of Zn²⁺_{aq} ions release because the same species, *i.e.*, Zn²⁺ ions, are used to achieve the antibacterial effect. Therefore, direct contact mechanism (**Mechanism 1**) which is a dominating mode of action of antibacterial pristine Zn(II)-based LDHs in liquid environment qualifies these types of LDHs to act as efficient antibacterial agents with a prolonged effect.

References

- [1] J.K. Nyborg, O.B. Peersen, That zincing feeling: the effects of EDTA on the behaviour of zinc-binding transcriptional regulators, *Biochem. J.* 381 (2004) e3.
- [2] S. Ringertz, G. Kronvall, On the theory of the disk diffusion test, *APMIS.* 96 (1988) 484–490.
- [3] N. Fatin-Rouge, K. Starchev, J. Buffle, Size Effects on Diffusion Processes within Agarose Gels, *Biophys. J.* 86 (2004) 2710–2719.
- [4] S. Liu, E. Killen, M. Lim, C. Gunawan, R. Amal, The effect of common bacterial growth media on zinc oxide thin films: identification of reaction products and implications for the toxicology of ZnO, *RSC Adv.* 4 (2014) 4363–4370.
- [5] L. Esteban-Tejeda, F. Palomares, B. Cabal, R. López-Píriz, A. Fernández, D. Sevillano, L. Alou, R. Torrecillas, J. Moya, Effect of the Medium Composition on the Zn²⁺ Lixiviation and the Antifouling Properties of a Glass with a High ZnO Content, *Materials.* 10 (2017) 167.
- [6] J. Pasquet, Y. Chevalier, J. Pelletier, E. Couval, D. Bouvier, M.-A. Bolzinger, The contribution of zinc ions to the antimicrobial activity of zinc oxide, *Colloids Surf. Physicochem. Eng. Asp.* 457 (2014) 263–274.
- [7] D.L. Perry, *Handbook of inorganic compounds*, 2nd ed, Taylor & Francis, Boca Raton, 2011.
- [8] S. Mittapally, R. Taranum, S. Parveen, Metal ions as antibacterial agents, *J. Drug Deliv. Ther.* 8 (2018) 411–419.
- [9] S. Midori-Ku, Comparative Bacteriolytic Mechanism for Ag⁺ and Zn²⁺ Ions against *Staphylococcus Aureus* and *Escherichia Coli*: A review, *Escherichia Coli.* (2019) 12.

General conclusions and perspectives

By taking advantage of working at LCPME laboratory in the “ Chimie et Spectrochimie des Interfaces ” (CSI) team of multidisciplinary skills including physical chemistry, microbiology and biophysics, we were able to address the topic of “Antibacterial Mechanisms of Pristine Zinc-based Layered Double Hydroxides”. Our work was actually based on original experimental approaches allowing us to implement spectroscopic and microscopic analysis to decipher the followed antibacterial mechanisms of pristine LDHs.

Our primary results suggested that the antibacterial activity of pristine LDHs is dependent on the first place on the nature of constituent divalent metal, which propelled us to focus on Zn(II)-based LDHs showing the greatest antibacterial effect. The antibacterial activity of these type of LDHs was more pronounced in case where LDH samples released more Zn^{2+}_{aq} ions in broth culture media thus validating the suggested antibacterial mechanism of divalent metal release (**Mechanism 2**). Therefore, several properties of pristine d LDHs can be tuned in a way that the antibacterial effect by metal ions release could be enhanced, including:

- nature of constituent divalent metal or loaded NP to be released, *i.e.*, Zn^{2+} having the greatest effect against *S. aureus* and *E. coli*
- increasing the release of the divalent cations in different possible ways:
 - o increasing the divalent to the trivalent metal molar ratio of LDH {M(II)/Al(III)}
 - o lowering the crystallinity of LDH powders
 - o introducing intercalating anions having lower affinity to the layers
 - o decreasing the size of LDHs which could provide an impact on the amount of metal ions released, *i.e.*, smaller particles release more metal ions

The antibacterial activity of Zn(II)-based LDHs was also controlled by direct surface interactions between the LDH surface and the cell wall of *S. aureus* bacteria (**Mechanism 1**). This was clearly evidenced by the superior antibacterial effect of LDH nanoparticles presenting a greater surface area of interactions compared to that of micron-sized LDHs. Therefore, the LDH particle size plays a crucial role in the antibacterial activity governed by direct surface interactions. AFM-based force spectroscopy further validated the presence of specific surface interactions between Zn(II)-based LDHs and *S. aureus*. These specific surface interactions were neither related to the morphology of

LDHs nor to their Al(III) constituent trivalent metal, but rather to the presence of Zn(II) as a divalent metal in the structure. Thus, Zn(II)-based NPs were specifically able to recognize and adhere to *S. aureus* cells thus imposing serious damages to their cell walls by direct surface interactions.

Furthermore, the enhancement of antibacterial activity of Zn(II)-based LDHs could also be achieved by the possible generation of ROS (**Mechanism 3**) in presence of UVA light. In other words, Zn(II)-based LDHs may produce ROS in response to UVA light, thus maximizing the rate and efficiency of the achieved antibacterial activity from a partial bactericidal effect in dark conditions (88.9%) to a complete killing effect (100%) in UVA conditions. This gives a sign about the dual effect between the LDH NPs and the possible generated ROS. This is actually achieved by imposing greater damage to the cell wall of *S. aureus* and more pronounced alteration in their biochemical composition. Therefore, alongside the antibacterial activity of Zn(II)-based LDHs governed by the release of Zn²⁺ ions (**Mechanism 2**) and direct contact (**Mechanism 1**), the antibacterial activity of these LDHs may further be improved by the generation of ROS (**Mechanism 3**) in the presence of a suitable light source. It is true that we provided a primary evidence concerning the generation of ROS by using histidine as a scavenger of produced radicals. However, a suitable method should be adapted in the near future to experimentally evaluate and measure generated ROS such as, fluorescence spectroscopy using fluorescent dye probes, chromatography methods, or ESR.

We were not just satisfied by validating the three mentioned antibacterial mechanisms of Zn(II)-based LDHs, but we also wanted to determine which is the dominant mechanism in different antibacterial tests assays. Apparently, in agar disc diffusion tests, the only existing mechanism was the release of Zn²⁺_{aq} ions (**Mechanism 2**) due to the limit of diffusion of LDH particles and the short lifespan of the possible generated ROS in agar medium. On the other hand, **Mechanism 2** was less pronounced in liquid broth environments, where the antibacterial effect was dominated by the direct contact mechanism (**Mechanism 1**). In buffer media employed in CFU count experiments, the release of metal ions was absent, and the antibacterial activity mechanism in liquid buffer media was governed solely by the direct contact mode of action (**Mechanism 1**). Whereas, the possible generated ROS (**Mechanism 3**) in presence of UVA light could further enhance the effect observed in liquid environments, yet not in agar solid ones. In this context, we would like to comment on several previous investigations dealing with antibacterial molecules-

loaded LDHs. In fact, most of these reports claimed that pristine LDHs could not provide an antibacterial effect and served only as a support/host for the antibacterial molecules. Indeed, not all pristine LDHs are non-antibacterial. Herein, we provide strong evidences about the superior ability of pristine Zn(II)-based LDHs to serve as efficient antibacterial agents through different governed mechanisms in several antibacterial test assays. Therefore, before claiming that pristine LDHs are non-antibacterial, one should take into consideration which antibacterial test is carried out and which mechanism is dominating in a certain environment.

We were also able to determine one great advantage of the antibacterial Zn(II)-based LDHs over simple Zn²⁺ ions salt, where the former was able to provide a prolonged bactericidal activity unlike the latter which possess a “one-shot” bactericidal effect, similar to that of traditional antibiotics. Such remarkable advantage also applies for the direct contact mechanism (**Mechanism 1**) in comparison to the simple release of Zn²⁺ ions (**Mechanism 2**). Therefore, direct contact mechanism (**Mechanism 1**) which is a dominating mode of action of antibacterial pristine Zn(II)-based LDHs in liquid environments qualifies these types of LDHs to act as efficient antibacterial agents with a prolonged effect.

This thesis work provides an insight for the promising applications of pristine Zn(II)-based LDH as efficient antibacterial agents. Once the mechanism of these LDHs is well known in a certain environment, one could easily tune their physico-chemical properties to match the targeted application. With the current presented antibacterial performance and the future improvement on LDH-based materials, we can reasonably aim for real and optimized applications as water purification, textile industries, antibacterial coatings and paint additives.

In case where the toxicity of these materials is tested and verified as non-toxic for human cells, their applications could even be extended to the medical field, *e.g.*, wound healing dressings, medical tools and bone implants. We can also take advantages of the presence of divalent metal or intercalating anion within the layer to address several dual applications. For example, the presence of aluminum within the structure would help in anticorrosion resistance, and therefore an anti-corrosive antibacterial coating could be obtained. The possibility of intercalating different anions within the interlayer such as antimicrobial peptides or lysozymes would yield of even a more efficient antimicrobial agent due to the dual effect of both loaded antibacterial molecules and Zn(II)-based LDHs.

Concerning the possible enhancement of LDHs antibacterial activity by the generation of ROS, one could also think of a way to induce ROS generation in presence of visible light rather than higher cost UV one. This could actually be achieved by doping Zn(II)-based LDHs with other divalent/trivalent metals. For example, a ternary Zn(II)Co(II)Al(III) or Zn(II)Cr(III)Al(III) LDHs able to absorb light in the visible region. Of course, the generation of ROS by these ternary LDHs should be confirmed and established in the first place by the previously suggested experimental protocols.

One last important point that we would like to highlight is that the antibacterial activity mechanisms of Zn(II)-based LDHs were studied against a single bacterial strain, *i.e.*, *S. aureus*. Therefore, the antibacterial performance of these LDHs should be determined against several types and strains of bacteria before generalizing its potential use in any antibacterial application field. Although we expect the same mechanisms governs the action of Zn(II)-based LDHs toward different bacterial strains, yet, similar experimental set ups to ours should be performed to validate such a hypothesis.

Annex I

Publications:

J. Awassa, D. Cornu, S. Soulé, C. Carteret, C. Ruby, S. El-Kirat-Chatel, Divalent metal release and antimicrobial effects of layered double hydroxides, *Appl. Clay Sci.* 216 (2022) 106369. DOI: 10.1016/j.clay.2021.106369.

J. Awassa, D. Cornu, C. Ruby, S. El-Kirat-Chatel, Direct contact, dissolution and generation of reactive oxygen species: How to optimize the antibacterial effects of layered double hydroxides, *Colloids Surf. B.* 217 (2022) 112623. DOI: 10.1016/j.colsurfb.2022.112623.

J. Awassa, S. Soulé, D. Cornu, C. Ruby, S. El-Kirat-Chatel, Understanding the role of surface interactions in the antibacterial activity of layered double hydroxide nanoparticles by Atomic Force Microscopy, *Nanoscale*, **in Press** (2022). DOI: 10.1039/D2NR02395D.



Divalent metal release and antimicrobial effects of layered double hydroxides

Jazia Awassa, Damien Cornu, Samantha Soulé, Cédric Carteret, Christian Ruby*, Sofiane El-Kirat-Chatel

Université de Lorraine, CNRS, LCPME, F-54000 Nancy, France

ARTICLE INFO

Keywords:

LDHs
Dissolution
Bacterial inhibition
Crystallinity
Zinc
Copper

ABSTRACT

Resistance to antimicrobial agents is responsible for major social and economic losses. The World Health Organization estimated 700,000 global deaths a year due to antimicrobial resistance. The use of layered double hydroxides (LDHs) as antibacterial materials could present a way to reduce the risk of bacterial infections and antibacterial resistance, by partial release of metallic ions in aqueous dispersion. The partial dissolution of different synthetic LDHs $M^{II}-Al^{III}$ ($M = Zn, Cu, Ni, Co, Mg$) was studied in Lysogeny Broth (LB) and Tryptic Soy Broth (TSB), growth media of *Escherichia coli* (*E. coli*) and *Staphylococcus aureus* (*S. aureus*) bacteria, respectively. The influence of several parameters (crystallinity, $M^{II}:Al^{III}$ ratio, type of intercalated anion (CO_3^{2-} , Cl^- , NO_3^- , ClO_4^-) and nature of M^{II} cations) was investigated. In the absence of any post-synthetic hydrothermal treatment, $Zn^{II}-Al^{III}$ LDH showed a release of Zn^{II} ions 6 times enhanced. Upon increasing $Zn^{II}:Al^{III}$ molar ratio to 3: 1 and exchanging carbonate anions with other anions having lower intercalating affinities, a similar effect was observed. The dissolution properties of $M^{II}-Al^{III}$ LDHs were correlated with the thermodynamic stability of their $M^{II}(OH)_2$ hydroxide counterparts with the exception of Cu^{II} -based LDH, which showed an amplified release of Cu^{II} due to its irregular structure presenting defects. Finally, the antibacterial activity was only noted for Zn^{II} and Cu^{II} -based LDHs. The antimicrobial effect of the studied LDHs was linked in the first place to the nature of divalent metal itself, and to the amount of released M^{II} ions into the culture media in the second place. This effect was more easily identified in $Zn^{II}-Al^{III}$ LDHs whose minimum inhibitory concentration was decreased significantly from 12 to 0.375 $mg \cdot mL^{-1}$ when higher amounts of Zn^{II} ions were released.

1. Introduction

Layered double hydroxides (LDHs) are clay lamellar solids having a structure based on the stacking of brucite-like sheets comprising divalent and trivalent metal hydroxides. These sheets hold a net positive charge which is compensated by negatively charged intercalating anions and water molecules present in the interlamellar region. The general formula of LDH can be expressed as: $[M(II)_{(1-x)}M(III)_x(OH)_2]^{x+} [A^{n-}]_{x/n} \cdot yH_2O^x$, where M(II) and M(III) are divalent and trivalent metal cations, respectively, and A^{n-} is an n-valent intercalating anion (Bini and Monteforte, 2018; Rives, 2001; Theiss et al., 2016). Due to their interesting properties, including anion exchangeability, compositional flexibility, and biocompatibility, LDHs have found themselves various technological applications such as catalysis (Yang et al., 2021), sorption of pollutants (Johnston et al., 2021), bio-sensors (Inmauddin, 2019), drug storage delivery (Bi et al., 2014), photocatalytic water remediation

(Wang et al., 2021) and antimicrobial materials (León-Vallejo et al., 2019; Mishra et al., 2018).

Nowadays, the fabrication of different materials avoiding biofouling or pathogenic bacteria proliferation is highly demanded (Forano et al., 2018). Under this aspect, LDH and LDH-composite materials were utilized in different antimicrobial applicational fields as water purification (Kamal et al., 2018; Moaty et al., 2016), food packaging (Cheng et al., 2019; Tammara et al., 2014), wound healing dressings (Zhang et al., 2020), and textile industries (Mallakpour et al., 2021). In fact, many surveys showed that LDHs possess high potential as carriers of biological antibiotics due to their controlled release rate (Djebbi et al., 2016; Salguero et al., 2020; Wang and Zhang, 2012). Antibiotics can treat bacterial infections, however, the excessive use of antibiotic had led to emergence of new resistant strains (El-Shahawy et al., 2018; Williams et al., 2019), where the World Health Organization (WHO) estimates 700,000 global deaths per year due to antimicrobial resistance

* Corresponding author.

E-mail address: Christian.ruby@univ-lorraine.fr (C. Ruby).

<https://doi.org/10.1016/j.clay.2021.106369>

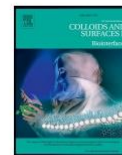
Received 14 October 2021; Received in revised form 18 November 2021; Accepted 27 November 2021

0169-1317/© 2021 Elsevier B.V. All rights reserved.



Contents lists available at ScienceDirect

Colloids and Surfaces B: Biointerfaces

journal homepage: www.elsevier.com/locate/colsurfb

Direct contact, dissolution and generation of reactive oxygen species: How to optimize the antibacterial effects of layered double hydroxides

Jazia Awassa, Damien Cornu^{*}, Christian Ruby, Sofiane El-Kirat-Chatel

Université de Lorraine, CNRS, LCPME, Nancy F-54000, France

ARTICLE INFO

Keywords:

LDH
Antibacterial mechanism
Direct contact
Metallic ions release
Antibacterial molecules release
ROS generation

ABSTRACT

Infections by pathogenic bacteria have been threatening several fields as food industries, agriculture, textile industries and healthcare products. Layered double hydroxides materials (LDHs), also called anionic clays, could be utilized as efficient antibacterial materials due to their several interesting properties such as ease of synthesis, tunable chemical composition, biocompatibility and anion exchange capacity. Pristine LDHs as well as LDH-composites including antibacterial molecules and nanoparticles loaded-LDHs were proven to serve as efficient antibacterial agents against various Gram-positive and Gram-negative bacterial strains. The achieved antibacterial effect was explained by the following mechanisms: (1) Direct contact between the materials and bacterial cells driven by electrostatic interactions between positively charged layers and negatively charged cell membranes, (2) Dissolution and gradual release over time of metallic ions or antibacterial molecules, (3) Generation of reactive oxygen species.

1. Introduction

Infectious diseases caused by microbial contamination are threatening human health all over the world [1]. Infections by pathogenic microorganisms are of serious concern to several fields such as food industries [2], textile industries [3], healthcare [4], and pharmaceutical products [5]. Traditional antibiotic drugs can usually treat bacterial infections, however, their extensive use had led to bacterial resistance and the spread of resistant strains [6,7]. Recent advances in the field of material science had opened up new gates for designing new antimicrobials based on synthetic inorganic materials [8–10]. In fact, inorganic antibacterial materials are considered advantageous over organic antibacterial materials due to their higher stability, recyclability and improved safety [11].

Among the various inorganic materials, layered double hydroxides (LDHs) were extensively studied due to their interesting properties as anion exchangeability, compositional flexibility, and biocompatibility, thus making them good candidates for several potential applications as catalysis [12,13], sorption of pollutants [14,15], biosensors [16], drug storage delivery [17,18], and antimicrobial materials [12,19–22]. Layered double hydroxides (LDHs), also known as anionic clays, are lamellar solids having a general formula expressed as $[M(II)_{1-x}M(III)_x(OH)_2]^{x+} [A_{x/n}^{n-}, yH_2O]^{x-}$, where M(II) and M(III) represent divalent and

trivalent metallic cations respectively, and A^{n-} is an exchangeable intercalating anion. The LDH structure (Fig. 1 A) is based on the stacking of positively charged brucite-like sheets comprising the divalent and trivalent cations linked by OH units coordinated at the octahedral positions forming sheets, which are then stacked up on top of each other to yield a layered structure similar to that of brucite mineral $[Mg(OH)_2]$ [23–27]. These brucite-like sheets hold a net positive charge which is compensated by negatively charged anions along with water molecules in the interlaminar regions.

LDH-based materials were utilized for several biological applications especially antimicrobial ones [8,29,30]. In fact, several surveys showed that LDHs possess high potential as carriers of functional antibacterial molecules as antibiotics because of their high biocompatibility, high chemical stability, and controlled release rate [31–33]. In addition, LDH can also be loaded with nanoparticles (NPs) such as gold, silver, copper and zinc oxide NPs which are known to treat several diseases caused by bacterial infections [19,34–38]. The assembly of metallic NPs in inorganic matrices as of LDHs can provide an inexpensive and biocompatible means to help limit the problem of aggregation and high exposure dose of free NPs [39]. Moreover, recent studies showed that even pristine LDHs, more precisely Zn and Cu-based pristine LDHs, could induce an efficient antibacterial without any further modification [22,40–43].

Each type of antibacterial LDH, e.g. antibacterial molecules-loaded

^{*} Corresponding author.

E-mail address: Damien.cornu@univ-lorraine.fr (D. Cornu).

<https://doi.org/10.1016/j.colsurfb.2022.112623>

Received 17 March 2022; Received in revised form 7 June 2022; Accepted 9 June 2022

Available online 11 June 2022

0927-7765/© 2022 Elsevier B.V. All rights reserved.

Revised ms Nanoscale R1: NR-COM-05-2022-002395

Understanding the Role of Surface Interactions in the Antibacterial Activity of Layered Double Hydroxide Nanoparticles by Atomic Force Microscopy

*Jazia Awassa, Samantha Soulé, Damien Cornu, Christian Ruby, Sofiane El-Kirat-Chatel**

Université de Lorraine, CNRS, LCPME, F-54000 Nancy, France

*Corresponding author: Sofiane El-Kirat-Chatel: elkirat1@univ-lorraine.fr

ABSTRACT

Understanding the mechanisms of interactions between zinc-based layered double hydroxides (LDHs) and bacterial surfaces becomes of great importance to improve the efficiency of these antibiotic-free antibacterial agents. In fact, the role of surface interactions in the antibacterial activity of zinc-based LDH nanoparticles compared to that of dissolution and generation of reactive oxygen species (ROS) is still not well documented. In this study we show that synthesized ZnAl LDH nanoparticles exhibit a strong antibacterial effect against *Staphylococcus aureus* and cause serious cell wall damages as revealed by growth test and atomic force microscopy (AFM)

1



Annex II

Oral Presentations:

J. Awassa, D. Cornu, S. Soulé, C. Carteret, C. Ruby, S. El-Kirat-Chatel, What are the physico-chemical parameters that influence the dissolution of antimicrobial layered double hydroxides? *XVIème colloque annuel du Groupe Français des Argiles*, Nantes, France, May 17th-20th, 2021.

J. Awassa, D. Cornu, S. Soulé, C. Carteret, C. Ruby, S. El-Kirat-Chatel, Antimicrobial effect of pristine layered double hydroxides: A study of the Mechanisms of interactions between LDHs and microorganisms, *LCPME Scientific Day*, Nancy, France, October 9th, 2021.

J. Awassa, D. Cornu, S. Soulé, C. Carteret, C. Ruby, S. El-Kirat-Chatel, Divalent metal release and antibacterial effects of layered double hydroxides, *XVII Clay Conference*, Istanbul, Turkey, July 25th-29th, 2022.

J. Awassa, S. Soulé, D. Cornu, C. Ruby, S. El-Kirat-Chatel, Deciphering the role of surface interactions in the antibacterial activity of layered double hydroxides by Atomic Force Microscopy, *XVII Clay Conference*, Istanbul, Turkey, July 25th-29th, 2022.

Poster Presentations:

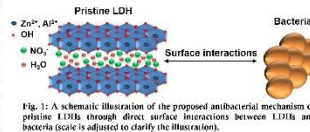
J. Awassa, S. Soulé, D. Cornu, C. Ruby, S. El-Kirat-Chatel, Deciphering the role of surface interactions in the antibacterial activity of layered double hydroxides by Atomic Force Microscopy, *NANOinBIO*, May-June 30th-5th, 2022.

J. Awassa, S. Soulé, D. Cornu, C. Ruby, S. El-Kirat-Chatel

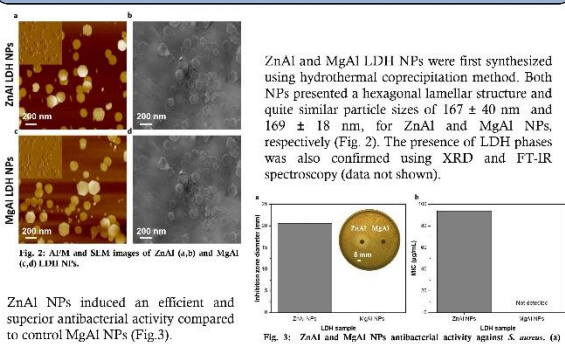
mail: elkirat@univ-lorraine.fr
Université de Lorraine, CNRS, LCPME, F-54000 Nancy, France

1. Introduction

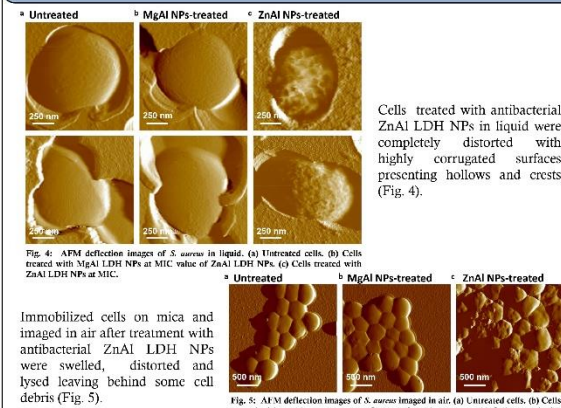
The excessive use of traditional antibacterial drugs, e.g. antibiotics, led to the emergence of new antibiotic-resistant bacteria.^{1,2} On the other hand, recent studies showed that pristine layered double hydroxides (LDHs), more precisely zinc-based LDHs, could serve as efficient antibiotic-free antibacterial agents.³⁻⁶ Cell wall damages by direct interactions with bacterial surfaces is one possible mechanism explaining the antibacterial activity of pristine LDHs (Fig. 1).^{3,4,6-9} Despite the fact that such hypothesis was proposed to explain the antimicrobial effect of pristine LDHs, the followed antibacterial mechanism is still not well understood, where the proof of evidence by real experimental set ups is still scarce. Herein, synthesized ZnAl LDH nanoparticles (NPs) showed a strong antibacterial effect against *Staphylococcus aureus* and caused serious cell wall damages as revealed by growth tests and atomic force microscopy (AFM) imaging, respectively. An original approach was used to functionalize AFM tips with LDHs to probe their interactions with live *S. aureus* cells by means of AFM-based single-particle force spectroscopy (SPFS).^{10,11} The force spectroscopy analysis revealed that antibacterial ZnAl LDHs possessed a specific recognition to *S. aureus* cells with high adhesion frequency and remarkable force magnitudes.



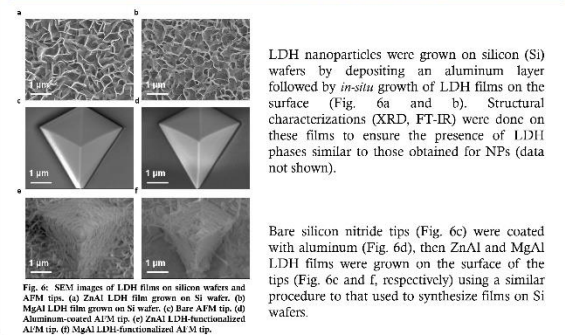
2. Antibacterial activity of ZnAl LDH NPs



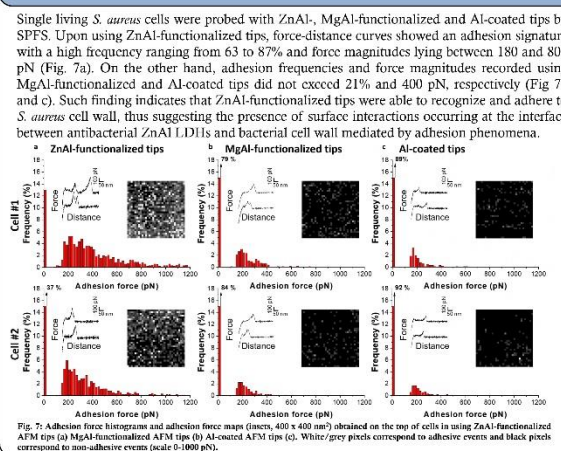
3. Bacterial cell wall damaged by ZnAl LDHs



4. LDH-functionalized tips for adhesion force measurements with bacteria



5. ZnAl NPs specific interactions with *S. aureus*



6. Conclusions

We investigated the role of surface interactions in the antibacterial activity of ZnAl LDH NPs. Synthesized ZnAl LDH NPs showed a strong antibacterial effect against *S. aureus* and caused serious cell wall damages. Further, we developed an original approach to functionalize AFM tips with LDH NPs in order to probe their interactions with live *S. aureus* cells by means of AFM-based SPFS. The force spectroscopy analysis revealed that antibacterial ZnAl NPs possessed a specific recognition to *S. aureus* cells with high adhesion frequency and remarkable force magnitudes. Such finding provided a first insight into the antibacterial mechanism of Zn-based LDHs by direct surface interactions through which they are able to recognize and adhere to bacterial cell walls which leads to their damage and subsequent growth inhibition (Fig. 8).

Fig. 8: A schematic illustration of antibacterial activity of ZnAl LDH NPs by direct surface interactions (scale is adjusted to clarify the illustration).

ACKNOWLEDGMENTS:
We would like to acknowledge the spectroscopy and microscopy Service Facility of SMI LCPME (Université de Lorraine-CNRS-<http://www.lcpme.cnrs-nancy.fr>). Jazia Awassa acknowledges the French Ministry of Higher Education for her PhD grant.

1. Chrisaki, E.; Marcina, M.; Tofanides, A. *J. Mol. Evol.* (88), 2020.
2. Nishihara, C. *Nat. Rev. Microbiol.* (19), 2020.
3. Awassa, J.; Cornu, D.; Ruby, C.; El-Kirat-Chatel, S. *Chemistry*, 2022.
4. Moaty, S.; Farzhang, A.; Khaled, R. *Mater. Sci. Eng. C* (68), 2016.
5. Awassa, J.; Cornu, D.; Soulé, S.; Carteret, C.; Ruby, C.; El-Kirat-Chatel, S. *Appl. Clay Sci.* (216), 2022.
6. Datta, S.; Jana, T.; Mukherjee, S.K.; Maiti, K.; Datta, A.; Kumar, A.; Chatterjee, K. *ChemistrySelect* (5), 2020.
7. Leon-Vallejo, A.M.; Velázquez-Herrera, E.D.; Semplici, A.; Landeta-Cortes, G.; Ferrer, G. *Appl. Clay Sci.* (180), 2019.
8. Tahiri, H.A.; Adilji, M.; Ammam, A.; Medjahed, B.; Guetzen, B.; Ramdani, A.; Bendjedouch, C.K.; Bouachiki, N.; Chami, N. *Rev. Roum. Chim.* (66), 2020.
9. Lebo-Sanchez, M.; Nájera-Medriker, G.; Luna, G.; Segura-Pérez, V.; Rivera, J.A.; Ferrer, G. *Appl. Clay Sci.* (153), 2018.
10. G. Hinterdorfer, P. and Dufrene, Y. P. *Nat. Methods* (3), 2006.
11. Beausart, A.; Feuille, C.; El-Kirat-Chatel, S. *Nanoscale* (12), 2020.

Résumé étendu de la thèse en français

Tableau des figures	228
1. Introduction générale	229
2. Résumé des travaux de recherche : Discussion générale	230
3. Conclusions et perspectives générales	235

Tableau des figures

Figure 1. Une illustration schématique de l'étude systématique visant à étudier les différents paramètres physico-chimiques affectant l'activité antibactérienne des HDLs gouverné par le mécanisme de libération des ions métalliques divalents.	231
Figure 2. Une illustration schématique des interactions sondées entre les cellules vivantes de <i>S. aureus</i> et les pointes AFM HDL-fonctionnalisées.....	233
Figure 3. Une illustration schématique des dommages topographiques et composition biochimique des cellules de <i>S. aureus</i> induit par les NPs ZnAl HDL dans des conditions sombres et UVA..	234
Figure 4. Une représentation schématique de la contribution du contact direct (Mécanisme 2) et de la libération d'ions (Mécanisme 1) à l'effet antibactérien des NPs ZnAl HDL.....	235

1. Introduction générale

La contamination bactérienne et les infections associées par les microorganismes pathogènes sont reconnues depuis plusieurs années comme une menace critique affectant la qualité des soins en santé humaine dans le monde entier. Avec la propagation rapide des phénomènes de résistance antimicrobiennes causés par l'utilisation excessive d'antibiotiques, un intérêt croissant pour la fabrication de nouveaux agents antibactériens est apparu. Dans ce contexte, l'utilisation d'hydroxydes doubles lamellaires (HDL) et de matériaux composites contenant des HDL en tant qu'agents antibactériens efficaces pourrait devenir une solution à ce problème.

En fait, de nombreuses études ont montré que les HDL possèdent un potentiel élevé en tant que vecteurs de molécules antibactériennes en raison de leur capacité à intercaler des molécules anioniques de grande taille. Cependant, la majorité des biomolécules intercalées est basée sur des antibiotiques commerciaux, ce qui limite l'utilisation d'hybrides molécules antibactériennes-HDL contre les bactéries résistantes. De plus, certains travaux ont porté sur l'ajout de nanoparticules (NPs) antimicrobiennes, par exemple, Ag⁰, Au⁰ et ZnO, dans la matrice des HDL pour fournir un effet antibactérien efficace. Bien que ces composites à base d'HDL chargés de NPs aient montré des effets antibactériens significatifs, leur éventuelle toxicité reste un défi majeur pour leur utilisation dans des applications antibactériennes.

D'autre part, certaines études récentes ont prouvé que les HDL non modifiés, plus précisément les HDL à base de Zn(II), pouvaient également agir comme des matériaux antimicrobiens efficaces. Selon la littérature, les mécanismes responsables de l'effet antibactérien des HDL sont : **(1)** les interactions par contact direct entre la surface des HDLs et la paroi bactérienne, **(2)** la libération d'ions métalliques divalents, et **(3)** la génération d'espèces réactives de l'oxygène (ROS) biologiquement toxiques par les HDL en présence de lumière. Malgré le fait que ces hypothèses aient été proposées pour expliquer les effets antibactériens des HDL, aucun montage expérimental n'a été mis en place pour valider ces mécanismes ni pour déterminer quel mécanisme domine l'activité antibactérienne.

Ce travail de thèse a porté sur l'étude des différents mécanismes antibactériens suggérés préalablement pour les HDL à base de Zn(II) en abordant plusieurs questions : « Les mécanismes proposés antérieurement existent-ils vraiment ? », « Comment les valider expérimentalement ? »,

« Quels paramètres physico-chimiques contrôlent l'action antibactérienne des HDL ? », « Quel rôle chaque mécanisme joue-t-il dans les différents tests antibactériens ? », et enfin « Quel mécanisme domine l'action antibactérienne ? »

Dans un premier temps, les propriétés générales des HDL sont décrites dans le **Chapitre 1**, suivies d'une explication des différents types et mécanismes d'activité antibactérienne des HDL et des composites des HDL précédemment étudiés dans la littérature. À la fin de ce chapitre, nous soulignons le grand avantage des HDL non modifiés par rapport aux composites des HDL et l'importance de mieux comprendre leur mode d'action antibactérien. Dans le **Chapitre 2**, nous fournissons une explication détaillée des différentes méthodes et techniques expérimentales utilisées pour atteindre les objectifs de ce travail. Nous commençons à aborder notre véritable travail de recherche dans le **Chapitre 3**, où nous présentons une étude globale menée sur différents échantillons d'HDLs non modifiés et démontrons que les paramètres physico-chimiques influencent l'activité antibactérienne des HDL contre *Staphylococcus aureus* et *Escherichia coli* et en particulier *via* la libération d'ions métalliques divalents (**Mécanisme 2**). Dans le **Chapitre 4**, nous passons à l'étude du mécanisme antibactérien des HDLs à base de Zn(II) par des interactions de contact direct (**Mécanisme 1**) en comparant l'efficacité antibactérienne des HDL de taille micrométrique et nanométrique et en utilisant la microscopie à force atomique (AFM) comme pour déterminer l'adhésion entre la surface des HDL et les bactéries *S. aureus* vivantes. De plus, l'amélioration de l'effet antibactérien des HDL à base de Zn(II) en présence d'un rayonnement UVA par la génération possible de ROS (**Mécanisme 3**) est abordée au **Chapitre 5**. Après avoir fourni des preuves expérimentales sur ces trois mécanismes, le rôle de chaque mécanisme contribuant à l'activité antibactérienne des HDL à base de Zn(II) est finalement déduit au **Chapitre 6**. Une telle évaluation nous permet enfin de déterminer le mécanisme dominant qui gouverne l'activité antibactérienne des HDL à base de Zn(II) contre la bactérie *S. aureus* dans différents tests antibactériens.

2. Résumé des travaux de recherche : Discussion générale

Lors d'une première étude, nous avons montré que la dissolution des ions métalliques divalents constitutifs (M^{2+}_{aq}) des poudres des HDLs non modifiés dans les milieux de culture liquide dépend fortement de leurs différentes propriétés physicochimiques, *e.g.*, la nature du métal divalent

constitutif M(II), la cristallinité, le rapport molaire M(II)/Al(III), ainsi que la nature de l'anion intercalé dans l'espace interlamellaire (A^{n-}). Ces paramètres contrôlent à leur tour l'effet antibactérien des HDLs (**Figure 1**).

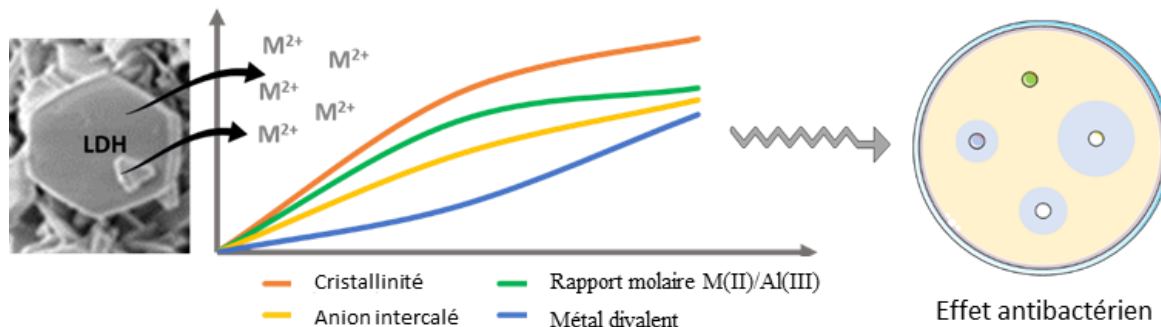


Figure 1. Une illustration schématique de l'étude systématique visant à étudier les différents paramètres physico-chimiques affectant l'activité antibactérienne des HDLs gouverné par le mécanisme de libération des ions métalliques divalents.

Les propriétés de dissolution de différentes HDL M(II)Al(III) en ions M^{2+} dans des milieux de culture bactériens sont liées à la stabilité thermodynamique de leurs homologues hydroxyde $M(OH)_2$. Une exception a été révélée pour les HDL à base de Cu(II) qui ont libéré une grande quantité de Cu^{2+} , probablement en raison de leur très faible cristallinité et de leur structure irrégulière présentant des défauts, ou en raison de leur grande affinité pour former des complexes organométalliques avec les composants du milieu de culture.

Le composé $Zn_2Al:CO_3$ HDL non exposée au traitement hydrothermal a montré plus de défauts et de petites particules agrégées et a libéré plus d'ions zinc dans le milieu de culture. De même, l'augmentation du rapport M(II)/Al(III) dans les échantillons des HDL à base de Zn(II) a également entraîné une libération accrue d'ions Zn^{2+} , probablement en raison de la plus grande quantité des ions Zn^{2+} initialement présents dans l'HDL et/ou en raison de la diminution de sa cristallinité. De plus, la cristallinité et la structure des poudres ont également été influencées par les réactions d'échange anionique qui visaient à éliminer les anions carbonate de Zn(II)Al(III) et à les échanger avec d'autres anions intercalants (chlorure, nitrate et perchlorate). Ainsi, Les poudres résultant de la réaction d'échange d'anions présentent une structure plus défectueuse avec des tailles de cristallites et des agglomérats plus petits, conduisent à une libération amplifiée d'ions Zn^{2+} .

L'activité antibactérienne des HDL M(II)Al(III) testées a été déterminée et seules les HDL à base de Zn(II) et de Cu(II) ont présenté un effet inhibiteur contre *E. coli* et *S. aureus*. L'activité

antimicrobienne supérieure des HDL Zn(II)Al(III) par rapport aux autres échantillons M(II)Al(III), même lorsqu'une quantité inférieure de M^{2+} en était libérée, est liée à la nature de leur métal divalent constitutif, *i.e.*, Zn(II). De plus, l'effet inhibiteur antibactérien des HDL M(II)Al(III), évalué à l'aide de tests de diffusion sur disque de gélose, est similaire à celui de leurs homologues correspondants aux sels de métaux divalents M(II), soutenant ainsi le mécanisme antibactérien des HDL par la libération des ions M^{2+} (**Mécanisme 2**). Cette hypothèse a été validée par la diminution de la concentration minimale inhibitrice (CMI) de l'HDL Zn(II)Al(III) avec des concentrations croissantes de Zn^{2+} libéré, initialement contrôlée par les différents paramètres physico-chimiques étudiés.

Après avoir validé le mécanisme de libération des ions métalliques divalents pour les HDL à base de Zn(II) (**Mécanisme 2**), nous avons étudié le mécanisme des interactions directes de surface entre les HDL et la paroi bactérienne (**Mécanisme 1**). L'activité antimicrobienne des NPs ZnAl HDL contre les bactéries *S. aureus* a été déterminée à l'aide de méthodes de diffusion sur disque d'agar et de macro-dilution en milieu de culture et comparée à l'effet des NPs MgAl HDL et des HDL ZnAl de taille micrométrique. La comparaison entre les propriétés antibactériennes des HDL ZnAl nanométriques et micrométriques a montré que les propriétés antibactériennes des NPs des ZnAl HDL vont au-delà de la simple dissolution des ions Zn^{2+} , et qu'elles sont également liées aux interactions de surface. De plus, l'imagerie AFM a révélé que l'inhibition de la croissance par les NPs des ZnAl HDL est associée à d'importantes modifications topographiques de la paroi cellulaire, tandis que les cellules traitées avec MgAl LDH NPs restent intactes. Ensuite, nous avons développé une approche originale pour faire croître des films d'HDL *in-situ* sur des pointes AFM et sonder l'interaction entre les HDL et les cellules vivantes de *S. aureus* en utilisant la spectroscopie de force (SF) basée sur l'AFM (**Figure 2**). Les caractérisations physico-chimiques basées sur la diffraction des rayons X (DRX) et la spectroscopie Infrarouge à transformée de Fourier (FT-IR) ont révélé que les films d'HDL présentaient des propriétés comparables à celles des NPs des HDL. Par rapport aux contrôles, les cartes de SF enregistrées avec des pointes ZnAl HDL-fonctionnalisées présentent une forte adhésion (centaines de pN) à haute fréquence, ce qui suggère que l'effet antimicrobien des NPs LDH à base de Zn(II) est au moins en partie dû à des interactions spécifiques et directes avec la paroi bactérienne. Cette découverte a fourni des informations précieuses sur la corrélation entre la capacité des HDL à base de Zn(II) à adhérer aux

surfaces bactériennes et leur capacité à inhiber la croissance des bactéries par les interactions de surface.

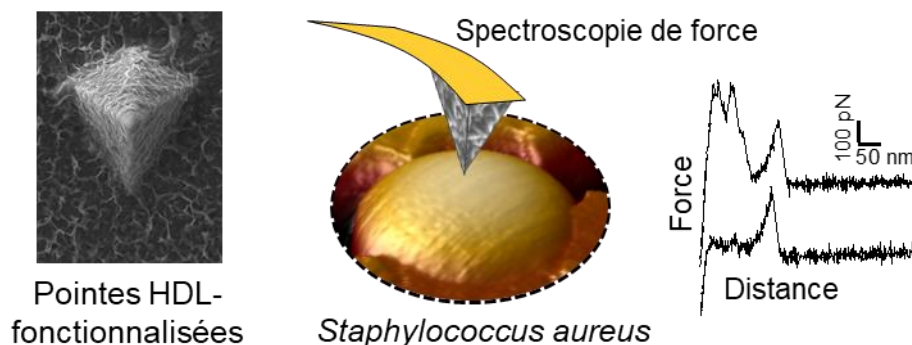


Figure 2. Une illustration schématique des interactions sondées entre les cellules vivantes de *S. aureus* et les pointes AFM HDL-fonctionnalisées.

De plus, l'efficacité bactéricide des NPs des ZnAl HDL contre *S. aureus* a été améliorée de 11% en présence de lumière UVA probablement en raison de la génération de ROS par les HDL en réponse à l'irradiation UVA (**Mécanisme 3**). Cela a également été associé à une augmentation du taux de mortalité des bactéries pendant la période d'irradiation. L'activité bactéricide des ROS produites serait moins prononcée en présence d'histidine agissant comme un piègeur de ROS. Un tel résultat a fourni une première preuve concernant la génération de ROS par les NPs ZnAl LDH en présence de lumière UVA. De plus, la spectroscopie FT-IR a révélé des changements remarquables dans les composants structurels des cellules imposés par le traitement des NPs des ZnAl LDH dans des conditions d'obscurité et en présence de rayonnement UVA, avec des altérations plus prononcées pour ces dernières (**Figure 3**). Les impacts de telles altérations ont été mis en évidence en observant la morphologie et les caractéristiques texturales des cellules *S. aureus* exposées au traitement avec les NPs d'HDL. Les cellules sont complètement déformées et présentent des surfaces rugueuses, en particulier lors du traitement avec les NPs d'HDL et l'irradiation UVA. Tous ces résultats suggèrent la présence d'un effet double entre les NPs des ZnAl LDH et les ROS générés pour fournir un effet antibactérien amplifié.

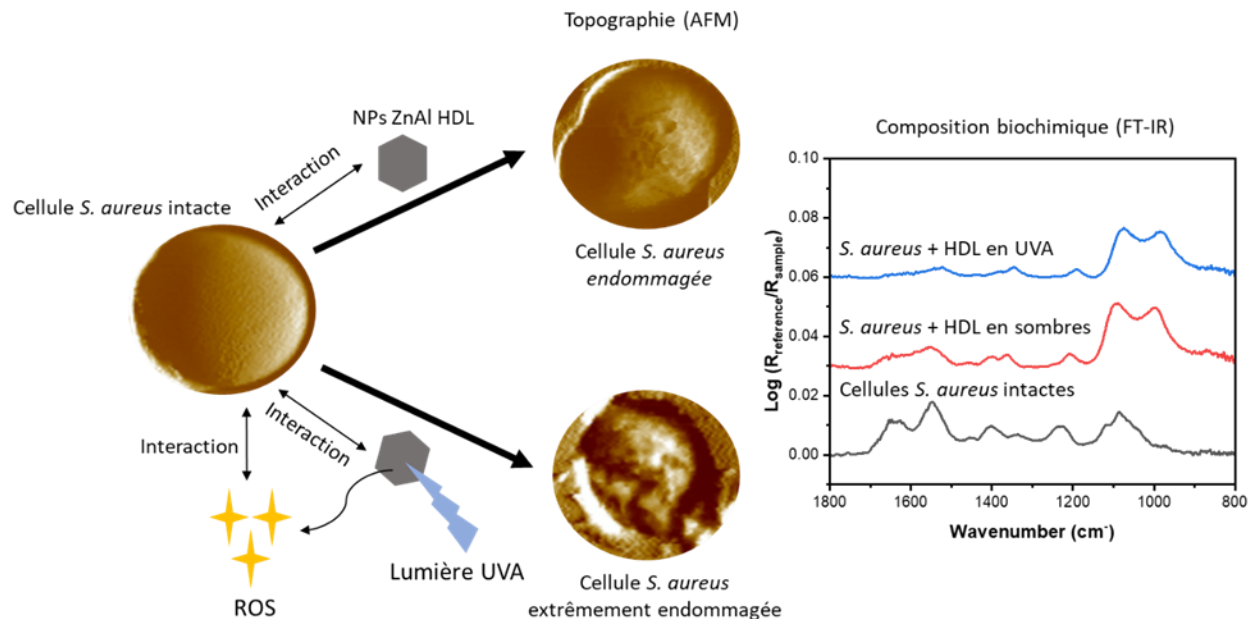


Figure 3. Une illustration schématique des dommages topographiques et composition biochimique des cellules de *S. aureus* induit par les NPs ZnAl HDL dans des conditions sombres et UVA.

Après avoir fourni des preuves expérimentales sur les trois mécanismes suggérés, la contribution de chaque mécanisme sur l'activité antibactérienne des HDLs à base de Zn(II) a été déterminée. La contribution de la libération d'ions métalliques divalents et des interactions directes de surface à l'activité antibactérienne des NPs des ZnAl HDL a été évaluée en utilisant l'EDTA agissant comme un piègeur d'ions $\text{Zn}^{2+}_{\text{aq}}$ libérés hors de l'HDL. Les propriétés antibactériennes des NPs ZnAl LDH dans les tests de diffusion sur disque de gélose (basés sur des phénomènes de diffusion) ont été uniquement attribuées à la libération d'ions $\text{Zn}^{2+}_{\text{aq}}$ (**Mécanisme 2**), alors que la contribution du mécanisme de contact direct (**Mécanisme 1**) a été exclue de ces tests en raison de la limite de diffusion des particules dans les gels d'agar. Au contraire, l'activité antibactérienne des NPs d'HDL ZnAl dans les tests CMI effectués dans du milieu de culture TSB liquide est dominée par le mécanisme d'interactions directes de surface, alors que la libération d'ions métalliques divalents ne contribue qu'à 20-24% à l'activité antibactérienne dans ce type d'expériences. Cette contribution limitée a également été démontrée par les dommages moins importants de la paroi cellulaire induits par les ions $\text{Zn}^{2+}_{\text{aq}}$ libérés. De plus, les ions $\text{Zn}^{2+}_{\text{aq}}$ libérés par les NPs des HDL ZnAl n'ont pas participé à l'efficacité bactéricide déterminée par les expériences de comptage d'UFC (unité formant colonie) en raison du très faible profil de libération des ions Zn^{2+} dans le tampon TBS.

Enfin, nous souhaitons souligner le grand avantage des HDL ZnAl par rapport au simple sel d'ions Zn^{2+} car les premiers peuvent fournir une activité bactéricide prolongée contrairement aux seconds qui possèdent un effet bactéricide « one shot ». Une telle démonstration s'applique également au mécanisme de libération des ions Zn^{2+}_{aq} car les mêmes espèces, *i.e.*, les ions Zn^{2+} , sont utilisées pour obtenir l'effet antibactérien. Par conséquent, le mécanisme de contact direct (**Mécanisme 1**) qui est un mode d'action dominant des HDL antibactériens à base de Zn(II) dans un environnement liquide montre que ces HDL peuvent agir comme des agents antibactériens efficaces avec un effet prolongé et plus prononcé sur la topographie des cellules (**Figure 4**).

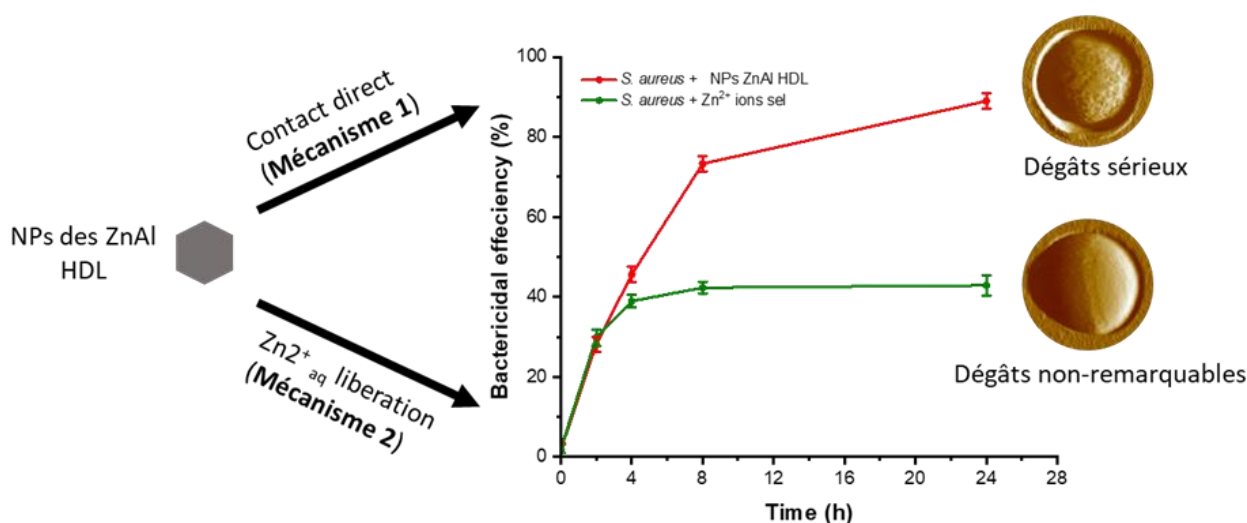


Figure 4. Une représentation schématique de la contribution du contact direct (**Mécanisme 2**) et de la libération d'ions (**Mécanisme 1**) à l'effet antibactérien des NPs ZnAl HDL.

3. Conclusions et perspectives générales

Grâce au travail réalisé au laboratoire LCPME au sein de l'équipe Chimie et Spectroscopie des Interfaces (CSI) aux compétences multidisciplinaires en physico-chimie, microbiologie et biophysique, nous avons pu aborder le sujet des « Mécanismes Antibactériens des Hydroxydes Doubles Lamellaires à Base de Zinc ». Notre travail s'est basé sur des approches expérimentales originales nous permettant de mettre en œuvre des analyses spectroscopiques et microscopiques pour déterminer les mécanismes antibactériens des HDL.

Nos principaux résultats suggèrent que l'activité antibactérienne des HDL non modifiés dépend en premier lieu de la nature du métal divalent constitutif, ce qui nous a poussé à nous concentrer sur

les HDLs à base de Zn (II) présentant le plus grand effet antibactérien. L'activité antibactérienne de ces types d'HDL était plus prononcée dans le cas où les échantillons libéraient plus d'ions Zn^{2+}_{aq} dans le milieu de culture liquide, validant ainsi le mécanisme antibactérien suggéré de dissolution de métal divalent (**Mécanisme 2**). L'activité antibactérienne des HDL à base de Zn(II) était également contrôlée par des interactions de surface directes entre les HDL et la paroi de *S. aureus* (**Mécanisme 1**). Cela a été clairement mis en évidence par l'effet antibactérien supérieur des nanoparticules d'HDL présentant une plus grande surface d'interactions par rapport à celle des HDLs de taille micrométrique. La spectroscopie de force basée sur l'AFM a, en outre, validé la présence d'interactions de surface spécifiques entre les HDL à base de Zn(II) et les bactéries *S. aureus*, causant d'importants dommages à leurs parois. De plus, l'augmentation de l'activité antibactérienne des HDL à base de Zn (II) pourrait également être obtenue par la génération de ROS (**Mécanisme 3**) en présence de rayonnement UVA, avec des dommages structurels, morphologiques et biochimiques des parois bactériennes plus prononcés.

En plus de valider les trois mécanismes antibactériens suggérés pour les HDL à base de Zn(II), nous voulions également déterminer précisément la contribution de chaque mécanisme dans les différents tests antibactériens réalisés. Apparemment, dans les tests de diffusion sur disque d'agar, le seul mécanisme existant serait la libération d'ions Zn^{2+}_{aq} (**Mécanisme 2**) en raison de la limite de diffusion des particules de HDL. D'autre part, le mécanisme 2 était moins prononcé dans le milieu de culture liquide, où l'effet antibactérien était gouverné par le mécanisme de contact direct (**Mécanisme 1**). Dans les tampons, la libération d'ions métalliques était absente et le mécanisme d'activité antibactérienne était régi uniquement par le mode d'action par contact direct (**Mécanisme 1**). Enfin, les ROS qui seraient générés en présence de lumière UVA (**Mécanisme 3**) pourraient renforcer l'effet observé en environnement liquide, mais pas en environnement solide (agar).

Ce travail de thèse donne un aperçu des applications prometteuses des HDL à base de Zn(II) en tant qu'agents antibactériens efficaces. Une fois le mécanisme des HDL déterminé dans un certain environnement, on peut donc ajuster leurs propriétés physico-chimiques pour répondre à l'application visée. Avec les performances antibactériennes effectivement observées et l'amélioration future des matériaux HDL, nous pouvons raisonnablement envisager des applications comme la purification de l'eau, les revêtements antibactériens et les additifs duciment. Dans la mesure où la toxicité éventuelle de ces matériaux serait contrôlée, leurs applications

pourraient même être étendues au domaine médical. Par exemple, les pansements cicatrisants, les outils médicaux et les implants osseux. Nous pouvons également tirer parti de la présence d'un métal divalent ou d'un anion intercalant pour répondre à plusieurs applications double. Par exemple, la présence d'aluminium contribuerait à la résistance anticorrosion, et donc un revêtement antibactérien anticorrosif pourrait être obtenu.

Un dernier point important que nous voudrions souligner est que les mécanismes de l'activité antibactérienne des HDL à base de Zn(II) ont été étudiés vis-à-vis d'une seule souche bactérienne, *i.e.*, *S. aureus*. Par conséquent, la performance antibactérienne des HDL doit être déterminée contre plusieurs types et souches de bactéries avant de généraliser son utilisation potentielle comme agent antibactérien. Bien que nous nous attendions à ce que les mêmes mécanismes régissent l'action des HDL à base de Zn(II) envers différentes souches bactériennes, des montages expérimentaux similaires aux nôtres devraient être réalisés pour valider une telle hypothèse.

Antibacterial mechanisms of pristine zinc-based layered double hydroxides

Abstract:

Layered double hydroxides (LDH) are solid compounds constituted by the stacking of divalent M(II) and trivalent M(III) metal hydroxide sheets separated by an interlayer of anions and water molecules. Due to the versatility of LDH in terms of their tunable physico-chemical properties, a growing interest arises for investigating their different antibacterial activity mechanisms. This thesis work aims at studying the different proposed hypotheses explaining the antibacterial effect of pristine zinc-based LDHs: (1) direct interactions between the surface of LDH and bacterial cell walls, (2) release of constituent divalent metal ions, (3) generation of reactive oxygen species (ROS). First a global investigation was performed to determine the different physico-chemical parameters influencing the antibacterial activity of pristine M(II)Al(III) LDHs (M= Zn, Cu, Ni, Co, Mg). The antimicrobial effect of LDHs against Gram-positive *Staphylococcus aureus* and Gram-negative *Escherichia coli* bacteria was linked in the first place to the nature of divalent metal itself, and to the amount of released M^{2+}_{aq} ions into the culture media in the second place. This effect was more easily identified in Zn(II)-based LDHs possessing the strongest antibacterial activity and whose antibacterial properties depended on their release profile of Zn^{2+}_{aq} ions (Mechanism 2) initially controlled by the different physico-chemical parameters. Moreover, the direct contact mechanism (Mechanism 1) was validated for Zn(II)-based LDHs by comparing the antibacterial activity of micron-sized LDHs against *S. aureus* to that of LDH nanoparticles (NPs) exhibiting a greater antibacterial effect. The presence of specific surface interactions between Zn(II)-based LDHs and the cell wall of *S. aureus* was further validated by atomic force microscopy-based force spectroscopy (AFM-FS). The enhancement of the antibacterial properties of Zn(II)-based LDH NPs by ROS generation (Mechanism 3) in presence of UVA light was also assessed. After providing experimental evidences about the three suggested mechanisms, the role of each mechanism contributing to the antibacterial activity of Zn(II)-based LDHs in different antibacterial tests assays was determined.

Keywords: LDH, Zinc, Antibacterial mechanism, Direct surface interactions, Divalent metal ions release, ROS generation, AFM.

Mécanismes antibactériens des hydroxydes doubles lamellaires à base de zinc

Résumé :

Les hydroxydes doubles lamellaires (HDL) sont des composés solides constitués par un ensemble de feuilles d'hydroxydes métalliques divalents M(II) et trivalents M(III) entre lesquels s'insèrent des anions et des molécules d'eau. En raison de la flexibilité des HDL en termes de propriétés physico-chimiques, l'étude des différents mécanismes antibactériens qui leurs sont associés présente un intérêt croissant. Ce travail de thèse vise à étudier différentes hypothèses proposées pour expliquer l'effet antibactérien des hydroxydes doubles lamellaires (HDL) à base de zinc : (1) interactions directes entre la surface des HDL et les parois bactériennes, (2) libération d'ions métalliques divalents en solution depuis les feuillets des HDL, (3) génération d'espèces réactives de l'oxygène (ROS). Lors d'une première étude, une investigation globale a été réalisée pour déterminer les différents paramètres physico-chimiques influençant l'activité antibactérienne des HDLs M(II)Al(III) (M= Zn, Cu, Ni, Co, Mg). L'effet antimicrobien des HDLs contre les bactéries Gram-positives *Staphylococcus aureus* et Gram-négatives *Escherichia coli* a été corrélé en premier lieu à la nature du métal divalent, et en second lieu à la quantité d'ions M^{2+}_{aq} libérés dans le milieu de culture. Cet effet était plus prononcé pour les HDLs à base de Zn(II) possédant la plus forte activité antibactérienne et dont les propriétés antibactériennes dépendent du profil de libération des ions Zn^{2+}_{aq} (Mécanisme 2) contrôlée initialement par les différents paramètres physico-chimiques étudiés. De plus, rôle du contact direct (Mécanisme 1) a été validé pour les HDLs à base de Zn(II) en comparant l'activité antibactérienne d'HDLs de taille micrométrique contre *S. aureus* à celle des nanoparticules (NPs) d'HDL présentant un effet antibactérien supérieur. La présence d'interactions spécifiques entre les HDLs à base de Zn(II) et la paroi de *S. aureus* a été validée par microscopie à force atomique en mode spectroscopie de force (AFM-FS). L'amélioration des propriétés antibactériennes des NPs d'HDL à base de Zn(II) par la génération de ROS (Mécanisme 3) en présence de lumière UVA a également été évaluée. Après avoir fourni des preuves expérimentales sur les trois mécanismes suggérés, la contribution de chaque mécanisme dans l'activité antibactérienne des HDLs à base de Zn(II) a été déterminé.

Mots-clés : HDL, Zinc, Mécanisme antibactérien, Interactions directes de surface, Libération d'ions métalliques divalents, Génération de ROS, AFM.

